Universitat Autònoma de Barcelona

Nickel and Cobalt Bis(imino)pyridine Complexes as Catalysts for the Hydrogen Evolution Reaction

Bing Jiang

Universitat Autònoma de Barcelona

Nickel and Cobalt Bis(imino)pyridine Complexes as Catalysts for the Hydrogen Evolution Reaction

Bing Jiang

PhD Thesis

Programa de Doctorat en Química

Dr. Xavier Sala, Dr. Nuria Romero & Prof. Antoni Llobet

Departament de Química

Facultat de Ciències

2019

Memòria presentada per aspirar al Grau de Doctor en Química per Bing Jiang

Bing Jiang

Vist i plau

Dr. Xavier Sala Román

Departament de Química
Facultat de Ciències
Universitat Autònoma de Barcelona

Dr. Nuria Romero Fernández

Departament de Química
Facultat de Ciències
Universitat Autònoma de Barcelona

Prof. Antoni Llobet Dalmases

Departament de Química
Facultat de Ciències
Universitat Autònoma de Barcelona
Institute of Chemical Research of Catalonia (ICIQ)

Bellaterra, 03 de Julio de 2019

Acknowledgements

Looking back over the past years studying in Barcelona, a definitely extraordinary period for me, I would like to express my appreciation to all the people who contributed during my Ph. D. student stage to either my work or life. Were it not for their support, I would hardly be where I am today.

First and foremost, I would like to acknowledge my advisors Dr. Xavier Sala, Prof. Antoni Llobet for accepting me into the SelOxCat group and therefore allowing me to start my doctoral studies in the Autonomous University of Barcelona (UAB). Throughout the whole period, Xavier and Antoni tried their best to provide necessary conditions for improving the research project. They were so patient, supportive and encouraging in guiding me towards the right direction with the right way. Special thanks to Antoni for giving me the opportunity to work several months in Institute of Chemical Research of Catalonia (ICIQ), so that I could experience in another out-standing research institute. I also must express my sincere gratitude to Dr. Nuria Romero for her meticulous help since she joined our group and became one of my supervisors. Nuria was always available whenever I needed her to discuss various issues, and really helped me solve many problems, big or small. Without a shadow of doubt, all my supervisors built the foundation for everything towards my doctoral degree. Thanks from my deep heart to them not only for completing this Thesis, what also meaningful for me is the keen and rigorous attitude with regard to chemical research as all of them showed to me.

I would also like to acknowledge Dr. Jordi García-Antón, Dr. Lluís Escriche and Dr. Roger Bofill for giving nice talk, suggestion and encouragement so many times. Thanks Jordi for helping me integrate into this collective from the very beginning, and regular Urbasa time will be part of my memory.

This project could not be carried out without the work from research support units in UAB and ICIQ. So I do appreciate the Servei d'Anàlisi Química (SAQ) for elemental analysis and SeRMN for NMR experiments in UAB, specially the kindness of Pau Nolis for assigning NMR spectra of cobalt complexes. Thanks also to the Heterogeneous Catalysis Unit and X-Ray Diffraction Unit in ICIQ who are responsible for all the MS, EPR and crystallography analysis, respectively, in this Thesis.

It was such a pleasure to work in a friendly and harmonious atmosphere with my lovely lab-mates during my UAB time. I extend my gratitude to Haijie, Rosa, Jonathan, Jordi C, Nacho, Laura for every single help in the work and fun in the life, and particularly to Marcos who offered me tremendous support for electrochemistry and later communication with X-ray and MS units in ICIQ. Also thanks to master and TFG students who shared time together in SelOxCat, Javi, Albert, Álex, Laia, Laura S, Miquel, Lluís S, Victor, Fernando, Hector, Selene, Èric.

Besides, I cannot forget all the nice people I met in Tarragona when I work in Llobet's group in ICIQ. Thanks first go to Dr. Carolina Gimbert who guided me with her expertise in molecular catalysts. I also must thank others in the group, Mª José, Chuanjun, Abi, Asmau, Sergi, Yuanyuan, Primavera, Marta, Navid, Laura D, Jan H, Nataliia, Roc. Pablo is specially acknowledged for running DFT calculations which is of great importance.

I want to say million thanks to all my friends who spent the past years with me in Barcelona, the people in Inorganic Chemistry, Changyong, Merche, Quim, Natalia, Jordi B, Katia, Jose, Míriam, Dani, João, Selene, et al.; the Chinese friends in UAB, Ziliang, Yanan, Jinqiang, Rong, Zhijie, Hong, Yu, Peng, Fangchang, Yuping, Mengdi, Chunyi, Chengcheng, Jie, et al.

I am very much indebted to my beloved parents for their constant confidence, understanding and support. Their love is always telling me that family is my eternal harbor and backing. Thanks to dear Haixia because she shared all my emotions, the encouragement and warmth from her helped me through the tough times.

Finally, I would like to thank Chinese Scholarship Council (CSC) for funding me to study abroad. I also greatly appreciate the funding from Ministerio de Ciencia, Innovación y Universidades (CTQ2011-26440 & CTQ2015-64261-R) which supported the present work.

Glossary of Terms and Abbreviation

1D	Monodimensional
2D	Bidimensional
BF_4^-	Tetrafluoroborate
Bn	benzyl
COSY	Correlation Spectroscopy
Cp^*	1,2,3,4,5-Pentamethylcyclopentadiene
CPE	Controlled Potential Electrolysis
CV	Cyclic Voltammetry
δ	Chemical Shift
DCE	1,2-Dichloroethane
DCM	Dichloromethane
DFT	Density Functional Theory
DMF	N,N-dimethylformamide
E	Potential
$E_{1/2}$	Half Wave Potential
ε	Extinction Coefficient
EPR	Electron Paramagnetic Resonance
ESI-MS	Electrospray Ionization Mass Spectrometry
F	Faraday Constant
GHG	Greenhouse Gas
HEC	Hydrogen Evolution Catalyst
HER	Hydrogen Evolution Reaction
HMBC	Heteronuclear Multiple Bond Correlation
HSQC	Heteronuclear Single-Quantum Correlation
i	Current
J	Coupling Constant
M	Molar
m/z	Mass-to-Charge Ratio

MeCN	Acetonitrile
MeOH	Methanol
MLCT	Metal to Ligand Charge Transfer
MS	Mass Spectrometry
η	Overpotential
nBu_4NPF_6	Tetrabutylammonium Hexafluorophosphate
NHE	Normal Hydrogen Electrode
NMR	Nuclear Magnetic Resonance
NOESY	Nuclear Overhauser Effect Spectroscopy
OEC	Oxygen Evolution Catalyst
OER	Oxygen Evolution Reaction
PCET	Proton Coupled Electron Transfer
PEC	Photoelectrochemical
Ph	Phenyl
pK_a	Acid Dissociation Constant
ppm	Parts per Million
PS I	Photosystem I
PS II	Photosystem II
PV	photovoltaic
R	Ideal Gas Constant
rt	Room Temperature
s	Singlet
t	Triplet
TFA	Trifluoroacetic Acid
TOF	Turnover Frequency
TON	Turnover Number
tt	Triplet of Triplets
UV-vis	Ultraviolet-visible Spectroscopy
vs.	versus

Table of contents

Chapter 1
General Introduction

1.1 Global Energy Concern

Energy is affirmatively the lifeline for modern productivity and living. Our sustainable development of economic, social and physical welfare cannot be guaranteed without an abundant, uninterrupted supply of energy, so the security of energy supply is therefore being of major concern for the whole world. It is expected that the energy efficiency will be greatly improved to generate a single unit of gross domestic product (GDP). However, the larger world's population (estimated over 9 billion) and 2.5 times bigger economic scale in 2050 than 2015 impel the global energy demand continues to massively grow by 6,142 Mtoe (Figure 1.1).[1] Currently, fossil fuels such as coal, oil, and natural gas provide about 85% of world's energy needs.[2] As a result of combusting these non-renewable energy resources, the significantly increased CO_2 concentration in Earth's atmosphere along with the emissions of other greenhouse gases (GHG, including CH_4, N_2O, fluorinated gas, etc.) is causing a planet-warming effect and large-scale climate changes, e.g. the progressive melting of the planet ice crust and the shutdown of the ocean circulation system.[3,4] Also, the huge quantities of pollutants produced are harmful to both the environment and the human health.

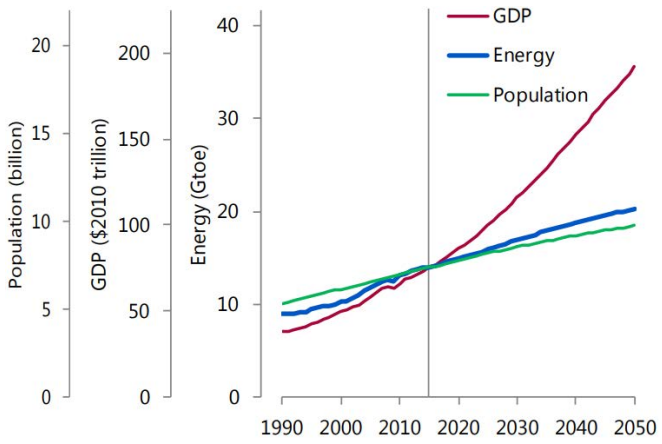

Figure 1.1 World population, real GDP and primary energy consumption during the period 1990 to 2050.[1]

Therefore, there is a strong impetus to replace fossil fuels by sustainable and environmentally-friendly alternative sources of energy. Both political and scientific communities have been putting efforts in rising the contribution of renewable energy in the overall energy consumption. Renewable energy, in the sense that the reserves are functionally inexhaustible or can be supplemented at the same rate as consumption, includes forms of solar, hydroelectric power, biomass, wind, ocean thermal, tidal, and geothermal energy. Although each type of these sources contributes to energy supply, the limitless sunlight is especially appealing because it is by far the largest exploitable resource, providing the Earth with more energy than all that consumed by humans throughout an entire year in one hour.[5] To accomplish the task of developing renewable energy technologies, huge amounts of capital is invested into this field, solar energy representing 35% of the total investment (Figure 1.2).

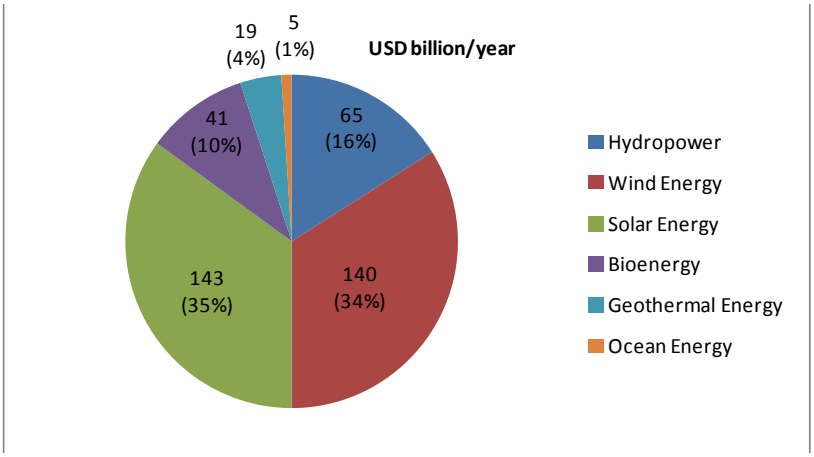

Figure 1.2 Renewable power investments under Remap (2015–2020, by technology).[6]

Scientific studies of photovoltaics or photoelectrochemical solar cells that can convert sunlight to electricity or fuels, respectively, has been an attractive area in the past decades. However, solar energy suffers an innate limitation: its intermittent nature.[6] The energy flux of sunlight that arrives at the earth's surface is not constant and varies significantly along the day, season of the year, weather conditions, and location. If this intermittency is particularly important when sunlight is converted into electric power, which cannot be stored, the problem can be overcome when this energy is stored in the chemical bonds of a fuel (i.e. hydrogen gas), from which can be recovered on demand.

1.2 Hydrogen

Hydrogen is the most abundant element in the Earth's crust (accounting for about 15 mol%), but is not readily found in its molecular gaseous form given its low molecular weight. Instead, hydrogen is vastly found combined with other elements in hydrocarbons and water.[7] As a fuel, and when produced from renewable resources, hydrogen is an available renewable energy carrier; its combustion only generates water as byproduct (thus, zero greenhouse gas emission) and its high energy density (140 MJ/kg) is three times higher than that of petroleum (47 MJ/kg).[8,9] However, given the unavailability of its molecular form in our planet, it needs to be produced from any primary energy source prior to its consumption as the fuel.

1.2.1 Hydrogen production

Nowadays, about 0.1 GT of molecular hydrogen are produced annually,[9] being mainly consumed in oil refining and metallurgy, with a small portion already utilized as a fuel in different types of vehicles. There are several different technologies to generate dihydrogen, but those dominant still rely on fossil fuels (48% from natural gas, 30% from heavy oils and naphtha, 18% from coal), renewable H_2 being still only about 4% of the overall production of this gas.[10] The following subsections describe the main methods currently employed to produce H_2, including the renewable alternatives tackled in this PhD Thesis.

1.2.1.1 Steam reforming

Steam reforming (SR) is the process that converts catalytically hydrocarbons and steam to H_2. The process consists on the following steps: remove impurities, reforming or synthesis gas (syngas) generation, water gas shift (WGS), and methanation or gas purification. Generally, the reforming reaction (eq. 1) is controlled at high temperatures, 700–850 °C, pressures up to 3.5 MPa and steam to carbon ratios of 3.5, so as to obtain the desired purified H_2 and prevent coke from forming on the catalyst surface (which is usually based on nickel).[11] Additional H_2 may be produced via a WGS reactor (eq. 2), by passing the gases to react with steam over a cobalt or iron oxide catalyst. Finally, the gas mixture passes either through a CO_2-removal followed by methanation (eq. 3) or a

pressure swing adsorption (PSA) step to remove residual traces of carbon oxides, leaving H_2 near to be 100% pure. Among all raw materials, methane is the most common one used for large scale hydrogen production in the chemical process industries, with conversion efficiencies in the 74–85% range at an estimated cost of around \$1.8 kg^{-1}.[10]

Reforming: $C_nH_m + n\ H_2O \rightarrow n\ CO + (n + m/2)\ H_2$ (1)

Water gas shift reaction: $CO + H_2O \rightarrow CO_2 + H_2$ (2)

Methanation: $CO + 3\ H_2 \rightarrow CH_4 + H_2O$ (3)

1.2.1.2 Hydrocarbon pyrolysis

Hydrocarbon pyrolysis has been widely studied since the 1900s in the fields of aerospace, fuel cells, and hydrogen production. Unlike the steam reforming process (see above), in this method the hydrocarbon undergoes thermal decomposition and self-generates H_2 with no other reactants involved, as shown in Eq. 4. For instance, the direct thermo-catalytic decomposition of methane is carried out at temperature up to 980 °C and atmospheric pressure. By this technology, the energy consumed to produce H_2 (37.6 kJ/mol) is less than that consumed in steam methane reforming (63.3 kJ/mol).[12] Besides, the absence of CO_2 in the pyrolysis process eliminates the WGS and CO_2 removal steps, simplifying the requirements for handling by-products, i.e., elemental carbon. Therefore, the economic cost of hydrogen production from pyrolysis is more than thirty percent lower than that from SR. From the perspective of environmental protection, it would be more beneficial to generate H_2 through this catalytic dissociation of hydrocarbons, only accompanied by carbon and without emission or sequestration of CO_2.

$$C_nH_m \rightarrow n\ C + m/2\ H_2 \quad (4)$$

1.2.1.3 Water electrolysis

The major concern associated with the above methods for H_2 production is the necessity of depleting fossil fuels to drive the processes, rendering the perceived status of hydrogen as a clean fuel questionable. So, a very appealing feedstock for the purpose of getting hydrogen in a renewable manner would be water, which is carbon-neutral,

abundant and nearly costless. Based on scientific principles demonstrated in the early 1800s,[13] water electrolysis become an effective and well-known method to produce H_2. The splitting of water is thermodynamically disfavored and therefore the overall reaction is driven by supplying electrical energy in the form of potential. Then hydrogen is produced at the cathode while oxygen is evolved on the anode via the reaction in Eq.5. The half reactions of the process are shown below (Eq.12 and 13).

$$H_2O \rightarrow H_2 + 1/2\ O_2 \qquad (5)$$

The minimum amount of reaction enthalpy that has to be electrically applied is the change in Gibbs energy, ΔG, which is shown in terms of enthalpy of reaction (ΔH), temperature (T) and entropy of reaction (ΔS) in Eq.6. At standard temperature and pressure under theoretical conditions, the reversible voltage (V_{rev}) of water splitting is −1.23 V according to Eq.7, where n is the number of electrons transferred and F is Faraday's constant.

$$\Delta G^\circ = \Delta H^\circ - T\Delta S^\circ \qquad (6)$$

$$V_{rev} = -\frac{\Delta G^\circ}{nF} \qquad (7)$$

Therefore, the energy theoretically consumed for the production of 1 m^3 of H_2 is 2.94 kWh when the current efficiency is 100%.[13] Noticeably, −1.23 V is the calculated value with the condition that all components are in the gas phase, i.e., the water consumed in the reaction is vaporized. In reality, the cell voltage of an operating electrolysis cell is considerably higher than the theoretical reversible voltage derived from thermodynamics so as to accelerate the prohibitive slow reaction to a practical rate. This extra voltage is known as overpotential, and it is always due to mass transportation, charge transfer and resistance of electrolyte and electrodes in the electrolysis process.[13] Together with the use of electrolytes, the use of efficient electrocatalysts is key to minimize overpotentials when splitting water.

To date, the main electrolysis technologies are alkaline electrolysis (AEL), proton exchange membrane electrolysis (PEMEL) and solid oxide electrolysis (SOEL) on the basis of the electrolyte used in the electrolysis cell.[14]

1.2.2 Hydrogen storage, transportation

At room temperature and atmospheric pressure, hydrogen gas has a very low mass density (1 kg of hydrogen fills a volume of 11 m^3), making its storage and transportation in a safe, reliable and cost-effective way a challenging matter.[15] The most common and mature method is high pressure gaseous hydrogen storage by compressing H_2 in high pressure gas cylinders up to 77 MPa.[16] Another developed technique is the liquefaction of H_2 below its boiling point at −253 °C and its storage in cryogenic tanks. However, despite the higher density of liquid H_2 that increase its storage efficiency, this method needs of intensive energy supply and is highly time consuming if compared with compressed hydrogen gas.

The capacity of certain materials to chemically store H_2 in a reversible manner has been extensively studied.[17,18] Metal hydrides, formed through the reaction of molecular hydrogen with metals or their alloys, are well known for their ability to absorb hydrogen and later release it, either at room temperature or through a heating process. Metal-hydrogen compounds (M-H) produced from light metals such as Na, Li, Be, Mg and Al received great attention due to their high capacity of hydrogen storage at relatively low costs. Thus, for instance, Mg_2FeH_6 and $Al(BH_4)_3$ show extremely high volumetric densities (about 150 kg/m^3) at ambient temperature and pressure.[16] Alanates ($MAlH_4$) and borohydrides (MBH_4) (M = Li, Na, Mg) have also received much attention. Among them, $LiBH_4$ is the hydride compound possesses the highest gravimetric hydrogen density (up to 18 wt%) at room temperature.[15] The chemical storage of H_2 can also be achieved in liquid organic hydrogen carriers such as cycloalkane, methanol and formic acid, with a gravimetric density of 6–8 wt%, 12.6 wt% and 4.3 wt%, respectively. In addition, liquid inorganic hydrides such as ammonia borane, hydrous hydrazine and hydrazine borane can also be carriers, having volumetric hydrogen capacities of 19.6 wt%, 12.5 wt% and 15.4 wt%, respectively.[19]

Alternatively, H_2 storage can be obtained by physisorption in which hydrogen is weakly adsorbed at the material surface and released reversibly. Due to the weak interaction formed, significant physisorption is only observed at low temperatures (<273 K). The most widely studied carriers are porous materials including carbon-based

materials (carbon nanotubes, fullerenes), zeolites and metal organic frameworks (MOFs).[20–23]

1.3 Natural photosynthesis and artificial photosynthesis

1.3.1 Natural photosynthesis

Natural photosynthesis plays an extremely important role in green plants and other organisms which utilize sunlight, water and CO_2 to synthesize energy-rich carbohydrates, storing solar energy in chemical fuels, as depicted in Eq.8.[24]

$$6\ CO_2 + 6\ H_2O + 48\ h\nu \rightarrow C_6H_{12}O_6 + 6\ O_2 \qquad (8)$$

In photosynthesis, the light-harvesting occurs by means of two large protein complexes called photosystem I (P700, PS I) and II (P680, PS II), which consist on a light-harvesting antenna (chlorophyll a and b) and catalytic metal clusters inlaid in proteins (Figure 1.3). When PS II is excited by absorbing a photon, the reaction center chlorophyll molecule transiently loses an electron, becoming after oxidation a very strong oxidizing agent which is able to accept electrons from water, resulting (after the absorption of 4 photons) in oxygen and protons production in the lumen (Eq. 9). This water oxidation reaction (WOR) is catalyzed by a water oxidation catalyst (WOC), a Mn_4CaO_5 cluster with cubane-like structure which mediate catalysis upon four-photon excitation to the highest oxidation state.[25,26] The photoexcited electrons from PS II are transmitted to the plastoquinone pool (PQ) and further transferred through several electron relays, such as cytochrome b6/f (Cyt b6/f) and plastocyanin (PC), to terminus PS I. In sunlight-excited PS I and after further electron transfer induced by the participation of ferredoxin (Fd) and ferredoxin NADP reductase (FNR), the cofactor $NADP^+$ (nicotinamide adenine dinucleotide phosphate) is reduced to NADPH (nature's form of hydrogen, Eq. 10). The latter is later on able to transform CO_2 to carbohydrates in the dark process (Calvin cycle).

$$2\ H_2O + 4\ h\nu \rightarrow O_2 + 4\ H^+ + 4\ e \qquad (9)$$

$$2\ NADP^+ + 4\ H^+ + 4\ e + 4\ h\nu \rightarrow 2\ NADPH \qquad (10)$$

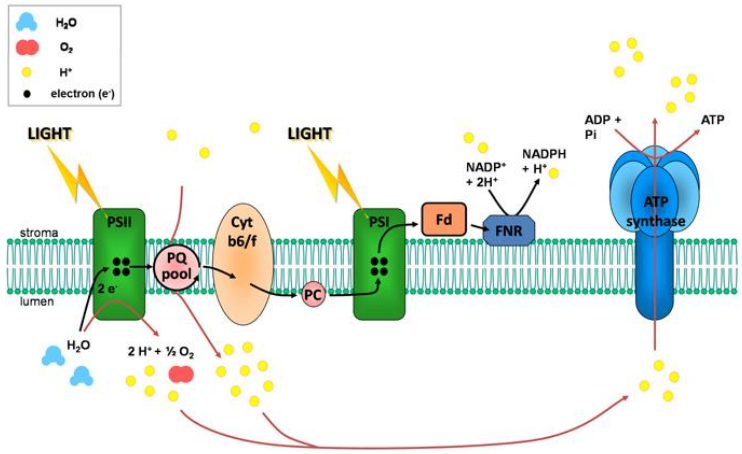

Figure 1.3 The photosynthetic electron transfer chain in the thylakoid membrane containing photosystem II reaction centers P680 and photosystem I reaction centers P700. Adapted from literature.[27]

On the other hand, hydrogenase (H_2ase) enzymes present in many green algae and bacteria are competent to reduce protons to H_2. These enzymes can be classified in three different types ([FeFe], [NiFe], and [Fe] hydrogenases, Figure 1.4)[28] according to the metal ion present in the catalytically active sites. [Fe]-H_2ase (or H_2-forming methylenetetrahydromethanopterin dehydrogenases, Hmd hydrogenase) catalyzes the dehydrogenation of methylene-tetrahydromethanopterin (methylene-H_4MPT) to form H_2 and methenyltetrahydromethanopterin (Eq.11).[29] On the other hand, [FeFe]- and [NiFe]-H_2ases have been shown to mediate at high rates the simplest reversible reaction $H_2 \leftrightarrow 2H^+ + 2e^-$, functioning to either oxidize H_2 in the energy-producing processes or reduce protons to dihydrogen during fermentative growth.[30] The direction of this reaction (H_2 uptake vs. production) depends on cellular location of H_2ases, and the redox potential of the components interacting with the enzyme. In the presence of H_2 and an electron acceptor, hydrogenases located in the periplasm or the membrane are generally associated with H_2 uptake, that is converting H_2 into protons and electrons which are transferred from the hydrogenase into the quinone pool and forming part of the bacterial respiratory chain. Conversely, H_2ases located in the cytoplasm are associated with H_2 evolution. Generally speaking, [FeFe]-H_2ase exhibits better activity than [NiFe]-H_2ases to produce dihydrogen.[31]

$$H^+ + \text{methylene-}H_4\text{MPT} \leftrightarrow H_2 + \text{methenyl-}H_4\text{MPT}^+ \qquad (11)$$

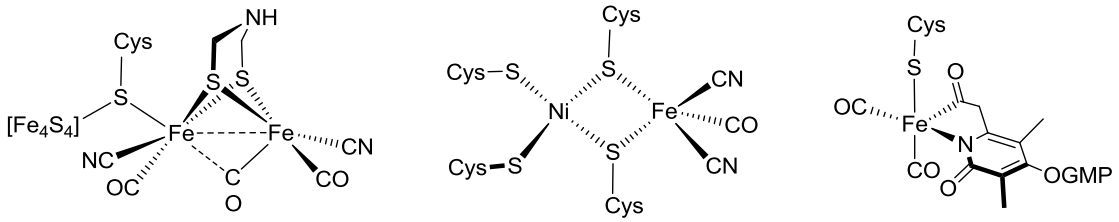

Figure 1.4 Structural representation of the active sites of [FeFe]-H_2ase (left), [NiFe]-H_2ase (center), and [Fe]-H_2ase (right) in Nature.[32]

1

1.3.2 Artificial photosynthesis

Originated from the desire to mimic natural photosynthesis to store solar energy in chemical bonds, artificial photosynthesis is dealing with issues like reducing CO_2 to carbon-based fuels (methane, methanol or formic acid), nitrogen to ammonia, and very importantly split water to H_2 (and O_2) as a clean renewable energy carrier. The generation of H_2 from water undergoes two catalytic steps: (i) the oxidation of two water molecules into O_2 and four protons (WOR, Eq. 12) and (ii) the subsequent reduction of protons to molecular H_2 (hydrogen evolution reaction (HER), Eq.13).

$$2\ H_2O \rightarrow O_2 + 4\ H^+ + 4\ e^- \qquad E = 1.23\ V - 0.059\ pH\ V\ vs.\ NHE \qquad (12)$$

$$4\ H^+ + 4\ e^- \rightarrow 2\ H_2 \qquad E = 0\ V - 0.059\ pH\ V\ vs.\ NHE \qquad (13)$$

Upon decades of development, sustainable solar hydrogen production systems have been evolved mainly to three different types of devices as schematically depicted in Figure 1.5: photovoltaic–electrolysis (PV-EC) systems, particulate photocatalytic (PC) systems, and photoelectrochemical (PEC) cells.[33]

A PV-EC (Figure 1.5a) is a system that couples a PV device with a standard water electrolyzer, in which the power generated from an independent solar cell is transferred to an EC cell in order to trigger the HER and the WOR. Since in the PV-EC device the light absorber is kept completely out from water electrolyte, the PV cell could be fairly stable without corrosion. The other major advantage of this system is that both PV and water electrolysis are mature and commercialized technologies, achieving high solar to hydrogen (STH) conversion efficiencies (above 10%).[34] However, PV–EC systems suffer

from the highest complexity in PV designs. Moreover, although the electricity from PV devices is competitive with the grid, the hydrogen produced from this approach has a considerably high price relative to steam reforming (due to the cost of coupling both PV and EC systems), which discourages its wide application.[35]

In contrast, PC water splitting devices depicted in Figure 1.5b require the smallest complexity, with the only involvement of sunlight, water and PC particles dispersed in the medium. In such a kind of systems, the photogenerated charge diffuses to the active sites on the surface of a semiconductor light absorber, which generally assemble separate WOR and HER catalysts together. Thus, a mix of H_2 and O_2 gases is produced from each PC particle. Combining light absorbers of appropriate band gap and stability with efficient HER and WOR catalysts and efficiently transfer electrons among them all in a single particle is of upmost complexity. Thus, the obtained STH efficiencies are typically far from those required for practical commercial application.

A PEC cell (Figure 1.5c) is a device category with compromised complexity, available materials, and generally overall efficiency between PV-EC and PC systems. A prototypical type of PEC cell is composed of two photoelectrodes: a photoanode and a photocathode, each with a semiconductor/electrolyte junction.[36] The photoanode usually have a configuration of WOC/protection layer/dopant:light absorber/substrate, while the photocathode is represented as HEC/protection layer/dopant:light absorber/substrate.

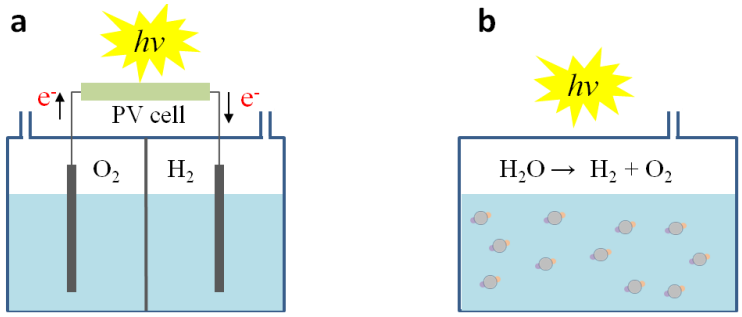

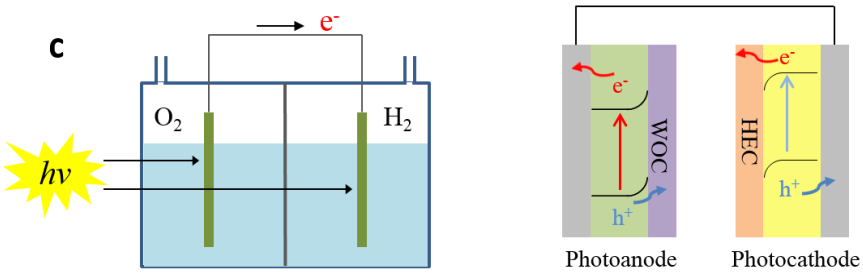

Figure 1.5 Schematic diagrams of different solar to hydrogen systems by splitting water. (a) PV-EC cell. (b) Particulate PC system and illustration of a PC particle. (c) Two-photoelectrode PEC cell and illustration of n-type photoanode and p-type photocathode.[36]

In a PEC, the water splitting reaction can be summarized to four steps: light absorption by a photo-absorber, charge separation in the photo absorber, charge transfer to an electrocatalyst (WOC or HEC), catalyst-mediated WOR or HER at surface of electrode. Thus, photo-absorber and electrocatalyst are key components for manufacturing an effective PEC. Photo-absorber could be not only inorganic materials, like semiconductors TiO_2, $BiVO_4$ and CdTe,[37,38] but also molecular dye sensitizers, $[Ru(bpy)_3]^{2+}$ and $[Ir(ppy)_2(bpy)]^+$ for instance.[39]

Like mentioned in the previous subsection 1.2.1.3 Water Electrolysis extra voltage is needed in the water splitting process, both half reactions WOR and HER require significant overpotentials. Therefore, anodic and cathodic compartments of above devices are usually equipped with proper WOCs and HECs, respectively, to accelerate the multiple electron/proton transfers in the reactions. In many studies, the two kind of electrocatalysts are separately investigated in a specific half reaction by using a sacrificial electron donor (in WOR) or acceptor (in HER).[40] Since the opening work on water splitting by utilizing TiO_2 photoanode under UV light irradiation in 1970s, lots of solid materials have been actively developed as catalysts to perform this photoelectrocatalytic reaction.[41] Besides, homogeneous catalysts that mimic the photosynthetic reaction center in natural photosynthesis are also under extensive investigation, such as various complexes of Ru, Ir, Ni and Co.[42–44] Compared with inorganic catalysts, molecular catalysts exhibit many advantages, for example, the environment and redox property of catalysts can be tuned through ligand design; clear structures are favorable for mechanistic analysis and experimental repeatability; outstanding metal-atom economy of molecular catalysts when

they are dissolved in solution of sacrificial reactants, or immobilized onto the surface of semiconductor or dye-sensitized semiconductor.[45] Due to the focus of this PhD Thesis in the use of molecular complexes as electrocatalysts for the HER, the following subsections will focus on the details of such a kind of systems.

1.4 Evaluation and benchmarking of hydrogen evolution electrocatalysts

During the study of the HER mediated by homogenous catalysts, some typical catalytic parameters are essential to evaluate their activity and to compare (benchmark) their catalytic performance with previously reported systems.

A) Overpotential (η): It is defined as the difference between the potential at which the catalyst reduces protons under the operating conditions (E_{cat}) and the standard reduction potential ($E°_{HA/H2}$). The E_{cat} can be presented in three variable forms, onset potential (E_{on}), half-wave potential ($E_{cat/2}$) and potential at the maximum current (E_P). $E_{cat/2}$ is the value recommended to calculate overpotential for catalysis in acidic media,[8] and it is used for our calculation in later Chapter. The value of $E°_{HA/H2}$ varies depending on the acid and solvent used for catalysis. The expressions to calculate overpotential and $E°_{HA/H2}$ in aqueous media are shown in Eq.14 and Eq.15, respectively.

$$\eta = \left|E_{cat/2} - E^0_{HA/H2}\right| \qquad (14)$$

$$E^0_{HA/H2} = E^0_{H^+/H_2} - \frac{2.303RT}{F} pK_a + \epsilon_D - \frac{RT}{2F} \ln \frac{C_0}{C_{H_2}} \qquad (15)$$

Where $E^0_{H^+/H_2}$ is the standard potential for the reduction of protons, C_0 is the acid concentration, C_{H_2} is the concentration of dissolved H_2, ϵ_D is the diffusion rate of products vs. reactants,[46] R is ideal gas constant = 8.314 JK^{-1} mol^{-1}, T = 298 K, and F is the Faraday constant (96485.33 A/mol).

B) Turnover number (TON) and turnover frequency (TOF): TON is the number of moles of hydrogen generated per mole of homogeneous catalyst used (Eq.16) directly related to the overall stability of the complex.

$$TON = n_{H2}/n_{cat} \qquad (16)$$

But TOF, the turnover number per time unit, is generally used to measure the kinetics in homogeneous catalysis. TOFs values for HER electrocatalysts can be determined either from bulk electrolysis or cyclic voltammograms, the second being the option of choice in this manuscript. Its specific calculation is described in the Experimental Section of Chapter 3.

C) Faradaic efficiency: The Faradaic efficiency is the efficiency of electrons transferred in a system for an electrochemical reaction, specifically, in the case of the HER, it is a measure of the percentage of electrons effectively used in the conversion of H^+ to H_2. This value is calculated by comparing the measured amount of hydrogen, measured by a Clark-type H_2 microsensor device for headspace analysis in this Thesis, to the total amount of charge passed during controlled potential electrolysis. The calculation of Faradaic efficiency is reported in Chapter 3.

1.5 Hydrogen evolution catalysis

Compared to the WOR, which involves four electron transfers from water to form an O_2 molecule, the HER is a simpler process, requiring two electrons and two protons to produce a molecule of H_2. However, the kinetic barriers for generating H_2 in the absence of a catalyst are high, that promoting the investigation of a large variety of catalysts for this reaction. The most efficient materials known for the electrochemical production of H_2 by the HER are Pt group metals which operate at low overpotential through well-established mechanistic steps.[47] However, platinum is rather expensive (average price $845.4 per ounce in 2019)[48] and rare, providing a strong impetus for developing cheap alternatives based on earth-abundant catalysts. In nature, proton reduction occurs at homogenous Fe-Fe, Ni-Fe and Fe sites within hydrogenase enzymes as described above (see Section 1.3.1). These natural catalysts employ Earth-abundant metals to catalyze the HER at thousands of turnovers per second and overpotentials lower than 100 mV. Thus, considerable efforts are currently focused to develop robust molecular catalysts based on non-noble metals.[49–51]

As shown in Scheme 1.1, a reducible metal complex, L_nM, may undergo a variety of different pathways to catalyze the HER via a monometallic mechanism.[32] Following

the standard electrochemical notation, the electron transfer and chemical transfer processes are denoted as E and C, respectively. Generally, the two-electron two-proton transfers of electrocatalytic hydrogen evolution can differ to five possible modes; ECEC, EECC, ECCE, CECE, and CCEE.[52] Which specific mechanistic route the catalyst adopts is jointly determined by different factors such as the pK_a of the metal complex at each oxidation state and the pK_a of acid used in the catalytic system. Thus, for complexes containing electron-donating ligand and a very strong HA acidity, the initial protonation of the catalyst would be more favorable than the corresponding reduction.

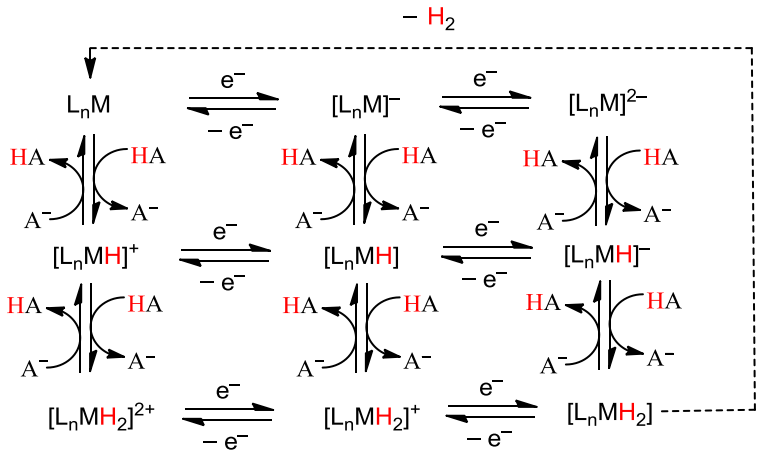

Scheme 1.1 Possible proton and electron transfers involved in the HER catalyzed by a reducible molecular complex.[32]

1.5.1 Nickel catalysts for HER

Nickel is a group 8 transition metal with electron configurations [Ar] $3d^8$ $4s^2$. Its redox-active nature, from Ni^0 to Ni^{IV}, and its cheapness (average price 13.7 $/kg in 2019)[53] make Ni an appropriate alternative to noble platinum or palladium in the design of molecular catalysts. HER mediated by Ni complexes normally involve the reduction from Ni^{II} to Ni^{I}, accompanied by the corresponding geometrical transformation from a square planar to a tetrahedral environment.[54,55] In this section, a selection of the most relevant dinuclear and mononuclear HER electrocatalysts based on Ni is presented.

1.5.1.1 Bioinspired dinuclear complexes based on Ni for HER

The presence of nickel in the active site of natural [NiFe]-H_2ases inspired chemists to prepare model complexes. Initial reports of those models, even if structurally similar to the biological systems, did not show HER catalytic activity until a trinuclear Ni_2Fe complex, [('S_2'){Ni(PMe_3)}$_2$Fe-(CO)('S_2')$_2$] ('S_2'$^{2-}$ = 1,2-benzenedithiolate(2–)) (**1**, Figure 1.6), was reported by Sellman in 2004. H_2 production rates were very low, with TOF values smaller than 0.1 h^{-1}.[56–58] Significant improvements for functional NiFe models were obtained by Artero[59] and coworkers by replacing the Fe center by a Ru center (the Fe center in the enzyme is a redox inactive low-spin Fe(II) species), leading to NiRu complexes. The novel complex [Ni-(xbsms)Ru(CO)$_2$Cl$_2$] (**2**) synthesized in 2006 bearing the tetradentate S_4-donor ligand xbsms (1,2-bis(4-mercapto-3,3-dimethyl-2-thiabutyl)benzene) was the primal example of active heterodinuclear catalyst for HER.[59]

Table 1. Catalytic hydrogen evolution by NiFe models.

Entry	Complex	E_p (V)[a]	η (V)	TOF (h^{-1})[b]	acid	Ref.
2	[Ni-(xbsms)Ru(CO)$_2$Cl$_2$]	– 1.66	0.88	3	Et_3NH^+	57
3	[Ni(xbsms)Ru(*p*-cymene)Cl]$^+$	– 1.65	0.87	6.5	Et_3NH^+	58
4	[Ni(emi)Ru(*p*-cymene)Cl]$^-$	– 1.60	0.82	6.6	Et_3NH^+	58
5	[Ni(emi)Ru(CO)$_2$Cl$_2$]$^{2-}$	– 1.57	0.79	1.6	Et_3NH^+	58
6	[Ni(xbsms)Ru(DMSO)Cp]$^+$	– 1.44	0.66	4.3	Et_3NH^+	59
7	[Ni(xbsms)Ru(CO)Cp]$^+$	– 1.65	0.87	5.3	Et_3NH^+	59
8	[Ni(xbsms)Ru(MeCN)Cp*]$^+$	– 1.40	0.62	9.3	Et_3NH^+	60
9	[Ni(xbsms)Ru(CO)Cp*]$^+$	– 1.60	0.82	2.2	Et_3NH^+	60
10	[Ni(xbsms)Fe(CO)Cp]$^+$	– 1.20	0.73	5	CF_3COOH	61
	Complex	$E_{cat/2}$ (V)[c]	η (V)[d]	TOF (s^{-1})[e]	acid	
11	[(dppe)Ni(pdt)(μ-H)Fe(CO)$_3$]$^+$	–1.20	0.50	20	CF_3CO_2H	64
12	[(dppe)Ni(pdt)(μ-H)Fe(CO)$_2$PPh$_3$]$^+$	–1.30	0.60	50	CF_3CO_2H	64
13	[(dppe)Ni(pdt)(μ-H)Fe(CO)$_2$PPh$_2$(2-Py)]$^+$	–1.30	0.60	50	CF_3CO_2H	64

14	$[(dppe)Ni(pdt)(\mu\text{-}H)Fe(CO)_2P(OPh)_3]^+$	–1.32	0.62	50	CF_3CO_2H	64
15	$[(dcpe)Ni(pdt)(\mu\text{-}H)Fe(CO)_3]^+$	–1.46	0.59	50	$ClCH_2CO_2H$	65
16	$[(dppe)Ni(edt)(\mu\text{-}H)Fe(CO)_3]^+$	–1.23	0.49	240–310	CF_3CO_2H	65
17	$[(dcpe)Ni(edt)(\mu\text{-}H)Fe(CO)_3]^+$	–1.45	0.59	20	$ClCH_2CO_2H$	65
18	$[(dppe)Ni(edt)(\mu\text{-}H)Fe(CO)_2PPh_3]^+$	–1.45	0.54	60–120	$ClCH_2CO_2H$	65
19	$[(dppe)Ni(pdt)(\mu\text{-}H)Fe(dppe)CO]^+$	–1.61	0.85	23	$ClCH_2CO_2H$	32
20	$[(dppe)Ni(pdt)(\mu\text{-}H)Fe(dppbz)CO]^+$	–1.61	0.85	30	$ClCH_2CO_2H$	32

Abbreviations: xbsms = 1,2-bis(4-mercapto-3,3-dimethyl-2-thiabutyl)benzene; *p*-cymene = 1-Methyl-4-(propan-2-yl)benzene; emi = *N*,*N*-ethylenebis(2-mercaptoisobutyramide); Cp = cyclopentadiene; Cp^* = pentamethylcyclopentadienyl; dppe = 1,2-bis(diphenylphosphino)-ethane; pdt = 1,3-propanedithiolate; dcpe = 1,2-bis(dicyclohexylphosphino)ethane; edt = 1,2-ethylenedithiolate; dppbz = 1,2-bis(diphenylphosphino)benzene. [a] Catalytic peak potential measured in the presence of three equivalents of acid vs. Ag/AgCl in DMF. [b] TOF were determined by bulk electrolysis experiments in DMF solution. [c] Potential at $i_{cat}/2$ determined in CH_2Cl_2. [d] Overpotentials calculated from $|E_{cat} - E_{(H2/HA)}|$ in MeCN solution. [e] Estimated from acid-independent region of i_c/i_p vs. [acid] plot.

Later on, dinuclear NiRu complexes bearing the xbsms ligand or the N_2S_2 ligand emi *N*,*N*-ethylenebis(2-mercaptoisobutyramide) (**3**-**9**) were prepared and electrochemically applied to catalyze the HER at higher rates (TOF > 2 h^{-1}, see Table 1).[60–62] The introduction of the Cp^* anion in the series of complexes (**6**-**9**) allowed somehow reducing the observed overpotentials. This reduction is explained by the electron-donating nature of the anionic Cp^- or Cp^{*-} ligand that increases the electron richness of the metal centers in the dinuclear complexes. Besides, the binuclear NiFe complex **10** (similar to **7** but replacing Ru by Fe accompanying the Ni site) was reported in 2010 showing overpotential and stability values comparable to those of functional NiRu models. The catalytic mechanism for this complex was proposed to be similar to that of the NiRu counterpart, involving bridging hydride species.[63,64]

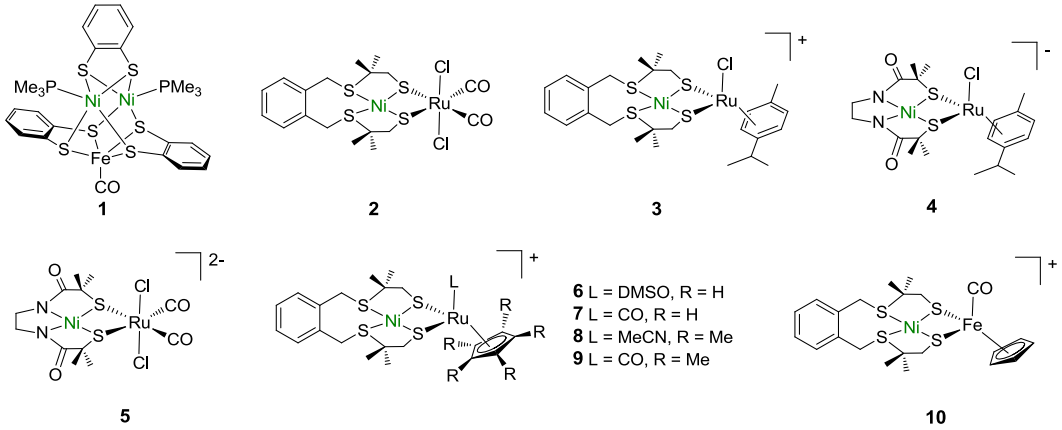

Figure 1.6 Trinuclear and binuclear functional [NiFe]-hydrogenase models.

In 2009, the nickel-iron thiolato hydride complex $[(dppe)Ni(pdt)(\mu\text{-}H)Fe(CO)_3]^+$ (dppe = 1,2-bis(diphenylphosphino)ethane; pdt = 1,3-propanedithiolate, **11**, Figure 1.7) was reported to be HER–active.[65] From this starting point, the group of Rauchfuss developed a series of hydride–containing $Ni^{II}Fe^{II}$ compounds (**12-20**, Figure 1.7) to structurally mimic the Ni-R state intermediate of the NiFe enzymes (see Scheme 1.2 left).[65–67] Thanks to the variable stability of the formed radical hydride complex, the initial one electron reduction couple exhibits different reversibility. For these compounds bearing di- and tricarbonyl groups the reduction is irreversible, except for **14** whose free radical is believed to be stabilized on the $P(OPh)_3$ ligand by spin delocalization. Complexes **11-20** were investigated by using CF_3CO_2H or $ClCH_2CO_2H$ as proton source in organic media (CH_2Cl_2), resulting all of them were catalytically active in the HER (Table 1). Complexes **12-14** were obtained from complex **11** through substitution of CO groups by phosphine or phosphite ligand, this increasing the catalytic rate by about 2 times. Analogous substitution of CO by PPh_3 ligands in the ethanedithiolate complex **16** resulted in complex **18**, which operates at a slower rate due to catalyst decomposition. Compared with 1,3-propanedithiolate derivatives **11** and **12**, both 1,2-ethylenedithiolate derived complexes **16** and **18** exhibit faster kinetics (higher TOF values) (see kinetic data from corresponding entries of **11**, **12**, **16**, **18** in Table 1), demonstrating the strong effect of the the nature of the dithiolate in the observed catalytic rates.

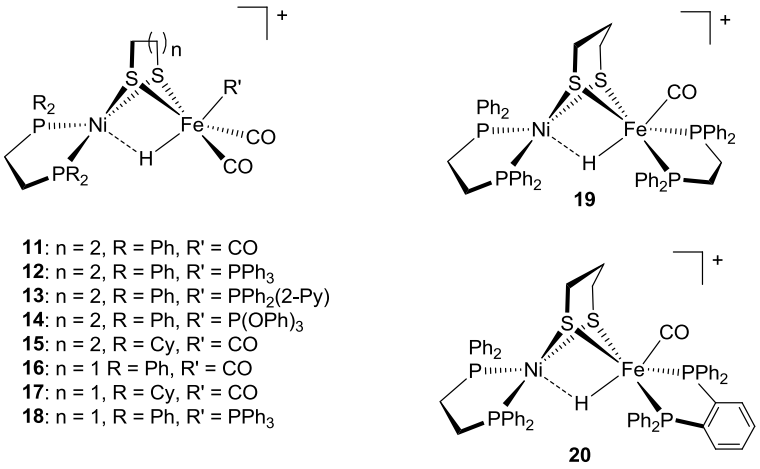

Figure 1.7 Hydride containing NiFe hydrogenase models for HER.

Unlike biological [NiFe]-H_2ases where the Fe^{II} oxidation state is kept along the catalytic cycle (Scheme 1.2, left), the mechanism of hydrogen evolution by these [(diphosphine)-Ni(dithiolate)(μ-H)FeL_3]$^+$ models involves Fe^I intermediates (Scheme 1.2, right). It starts with a 1 e^- reduction of the $Ni^{II}Fe^{II}$ hydride to give a mixed-valent complex. Instantaneously, the reduced species reacts with acid probably with S acting as proton relay, then releasing H_2, affording mixed-valent $Ni^{II}Fe^I$ species (for di- and tricarbonyls) or Ni^IFe^{II} complexes (for monocarbonyls). Reduction of the mixed-valent species provides neutral intermediates without the hydride. The form of the reduced hydride-free species differ in the geometry of the Ni center, i.e., the reactive $Ni^{II}Fe^0$ form in which the geometry around the Ni center is square planar and the Ni^IFe^I form where the Ni center adopts a tetrahedral arrangement. But the Ni^IFe^I species easily convert to the $Ni^{II}Fe^0$ form, the latter state with enhanced basicity easing the final protonation step of the catalytic cycle.[67,68]

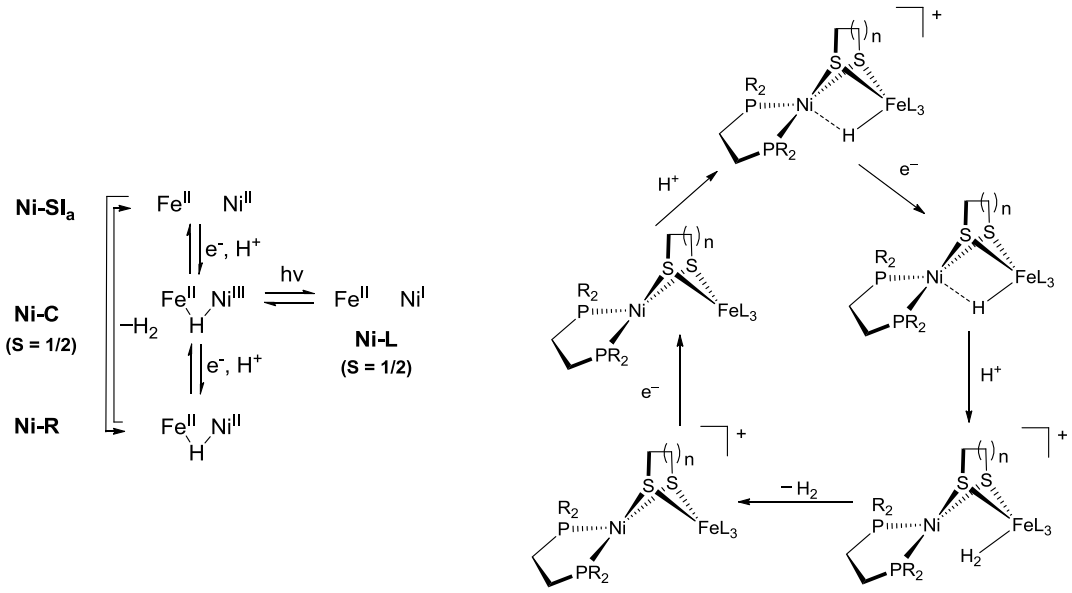

Scheme 1.2 Proposed mechanistic pathways for [NiFe]-H_2ase[69] (left) and NiFe dithiolato hydrides[32] (right).

1.5.1.2 Mononuclear complexes based on Ni for HER

Despite numerous works on biomimetic multinuclear complexes, the most extensive research on catalytically active proton reduction compounds is allocated to mononuclear complexes, yielding a large amount of this kind of catalysts in the past decades. Given its d^8 electronic configuration as mentioned above, Ni^{II} tends to adopt a tetradentate square planar geometry. Thus, tetraaza-macrocyclic planar ligands having four N atoms as coordination sites can provide a favorable environment for Ni^{II} and offer stable Ni complexes. The report of tetraaza macrocyclic nickel complexes that catalyze the HER can be traced back to the groundbreaking work of Fisher and Eisenberg.[70] Pursuing the electrocatalytic reduction of CO_2 by using complex **21** (depicted in Figure 1.8) in H_2O/MeCN solution, H_2 was found in the gas product mixture together with CO at a 2:1 CO/H_2 ratio. The analogue complex **22** yielded predominantly H_2 from proton reduction in acidic (pH < 2) aqueous solution when studying the CO_2 reduction reaction.[71] In 1992, the macrocyclic Ni complex **23** $[Ni(CR)]^{2+}$ ((CR = 2,12-dimethyl-3,7,11,17-tetraazabicyclo(11.3.1)-heptadeca-1(17),2,11,13,15-pentaene) reported by Crabtree was capable of reducing protons in a pH 2 phosphate buffer solution. The authors evidenced that the macrocyclic ligand is redox active in the catalytic processes as the radical species

$[Ni^{II}L^{\bullet-}]^+$ after a first one-electron reduction was characterized by EPR spectroscopy.[72] The ligand-assisted HER aroused other complexes to appear such as those based on glyoxime ligands (**24-25**), for which one-electron redution also leads to $[Ni^{II}L^{\bullet}]^+$ and two-electron reduced species were assigned to $[Ni^{I}L^{\bullet-}]$ or $[Ni^{II}L^{\bullet\bullet}]$ by transient UV-vis spectra and X-band EPR.[73]

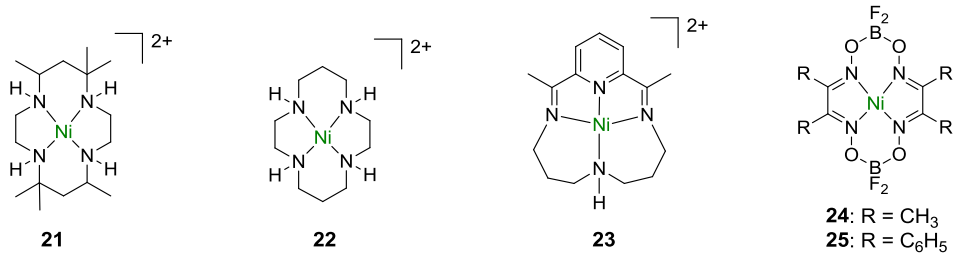

Figure 1.8 Nickel tetraaza macrocyclic complexes for the HER.

Ligands with electron-rich and π acidic sulfur donors are attractive as well for designing molecular catalysts given their proven capacity to stabilize metals at typically unstable low-oxidation-states. To mimic the active site of functional [NiFe]-H_2ases, where the nickel center is ligated by four cysteinate residues (Figure 1.4), Ni complexes containing four S donors were developed. One of the first complexes of such a kind was the Ni thiolate electrocatalyst **26** depicted in Figure 1.9 reported by Sarkar and coworkers,[74] which exhibits radical nature and presents as $[Ni^{II}(L^{2-})(L^{-\bullet})][PPh_4]$ according to various characterization techniques. In a MeCN solution of *p*-toluene sulfonic acid (*p*-TsOH), **26** electrocatalyzes the HER at unprecedented low potential E_p = −0.69 V vs. Ag/AgCl in water. Moreover, the S atoms protonate upon addition of *p*-TsOH before proton reduction, which means that the dithiolene ligand could play the role of proton relay. This role was also proved in the case of complexes **27-29** (Figure 1.9) by Artero and co-workers by studying the HER activity of Ni aryldithiolene complexes.[75] In addition to protonation at S donor sites, theoretical investigations indicated that the two electrons reduction occurs on the ligand scaffold, involving a dianion and retaining the Ni^{II} oxidation state throughout the whole catalytic cycle. The non-innocent nature of the dithiolene ligand framework was observed again in later reported Ni complexes **30-31**, among which **31** possesses a remarkable TON of 2×10^4 at 410 mV overpotential.[76,77] By

structurally modifying the peripheral π system of the dithiolene ligand scaffold, the group of Sakai developed other catalysts (**32-33**) featuring even lower overpotential.[78] In aqueous borate buffer solutions at pH = 9.0, overpotential of **32** and **33** were measured to be 227 mV and 173 mV, respectively. Based on the obtained Pourbaix diagrams and DFT calculations, the authors attribute the low HER overpotential of these complexes (**31-33**) to the involvement of ligand-centered proton-coupled electron transfer pathways.

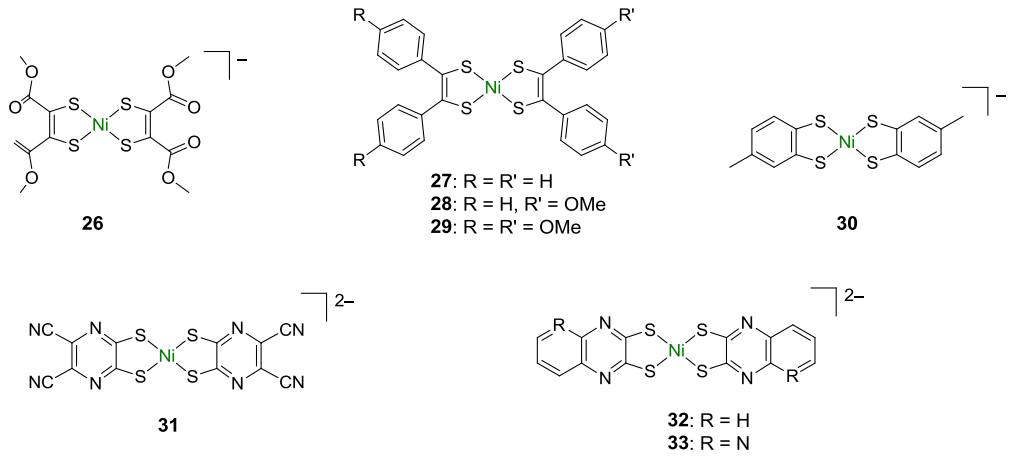

Figure 1.9 Nickel thiolate complexes employed in the electrocatalytic HER.

Phosphine donors are also π back-donating and are therefore widely utilized in the ligand scaffold for HER catalysts. Nickel bis(diphosphine) complexes with pendant amines normally as proton relay are prominent examples developed by DuBois and coworkers.[79,80] The first DuBois-type electrocatalyst for proton reduction is $[Ni(P_2^{Ph}N_2^{Ph})_2(CH_3CN)](BF_4)_2$ (**34**, $P_2^{Ph}N_2^{Ph}$ = 1,3,5,7-tetraphenyl-1,5-diaza-3,7-diphosphacyclooctane, Figure 1.10) reported in 2006, evaluated in HER in MeCN solution of 1:1 [H^+-DMF]OTf/DMF, showing a TOF of 350 s^{-1} (slightly higher than the 130 s^{-1} observed in triflic acid). As shown in Scheme 1.3, two potential pathways (EECC and ECEC)[81] affording either the *endo* or the *exo* intermediate isomers after the transfer of two electrons and two protons were proposed. Though the *exo* isomer is kinetically favored in the equilibrium of the two isomers, the *endo* isomer is the only transition state favorable to release dihydrogen, because HER occurs only when the proton at the *endo* position with respect to Ni is close enough to the catalyst metal center.[80,82]

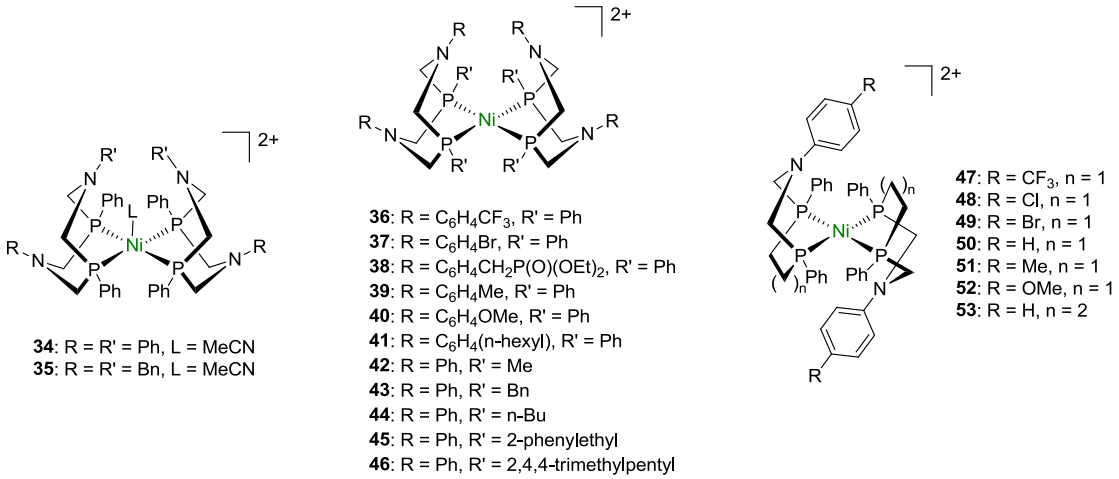

Figure 1.10 Ni tetraphopshine electrocatalysts for HER.

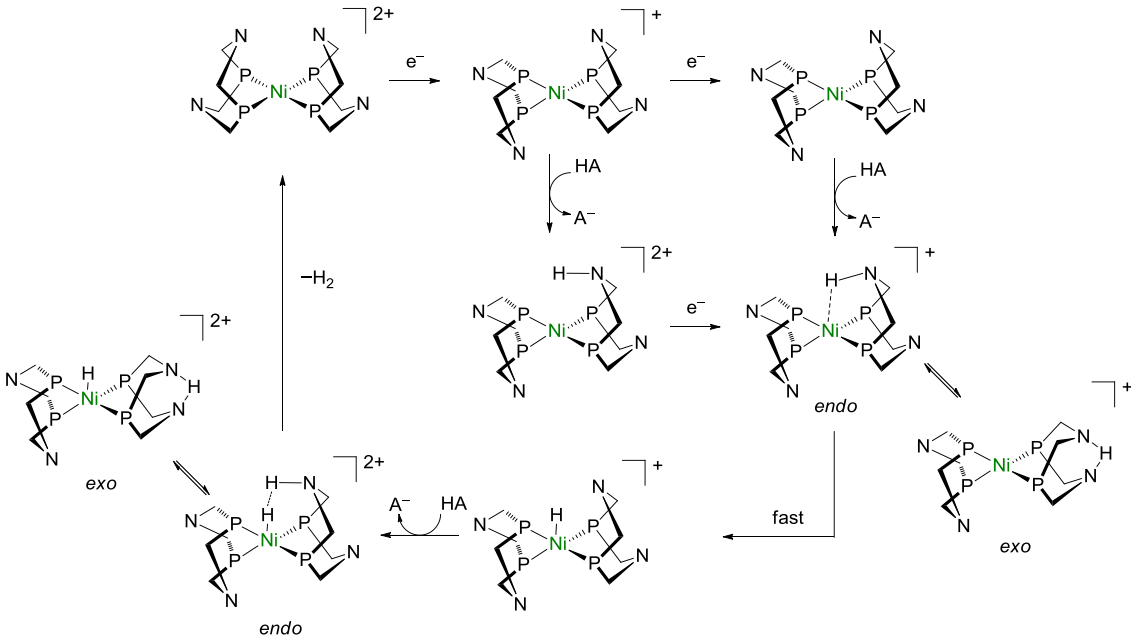

Scheme 1.3 Proposed pathways of hydrogen evolution by DuBois-type nickel catalyst.[81]

The activity of hydrogen generation of the DuBois-type of catalysts can be tuned by modifying the substituents on the N and P atoms of the ligands. Thus, for instance, exchanging the phenyl by a benzyl group on the N atom of complex **34**, leading to complex **35** (Figure 1.10), reduces the TOF in the HER in almost three orders of magnitude (TOF 350 s^{-1} and < 0.5 s^{-1} for **34** and **35**, respectively). This loss of activity is

related to forming the inactive *exo*-protonated isomer when **35** reacts with a proton before reduction.[83] The introduction of other substituents at the para position of the amine phenyl moiety was also assessed. Thus, in complexes **36-40** (Figure 1.10), the introduction of more electron-withdrawing substituents shifts the potentials of $Ni^{II/I}$ and $Ni^{I/0}$ reductions to more positive values (Figure 1.11, left), and increases the rate of the HER in MeCN. Among them, **38** exhibits the highest TOF (calculated from CV, Figure 1.11 right), 1850 s^{-1} at 0.37 V overpotential under optimized conditions. On the other hand, complex **36** bearing electron-withdrawing CF_3 groups exhibited the lowest catalytic rate because of its low basicity, which prevents the reduced species to be readily protonated.[84] The introduction of diverse substituents on the P atoms gave a series of $[Ni(P_2^RN_2^{Ph})_2](BF_4)_2$ complexes (**42-46**, Figure 1.10). Similarly to the effects observed on the N atoms, the substitution in this case roughly followed the rule that more electron-withdrawing groups led to more positive $Ni^{II/I}$ redox events. Besides, P-substituents exert steric effects on the redox potentials and the reaction rates. Thus, bulkier substituents shield more space near the Ni center, resulting in slower catalytic rates due to protonation more likely occurring at the non-productive *exo* position of the N atom. The authors also found beneficial the addition of water, which seems to be capable of promoting active *endo* protonated intermediates.[85]

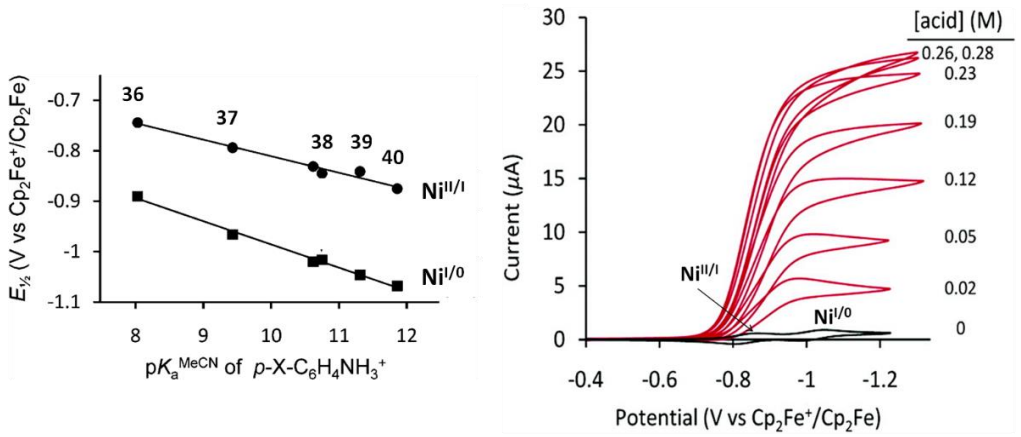

Figure 1.11 (Left) $E_{cat/2}$ for $Ni^{II/I}$ and $Ni^{I/0}$ couples of complexes **36-40**, and (right) cyclic voltammograms of complex **38** (0.7 mM) in the absence (black trace) and in the presence of different concentrations of acid (acid = 1:1 DMF:$[(DMF)H]^+OTf^-$; red traces) in MeCN.[84]

Since the activity is affected by the formation of inactive *exo* protonated species, another effective design direction could be tuning the diphosphine ligand to possess a single amine moiety. The resulted structure is then forced to chair conformation, presenting a favored *endo-endo* transition state for protonated intermediates. Therefore, complexes **47-52** (Figure 1.10) bearing seven membered rings and **53** bearing an eight membered ring are obtained based on tuning on the electronic and catalytic properties of DuBois complexes.[86–88] Benefiting from the formed favorable structures, they display much higher TOFs, about 6 times those of analogous complexes **37-40**. Particularly active is complex **50**, which catalyzes the HER at a rate of 33000 s^{-1} with an overpotential of 0.625 V when [H^+-DMF]OTf is used as proton source, and reach even faster 106000 s^{-1} if water is added to the reaction mixture. Comparing the activity in different conditions, water as proton reagent is definitely a powerful accelerator. Besides, acidic ionic liquids, e.g. (DMF)H]NTf_2 (NTf_2 = bis(trifluoro-methanesulfonyl)amide) working together with water can remarkably increase the rate of catalysis, offering complex **41** a TOF as high as 3000000 s^{-1}.[89]

1.5.2 Cobalt catalysts for HER

Cobalt (Co) is the 32nd most abundant element in the Earth's crust,[90] and a group 9 transition metal with electron configurations [Ar] $3d^7$ $4s^2$. The Co price fluctuated over the past two years but fell back to near 34 \$/kg,[91] nowadays significantly lower than that of precious metals such as Pt. Its price advantage and relatively high catalytic performance led Co to be an attractive non-precious metal for the electrochemical HER.[92] To stabilize the lower oxidation states of the Co center typically required in HER catalysis (Co^I intermediate species typically required, see Chapter 4 for a detailed mechanistic description), different ligands rendering assistance have been designed.

The π-acceptor nature of the oxime ligand framework led to efficient cobaloxime complexes for proton reduction catalysts. Thus, Espenson *et al.*, reported for the first time a cobaloxime system [$Co(dmgBF_2)_2(H_2O)_2$] ($dmgBF_2$ = difluoroboryl-dimethylglyoxime, **54**, Figure 1.12) that electrocatalyzes the reaction $Cr^{2+} + Cl^- + H^+ = CrCl^{2+} + 1/2H_2$ to evolve H_2.[93] When Artero and coworkers[94] examined **54** in a nonaqueous DMF solution, addition of Et_3NH^+ did not trigger the catalytic wave in the cyclic voltammogram (CV),

reflecting a low TOF in CV time scale, but bulk electrolysis on a graphite electrode at a potential 350 mV more negative than the $Co^{II/I}$ reduction potential (−0.90 V vs. Ag/AgCl) promoted the evolution of dihydrogen with a TON of 80 over 17 h. A related work studied the effect of methyl/phenyl substituents on the oxime ligand, showing that the diphenylglyoxime complex **56** with more positive $Co^{II/I}$ redox couple (−0.28 V vs. SCE vs. the −0.55 V vs. SCE of the methyl derivative **55**), had lower electrocatalytic activity.[95] Investigation of the HER electrocatalytic activity of both **55** and **56** under various proton sources indicated that the acid strength was of paramount importance for the catalytic pathways.

However, the pseudomacrocyclic structure of cobaloximes is relatively unstable and prone to hydrolysis in strongly acidic solutions. Therefore, Artero *et al.*[96] designed a ligand framework with a bridging propyl unit instead of two glyoxime units. The resulted complexes **57-58** depicted in Figure 1.12 possess similar catalytic activity to previous cobaloximes **54-55** but are able to work at lower overpotentials and are more robust from the point view of stability. The same authors also proposed a mechanism for the HER involving a Co^{III}-H intermediate and protonation at the O–H…O bridge in a proton-coupled electron transfer step. A further improvement of the stability of these cobalt catalysts was achieved through grafting the molecules onto electrode surfaces. Adsorbed **54** onto a glassy carbon electrode could work in pH 4 acetate solution to generate dihydrogen at an overpotential of 400 mV, with a sharply increased TON of 5000000 in about 16 h.[97] As a second example of the grafting strategy, a complex analogue to **57** (axial ligand is Cl) covalently linked to multiwalled carbon nanotubes gave a material electrocatalytically active for hydrogen generation in pure aqueous solution. It is worthy to note that this material is tremendously stable, showing a TON of 55000 after 7 h of continuous operation in a pH 4.5 acetate buffer and at an applied potential of −0.59 V vs. RHE. In contrast, complex **57** significantly degrade (after only 50 turnovers) in nonaqueous media.[98,99]

The tetraaza ligand CR (depicted above in Ni catalyst **23**) was coordinated to a Co center, giving the macrocyclic Co complex **59** in 2012. **59** was used as an electrocatalyst for the HER in acidic and neutral aqueous solution, with a high Faradaic

efficiency of >90%.[100] Exchanging of coordinated water by chloride ligands afforded complex **60**, which displayed both electrocatalytic and photocatalytic activity for hydrogen production.[101,102] In the case of photo-induced HER, **60** exhibits even better catalytic performance and stability than cobaloxime **57**, and a higher TON (1002) was achieved for **60** at concentration of 10^{-4} M. Llobet's group[103] later thoroughly examined the kinetics of involved steps, offering deeper understanding for this Co catalyst system. The ability to accommodate metal center, thus forming efficient catalysts, plus the mentioned ligand non-innocent properties, made it would be interesting to explore the ligand scaffold bearing the pyridyldiimine moiety, and actually this is the subject of this Thesis.

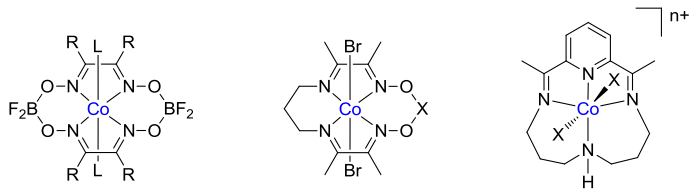

54: R = Me, L = H_2O
55: R = Me, L = MeCN
56: R = Ph, L = MeCN

57: X = H
58: X = BF_2

59: X = H_2O, n = 3
60: X = Cl, n = 1

Figure 1.12 Cobalt macrocyclic catalysts.

Pyridine moieties can strongly coordinate to diverse transition metal ions and thus be appropriate groups to be used in the synthesis of hydrogen evolution electrocatalysts. A notorious example of a polypyridyl-based cobalt complex for the HER was reported in 2010 by Chang and coworkers.[104] The Co^{II} complex **61** bearing the tetradentate ligand PY4 (PY4 = 2-bis(2-pyridyl)(methoxy)-methyl-6-pyridylpyridine) reduces the protons of trifluoroacetic acid (TFA) to H_2 in MeCN at a potential near to that of the corresponding $Co^{II/I}$ couple (overpotential about 0.4 V) with TOF calculated to be *ca.* 40 h^{-1}. It is interesting to note that the corresponding Zn complex bearing the same ligand is inactive for HER catalysis, highlighting the necessity of a redox-active metal center. To improve the water solubility of this complex, slight modifications on the ligand used led to complexes **62-63** (Figure 1.13), which exhibited enhanced electrocatalytic currents in pH 4.0 buffered solutions.[105] Among them, the catalytic activity of the CF_3-containing complex **63** was much lower than that of **62**. This trend shared by several reports

highlights the lower reactivity of the Co^{I} species when surrounded by electron-withdrawing groups,[106,107] resulting in a less electron-rich and less nucleophilic metal center. Chang's group later synthesized the cobalt complexes **64-66** (Figure 1.13) bearing the pentadentate ligand 2,6-bis(1,1-bis(2-pyridyl)ethyl)pyridine ($PY5Me_2$), whose platform was previously demonstrated to facilitate a molybdenum-oxo complex generating H_2 from water.[107,108] The CV of **64** in a pH 7 phosphate buffered solution showed a $Co^{II/I}$ reduction peak at −1.00 V vs. SHE and a catalytic wave 0.2 V more cathodic. Tested by controlled potential electrolysis (CPE), **64** demonstrated to be a robust and active catalyst, based on the 100% Faradaic efficiency and 55000 TONs achieved during a 60 h experiment. Substitution on the central pyridine ring of the $PY5Me_2$ ligand by introducing electron-withdrawing CF_3 (**65**) or electron-donating NMe_2 groups (**66**) tuned both the redox potentials of the $Co^{II/I}$ wave and the overpotential at which the catalytic processes is observed. Thus, complex **65** exhibited the most positive potentials while **66** shifted to the most negative potentials (**64** remaining central among the three complexes, Figure 1.14). Furthermore, the mechanistic analysis of the HER by **64** highlighted anation of the complex by the conjugate base of the employed acid, i.e., the acetate anion when acetic acid was used as proton souce.[106] Apart from the above complexes which undergo metal-centered reductions, pentadentate redox-active pyridino-bis-bipyridine ligands and their corresponding cobalt complexes were also synthesized (see Figure 1.13, right). Analyzed by CV, three cathodic processes were observed for complex **67** at −1.20 V, −1.79 and −1.94 V vs. Fc^{+}/Fc, which were assigned to the $Co^{II/I}$ event and two successive reduction of the two bipyridine moieties of the ligand, respectively.[109] The derivative complex **68**, bearing a CF_3 group, not only shifted the $Co^{II/I}$ couple positively by 61 mV, but also shifted the ligand centered reductions by 80 mV. Upon adding acetic acid into MeCN, both compounds trigger two discrete catalytic waves which match well with the ligand reduction potentials in the absence of acid.

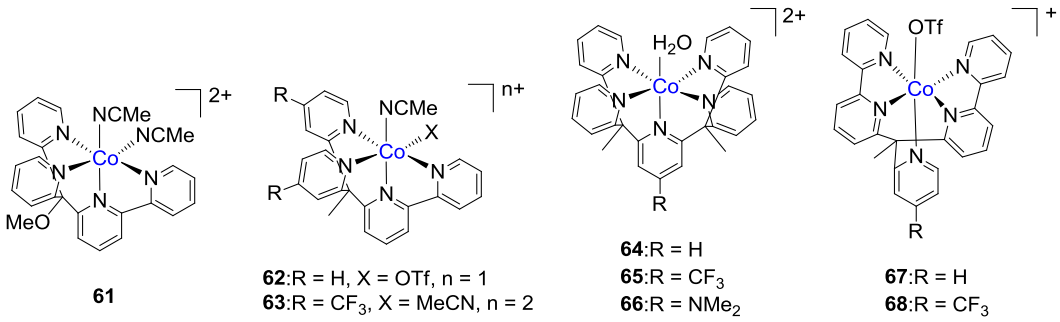

Figure 1.13 Co polypyridyl complexes for electrocatalytic H_2 production.

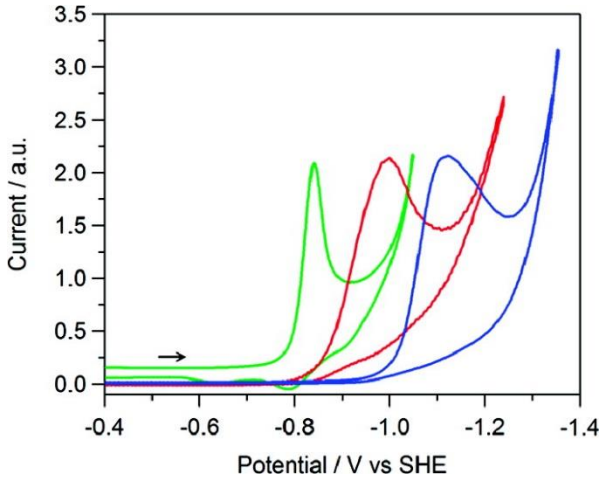

Figure 1.14 Cyclic voltammograms of **64** (red), **65** (green) and **66** (blue) in pH 7 phosphate (1.0 M) buffered solution.[107]

Due to the appealing features mentioned above when dealing with Ni catalysts (Section 1.5.1), phosphine donors have been applied to prepare Co molecular electrocatalysts as well (Figure 1.15). DuBois *et al*. extended to Co their successful Ni-based system bearing two bisphosphine ligands (see complex **34** in Figure 1.10 above) to afford complex **69**. Loss of one diphosphine ligand was observed in the presence of triflic acid, and so far the resulting cobalt complex **70** bearing a single bidentate $P^{Ph}_2N^{Ph}_2$ ligand, was proposed to be the real active catalyst in HER.[110] Studied by CV in MeCN solution of *p*-bromoanilinium tetrafluoroborate, complex **70** gave a TOF of 90 s^{-1} with a catalytic half peak potential at −0.99 V (calculated overpotential 0.285 V). Though this Co derivative exhibited somewhat slower rate than the Ni analogue (350 s^{-1}), the overpotential of the Co catalyst was about 65 mV lower compared to that of Ni. When

modifying the Ph groups on the phosphorous atoms in catalyst **70** by *t*-Bu substituents to form complex **71**, the TOF was improved to 160 s^{-1} while the overpotential also decreased to 160 mV.[111] Bullock *et al.* later synthesized another tetradentate Co complex **72**, which gave a TOF value of 980 s^{-1} at overpitential of 1.21 V when a $[(DMF)H]^+$/DMF buffer was used as proton source, this TOF dramatically increasing to 18000 s^{-1} upon addition of water with an overpotential of 1.27 V.[112] This complex allowed to isolate two very important intermediates of Co^I and Co^{III}-H, which facilitated the mechanistic analysis of the catalytic system. As depicted in Scheme 1.4 (top), the initial Co^{II} species (**72**) was first reduced to Co^I. Afterwards, the resulting pendant amines then serve as proton relays, forming the catalytic isomer *endo*-Co^I after protonation. Co^{III}-H, formed through a rapid intramolecular proton transfer from amine nitrogen to Co, was then one-electron reduced to Co^{II}-H. *Endo* protonation again at a pendant amine yields *endo*-Co^{II}-H, which was able to form a H-H bond and release H_2. A relevant breakthrough on the efficiency of molecular Co catalysts was achieved in 2014 when Sun *et al*. reported complex **73** (Figure 1.15). This system bearing a tetradentate phosphine ligand and exhibiting an octahedral coordination environment around the Co^{II} metal ion, exhibits the catalytic onset potential at −0.50 V vs. NHE in pH 7 phosphate buffer, which corresponds to an extremely low overpotential of 80 mV.[113] Complex **73** is such an active and stable electrocatalyst that CPE at 1.0 V vs. NHE for 20 h affords a TON of 92400, without observable deactivation. The DFT calculations for the HER reaction mechanism of **73** implied involvement of the phosphate anion from the employed buffer (Scheme 1.4, bottom).[114] Thus, when HPO_4^{2-} coordinates to the Co^{II} center by exchanging one of the two H_2O molecules, the mechanistic pathways evolves through two proton-coupled electron transfer (PCET) reductions. The first PCET process yields a one-electron reduced Co^I species and $H_2PO_4^-$, followed by the generation of a Co^{II}–H intermediate in the second reduction, leading to hydrogen release by the coupling of this Co^{II}–H and a proton from $H_2PO_4^-$. The energy barrier for this mechanism with an applied potential of −0.5 V was calculated to be 18.2 kcal mol^{-1}, in contrast to the 29.2 kcal mol^{-1} obtained if the involvement of the phosphate anion is not considered.

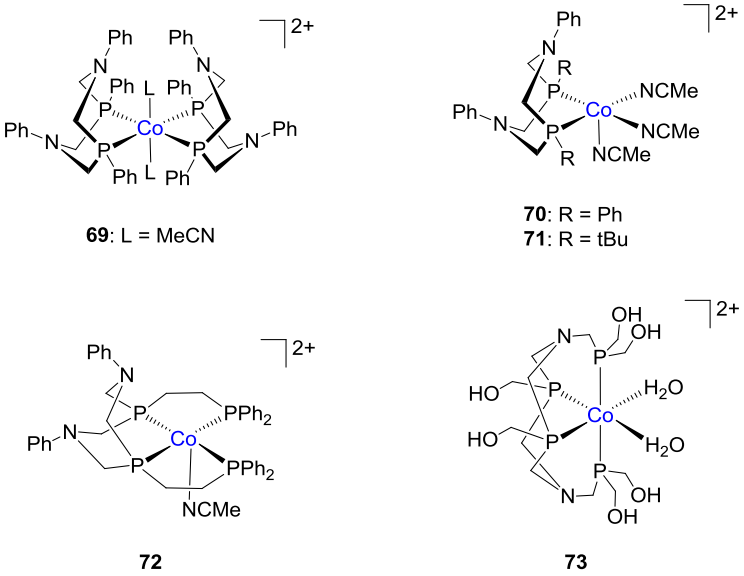

Figure 1.15 Co catalysts based on phosphine-rich ligands.

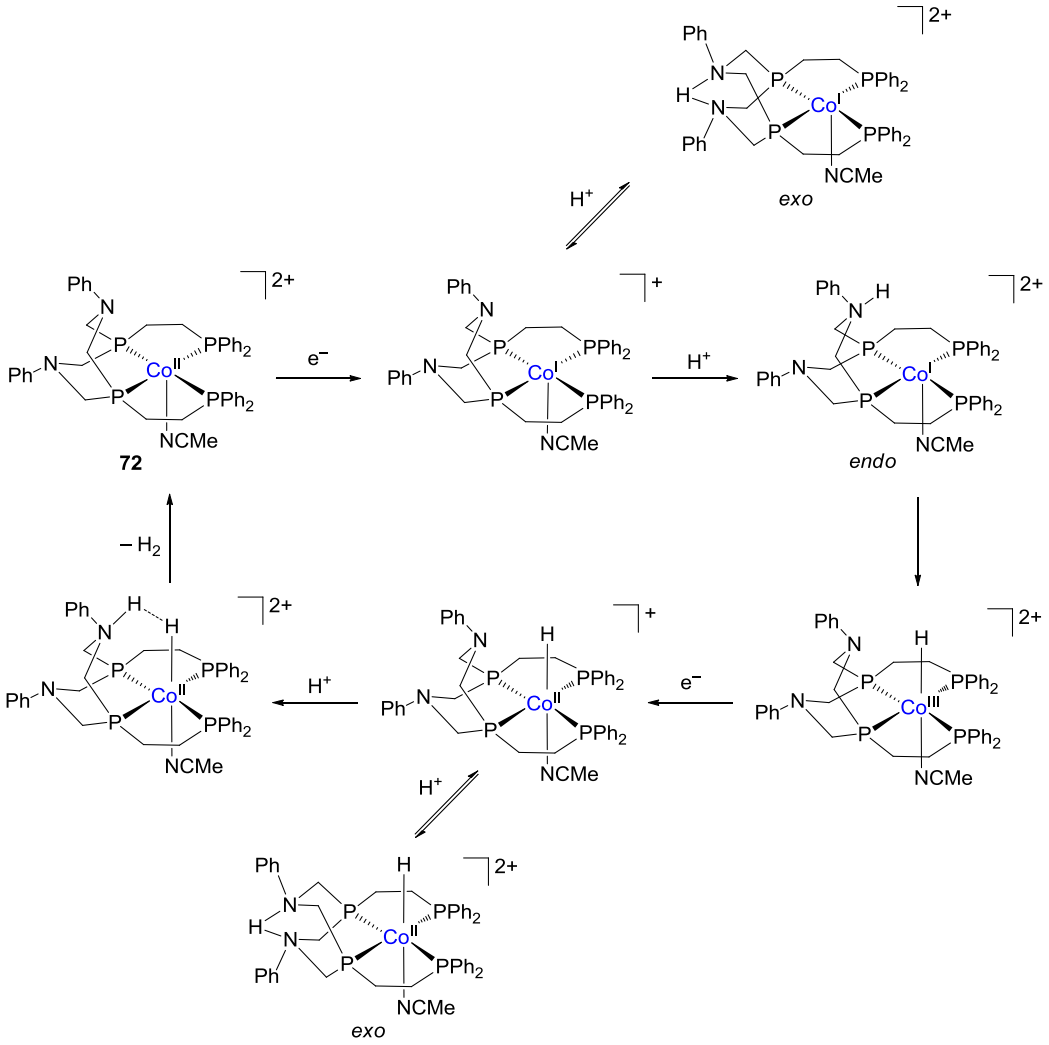
Ph
N
H
N
Ph
P
PPh2
Co
II
III
I
P
PPh2
NCMe
2+
+
exo
endo
72
H+
e−
– H2

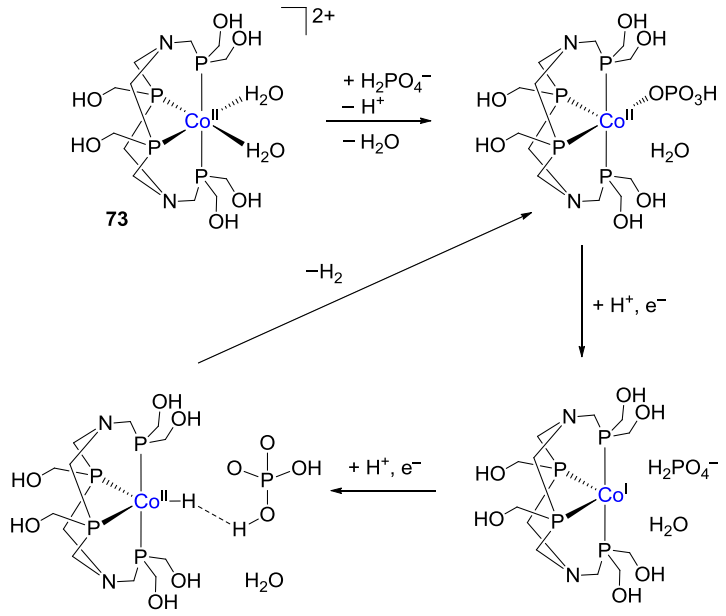

Scheme 1.4 The proposed mechanisms of complex **72** (top) and **73** (bottom) for the HER based on DFT calculations.

1.6 References

(1) *IEEJ Outlook 2018-Prospects and Challenges until 2050-Energy, Environment and Economy*; **2017**.
(2) Panwar, N. L.; Kaushik, S. C.; Kothari, S. *Renew. Sustain. Energy Rev.* **2011**, *15*, 1513–1524.
(3) Mathews, A. P. *Procedia Comput. Sci.* **2014**, *32*, 731–737.
(4) Trenberth, K. E. *Science* **2015**, *349*, 691–692.
(5) Lewis, N. S.; Nocera, D. G. *Proc. Natl. Acad. Sci. U. S. A.* **2006**, *103*, 15729–15735.
(6) Sen, S.; Ganguly, S. *Renew. Sustain. Energy Rev.* **2017**, *69*, 1170–1181.
(7) Møller, K. T.; Jensen, T. R.; Akiba, E.; Li, H. *Prog. Nat. Sci. Mater. Int.* **2017**, *27*, 34–40.
(8) Wang, M.; Chen, L.; Sun, L. *Energy Environ. Sci.* **2012**, *5*, 6763–6778.
(9) Ouyang, L. Z.; Huang, J. M.; Wang, H.; Wen, Y. J.; Zhang, Q. A.; Sun, D. L.; Zhu, M. *Int. J. Hydrogen Energy* **2013**, *38*, 2973–2978.
(10) Nikolaidis, P.; Poullikkas, A. *Renew. Sustain. Energy Rev.* **2017**, *67*, 597–611.
(11) Ersöz, A. *Int. J. Hydrogen Energy* **2008**, *33*, 7084–7094.
(12) Muradov, N. *Int. J. Hydrogen Energy* **2001**, *26*, 1165–1175.
(13) Rashid, M.; Al Mesfer, M. K.; Naseem, H.; Danish, M. *Int. J. Eng. Adv. Technol.* **2015**, *4*, 80–93.
(14) Speckmann, F.-W.; Bintz, S.; Groninger, M. L.; Birke, K. P. *J. Electrochem. Soc.* **2018**, *165*, 456–462.

(15) Züttel, A. *Mater. Today* **2003**, *6*, 24–33.
(16) Zheng, J.; Liu, X.; Xu, P.; Liu, P.; Zhao, Y.; Yang, J. *Int. J. Hydrogen Energy* **2012**, *37*, 1048–1057.
(17) Niaz, S.; Manzoor, T.; Pandith, A. H. *Renew. Sustain. Energy Rev.* **2015**, *50*, 457–469.
(18) Dalebrook, A. F.; Gan, W.; Grasemann, M.; Moret, S.; Laurenczy, G. *Chem. Commun.* **2013**, *49*, 8735–8751.
(19) Zhu, Q.-L.; Xu, Q. *Energy Environ. Sci.* **2015**, *8*, 478–512.
(20) Cheng, H. M.; Yang, Q. H.; Liu, C. *Carbon N. Y.* **2001**, *39*, 1447–1454.
(21) Pupysheva, O. V.; Farajian, A. A.; Yakobson, B. I. *Nano Lett.* **2008**, *8*, 767–774.
(22) Dong, J.; Wang, X.; Xu, H.; Zhao, Q.; Li, J. *Int. J. Hydrogen Energy* **2007**, *32*, 4998–5004.
(23) Witman, M.; Ling, S.; Gladysiak, A.; Stylianou, K. C.; Smit, B.; Slater, B.; Haranczyk, M. *J. Phys. Chem. C* **2017**, *121*, 1171–1181.
(24) Du, P.; Eisenberg, R. *Energy Environ. Sci.* **2012**, *5*, 6012–6021.
(25) Umena, Y.; Kawakami, K.; Shen, J. R.; Kamiya, N. *Nature* **2011**, *473*, 55–60.
(26) Kok, B.; Forbush, B.; McGloin, M. *Photochem. Photobiol.* **1970**, *11*, 457–475.
(27) Michelet, L.; Zaffagnini, M.; Morisse, S.; Sparla, F.; Pérez-Pérez, M. E.; Francia, F.; Danon, A.; Marchand, C. H.; Fermani, S.; Trost, P.; et al. *Front. Plant Sci.* **2013**, *4*, 470.
(28) Lubitz, W.; Ogata, H.; Rüdiger, O.; Reijerse, E. *Chem. Rev.* **2014**, *114*, 4081–4148.
(29) Shima, S.; Ermler, U. *Eur. J. Inorg. Chem.* **2011**, *2011*, 963–972.
(30) Frey, M. *Chembiochem* **2002**, *3*, 153–160.
(31) Vignais, P. M.; Billoud, B.; Meyer, J. *FEMS Microbiol. Rev.* **2001**, *25*, 455–501.
(32) Schilter, D.; Camara, J. M.; Huynh, M. T.; Hammes-Schiffer, S.; Rauchfuss, T. B. *Chem. Rev.* **2016**, *116*, 8693–8749.
(33) Kim, J. H.; Hansora, D.; Sharma, P.; Jang, J.-W.; Lee, J. S. *Chem. Soc. Rev.* **2019**, *48*, 1908–1971.
(34) Sapountzi, F. M.; Gracia, J. M.; Weststrate, C. J. (Kees-J.; Fredriksson, H. O. A.; Niemantsverdriet, J. W. (Hans). *Prog. Energy Combust. Sci.* **2017**, *58*, 1–35.
(35) Sivula, K. *J. Phys. Chem. Lett.* **2015**, *6*, 975–976.
(36) Nielander, A. C.; Shaner, M. R.; Papadantonakis, K. M.; Francis, S. A.; Lewis, N. S. *Energy Environ. Sci.* **2015**, *8*, 16–25.
(37) Sivula, K.; van de Krol, R. *Nat. Rev. Mater.* **2016**, *1*, 15010.
(38) Hu, S.; Shaner, M. R.; Beardslee, J. A.; Lichterman, M.; Brunschwig, B. S.; Lewis, N. S. *Science* **2014**, *344*, 1005–1009.
(39) Shon, J.-H.; Teets, T. S. *ACS Energy Lett.* **2019**, *4*, 558–566.
(40) Berardi, S.; Drouet, S.; Francàs, L.; Gimbert-Suriñach, C.; Guttentag, M.; Richmond, C.; Stoll, T.; Llobet, A. *Chem. Soc. Rev.* **2014**, *43*, 7501–7519.
(41) Fujishima, A.; Honda, K. *Nature* **1972**, *238*, 37–38.
(42) Fukuzumi, S.; Yamada, Y.; Suenobu, T.; Ohkubo, K.; Kotani, H. *Energy Environ. Sci.* **2011**, *4*, 2754–2766.
(43) Blakemore, J. D.; Crabtree, R. H.; Brudvig, G. W. *Chem. Rev.* **2015**, *115*, 12974–13005.
(44) Wang, M.; Yang, Y.; Shen, J.; Jiang, J.; Sun, L. *Sustain. Energy Fuels* **2017**, *1*, 1641–1663.
(45) Zhang, B.; Sun, L. *Chem. Soc. Rev.* **2019**, *48*, 2216–2264.

(46) Fourmond, V.; Jacques, P.-A.; Fontecave, M.; Artero, V. *Inorg. Chem.* **2010**, *49*, 10338–10347.
(47) Zou, X.; Zhang, Y. *Chem. Soc. Rev.* **2015**, *44*, 5148–5180.
(48) Platinum Prices - Interactive Historical Chart https://www.macrotrends.net/2540/platinum-prices-historical-chart-data (accessed May 16, **2019**).
(49) Coutard, N.; Kaeffer, N.; Artero, V. *Chem. Commun.* **2016**, *52*, 13728–13748.
(50) Wang, J. W.; Liu, W. J.; Zhong, D. C.; Lu, T. B. *Coord. Chem. Rev.* **2019**, *378*, 237–261.
(51) Queyriaux, N.; Jane, R. T.; Massin, J.; Artero, V.; Chavarot-Kerlidou, M. *Coord. Chem. Rev.* **2015**, *304–305*, 3–19.
(52) Wiedner, E. S.; Brown, H. J. S.; Helm, M. L. *J. Am. Chem. Soc.* **2016**, *138*, 604–616.
(53) Average prices for nickel worldwide 2014-2025 https://www.statista.com/statistics/675880/average-prices-nickel-worldwide/ (accessed May 16, **2019**).
(54) Gan, L.; Groy, T. L.; Tarakeshwar, P.; Mazinani, S. K. S.; Shearer, J.; Mujica, V.; Jones, A. K. *J. Am. Chem. Soc.* **2015**, *137*, 1109–1115.
(55) Wiese, S.; Kilgore, U. J.; DuBois, D. L.; Bullock, R. M. *ACS Catal.* **2012**, *2*, 720–727.
(56) Canaguier, S.; Artero, V.; Fontecave, M. *Dalt. Trans.* **2008**, *0*, 315–325.
(57) Sellmann, D.; Lauderbach, F.; Geipel, F.; Heinemann, F. W.; Moll, M. *Angew. Chem Int. Ed.* **2004**, *43*, 3141–3144.
(58) Lauderbach, F.; Prakash, R.; Götz, A. W.; Munoz, M.; Heinemann, F. W.; Nickel, U.; Hess, B. A.; Sellmann, D. *Eur. J. Inorg. Chem.* **2007**, *2007*, 3385–3393.
(59) Oudart, Y.; Artero, V.; J. Pécaut, A.; Fontecave, M. *Inorg. Chem.* **2006**, *45*, 4334–4336.
(60) Oudart, Y.; Artero, V.; Pécaut, J.; Lebrun, C.; Fontecave, M. *Eur. J. Inorg. Chem.* **2007**, *2007*, 2613–2626.
(61) Canaguier, S.; Vaccaro, L.; Artero, V.; Ostermann, R.; Pécaut, J.; Field, M. J.; Fontecave, M. *Chem. - A Eur. J.* **2009**, *15*, 9350–9364.
(62) Canaguier, S.; Fontecave, M.; Artero, V. *Eur. J. Inorg. Chem.* **2011**, *2011*, 1094–1099.
(63) Canaguier, S.; Field, M.; Oudart, Y.; Pécaut, J.; Fontecave, M.; Artero, V. *Chem. Commun.* **2010**, *46*, 5876–5878.
(64) Vaccaro, L.; Artero, V.; Canaguier, S.; Fontecave, M.; Field, M. J. *Dalt. Trans.* **2010**, *39*, 3043–3049.
(65) Barton, B. E.; Whaley, C. M.; Rauchfuss, T. B.; Gray, D. L. *J. Am. Chem. Soc.* **2009**, *131*, 6942–6943.
(66) Barton, B. E.; Rauchfuss, T. B. *J. Am. Chem. Soc.* **2010**, *132*, 14877–14885.
(67) Carroll, M. E.; Barton, B. E.; Gray, D. L.; Mack, A. E.; Rauchfuss, T. B. *Inorg. Chem.* **2011**, *50*, 9554–9563.
(68) Huynh, M. T.; Schilter, D.; Hammes-Schiffer, S.; Rauchfuss, T. B. *J. Am. Chem. Soc.* **2014**, *136*, 12385–12395.
(69) Schilter, D.; Nilges, M. J.; Chakrabarti, M.; Lindahl, P. A.; Rauchfuss, T. B.; Stein, M. *Inorg. Chem.* **2012**, *51*, 2338–2348.
(70) Fisher, B. J.; Eisenberg, R. *J. Am. Chem. Soc.* **1980**, *102*, 7361–7363.

(71) Schneider, J.; Jia, H.; Kobiro, K.; Cabelli, D. E.; Muckerman, J. T.; Fujita, E. *Energy Environ. Sci.* **2012**, *5*, 9502–9510.
(72) Efros, L. L.; Thorp, H. H.; Brudvig, G. W.; Crabtree, R. H. *Inorg. Chem.* **1992**, *31*, 1722–1724.
(73) Pantani, O.; Anxolabéhère-Mallart, E.; Aukauloo, A.; Millet, P. *Electrochem. commun.* **2007**, *9*, 54–58.
(74) Begum, A.; Moula, G.; Sarkar, S. *Chem. - A Eur. J.* **2010**, *16*, 12324–12327.
(75) Zarkadoulas, A.; Field, M. J.; Papatriantafyllopoulou, C.; Fize, J.; Artero, V.; Mitsopoulou, C. A. *Inorg. Chem.* **2016**, *55*, 432–444.
(76) Koshiba, K.; Yamauchi, K.; Sakai, K. *Angew. Chem Int. Ed.* **2017**, *56*, 4247–4251.
(77) Zarkadoulas, A.; Field, M. J.; Artero, V.; Mitsopoulou, C. A. *ChemCatChem* **2017**, *9*, 2308–2317.
(78) Aimoto, Y.; Koshiba, K.; Yamauchi, K.; Sakai, K. *Chem. Commun.* **2018**, *54*, 12820–12823.
(79) Wilson, A. D.; Newell, R. H.; McNevin, M. J.; Muckerman, J. T.; M. Rakowski DuBois, A.; DuBois, D. L. *J. Am. Chem. Soc.* **2006**, *128*, 358–366.
(80) Wilson, A. D.; Shoemaker, R. K.; Miedaner, A.; Muckerman, J. T.; DuBois, D. L.; DuBois, M. R. *Proc. Natl. Acad. Sci. U. S. A.* **2007**, *104*, 6951–6956.
(81) Rountree, E. S.; Dempsey, J. L. *J. Am. Chem. Soc.* **2015**, *137*, 13371–13380.
(82) Kachmar, A.; Vetere, V.; Maldivi, P.; Franco, A. A. *J. Phys. Chem. A* **2010**, *114*, 11861–11867.
(83) Appel, A. M.; Pool, D. H.; O'Hagan, M.; Shaw, W. J.; Yang, J. Y.; Rakowski DuBois, M.; DuBois, D. L.; Bullock, R. M. *ACS Catal.* **2011**, *1*, 777–785.
(84) Kilgore, U. J.; Roberts, J. A. S.; Pool, D. H.; Appel, A. M.; Stewart, M. P.; DuBois, M. R.; Dougherty, W. G.; Kassel, W. S.; Bullock, R. M.; DuBois, D. L. *J. Am. Chem. Soc.* **2011**, *133*, 5861–5872.
(85) Kilgore, U. J.; Stewart, M. P.; Helm, M. L.; Dougherty, W. G.; Kassel, W. S.; DuBois, M. R.; DuBois, D. L.; Bullock, R. M. *Inorg. Chem.* **2011**, *50*, 10908–10918.
(86) Helm, M. L.; Stewart, M. P.; Bullock, R. M.; DuBois, M. R.; DuBois, D. L. *Science* **2011**, *333*, 863–866.
(87) Stewart, M. P.; Ho, M.-H.; Wiese, S.; Lindstrom, M. Lou; Thogerson, C. E.; Raugei, S.; Bullock, R. M.; Helm, M. L. *J. Am. Chem. Soc.* **2013**, *135*, 6033–6046.
(88) Wiese, S.; Kilgore, U. J.; Ho, M.-H.; Raugei, S.; DuBois, D. L.; Bullock, R. M.; Helm, M. L. *ACS Catal.* **2013**, *3*, 2527–2535.
(89) Maher, A. G.; Passard, G.; Dogutan, D. K.; Halbach, R. L.; Anderson, B. L.; Gagliardi, C. J.; Taniguchi, M.; Lindsey, J. S.; Nocera, D. G. *ACS Catal.* **2017**, *7*, 3597–3606.
(90) Zhong, H.; Campos-Roldán, C.; Zhao, Y.; Zhang, S.; Feng, Y.; Alonso-Vante, N.; Zhong, H.; Campos-Roldán, C. A.; Zhao, Y.; Zhang, S.; et al. *Catalysts* **2018**, *8*, 559.
(91) London Metal Exchange: LME Cobalt https://www.lme.com/en-GB/Metals/Minor-metals/Cobalt#tabIndex=0 (accessed May 16, **2019**).
(92) Marinescu, S. C.; Winkler, J. R.; Gray, H. B. *Proc. Natl. Acad. Sci. U. S. A.* **2012**, *109*, 15127–15131.
(93) Connolly, P.; Espenson, J. H. *Inorg. Chem.* **1986**, *25*, 2684–2688.
(94) Mathieu Razavet; Vincent Artero, and; Fontecave, M. *Inorg. Chem.* **2005**, *44*,

4786–4795.
(95) Xile Hu; Bruce S. Brunschwig, A.; Peters, J. C. *J. Am. Chem. Soc.* **2007**, *129*, 8988–8998.
(96) Jacques, P.-A.; Artero, V.; Pécaut, J.; Fontecave, M. *Proc. Natl. Acad. Sci. U. S. A.* **2009**, *106*, 20627–20632.
(97) Berben, L. A.; Peters, J. C. *Chem. Commun.* **2010**, *46*, 398–400.
(98) Kaeffer, N.; Chavarot-Kerlidou, M.; Artero, V. *Acc. Chem. Res* **2015**, *48*, 1286–1295.
(99) Andreiadis, E. S.; Jacques, P.-A.; Tran, P. D.; Leyris, A.; Chavarot-Kerlidou, M.; Jousselme, B.; Matheron, M.; Pécaut, J.; Palacin, S.; Fontecave, M.; et al. *Nat. Chem.* **2013**, *5*, 48–53.
(100) McCrory, C. C. L.; Uyeda, C.; Peters, J. C. *J. Am. Chem. Soc.* **2012**, *134*, 3164–3170.
(101) Leung, C. F.; Chen, Y. Z.; Yu, H. Q.; Yiu, S. M.; Ko, C. C.; Lau, T. C. *Int. J. Hydrogen Energy* **2011**, *36*, 11640–11645.
(102) Varma, S.; Castillo, C. E.; Stoll, T.; Fortage, J.; Blackman, A. G.; Molton, F.; Deronzier, A.; Collomb, M.-N. *Phys. Chem. Chem. Phys.* **2013**, *15*, 17544–17552.
(103) Gimbert-Suriñach, C.; Albero, J.; Stoll, T.; Fortage, J.; Collomb, M.-N.; Deronzier, A.; Palomares, E.; Llobet, A. *J. Am. Chem. Soc.* **2014**, *136*, 7655–7661.
(104) Bigi, J. P.; Hanna, T. E.; Harman, W. H.; Chang, A.; Chang, C. J. *Chem. Commun.* **2010**, *46*, 958–960.
(105) Khnayzer, R. S.; Thoi, V. S.; Nippe, M.; King, A. E.; Jurss, J. W.; El Roz, K. A.; Long, J. R.; Chang, C. J.; Castellano, F. N. *Energy Environ. Sci.* **2014**, *7*, 1477–1488.
(106) King, A. E.; Surendranath, Y.; Piro, N. A.; Bigi, J. P.; Long, J. R.; Chang, C. J. *Chem. Sci.* **2013**, *4*, 1578–1587.
(107) Sun, Y.; Bigi, J. P.; Piro, N. A.; Tang, M. L.; Long, J. R.; Chang, C. J. *J. Am. Chem. Soc.* **2011**, *133*, 9212–9215.
(108) Karunadasa, H. I.; Chang, C. J.; Long, J. R. *Nature* **2010**, *464*, 1329–1333.
(109) Nippe, M.; Khnayzer, R. S.; Panetier, J. A.; Zee, D. Z.; Olaiya, B. S.; Head-Gordon, M.; Chang, C. J.; Castellano, F. N.; Long, J. R. *Chem. Sci.* **2013**, *4*, 3934–3945.
(110) Jacobsen, G. M.; Yang, J. Y.; Twamley, B.; Wilson, A. D.; Bullock, R. M.; Rakowski DuBois, M.; DuBois, D. L. *Energy Environ. Sci.* **2008**, *1*, 167–174.
(111) Wiedner, E. S.; Yang, J. Y.; Dougherty, W. G.; Kassel, W. S.; Bullock, R. M.; DuBois, M. R.; DuBois, D. L. *Organometallics* **2010**, *29*, 5390–5401.
(112) Wiedner, E. S.; Appel, A. M.; DuBois, D. L.; Bullock, R. M. *Inorg. Chem.* **2013**, *52*, 14391–14403.
(113) Chen, L.; Wang, M.; Han, K.; Zhang, P.; Gloaguen, F.; Sun, L. *Energy Environ. Sci.* **2014**, *7*, 329–334.
(114) Zhang, Y.; Liao, R. *Phys. Chem. Chem. Phys.* **2017**, *19*, 32589–32596.

Chapter 2
Objectives

The need for easily accessible renewable energies has resulted in the development of the artificial photosynthesis research area. Within this general issue, splitting water to obtain dihydrogen to be used as energy carrier is one of the most outstanding topics. Thus, researchers have been naturally attracted and their interest in obtaining new catalysts for the hydrogen evolution reaction (HER) has considerably grown. However, if large scale practical applications are envisaged, efficient analogues to the scarce and pricy noble metal-based catalysts typically employed must be developed. To this end, first row transition metal-based molecular complexes arise as interesting candidates. Therefore, the overall objective of this PhD Thesis is to synthesize and thoroughly characterize a new family of efficient HER molecular catalysts based on earth-abundant metals (Ni/Co) bearing pyridine diamine (PDI) redox-active ligands in their structure. The specific objectives of this Thesis can be summarized as follows:

I.

Molecular complexes bearing a redox active pyridine diimine (PDI) ligand scaffold have recently emerged as catalysts for the HER, among others. Tridentate PDI-based ligands are common but pentadentate scaffolds combining different donor atoms are rare. Thus, a first goal of this PhD Thesis is the synthesis of tunable pentadentate N_3P_2-PDI ligands (see Figure below) containing phosphine arms of different length (R_2) and substitutions in the pyridyl ring (R_1) and the preparation, full characterization and electrocatalytic evaluation in HER of their corresponding Ni complexes. An intriguing point here will be to determine the electron location when the complex is electrochemically reduced and how the different ligand configurations alter the catalytic performance of the obtained complexes in terms of overpotential, activity and stability.

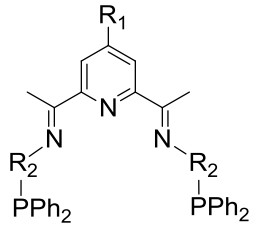

R_1 = H or Cl
R_2 = ethyl, propyl or phenyl

II.

Together with Ni, Co has proven to be an excellent alternative to precious metals for efficient HER catalysis at the molecular level. Thus, combination of the N_3P_2-PDI ligands prepared in **I** (see Figure above) to a Co metal center is a second goal of this PhD Thesis. Besides the thorough characterization of the set of new complexes, the potential diamagnetic character of Co(I) and Co(III) species, including Co(III)-H active sites, makes the mechanistic analysis of this family of complexes particularly appealing. Thus, after evaluating and benchmarking their HER activity and stability, the mechanistic pathways in proton reduction of these PDI-based Co complexes will be carefully analyzed through spectroscopic techniques to gain more insight about the operating mechanism and be able to rationally propose improved second-generation versions of the catalytic system.

Chapter 3

Symmetrical Nickel(II) Bis(imino)pyridine Complexes as Electrocatalysts for the Hydrogen Evolution Reaction

3.1 Introduction

Building a hydrogen-based economy to release the current dependence on fossil fuels for most practical uses has received a great deal of attention and consensus along the last decades.[1] Even if numerous methods exist to produce hydrogen gas, the electrocatalytic hydrogen evolution reaction (HER) is a known key technology for implementing large-scale H_2 generation. Thus, the pursuit of efficient and cheap electrocatalysts for the HER have led to considerable efforts toward earth-abundant transition-metal complexes, such as Ni-based coordination compounds.

In many traditional methods, ligands with different electronic and steric properties are used to tune the performance of transition metal-based catalysts. Thus, metal centers with open coordination sites and capability to accommodate multiple redox states are the essential components, leaving ligands as spectator species in catalysis. A relatively newer concept attracting more and more attention is the participation of such a ligand (the so-called non-innocent ligands) in the redox process, in cooperation with the metal center. Non-innocent ligands are involved in catalytic reactions by accepting/releasing electrons or forming/breaking chemical bonds.[2] In the specific case of HER, non-innocent ligands operate as an electron reservoir that can usually make complexes exhibit high catalytic activities. Also, alternative ligand hydride pathways are highly desirable to avoid the common metal hydride species, the typical HER intermediates, given the requirements for metal center described at the beginning of this paragraph.

Various types of non-innocent ligands coordinating a Ni center have been reported for the HER. For instance, a hangman Ni(II) metalloporphyrin triggered a catalytic wave with peak potential of −1.8 V vs. Fc^+/Fc in the presence of benzoic acid or –1.37 V in MeCN solution of tosic acid. DFT calculations revealed that the ligand is able to play a

similar role to that of the metal center, storing both electrons and protons in its C–H and O–H bonds.[3] Also, bis(dithiolene) complexes are a family of electrocatalysts usually assisted by the non-innocence of the S_4 ligand framework.[4] Finally, as mentioned in Chapter 1, the 2,6-bis(imino)pyridine (or pyridine diimine, PDI) ligands, which we will use in this study, are also typical redox-active species.

The use of the PDI ligand family is expanding fast given its relatively easy synthesis and ability to coordinate a wide range of metal ions, including transition and main group metals.[5] The ability of PDI ligands to accept one or more electrons generating anions at different oxidation level is well established[6] and the electronic structure of the different products shown in Figure 1. Thus, the mono-anionic radical form shows radical character distributed on the ligand framework. However, for two-electron reduced PDI scaffold several resonance forms exist: the asymmetric singlet (A),[7] the symmetric singlet (B),[8] the symmetric triplet (C),[9] or a form where the pyridine nitrogen atom has been removed from the conjugated π system of the ligand (D).[10] This ability to store up to three electrons for redox reactions contributes to the stabilization of the intermediates containing a low valence metal center by metal-to-ligand back donation of electron density, thus it can help reducing the overpotentials in catalytic reactions.

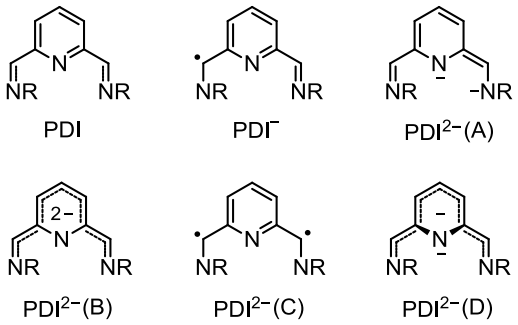

Figure 3.1 Electronic structures adopted by PDI ligands in various oxidation states.[11]

Redox non-innocence made PDI ligands valuable in diverse catalytic processes like hydrosilylation,[12] polymerization,[13] C-H activation,[14] and those related to energy conversion (reduction of CO_2 to methanol as well as protons to H_2.[15] In the reported PDI-based HER catalysts, the ligand is tridentate in most of the cases. Thus, for instance, complex (^{pyp}PDI)Ni(Cl)$_2$ (pyp = N-methyl-3-pyperidine, see Figure 3.2), which bears a

non-innocent PDI ligand together with a pendant base in the second coordination sphere, can catalyze the HER at a turnover frequency (TOF) of 2572 s^{-1} and a high rate constant of 2.7×10^6 $M^{-2}s^{-1}$. When the substituents on the nitrogen atoms were changed to phenyl groups ($(^{xyl}PDI)Ni(Br)_2$ (xyl = *m*-xylene) in Figure 3.2), the activity decreased to 3.7×10^4 $M^{-2}s^{-1}$.[16] Contrarily to the redox-active character of the ligands in the previous examples ($(^{pyp}PDI)Ni(Cl)_2$ and $(^{xyl}PDI)Ni(Br)_2$), the Ni(II) complex (H-^{iPrPh}PDI)Ni(Br)$_2$ (iPrPh = diisopropylphenyl), bearing an aldimine sidearm, shows the unpaired spin density residing mostly at the metal center after its one-electron reduction.[17] Berben's group reported in 2015 the aluminum(III) complexes (Ph-$^{iPrPh}PDI^{2-}$)Al(Cl)(THF) and (Ph-$^{iPrPh}PDI^{-}$)Al(Cl)$_2$ as HER catalyst, with the ligand respectively behaving as a dianion and a radical monoanion after reduction.[18]

Tetradentate PDI-based macrocyclic ligands also received much interest for H_2 production, as is the case for complexes $[(^{c(Pr2NH)}PDI)Ni]^{2+}$ and $[(^{c(Pr2PPh)}PDI)Ni]^{2+}$. Interestingly, both $Ni^{II/I}$ and ligand$^{0/\bullet-}$ couples in complex $[(^{c(Pr2PPh)}PDI)Ni]^{2+}$ shifts to more positive values relative to $[(^{c(Pr2NH)}PDI)Ni]^{2+}$, because the softer donor atom P stabilizes the Ni(I) state through π-back bonding. The study of both complexes in photocatalytic HER toward proton reduction also shows higher TON for $[(^{c(Pr2PPh)}PDI)Ni]^{2+}$ (960) than $[(^{c(Pr2NH)}PDI)Ni]^{2+}$ (<300) after 24 h.[19]

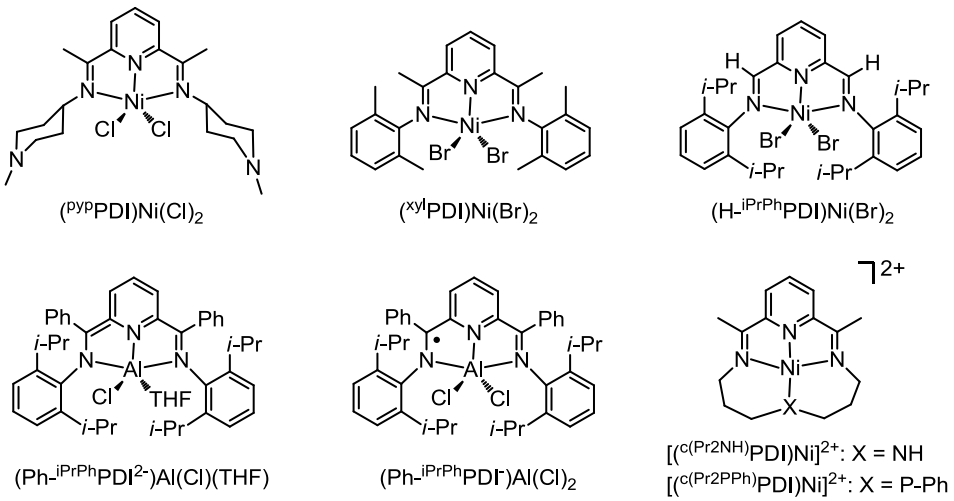

Figure 3.2 HER-relevant complexes of tri- or tetradentate PDI-based ligands.

There are very few examples of pentadentate PDI ligands that have been applied in HER catalysts. One relevant example is the Mn(I) complex $[(^{Ph2PPr}PDI)Mn(CO)]^+$

(Figure 3.3), which undergoes a reversible two-electron reduction at –1.92 V vs. Fc^+/Fc in the cyclic voltammogram, tentatively assigned to the formation of (PDI^-)Mn(0) species.[20] Chemical reduction of [(^{Ph2PPr}PDI)Mn(CO)]$^+$ with excess Na−Hg proved a low-spin Mn(I) complex featuring a PDI radical monoanion, as confirmed by EPR spectroscopy and supported by density functional theory (DFT) calculations.[21] [(^{Ph2PPr}PDI)Mn(CO)]$^+$ exhibits electrocatalytic activity to generate H_2 in acetonitrile solution, but only in the presence of both Brønsted acids (H_2O or MeOH) and CO_2, with CO_2 to lower the pH value and then generate enough protons. Another example is the molybdenum compound [(^{Ph2PPr}PDI)MoO]$^{2+}$ (Figure 3.3). Reduction of H_2O to H_2 was mediated by this complex in acetonitrile, attaining a Faradaic efficiency of 96% during controlled potential electrolysis at –2.5 V vs. Fc^+/Fc.[22] In this case, contrarily to what was observed for complex [(^{Ph2PPr}PDI)Mn(CO)]$^+$ and in many other examples above, the PDI ligand scaffold is redox-innocent and does not directly participate in the catalytic process.

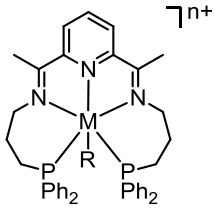

[(^{Ph2PPr}PDI)Mn(CO)]$^+$: M = Mn, R = CO, n = 1
[(^{Ph2PPr}PDI)MoO]$^{2+}$: M = Mo, R = O(trivalent bond), n = 2

Figure 3.3 Mn and Mo complexes with a pentadentate ^{Ph2PPr}PDI ligand.

Generally speaking, changing the electronic properties of the ligand strongly influence the reactivity and catalytic behavior of the corresponding transition metal complex. This fact, which is well established for metal-based redox catalytic process, should still be more crucial for ligand-based redox catalytic processes. Such modifications are typically achieved by introducing electron-withdrawing or electron-donating substituents at the ligand.

According to the line of the above thought, in this Chapter bare and substituted bis(imino)pyridine (PDI) [NNNPP] ligands, which encompass ketimine sidearms and can potentially act as redox-active species, were prepared, coordinated to a Ni center and assessed as electrocatalysts in organic media.

3.2 Results and discussion

3.2.1 Synthesis and characterization

3.2.1.1 Synthesis and characterization of ligands

Four diphenylphosphine-based ligands containing the bis(imino)pyridine scaffold have been successfully synthesized and characterized by NMR spectroscopy. The preparation of ligands ^{Ph2PEt}PDI (**L1**) and ^{Ph2PPr}PDI (**L2**) followed a procedure reported by Ben-Daat and co-workers.[5] In the synthesis, two equivalents of 2-(diphenylphosphino)ethylamine or 3-(diphenylphosphino)-1-propylamine reacted with one equivalent of 2,6-diacetylpyridine in the presence of *p*-toluenesulfonic acid (*p*-TsOH) as catalyst in toluene (Scheme 3.1). The use of molecular sieves to release the water formed in the condensation reaction drives the reaction to completion. The recorded ^{1}H and ^{31}P{^{1}H} NMR spectra (see Figures S1–S4 in the supporting information) are in accordance with the reported values for ^{Ph2PEt}PDI and ^{Ph2PPr}PDI ligands.

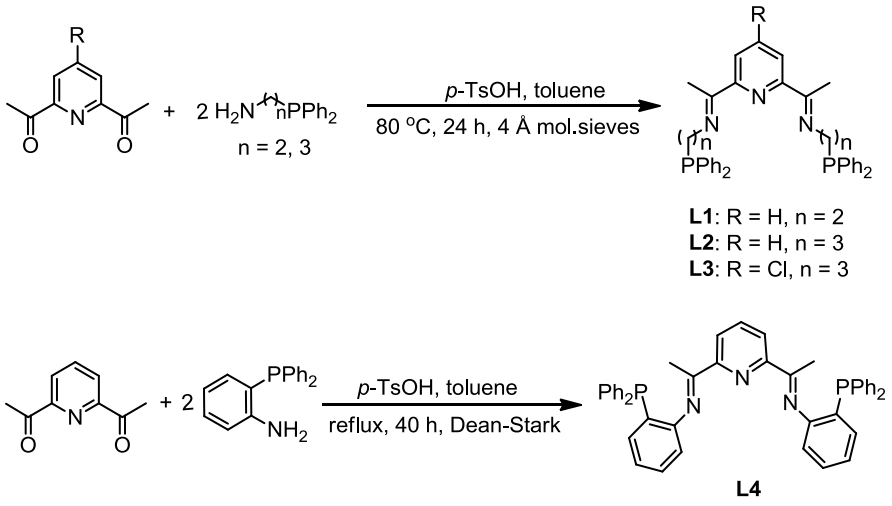

Scheme 3.1 Synthetic scheme for the ligands employed in this Chapter.

The preparation of ^{Ph2PPr}PDI(*p*)Cl (**L3**) was performed in a three-step reaction. Basification of the 4-Chloropyridine hydrochloride followed by the use of the resulting 4-Chloropyridine crude product to prepare 4-Chloro-2,6-diacetylpyridine was achieved following a reported method.[23] Finally, the condensation of 4-Chloro-2,6-diacetylpyridine with 3-(diphenylphosphino)-1-propylamine under identical conditions to **L2** (Scheme 3.1)

yield, upon crystallization of crude product in a MeOH and diethyl ether mixed solution at –35°C, the desired ligand **L3** as yellow crystals. The ^{1}H NMR spectrum showed a similar pattern as for **L2**, except for the absence of the proton at the para position of the pyridine scaffold, demonstrating the success of Cl-substitution at the corresponding position (Figure 3.4). ^{31}P{^{1}H} NMR spectra of **L3** features a singlet at –15.35 ppm (Figure S5).

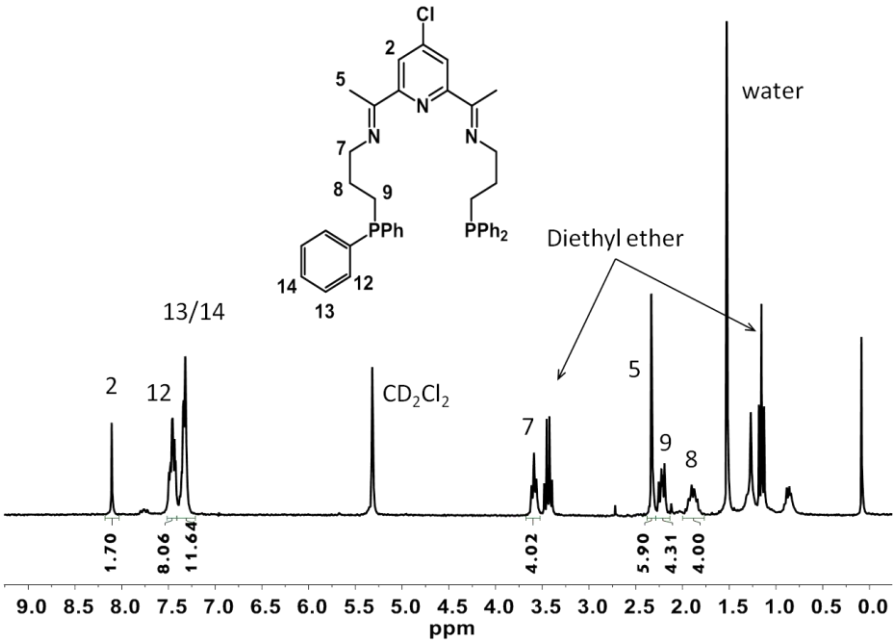

Figure 3.4 ^{1}H NMR spectra of **L3** (250 MHz, CD_2Cl_2, 304 K).

A number of complexes containing a PDI ligand derived from the P, N-donor 2-(diphenylphosphino)benzenamine ($^{Ph2P}PhNH_2$) scaffold have been prepared,[24–26] in most of which the $^{Ph2P}PhNH_2$-moiety acts as a bidentate chelating ligand. 2-(diphenylphosphino)-benzenamine was prepared according to a reported protocol.[27] So, numerous efforts were made in this work to introduce the $^{Ph2P}PhNH_2$ by reacting it with half equivalent of 2,6-diacetylpyridine to afford the new Schiff base ligand **L4** (Scheme 3.1). After attempting various conditions, it was found that refluxing the reactants in toluene for 40 h in the presence of *p*-TsOH as catalyst could produce the ^{Ph2PPh}PDI product (**L4**), as depicted in Scheme 3.1. Purification through washing the crude solid product with acetone, followed by re-dissolving the crude in a MeOH/CH_3Cl mixed solution and

slowly evaporating the volatiles, yielded pure **L4** as yellow crystals, which were obtained in extremely low yield ca. 1%. The crystalline product was characterized by ^{1}H NMR spectroscopy (Figure 3.5), ^{31}P{^{1}H} NMR spectroscopy (Figure S6), and X-ray Diffraction (Figure 3.6) as well. The low yield of the product could be explained by the p-π-conjugation lowering the electron density on the N atom of 2-(diphenylphosphino)benzenamine, along with steric hindrance from the rigid phenyl frame, thereby reducing the nucleophilic attack capability to the carbonyl groups of 2,6-diacetylpyridine. Due to the handicap to get a moderate amount of pure ligand **L4**, we did not attempt to synthesize the corresponding metal complexes with this ligand.

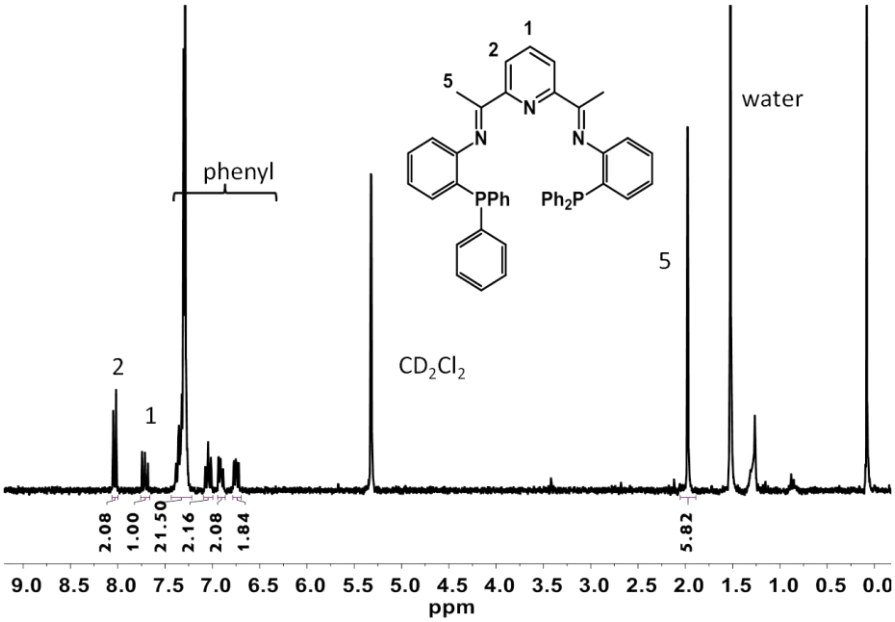

Figure 3.5 ^{1}H NMR spectrum of **L4** (250 MHz, CD_2Cl_2, 301 K).

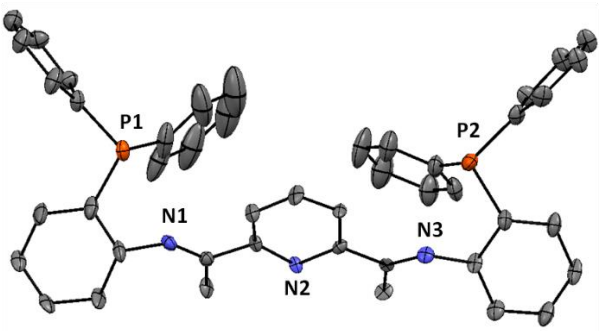

Figure 3.6 ORTEP drawing of **L4** with 30% probability thermal ellipsoids. Hydrogen atoms are omitted for clarity.

3.2.1.2 Synthesis and characterization of complexes

Heating ligand **L1** with 1 equivalent of the metal precursor $NiCl_2 \cdot 6H_2O$ in EtOH under N_2 atmosphere for 1 day afforded a dark maroon solution. Following solvent removal in vacuo and washing with diethyl ether gave a brown-red powder. Unlike for the longer alkyl chain ligands **L2** and **L3** that form Ni complexes (**1**(Cl) and **2**(Cl), see below in this section) which are easy to crystallize in high yields, despite numerous efforts we were not able to grow single crystals suitable for X-ray diffraction for this **L1**-containing solid. The mass spectra of this powder recorded in a MeOH solution (Figure S7) exhibited a wide array of peaks. Among them, only those at m/z = 337.6 and 710.1 can be tentatively assigned to $[L1+Ni+MeOH]^{2+}$ and $[L1+Ni+Cl+MeOH]^{+}$, respectively, or to the species with analogous m/z without coordinated MeOH but bearing two oxidized phosphorus atoms. With the available data, it is still unassured whether the ethyl-bridging arms produce PDI ligands capable of κ^5-*N*,*N*,*N*,*P*,*P*-coordinating to a nickel center.

Under anaerobic conditions, the pentadentate ligand **L2** is coordinated to a Nickel center by reacting the ligand with 1 equivalent of $NiCl_2 \cdot 6H_2O$ in refluxing EtOH overnight (Scheme 3.2). Partial evaporation of the EtOH solvent followed by a slow addition of diethyl ether induces precipitation, Purification of the obtained dark solid was carried out via crystallization by the slow diffusion of diethyl ether into a solution of product in DCM, yielding [Ni(^{Ph2PPr}PDI)(Cl)](Cl) (**1**(Cl)) as blue-purple crystals (85% yield). The same synthetic conditions were applied for the preparation of [Ni(^{Ph2PPr}PDI(*p*)Cl)(Cl)](Cl) (**2**(Cl)) from **L3** except for the solvent of crystallization. In this case, blue-green crystals were obtained in a similar yield (87%) from the slow diffusion of diethyl ether into a solution of **2**(Cl) in a DCM/EtOH mixture. Complexes **1**(Cl) and **2**(Cl) were thoroughly characterized by means of mass spectroscopy (ESI-MS), UV-vis spectroscopy, X-ray diffraction and elemental (C, H, N) analysis.

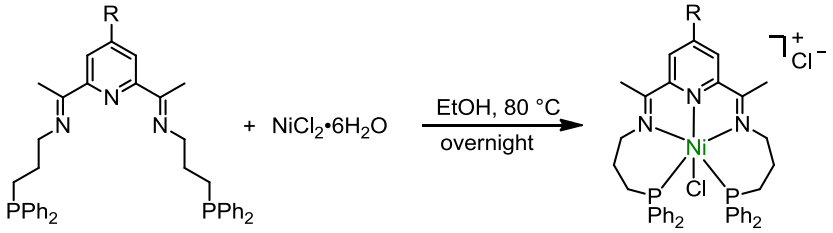

L2: R = H
L3: R = Cl

1(Cl): R = H
2(Cl): R = Cl

Scheme 3.2 Synthesis of complexes **1**(Cl) and **2**(Cl).

The ESI-MS analyses in MeOH confirmed the presence of the cationic species $\mathbf{1}^+$ at m/z = 706.2, along with $[\mathbf{1} - Cl]^+$ (m/z = 671.2) and $[\mathbf{1} - Cl]^{2+}$ (m/z = 335.6) for **1**(Cl) (Figure S8), and species $\mathbf{2}^+$ (m/z = 742.0), $[\mathbf{2} - Cl]^+$ (m/z = 705.1) for **2**(Cl) (Figure S9). Experimental and simulated isotopic distributions are in agreement with the proposed molecular composition. The UV-vis spectra of the Ni complexes **1**(Cl) and **2**(Cl) in DMF are shown in Figure 3.7. They are dominated by intense intraligand UV processes along with weak absorptions in the visible region. **1**(Cl) displays a peak at 331 nm while **2**(Cl) shifts slightly to 324 nm, originating from $\pi-\pi^*$ transitions of the ligands. In addition, **1**(Cl) and **2**(Cl) show broad absorptions centered at 585 nm and 621 nm, respectively, which are associated with d-d transitions in the octahedral environment. These species thus absorb in the yellow and orange region of the visible part of electromagnetic spectrum, showing purple-blue and blue-green colors, respectively.

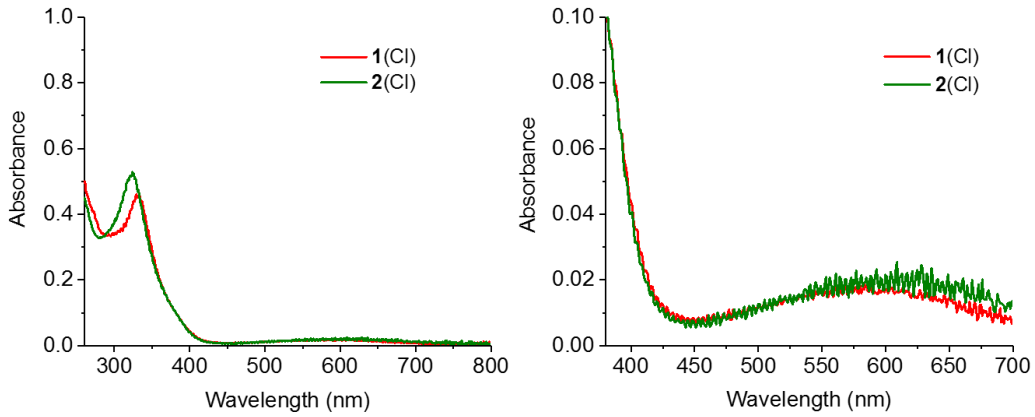

Figure 3.7 UV-vis spectra of **1**(Cl) (red) and **2**(Cl) (green) in DMF (left) and magnification of the visible region for both complexes (right).

As shown in Figure 3.8, the X-ray single-crystal structures revealed mononuclear cationic units where the divalent nickel ion is ligated in an $[N_3P_2Cl]$ environment. The geometry around the Ni center can best be described as distorted octahedral with three N atoms and the coordinated Cl placed on the equatorial plane, and two phosphorus atoms from diphenylphosphine groups occupying the axial positions, thus being in *trans* position to each other. Selected bond distances and angles are given in Table 3.1. Inspection to the metrical parameters indicated that the distortion from ideal octahedral geometry are mainly imposed by the N(1)–Ni(1)–N(3) and P(1)–Ni(1)–P(2) angles due to the PDI ligand rigidity/sterics. The observed Ni–N distances 1.987–2.127 Å are consistent with other neutral PDI derived Ni(II) complexes.[28,29] However, both complexes show noticeably longer Ni–P bonds than those reported for high spin Ni(II) complexes bearing chelating diphenylphosphine scaffolds,[26,30] reaffirming that ligand rigidity come into play in **1**(Cl) and **2**(Cl). It's interesting to note that the Ni(II) ion of **2**(Cl) sits directly in the plane of the pyridine diimine backbone, whereas the Ni center in **1**(Cl) slightly deviated from such a plane (0.022 Å). A closer inspection of the geometry of **2**(Cl) reveals that Cl(1)–N(2)–Ni(1)–Cl(2) acts as the symmetry axis (C_2) of the cation, leaving not only the pyridine diimine skeleton be absolutely symmetrical, e.g. the two Ni–N_{imine} bond lengths are identical (2.105 Å) so do the N2–Ni(1)–N_{imine} bond angles (76.81°), but also the two *trans* diphenylphosphine groups (Ni–P bond distances of 2.467 Å each). The presence of the Cl counterion and crystallized water molecules (2 in **1**(Cl) and 3 in **2**(Cl)) are in agreement with the resulting elemental analyses for both complexes.

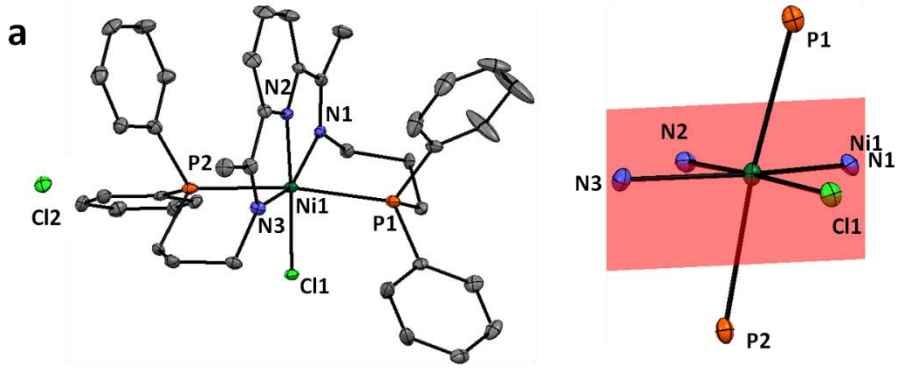

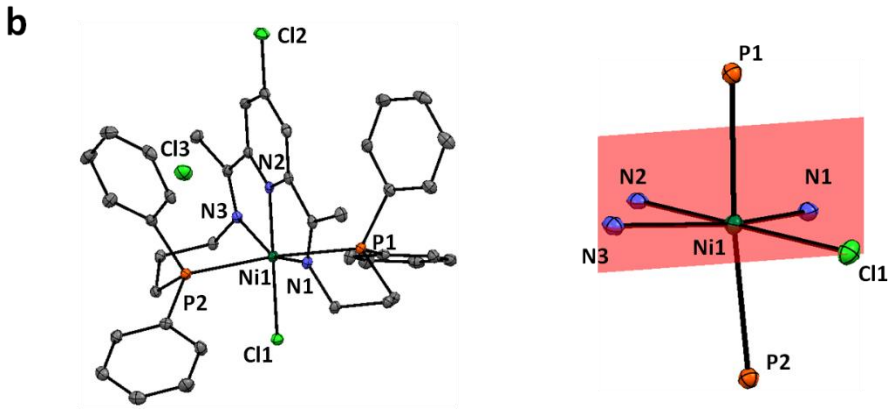

Figure 3.8 ORTEP drawing of **1**(Cl) (a left) and **2**(Cl) (b left) with 30% probability thermal ellipsoids. Hydrogen atoms and crystallized water molecules are omitted for clarity. ORTEP representation of the first coordination sphere of **1**(Cl) (a right) and **2**(Cl) (b right) showing that Cl(1), N(1), N(2) and N(3) are located in the equatorial plane of a octahedron.

Table 3.1 Experimental bond lengths (Å) and angles (deg) determined for **1**(Cl) and **2**(Cl).

Bond/Compound	**1**(Cl)	**2**(Cl)
Ni(1)–N(1)	2.108(3)	2.1051(18)
Ni(1)–N(2)	1.987(3)	1.992(2)
Ni(1)–N(3)	2.127(3)	2.1051(18)
Ni(1)–P(1)	2.4945(11)	2.4669(6)
Ni(1)–P(2)	2.4627(11)	2.4669(6)
Ni(1)–C(l1)	2.3709(8)	2.3914(8)
N(1)–Ni(1)–N(3)	153.97(10)	153.55(9)
P(1)–Ni(1)–P(2)	170.59(3)	173.75(3)
N(2)–Ni(1)–Cl(1)	177.55(9)	180.0

3.2.2 Electrochemical and electronic properties

The electrochemical features of **1**(Cl) and **2**(Cl) were studied in DMF in the presence of 0.1 M nBu_4NPF_6 as supporting electrolyte by using a three-electrode configuration and the corresponding cyclic voltammograms are shown in Figure 3.9 a.

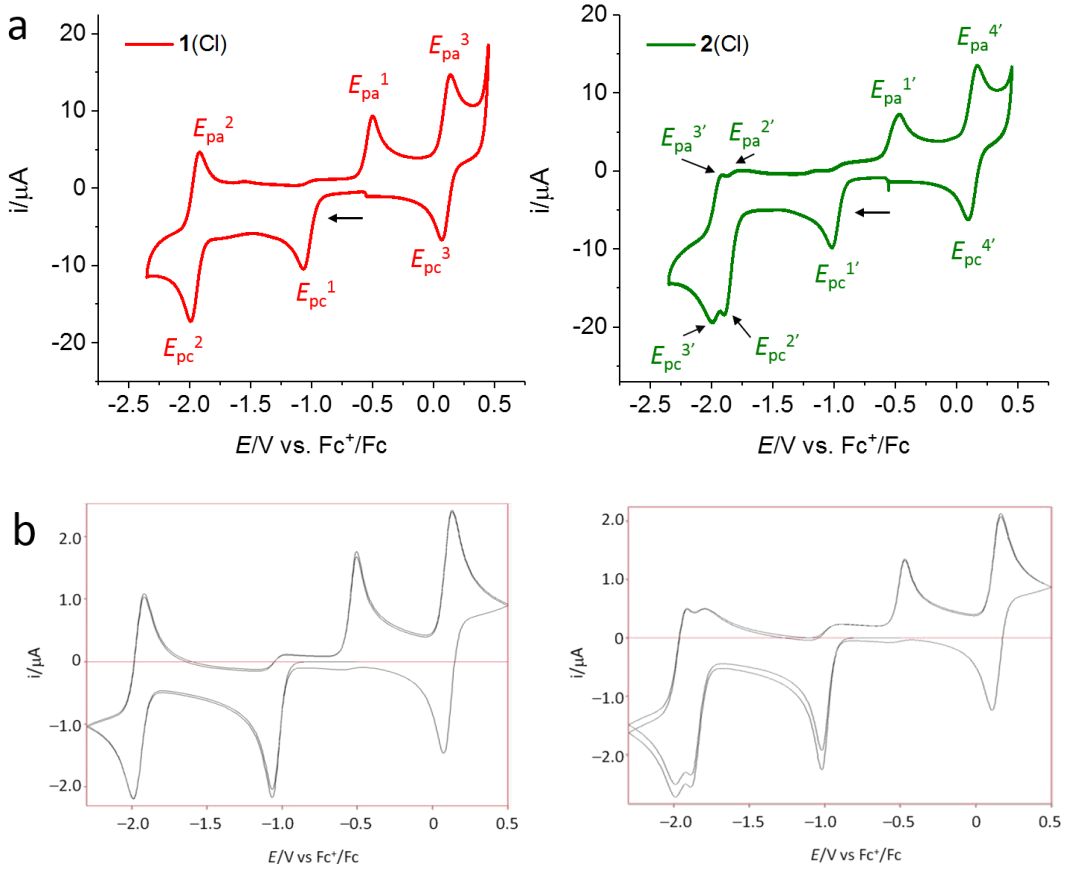

Figure 3.9 (a) Cyclic voltammograms of 1 mM **1**(Cl) (left) and **2**(Cl) (right) in DMF (0.1 M nBu_4NPF_6) at a scan rate of 100 mV/s. Glassy carbon is used as working electrode, Pt-mesh as counter electrode and $Ag/AgNO_3$ (0.1 M in MeCN) as reference electrode. (b) Simulated (*Digisim CV 2.0*®) CV of **1**(Cl) (left) and **2**(Cl) (right) at the identical conditions to experimental ones.

The cathodic scan, starting from the open circuit potential (ca. –0.55V vs. Fc^+/Fc) and recorded under N_2 atmosphere, displays an irreversible reductive wave at $E_{pc}^{1} = -1.07$ V and $E_{pc}^{1'} = -1.02$ V vs. Fc^+/Fc for **1**(Cl) and **2**(Cl), respectively, each coupled with a corresponding reoxidation wave at $E_{pa}^{1} = -0.50$ V or $E_{pa}^{1'} = -0.47$ V (Figure 3.9a). Thus, at a scan rate of 100 mV/s the two redox processes are separated by 0.57 V and 0.55 V for **1**(Cl) and **2**(Cl), respectively, showing the irreversible character of the process. The observed peak to peak separations resemble those previously reported for a coordinatively saturated Mn(II) complex bearing two PDI ligands in its structure (ΔE = 0.59 V),[31] attributed to a ligand-based reduction followed by intramolecular electron transfer

between the ligand and the metal center. Other plausible scenarios could be a reduction-triggered Cl-ligand dissociation resulting in structural rearrangement (from octahedral to pentacoordinate) or the exchange of the Cl-ligand by a solvent molecule.[32,33] Anyway, the separated CV couple is supposed to involve a reduced **1**(Cl) or **2**(Cl) intermediate at E_{pc}^{1} or $E_{pc}^{1'}$, which then quickly reacts to give a stable reduced species in solution. This reduced species can be transformed back to **1**(Cl) or **2**(Cl) in the reverse scan, but only at the more positive potential E_{pa}^{1} or $E_{pa}^{1'}$. When scanning to more negative potential, **1**(Cl) shows a quasi-reversible one-electron reduction event at $E_{1/2}^{2} = -1.96$ V, but **2**(Cl) exhibits two very close quasi-reversible reductive peaks at $E_{pc}^{2'} = -1.90$ V and $E_{pc}^{3'} = -2.0$ V, that we tentatively assign to the reduction of the ligand framework. In the positive potential region, both complexes present a reversible oxidative couple at $E_{1/2}^{3} = 0.10$ ($\Delta E_p = 73$ mV) and $E_{1/2}^{4'} = 0.14$ V ($\Delta E_p = 75$ mV) for **1**(Cl) and **2**(Cl), respectively, assigned to the oxidation of the Nickel center from Ni(II) to Ni(III).

In order to support the mechanistic scenarios proposed above, CV simulations (modeled by the software *DigiSim CV 2.0*) were performed. The simulations using parameters shown in Scheme S1 provide the results in Figure 3.9b. For complex **1**(Cl), a EC-EC mechanism (where E stands for *electron transfer* and C for *chemical reaction*) was employed for the separated CV couple at potential E_{pc}^{1}/E_{pa}^{1}. The starting species **1**(Cl) (named as A in the mechanism) was one-electron reduced to intermediate B followed by a chemical reaction, yielding stable reduced species C. The reverse one-electron oxidation of C firstly generated intermediate D and finished with a chemical reaction going back to A. The successive one-electron reduction of species C to E and one-electron oxidation of A to G were also simulated together. For complex **2**(Cl), all the processes described above were simulated in the same method, except for the extra third one-electron reductive peak. In experimental CV, the peaks at $E_{pc}^{2'}$ and $E_{pc}^{3'}$ lost partial reversibility. Therefore coupling the reduction of two-electron reduced species E to F a decomposition pathway (E→H) was added. It can be seen that redox potentials for all electrochemical electron transfer steps in the simulations were in good agreement with that of experiment, and simulations successfully replicated the shape of the experimental CVs.

All experimental redox events for **1**(Cl) and **2**(Cl) are summarized in Table 3.2. Their comparison shows that the redox couples of **2**(Cl) shift to positive potentials with respect to **1**(Cl) which is attributed to the electron-withdrawing ability of the Cl substituent introduced in the PDI ligand backbone of **2**(Cl). Moreover, the $1e^-$ oxidation and $1e^-$ reduction differ only in 40–50 mV, likely indicating the metal-based character of both processes; whereas the second reduction wave varies up to about 100 mV, bias to be ligand-based. Additionally, the redox waves are well-reproduced in successive scanning up to 50 cycles under the same conditions (Figure S10 and S12), which demonstrates the stability of both complexes under redox stress in organic media. Furthermore, scan rate dependent CVs ranging from 10 to 1000 mV/s in DMF solution (0.1 M nBu_4NPF_6) were recorded. Plots of reduction currents (i_p) versus the square root of the scan rates are linearly correlated for both **1**(Cl) and **2**(Cl) (Figure S11 and S13), which is consistent with the Randles–Sevcik relation (Equation 2, see the Experimental Section below) and indicative of a diffusion-controlled process with the electrochemically active species freely diffusing in solution.

Table 3.2 Summary of redox potentials for complexes **1**(Cl) and **2**(Cl).

Complex	+3e⁻		+2e⁻				+e⁻			–e⁻	
1(Cl)			E_{pc}^2	E_{pa}^2	$E_{1/2}^2$	ΔE^2	E_{pc}^1	E_{pa}^1	ΔE^1	$E_{1/2}^3$	ΔE^3
			–1.99	–1.92	–1.96	0.075	–1.07	–0.50	0.57	0.10	0.073
2(Cl)	$E_{pc}^{3'}$	$E_{pa}^{3'}$	$E_{pc}^{2'}$	$E_{pa}^{2'}$			$E_{pc}^{1'}$	$E_{pa}^{1'}$	$\Delta E^{1'}$	$E_{1/2}^{4'}$	$\Delta E^{4'}$
	–2.0	–1.91	–1.90	–1.80			–1.02	–0.47	0.55	0.14	0.075

A better understanding of the redox processes observed for **1**(Cl) and **2**(Cl) was achieved via spectroelectrochemical experiments in DMF using nBu_4NPF_6 as supporting electrolyte. A transparent thin-layer electrochemical (OTTLE) cell was employed for this purpose, in which the electrochemical reduction and oxidation process of the complexes were triggered by means of slow CV scanning (2 mV/s) through a Pt mesh working electrode and monitored by UV-vis spectroscopy under N_2. Focusing the experiment at the potential range of the separated one-electron reduction (E_{pc}^1) and reoxidation (E_{pa}^1) process, the reduction potential (E_{pc}^1) band of **1**(Cl) leads to an obvious decrease of the

absorption band centered at 331 nm and appearance of two new absorption bands centered at 486 nm and 631 nm with isosbestic points found at 302 and 375 nm. Further reoxidation returns the UV-vis bands to their original shape and intensity (Figure 3.10). This behavior confirms the chemical reversibility of the irreversible redox processes observed by CV scanning. The same UV-vis band changes were observed for **2**(Cl) in an analogous experiment (Figure S22).

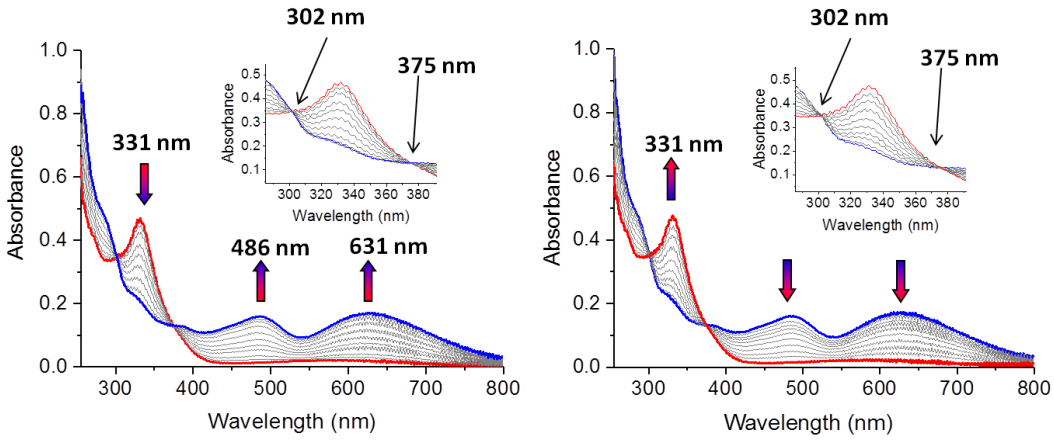

Figure 3.10 Spectroelectrochemical monitoring for the one-electron reduction (E_{pc}^{1}, left) and reoxidation (E_{pa}^{1}, right) processes of 2 M **1**(Cl) in DMF (0.1 M nBu_4NPF_6). Arrows indicate changes in band intensity during electrolysis.

Considering the paramagnetic nature of the octahedral Ni(II) complexes described in this Chapter, electron paramagnetic resonance (EPR) experiments were carried out in frozen MeCN solutions of **1**(Cl) and **2**(Cl). As displayed in Figure 3.11 (black traces), the resulting spectra showed that both **1**(Cl) and **2**(Cl) as "X-band EPR-silent". This phenomenon could be explained because the Ni(II) center in an octahedral environment produces an $S = 1$ ground state of significant zero-field splitting. Such "non-Kramers" signals are typically not observable as they would appear at fields and/or frequencies beyond the range of conventional X-band EPR spectrometers.[34]

In order to explore the electronic structure of the one-electron reduced species **1**(Cl) and **2**(Cl) formed at –1.07 V and –1.02 V, respectively (see Figure 3.9 above), X-band EPR spectra of the electrochemically formed products (generated by controlled potential electrolysis at the reductive potential E_{pc}^{1} or $E_{pc}^{1'}$) were recorded in frozen

MeCN at 77 K. The resonances (Figure 3.11, red lines) are found at $g_{\perp}$ = 2.1149, $g_{\parallel}$ = 2.0259 for one-electron reduced species of **1**(Cl) and $g_{\perp}$ = 2.1147, $g_{\parallel}$ = 2.0267 for one-electron reduced species of **2**(Cl). Thus, with all g values moderately larger than the expected $g_e \approx 2.0023$ for a radical based free electron,[35] an electronic configuration for which a considerable portion of the unpaired spin density localizes over the nickel ion center can be envisaged. The $g_{\perp} > g_{\parallel} > g_e$ pattern implies a d^9 Ni(I) complex (S = 1/2) of axial symmetry where the molecular z axis is contracted, meaning the one-electron reduction takes place in the metal center (Ni(II) to Ni(I)) despite the presence of a redox non-innocent bis(imino)pyridine ligand.[36,37]

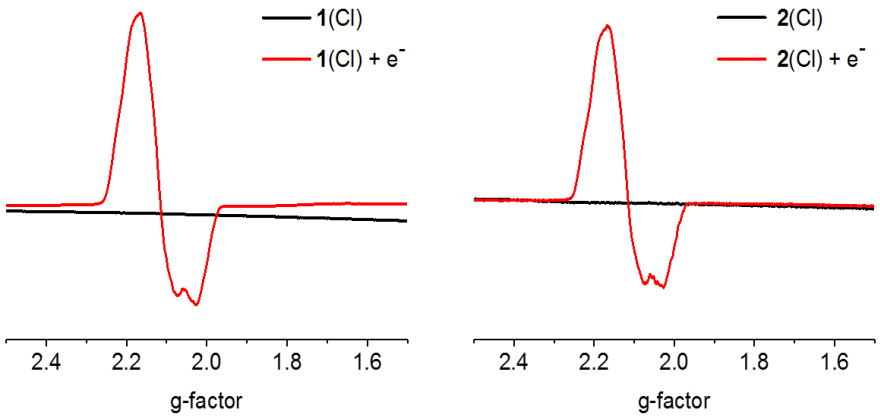

Figure 3.11 Left) X-band EPR spectra of **1**(Cl) (black line) and one-electron reduced species (red line); Right) X-band EPR spectra of **2**(Cl) (black line) and one-electron reduced species (red line). In frozen MeCN solution at 77 K (Frequency, 9.365 GHz; Power, 0.60 mW).

Complex **1**(Cl), along with the corresponding full set of mono- and di-reduced species of different structural/geometrical nature were studied by DFT calculations to gain more insight into their structures and electronic configurations. The calculated structures of the most stable species (**1**$^+$, [**1** – Cl]$^+$ and [**1** – Cl]^0, see Scheme 3.3) are depicted in Figure 3.12 and their selected geometrical parameters are listed in Table 3.3. Good agreement between experimental (X-ray) and computational (DFT) data for **1**(Cl) is observed (see Table 3.3), with experimental and theoretical bond distances and angles differing by less than 0.07 Å and 4.8°, respectively.

Table 3.3 Selected structural parameters for experimental and calculated $\mathbf{1}^+$, along with its reduced products.

Species[a]	$\mathbf{1}^{+}$ [b]	$\mathbf{1}^+$	$[\mathbf{1} - Cl]^+$	$[\mathbf{1} - Cl]^0$
Ni(1)–N(1)	2.108(3)	2.126	2.139	2.088
Ni(1)–N(2)	1.987(3)	2.004	1.974	1.975
Ni(1)–N(3)	2.127(3)	2.134	2.147	2.181
Ni(1)–P(1)	2.4945(11)	2.451	2.268	2.262
Ni(1)–P(2)	2.4627(11)	2.459	2.269	2.670
Ni(1)–Cl(1)	2.3709(8)	2.402		
N(1)–Ni(1)–N(3)	153.97(10)	153.98	154.17	154.95
P(1)–Ni(1)–P(2)	170.59(3)	175.35	111.44	112.90
N(2)–Ni(1)–Cl(1)	177.55(9)	179.18		

[a]The numbering scheme is the same as that in Figure 3.8. Bond distances are given in angstrom (Å) and angles in degree (deg). [b]The experimental parameters, and the rest are from DFT calculation.

The DFT-optimized geometry of $\mathbf{1}^+$ (Figure 3.12a (left), calculated with the M06 functional) was found to be a triplet as the most stable state ($S = 1$). As depicted in Figure 3.12a (right), two unpaired electrons are distributed over the complex. The spin density on the Ni center is 1.42, and 0.58 on PDI and Cl ligand, thus showing strong metal−ligand covalency.

The considered mechanistic pathways for the reduction of $\mathbf{1}^+$ are depicted in Scheme 3.3. The one-electron reduction of $\mathbf{1}^+$ was studied along with a chemical step of Cl-dissociation, a plausible origin for the redox irreversibility observed electrochemically (see E_{pc}^1 and E_{pa}^1 in Figure 3.9 above). Thus, we individually examined two different mechanisms: CE and EC, calculating the redox potentials of the E processes and the energies in the C processes.

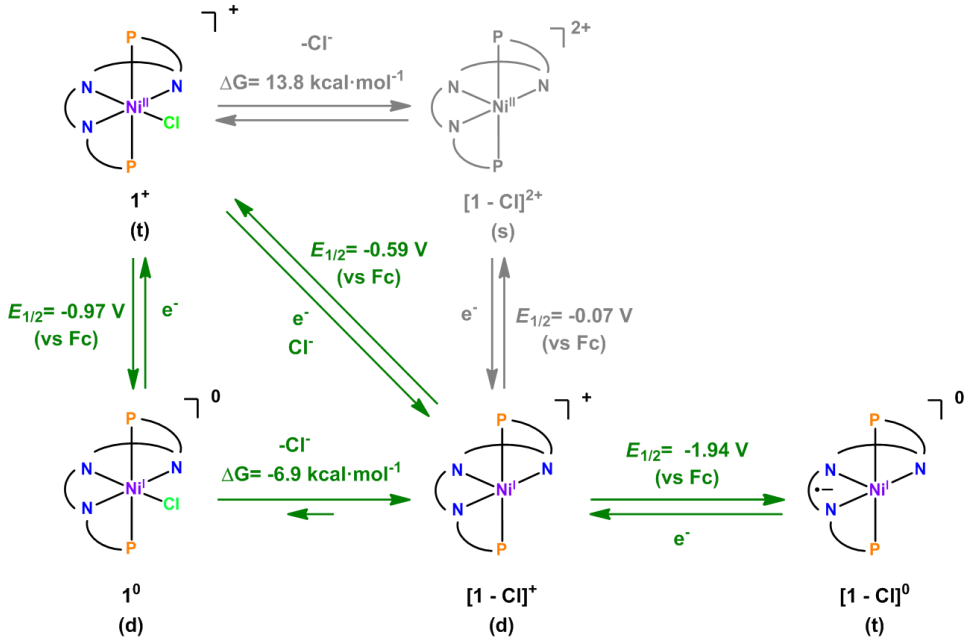

Scheme 3.3 Proposed mechanism of two successive reductions of $\mathbf{1}^{+}$. The pathways in gray are found to be disfavored through DFT analysis. (s) = singlet, (d) = doublet, (t) = triplet.

The dissociation of a chloride ligand from $\mathbf{1}^{+}$ to yield $[\mathbf{1} - \mathrm{Cl}]^{2+}$ is computed to be endothermic by 13.8 kcal mol^{-1}, indicating a disfavored process. This is further supported by the calculated reduction potential of this species $[\mathbf{1} - \mathrm{Cl}]^{2+}/[\mathbf{1} - \mathrm{Cl}]^{+}$, $E_{1/2}$ = –0.07 V vs. Fc^{+}/Fc, which is not observed experimentally in the recorded CV. On the other hand, reduction of $\mathbf{1}^{+}$ takes place at a calculated potential of $E_{1/2}$ = –0.97 V vs. Fc^{+}/Fc (comparable to the recorded reductive potential of –1.07 V) and leads to the intermediate doublet species $\mathbf{1}^{0}$. Subsequent Cl-dissociation proceeds downhill by –6.9 kcal mol^{-1}, yielding $[\mathbf{1} - \mathrm{Cl}]^{+}$, which adopts a distorted trigonal bipyramidal geometry. As shown in Figure 3.12b, in this species the spin of the unpaired electron resides primarily on the Ni center (0.83) and marginally near the ligand N center (0.17). Thus, in agreement with EPR data (see above) DFT calculations support the formation of d^9 Ni(I) species after a metal-centered one-electron reduction of $\mathbf{1}^{+}$. Reoxidation of the generated $[\mathbf{1} - \mathrm{Cl}]^{+}$ species coupled to Cl^{-} recoordination is computed to take place at $E_{1/2}$ = –0.59 V (potential comparable to the recorded experimental oxidative potential of –0.50 V) to recover the parent $\mathbf{1}^{+}$.

Further reduction of [**1** – Cl]$^{+}$ was computed to occur at $E_{1/2}$ = –1.94 V vs. Fc^{+}/Fc, negligibly deviating from the experimental value of $E_{1/2}$ = –1.96 V. As shown in Figure 3.12c, a spin density analysis for the reduced species [**1** – Cl]^{0} at the triplet state reveals that the new unpaired electron is basically located on the PDI ligand (1.15 relative to 0.17 in the case of the parent [**1** – Cl]$^{+}$).

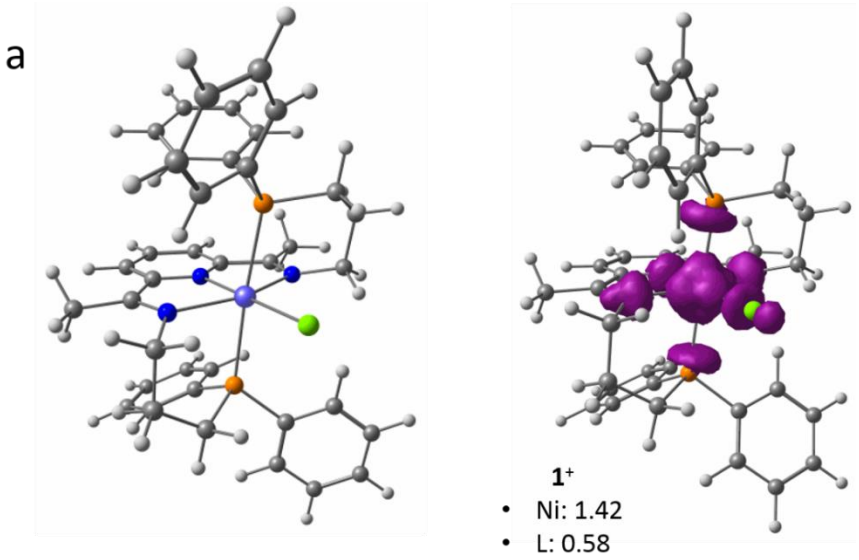

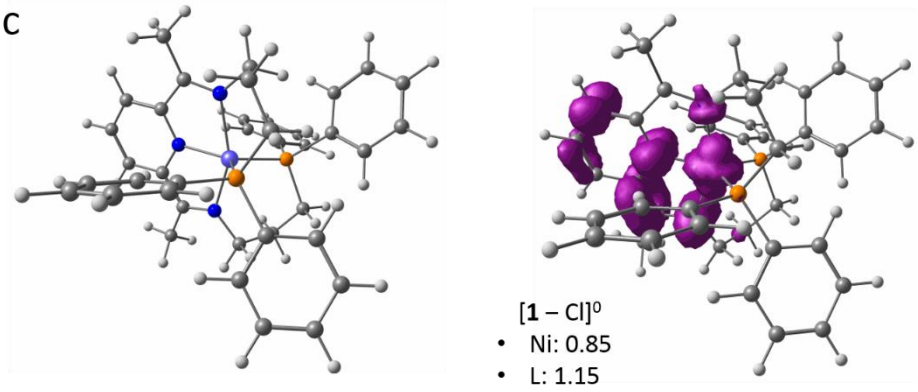

Figure 3.12 Optimized geometries (left) and DFT calculated spin density distributions (right) of starting $\mathbf{1}^{+}$ (a), one-electron reduced [**1** – Cl]$^{+}$ (b) and two-electron reduced [**1** – Cl]^{0} (c). Also given are spin densities in each state.

Overall, complex **1**(Cl) experiences a metal-based one-electron reduction followed by fast Cl dissociation yielding a pentacoordinate trigonal bipyramidal species. A second one-electron reduction is then ligand–based and takes place on the PDI scaffold. Though DFT calculations for complex **2**(Cl) are still in progress, we could presume it undergoes similar processes as **1**(Cl) for the first two one-electron reduction steps. However, the introduction of a Cl substituent in the PDI ligand allows observing a third reduction ($E_{pc}^{3'}$) slightly shifted to cathodic potentials, which is tentatively assigned to a second ligand-based process. DFT and EPR analysis of this tri-reduced species should confirm this assumption.

3.2.3 Electrocatalytical study of 1(Cl) and 2(Cl) in the presence of *p*-TsOH

The capacity of **1**(Cl) and **2**(Cl) to catalyze the hydrogen evolution reaction was monitored electrochemically. When *p*-TsOH (pK_a 2.6 in DMF)[38] was used as proton source and added to the complex solution in DMF, the CV profile of **1**(Cl) and **2**(Cl) at 100 mV/s scan rate gave an apparent mere catalytic wave at approximately –1.98 and –1.84 V, respectively (half-wave potential $E_{cat/2}$, see Figure 3.13), measured at 10 mM *p*-TsOH concentration. Functionalization at the para position of the pyridine scaffold of the PDI-based ligand with the electron-withdrawing Cl substituent effectively decrease the catalytic potential by ca. 140 mV (compare the voltammograms of **1**(Cl) and **2**(Cl) in Figure 3.13a-b), supporting the ligand based nature proposed for the second reductive

event of both complexes. In contrast to the tendency observed in the overpotentials, comparison of the peak current intensities under identical conditions, 173 μA for **1**(Cl) and 155 μA for **2**(Cl), indicates higher catalytic activity for the non-substituted **1**(Cl) species.

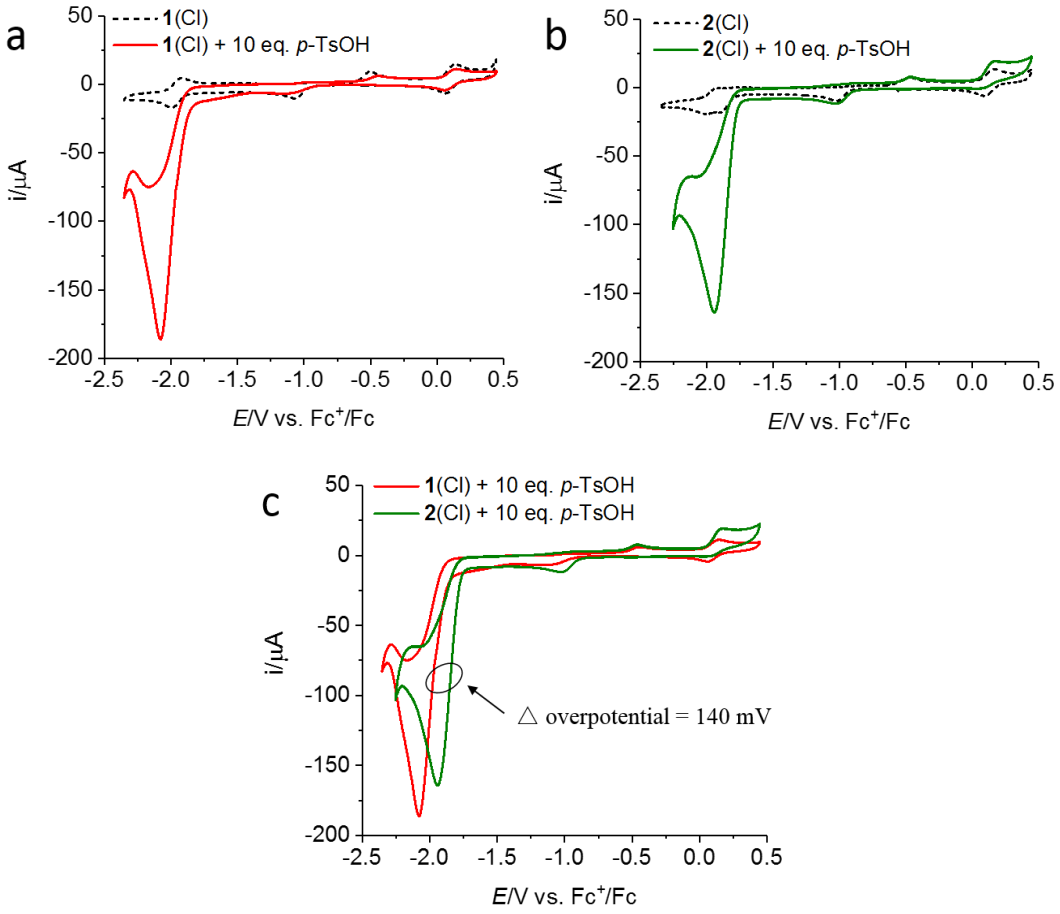

Figure 3.13 (a) Cyclic voltammograms of 1 mM **1**(Cl) in DMF (0.1 M nBu_4NPF_6) in the absence (black dash line) and presence (red solid line) of 10 mM of *p*-TsOH. (b) Cyclic voltammograms of 1 mM **2**(Cl) in DMF (0.1 M nBu_4NPF_6) in the absence (black dash line) and presence (green solid line) of 10 mM of *p*-TsOH. (c) Overlap of the cyclic voltammograms of 1 mM **1**(Cl) and 1 mM **2**(Cl) in DMF solution of 10 mM *p*-TsOH. △ indicates the difference of overpotentials between **1**(Cl) and **2**(Cl). Glassy carbon as the working electrode, Pt-mesh as the counter electrode and $Ag/AgNO_3$ as the reference electrode. Scan rate = 100 mV/s.

Proton-coupled electron-transfer (PCET) processes are frequently reported when Ni complexes or PDI-metal complexes catalyze the HER,[22,39,40] Thus, the involvement of such processes in the catalytic event observed was evaluated by recording CVs for **1**(Cl) in a DMF solution in the presence of various concentrations of *p*-TsOH, ranging from 0.02 mM to 0.6 mM. As shown in Figure S15, a constant reduction wave at –1.94 V was observed, suggesting that PCET is not involved in this case. Otherwise, a slope of E_{red}/–log[*p*-TsOH] = –59 mV would be expected.[41]

To quantify the HER rates and gather further information about the reaction pathways, kinetic studies for both complexes **1**(Cl) and **2**(Cl) were conducted by electrochemical methods. As shown in Figure 3.14a, by increasing the concentration of *p*-TsOH from 0 to 20 equivalents, the peak current strengths of 1mM **1**(Cl) increases systematically. This unidirectional current increment confirms an electrocatalytic chemical reaction. The plots of i_{cat} (i_{cat} is catalytic peak current) or the ratio of i_{cat}/ i_p (i_p is peak current of the catalyst in the absence of acid) versus the acid concentration follow a linear trend in both cases (see the inset in Figure 3.14a and Figure 3.14c, respectively). This indicates a second-order dependence of the reaction rate on the acid amount. After the addition of 20 eq. of acid, the current enhancement was no longer observed, and i_{cat} reaches a plateau, indicating zero order with respect to acid concentration. This conversion (second-order to zero-order), as reported in related literature,[42] means that the complex follows a HER mechanism involving one electrochemical preequilibrium step(s) of two protons (protonation of catalyst complex) preceding a rate-determining chemical step for H_2 elimination.

With fixed acid concentration (10 mM), a set of CVs were collected at a variety of complex concentrations from 1 to 2.5 mM. The linear correlation of i_{cat} versus **1**(Cl) concentration shows, according to Eq.2 (Experimental Section), that the reaction is first order to the nickel complex concentration (Figure 3.14b). Additionally, Figure 3.14c shows linear plots of i_{cat}/i_p vs. [*p*-TsOH] under non-saturating acid conditions ([*p*-TsOH] $\leq$ 20 mM) at different scan rates. Consequently, the rate law for hydrogen generation is overall third-order with a rate constant $k = 1.54 \times 10^4\ M^{-2}s^{-1}$, obtained from the plot of the slopes in Figure 3.14c versus $(1/\nu)^{1/2}$ (Figure S16). Moreover, when 1 mM **1**(Cl) in the

presence of 20 mM *p*-TsOH is polarized at 100 mV/s, the i_p of the $Ni^{I}L^{0/\bullet-}$ event is 17.0 μA and i_{cat} = 284.3 μA, corresponding with a i_{cat}/i_p value of 16.8, thus affording a k_{obs} of 54 s^{-1}.[43]

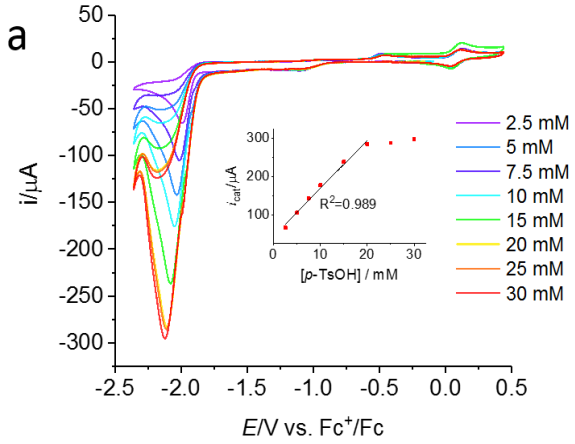

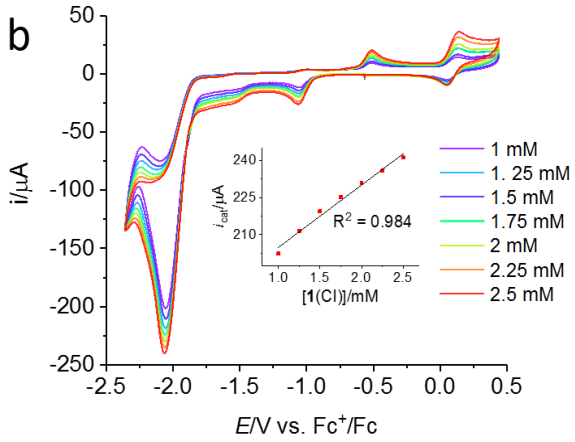

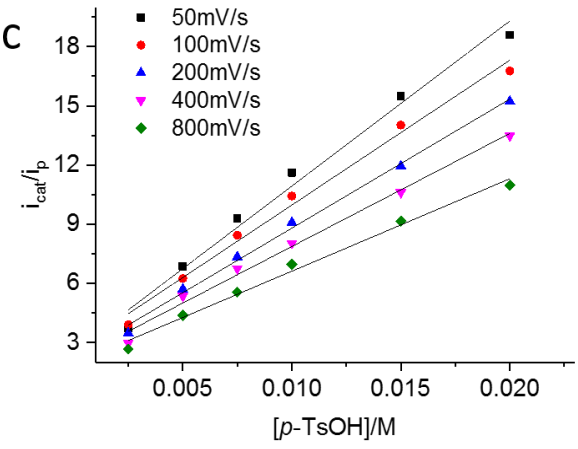

Figure 3.14 (a) Cyclic voltammograms of 1 mM **1**(Cl) in DMF (0.1 M nBu_4NPF_6) at various concentrations of *p*-TsOH at a scan rate of 100 mV/s. (Inset) Plots of catalytic current versus concentration of *p*-TsOH. (b) Cyclic voltammograms of various concentrations of **1**(Cl) in DMF (0.1 M nBu_4NPF_6) in the presence of 10 mM *p*-TsOH at a scan rate of 100 mV/s. (Inset) Plots of catalytic current versus concentration of **1**(Cl). Glassy carbon working electrode, Pt-mesh counter electrode and $Ag/AgNO_3$ reference electrode. (c) Plots of i_{cat}/i_p versus *p*-TsOH concentration for 1 mM **1**(Cl) in DMF (0.1 M nBu_4NPF_6). Solid black lines correspond to linear fits to the data for a given scan rate.

The same kinetic analysis was carried out for complex **2**(Cl). When a 100 mV/s scan rate was used, the single catalytic wave observed appears close to the reduction potential of the $Ni^{I}L^{0/-}$ process. Figure 3.15a shows the CVs of 1 mM **2**(Cl) after addition of an increasing amount of *p*-TsOH up to 25 equivalents. The rise of the acid concentration produces a catalytic wave whose maximum current intensity is linearly correlated to the acid concentration along the first 10 acid equivalents. At higher *p*-TsOH concentrations the relationship is nonlinear, seemingly the complex turns to be saturated with proton source for the HER, which is a similar trend in case of **1**(Cl).

Very differently, polarization at a scan rate of 10 mV/s induces two catalytic waves associated with the two redox process in close proximity within the range of −2.0 V to −1.91 V (Figure 3.15b). The apparent maximum current intensities of the −1.91 V wave display a linear dependence on the concentration of acid within 10 equivalents and a plateau from 10 to 25 equivalents, a behavior similar to that observed for the single catalytic process displayed by **1**(Cl) (see Figure 3.14a). Also, inspection into the CVs shows that the more negative catalytic wave (−2.0 V) change the peak-shaped curve when the *p*-TsOH concentration rises > 10 mM and, at the same time, the reverse anodic scan crosses the forward cathodic trace. So, the gathered data at this high *p*-TsOH concentration range suggests that the active species of **2**(Cl) transforms under electrocatalytic conditions. The decoordination of one of the P donor atoms of the PDI ligand or the isomerization of the Ni-H species formed could be plausible in this case.

Furthermore, the CV plots of **2**(Cl) at different catalyst concentrations in a 10 mM *p*-TsOH solution were recorded at 100 mV/s scan rate (Figure 3.15c), and the plots of i_{cat} versus [**2**(Cl)] reveals a linear trend with concentration of **2**(Cl) (inset of Figure 3.15c). Based on the plots of i_{cat}/i_p at different scan rates and the plot of the slopes in Figure 3.15d

versus $(1/v)^{1/2}$ (Figure S17), the rate constant for this overall three order reaction was calculated to be 7.20×10^3 M^{-2} s^{-1}, which is approximately one-half of the corresponding value for **1**(Cl). A rate value of 16 s^{-1} was obtained from a i_{cat}/i_p value of 9.1 under the condition of 1 mM **2**(Cl) in the presence of 10 mM *p*-TsOH at a scan rate of 100 mV/s.

All in all, the catalytic and kinetic study exposed above for **1**(Cl) and **2**(Cl) reveals that the presence of the *para* Cl-substituent on the pyridyl moiety of the PDI ligand has a dramatic effect for the capacity of these complexes as HER electrocatalysts. As expected, complex **2**(Cl) exhibits an apparent positively shifted catalytic potential due to the presence of *p*-Cl on the pyridine scaffold. However, the non-substituted **1**(Cl) complex shows higher HER activity upon addition of *p*-TsOH both in terms of rate constant and TOF. This is in agreement with previously reported studies about the structural perturbation of HER electrocatalysts, for which lower nucleophilicity (observed from more positive reduction potential in CV experiments) renders the structurally tuned complex less active for proton reduction.[44,45]

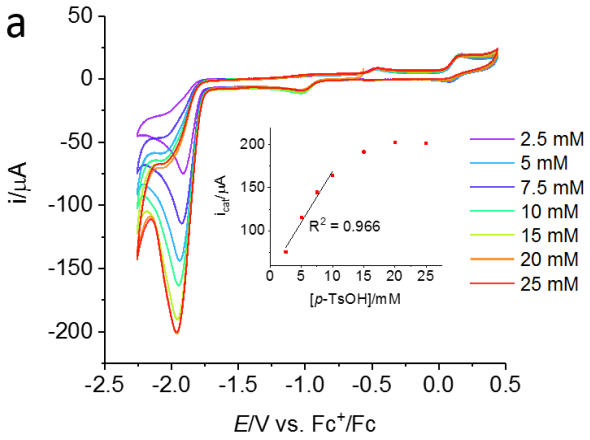

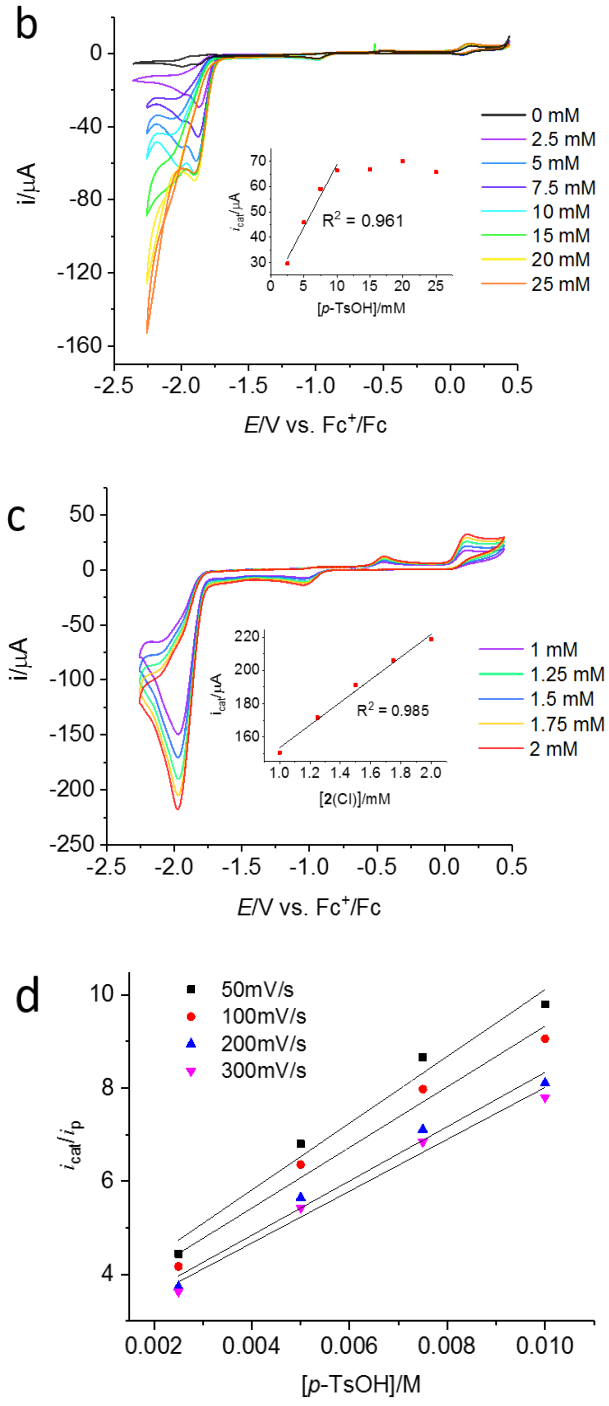

Figure 3.15 (a) Cyclic voltammograms of 1 mM **2**(Cl) in DMF (0.1 M nBu_4NPF_6) at various concentrations of *p*-TsOH at a scan rate of 100 mV/s. (Inset) Plots of catalytic current versus concentration of *p*-TsOH. (b) Cyclic voltammograms of 1 mM **2**(Cl) in DMF (0.1 M nBu_4NPF_6) at various concentrations of *p*-TsOH at a scan rate of 10 mV/s.

(Inset) Plots of catalytic current versus concentration of *p*-TsOH. (c) Cyclic voltammograms of various concentrations of **2**(Cl) in DMF (0.1 M nBu_4NPF_6) in the presence of 10 mM *p*-TsOH at a scan rate of 100 mV/s. (Inset) Plots of catalytic current versus concentration of **2**(Cl). (d) Plots of i_{cat}/i_p versus *p*-TsOH concentration for 1 mM **2**(Cl) in DMF (0.1 M nBu_4NPF_6). Solid black lines correspond to linear fits to the data for a given scan rate.

3.2.4 Short-term stability of 1(Cl) and 2(Cl) under HER conditions

In order to investigate whether the decomposition of the catalysts and the formation of heterogeneous species occurs on the surface of electrode or not, rinsing test experiments and i_{cat}-scan rate relationship experiments were performed by means of cyclic voltammetry. For the rinse test experiment, first, 30 uninterrupted cycles of CV scanning were carried out in the acidic 20 mM *p*-TsOH DMF solution of 1 mM **1**(Cl) or 10 mM *p*-TsOH for 1 mM **2**(Cl). Afterward, the glassy carbon working electrode was rinsed with solvent and immersed again in a fresh 20 mM (**1**(Cl)) or 10 mM (**2**(Cl)) *p*-TsOH solution with no catalyst, followed by CV recording. As shown in Figure 3.16, the comparison of such CV profiles reveals similar electroactivities for the rinsed and the glassy carbon electrodes, far below those observed for the studied catalysts in the same region, thus pointing to the molecular nature of the active species for both **1**(Cl) and **2**(Cl) under catalytic turnover. Both catalytic systems remain stable, providing catalytic peaks of similar activity before and after the set of consecutive CV experiments (Figure 3.16a and 3.16c).

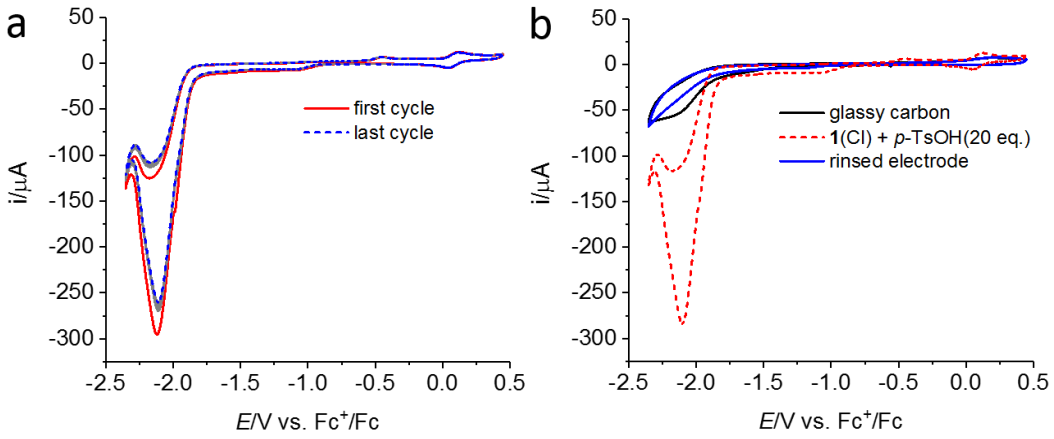

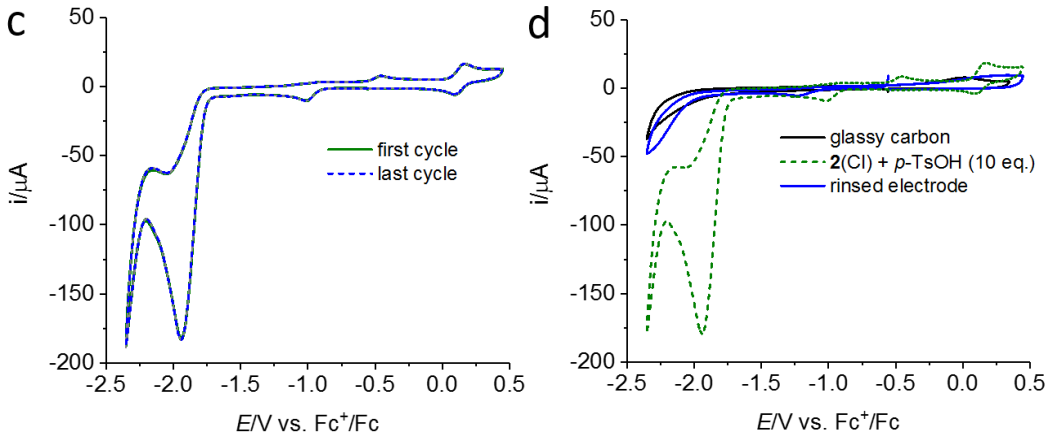

Figure 3.16 Rinse test for **1**(Cl) (top)and **2**(Cl) (bottom): (a) 30 cycles of successive cyclic voltammetric scanning of 1 mM **1**(Cl) in DMF (0.1 M nBu_4NPF_6) in the presence of 20 mM *p*-TsOH at a scan rate of 100 mV/s. (b) Cyclic voltammograms in the presence of 20 mM *p*-TsOH in DMF (0.1 M nBu_4NPF_6), (red dashed line) in the presence of **1**(Cl), (blue solid line) in the absence of **1**(Cl) by rinsed electrode, (black solid line) in the absence of **1**(Cl) by polished glassy carbon electrode. (c) 30 cycles of successive cyclic voltammetric scanning of 1 mM **2**(Cl) in DMF (0.1 M nBu_4NPF_6) in the presence of 10 mM *p*-TsOH at a scan rate of 100 mV/s. (d) Cyclic voltammograms in the presence of 10 mM *p*-TsOH in DMF (0.1 M nBu_4NPF_6), (green dashed line) in the presence of **2**(Cl), (blue solid line) in the absence of **2**(Cl) by rinsed electrode, (black solid line) in the absence of **2**(Cl) by polished glassy carbon electrode.

Moreover, CVs of 1 mM **1**(Cl) in the presence of 10 mM *p*-TsOH at different scan rates gave a linear dependence of i_{cat} on the square root of scan rates, indicating a diffusion-controlled homogeneous process (Figure 3.17). The same behavior was observed with **2**(Cl) in the 50 to 1000 mV/s scan rates range (Figure S18). Thus, all the above experimental results advocate, under the applied conditions in this test, for the stability of the studied complexes and the homogeneous nature of the catalytic species.[46]

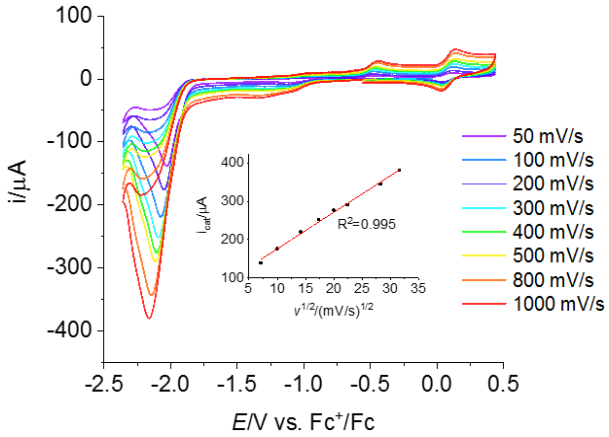

Figure 3.17 Cyclic voltammograms of 1 mM **1**(Cl) in DMF (0.1 M nBu_4NPF_6) in the presence of 10 mM *p*-TsOH at various scan rates. (Inset) The linear dependence of i_{cat} versus $\nu^{1/2}$.

3

3.2.5 Long-term stability of 1(Cl) and 2(Cl) under HER conditions

In order to unambiguously attribute the electrocatalytic current observed for both **1**(Cl) and **2**(Cl) to the reduction of protons to molecular hydrogen and calculate the corresponding Faradaic efficiencies of the catalytic process, controlled-potential electrolysis (CPE) experiments were performed in DMF in the presence of the catalysts (0.25 mM) and a glassy carbon rod as working electrode in an H-shape double-compartment cell. These experiments were coupled to a hydrogen Clark type sensor in the headspace of the cathodic compartment. Along the 3.5 h electrolysis of **1**(Cl) in the presence of 20 mM *p*-TsOH at a constant potential of –2.05 V vs. Fc^+/Fc, a total charge of 5.30 C passed by the system and 30.03 μmol of evolved hydrogen were generated. This indicates that **1**(Cl) operates at a high Faradaic efficiency > 99% according to Eq.1 (Where F is the Faraday constant (96485.33 A mol^{-1}), n_1 is the number of moles of electrons required to generate one mole of H_2, n_{H2} is the moles of H_2 experimentally measured, $Charge_{cat}$ is the passed charge during bulk electrolysis).[45] For the case of **2**(Cl), electrolysis in the presence of 10 mM *p*-TsOH at –1.93 V vs. Fc^+/Fc during 1 h resulted in a charge of 2.35 C and 8.65 μmol of evolved H_2, resulting in a Faradaic efficiency value of 71%.

$$\text{Faradaic efficiency} = F \times n_1 \times n_{H2} \times 100\%/\text{Charge}_{cat} \qquad (1)$$

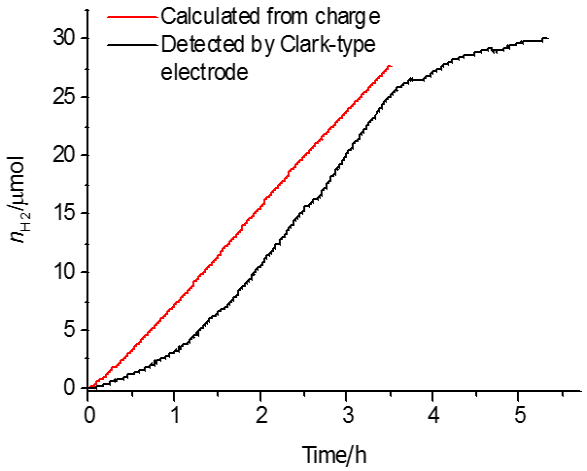

Figure 3.18 Amount of hydrogen gas evolved from controlled potential electrolysis of **1**(Cl) for 3.5 h at –2.05 V vs. Fc^+/Fc. Theoretical H_2 production calculated from the accumulated charge (red line) and; H_2 detected by a Clark-type electrode placed in the headspace (black line).

In parallel, CPE experiments at variable applied potential shows that the total charge of the bulk electrolysis increased when the potential was more negative (Figure 3.19a), accompanied by a color change from blue to dark green in each electrolysis (Figure 3.19b). Figure 3.19c exhibits the $i \sim t$ curve observed for a 30 minutes bulk electrolysis of **1**(Cl) at a potential of –2 V vs. Fc^+/Fc. Surprisingly, the current intensity starts to increase after a very short time from electrolysis charge on.

We could tentatively propose two possibilities for this current enhancement. One is the formation of Ni-based (nano)particles or a Ni thin film on the electrode which are more active for proton reduction than the original Ni complex **1**(Cl). The second one is the generation of an intermediate homogeneous active species that favors the proton reduction catalysis upon the two-electron reduction of the initial **1**(Cl) complex. The last possibility is likely more probable than the formation of heterogeneous species in the electrode surface, as the CV after CPE at –2 V showed a new oxidation wave slightly negative to the reoxidation peak (E_{pa}^1) of the separated couple (Figure 3.19d, star on the red curve), comparing with the initial species (Figure 3.19d, black). The transitory species vanished at the second cycle of successive scanning (Figure 3.10d, blue line). This new peak becomes broader and of much higher intensity if the duration of the CPE is extended (Figure S20), likely a catalytic reaction takes place at this potential. One proposal for the

origin of this new peak could be the reverse reaction, that is, the oxidation of the catalytically generated H_2,[47] triggered by a new species generated under catalytic turnover. In order to check the veracity of this proposal, CV cycles in a H_2 saturated solution containing complex **1**(Cl) were performed. As shown in Figure S19, the system does not trigger the generation of the new peak in this conditions, thus discarding the possibility of catalysis by original **1**(Cl). In addition, the catalytic onset potential measured immediately after electrolysis shifted by circa 270 mV, being now –1.6 V, implying that this new species may effectively reduce the catalytic overpotential for proton reduction. The vanishing of the new features from the second CV in a successive scanning shows the short-lived nature of this transitory species.

The CPE experiments for complex **2**(Cl) presented the same phenomenon. The current increased within the first minutes under reductive potential and then decreased (Figure S21a). Also, new redox-active species were found after the bulk electrolysis in the anodic scanning of the first CV at about – 0.2 V (Figure S21b). We suggest that both the new generated species and initial complex are active in the electrocatalytic HER. However, the very short–lived nature of the new species hampers its further characterization.

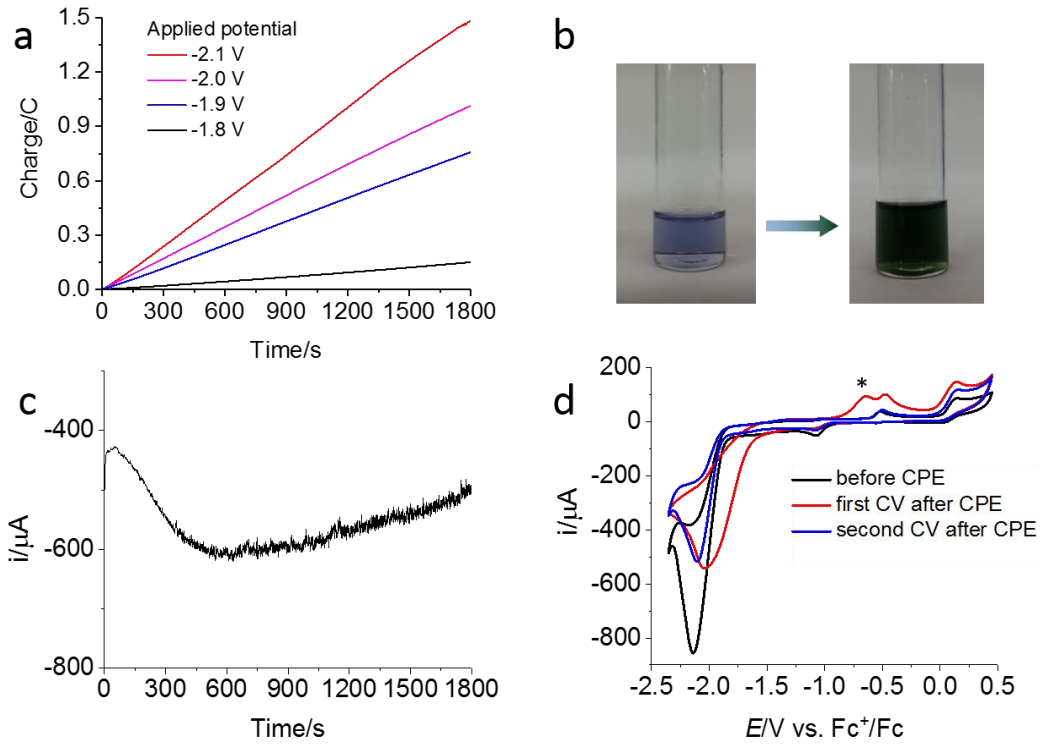

Figure 3.19 (a) Charge buildup versus time from electrolysis of 0.25 mM **1**(Cl) in DMF in the presence of 10 mM *p*-TsOH. (b) Color changed from blue to dark green upon CPE. (c) Plot of current versus time for controlled potential ($E_{cat/2}$ – 1.96 V) electrolysis of 1 mM **1**(Cl) in DMF in the presence of 10 mM *p*-TsOH. (d) Cyclic voltammograms of 1 mM **1**(Cl) before and after bulk electrolysis at -1.96 V in DMF in the presence of 10 mM *p*-TsOH. The asterisk indicates a new species generated after CPE.

3.2.6 Spectroelectrochemical characterization

In order to get insights into the new species generated after bulk electrolysis with **1**(Cl) and **2**(Cl), we performed spectroelectrochemical studies in the presence of acid using an UV-vis fiber optic probe. Figure 3.20 shows the electronic absorption changes monitored during a bulk electrolysis for **1**(Cl) at –1.9 V. It is clear that the process leads to a decrease in intensity of the band appearing at 332 nm while the intensity of the 486 nm and 631 nm bands increase, with an isosbestic point observable at 380 nm. Calculating from the accumulated charge (1.7381 C) and the moles of complex employed (8.5×10^{-7} mol), the turnover number is 11. Noticeably, this electronic absorption changes are the same than those observed above when studying the one-electron reduction of **1**(Cl)

spectroelectrochemically (OTTLE cell, see left part of Figure 3.10 in section 3.2.2) in the absence of acid. Thus, this confirms that the resting state of the catalyst is the one-electron reduced species ([**1** – Cl]$^+$). Similarly, **2**(Cl) was investigated through the same method showing the same phenomenon, that is, bulk electrolysis at –1.9 V gave a UV-vis absorption spectrum corresponding to the one-electron reduced species (Figure 3.20 c and Figure S22 right) of the original complex. The turnover number here is calculated to be 9. Thus, no signal attributable to a putative homogeneous intermediate responsible for the new oxidation peak shown in Figure 3.19 d or Figure S21b (* highlighted) was observed through UV-vis monitoring of the CPE experiment. However, based on the proved homogeneity observed in the short-term stability tests, we assign the new peaks observed in the CV right after the CPE to trace amount of new molecular species, whose absorption is overlapped to the corresponding dominant resting states [**1** – Cl]$^+$ or [**2** – Cl]$^+$.

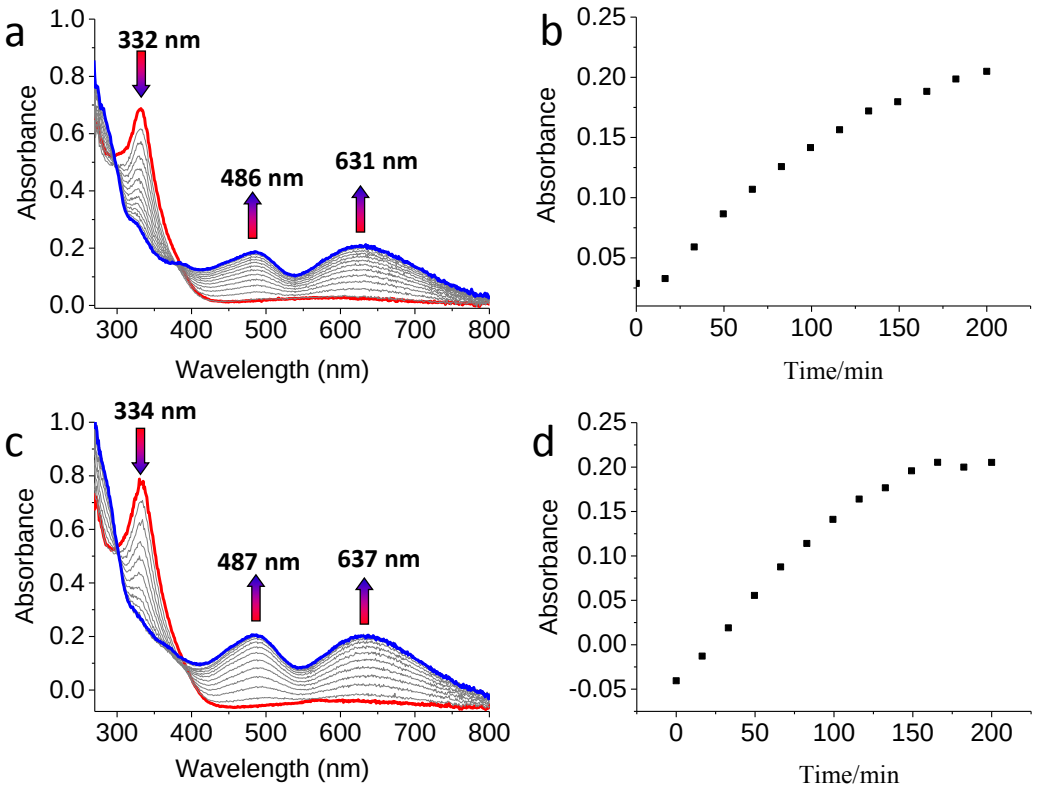

Figure 3.20. UV-vis absorption changes during the 200 minutes of bulk electrolysis of 0.05 mM **1**(Cl) (a) and **2**(Cl) (c) in the presence of 20 eq. *p*-TsOH in DMF measured by

UV-vis fiber optic probe. The absorptions at 631nm in (a) and 637 nm in (c) versus time are plotted (b) and (d), respectively.

3.3 Conclusion

Two reported ligands (**L1** and **L2**) and two new ligands (**L3** and **L4**) bearing a N_3P_2-PDI core have been prepared, among which **L2** and **L3** were successfully coordinated to a Ni center, forming two new hexacoordinated complexes bearing the pentadentate ligands, **1**(Cl) and **2**(Cl). The complexes have been thoroughly characterized by multiple physicochemical techniques (ESI-MS, elemental analyses, UV-vis, X-ray diffraction and CV as well). In both complexes, the central Ni is observed in a distorted octahedral environment by crystallographic analysis, where a Cl ligand sits in the equatorial plane. Computational DFT calculations suggest that this Cl ligand is decoordinated upon a metal-based one-electron reduction of the initial complex, while further reduction takes place in the PDI ligand scaffold. Both **1**(Cl) and **2**(Cl) resulted active catalysts for the hydrogen evolution reaction in organic (DMF) media using *p*-TsOH as proton source. **2**(Cl)**,** bearing an electron-withdrawing Cl substituent at para position of the pyridine scaffold show lower catalytic overpotential than **1**(Cl). However, kinetic analyses demonstrated that **2**(Cl) mediates the catalytic reaction at a slower rate. The homogeneous nature of the catalytic species was proven electrochemically, discarding the transition from molecular to heterogeneous including rinse test and the linear dependency of i_{cat} on $\nu^{1/2}$. For both **1**(Cl) and **2**(Cl), controlled-potential electrolysis leads to the formation of a more active intermediate species for proton reduction. These species is short-lived and present in low concentration in solution, which prevented its characterization thorough spectroscopic methods.

3.4 Experimental section

Materials

2,6-diacetylpyridine, 3-(diphenylphosphino)-1-propylamine, 2-(diphenylphosphino)-ethylamine, *p*-toluenesulfonic acid, 4 Å molecular sieves, $NiCl_2{\cdot}6H_2O$, 4-Chloropyridine hydrochloride, pyruvic acid, ammonium persulfate, trifluoromethanesulfonimide were purchased from Sigma-Aldrich and used as received.

Organic solvents were dried and distilled prior to use following the standard procedures.[48] The ligand ^{Ph2PPr}PDI and starting reagent 4-chloro-2,6-diacetylpyridine were prepared according to the literature.[5,23] All synthetic reactions and electrochemical studies were performed under an inert atmosphere inside a glovebox (MBraun) or by Schlenk and vacuum line techniques.

Electrochemical experiments

The electrochemical measurements were run with a BioLogic SP-150 potentiostat under N_2 atmosphere at room temperature. Cyclic voltammetry experiments were performed using a glassy carbon working electrode (ca. 0.07 cm^2), a platinum mesh auxiliary electrode and an $Ag/AgNO_3$ (0.1 M in MeCN) reference electrode. Ferrocene was used as internal standard and all the potentials were converted to Fc^+/Fc by subtracting 0.078 V from $Ag/AgNO_3$ potential. The working electrode was polished with alumina slurry, ultrasonically cleaned and rinsed with distilled water before use. DMF was used for the preparation of catalyst solution with 0.1 M nBu_4NPF_6 as supporting electrolyte.

Controlled potential electrolysis (CPE) experiments were conducted in a gas-tight two-compartment cell washed and dried in the oven overnight before use. The working compartment was fitted with a glassy carbon rod as working electrode and $Ag/AgNO_3$ (0.1 M) as reference electrode. The auxiliary compartment was fitted a Pt mesh counter electrode. Both compartments were purged with N_2 for 15 min followed by injecting a degassed complex solution with 20 mM *p*-TsOH in DMF (0.1 M nBu_4NPF_6) to the working compartment and blank DMF solution (0.1 M nBu_4NPF_6) to the auxiliary compartment.

Spectroelectrochemical measurement

Spectroelectrochemistry was recorded through two different methods.

OTTLE cell: All measurements were conducted under N_2 atmosphere with an optically transparent thin-layer electrochemical cell which used Pt minigrid as working electrode, Pt minigrid and silver wire as auxiliary and pseudoreference electrode respectively. The optical path length defined by the thickness of the P-E spacer was 0.2 mm. Electronic

absorption spectra were recorded using a Varian Cary 50 Bio UV-Visible spectrophotometer, and cyclic voltammograms were recorded using a BioLogic SP-150 potentiostat. The working solutions were prepared with a 2 mM complex solution in DMF with 0.1 M nBu_4NPF_6 as supporting electrolyte.

Fiber probe: Electronic absorption spectra were recorded using a Varian Cary 50 Bio UV-Visible spectrophotometer, and CPE were performed using a CHI 660C potentiostat. The working solutions were prepared with 0.05 mM catalysts in DMF with 0.1 M nBu_4NPF_6 as supporting electrolyte.

Computational Details

All calculations were carried out with the Gaussian09 (v. D.01) program package[49]. We employed Density Functional Theory (DFT) methodology using M06 functional including Grimme's empirical dispersion correction D3.[50,51] Two different basis sets were used: 6-31+G(d) for C, N, P, Cl and H,[52–54] and LANL2TZ(f) for Ni and Fe (including the associated pseudopotential).[55–59] The solvation was considered implicitly using the SMD model with DMF as solvent.[60] All geometry optimizations were computed in solution without symmetry restrictions. The nature of all computed stationary points was confirmed by vibrational frequency calculations. Free energy corrections were calculated at 298.15 K and 105 Pa pressure, including zero point energy corrections (ZPE). In addition, a correction term of 1.9 kcal/mol (at 298 K) was added when necessary to account for the standard state concentration of 1 M. Unless otherwise mentioned, all reported energy values are free energies in solution. Ferrocene (Fc) and Ferrocenium (Fc^+) complexes were optimized in the same conditions in order to refer the calculated redox potential to the Fc/Fc^+ couple. The excellent agreement between the calculated and experimental redox potentials in the systems reported here confirms the validity of this methodology.

TOF and rate constant determination[43]

Eq.2 (Randle-Sevcik eq.) and Eq.3 detail the relationship between the peak current and catalytic current with the corresponding parameters, respectively.

$$i_{\mathrm{p}} = 0.4463FA[cat]\sqrt{\frac{FvD}{RT}} \qquad (2)$$

$$i_{cat} = nFA[cat]\sqrt{Dk[\mathrm{H}^+]^2} \qquad (3)$$

Where i_{p} is the peak current in the absence of acid, F is the Faraday constant (96485.33 A/mol), A is the working electrode surface area (cm^2), [cat] is the catalyst concentration, $n = 2$ is the number of electrons transferred, is the scan rate, D is the diffusion constant, R is ideal gas constant = 8.314 JK^{-1} mol^{-1}, $T = 298$ K, and i_{cat} is the catalytic current in the presence of acid, $[H^+]$ is the acid concentration.

So the ratio of i_{cat}/ i_{p} (Eq.4) can be obtained from Eq.2 and 3.

$$\frac{i_{\mathrm{cat}}}{i_{\mathrm{p}}} = \frac{n}{0.4463}\sqrt{\frac{RTk[H^+]^2}{Fv}} \qquad (4)$$

Under pseudo first-order conditions where $k_{\mathrm{obs}} = k[\mathrm{H}^+]^2$, Eq.4 is simplified to Eq.5.

$$\frac{i_{\mathrm{cat}}}{i_{\mathrm{p}}} = \frac{n}{0.4463}\sqrt{\frac{RTk_{obs}}{Fv}} \qquad (5)$$

Eq.6 is obtained by simplification of Eq.5 to estimate the pseudo first-order rate constant k_{obs} or turnover frequency (TOF).

$$k_{\mathrm{obs}} = 1.94v\left(\frac{i_{cat}}{i_p}\right)^2 \qquad (6)$$

Then, Eq.7 is derived from Eq.4, consequently giving Eq.8 which is the slope of linear dependence of the ratio $i_{\mathrm{cat}}/i_{\mathrm{p}}$ vs. acid concentration at a specific scan rate.

$$\frac{i_{\mathrm{cat}}}{i_{\mathrm{p}}} = \frac{n}{0.4463}\sqrt{\frac{RTk}{Fv}}[H^+] \qquad (7)$$

$$\mathrm{slope} = \frac{n}{0.4463}\sqrt{\frac{RTk}{Fv}} \qquad (8)$$

Plots of this slope at different scan rates vs. $(1/\nu)^{1/2}$ yields a linear relationship, and the relationship between the slope of this line (the double slope) and the third order rate constant *k* is shown in Eq.9.

$$\text{double slope} = 0.72\sqrt{k} \qquad (9)$$

Finally, *k* can be calculated based on Eq.9.

H_2 detection

A Clark-type H_2 microsensor, polarized overnight before use, was equipped in the working compartment headspace of the CPE setup to measure the electrochemically produced H_2. During the electrolysis at the catalytic peak potential, the sensor signal consistently grew. When the signal reached a plateau after electrolysis, a calibration for the quantitative analysis of the generated H_2 was made (for each measurement). 0.05 mL of pure H_2 (pressure 1 bar) was injected into the headspace of the working compartment with a gas-tight glass syringe (0 to 0.25 mL). The added pure H_2 was mixed well with the gas in the headspace when the signal increased to another plateau. The increment between these two adjacent plateaus corresponds to a point of the calibration curve. The rest of points were obtained analogously by injecting 0.1 mL, 0.15 mL and 0.2mL of H_2, respectively. The moles of H_2 can be calculated from the ideal gas equation PV = nRT, where P is the pressure (1 atm), V is the volume, n is the number of moles, R is the ideal gas constant 0.082 $atm \cdot L \cdot mol^{-1}K^{-1}$ and T is the temperature 298 K. Figure 3.21 is an example of the calibration made in the H_2 analysis when **1**(Cl) is employed as electrocatalysts in DMF in the presence of *p*-TsOH as proton source.

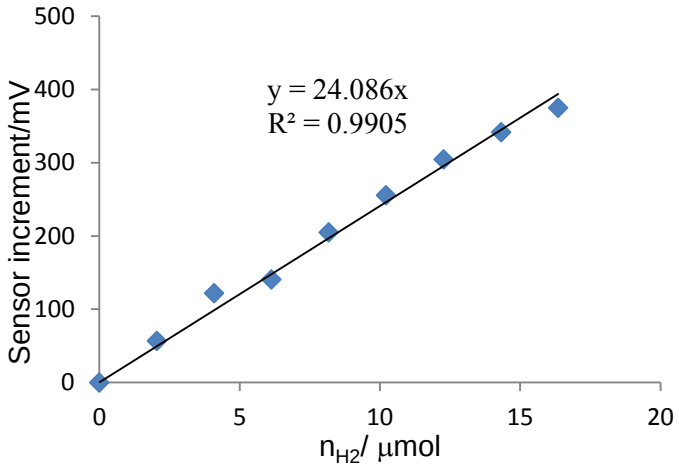

Figure 3.21. Calibration line for quantitative analysis of H_2 with **1**(Cl) as catalysts.

Spectroscopic Measurements

(1) NMR spectra were recorded by a Bruker Avance DRX 250 MHz NMR spectrometer at room temperature, with chloroform-d_3 or DCM-d_2 as the deuterated solvent. All the measurements have been done in the Servei de Ressonància Magnètica Nuclear of the Universitat Autònoma de Barcelona (SeRMN-UAB)

(2) Elemental analyses were performed by a Thermo Scientific Flash 2000 CHNS Analyzer from the Servei d'Anàlisi Química of the Universitat Autònoma de Barcelona (SAQ-UAB).

(3) Electrospray ionization mass spectra (ESI/MS) were obtained on the MicroTOF mass spectrometer that was coupled with a Cryospray source (Bruker Daltonics).

(4) X-Ray Crystallography measurements were carried out on a Bruker diffractometer Apex DUO equipped with a Kappa 4-axis goniometer, an APPEX 2 4K CCD area detector, a Microfocus Source E025 IuS using Mo *Ka*radiation, a Microfocus Source E025 IuS using Cu *Ka* radiation, Quazar MX multilayer Optics as monochromator and an Oxford Cryosystems low temperature device Cryostream 700 plus. Data collection with APEX II version v2013.4-1; data reduction with Bruker SAINT version V8.37A; absorption correction with SADABS v2016-2[61]. All the determinations were done in the X-ray Diffraction Unit of Institut Català d'Investigació Química (ICIQ)

(5) X-band EPR spectra were collected from a Bruker EMX-micro EPR spectrometer at cryogenic temperatures 7-10 K or 77 K in ICIQ.

(6) UV-vis spectra were obtained at room temperature using an Agilent/HP 8453 diode-array or a Varian Cary 50 Bio UV-Visible spectrophotometer operating in the range of 250 to 800 nm with 1 cm pathlength rectangular quartz cuvette.

Synthetic procedures

^{Ph2PEt}PDI (**L1**): ^{Ph2PEt}PDI was prepared according to the literature[5]. To a Schlenk flask, 2,6-diacetylpyridine (0.36 g, 2.21 mmol), 2-(diphenylphosphino)-ethylamine (1 g, 4.36 mmol), *p*-TsOH (30 mg) and 4 Å molecular sieves were mixed in toluene (14 mL), followed by stirring for 24 h at 80 °C. After cooling down to room temperature, the yellow solution was filtered through Celite by a cannula device. Then the resulted yellow oil after removing solvent under vacuum was dissolved in diethyl ether (2 mL) and placed at –35°C, ^{Ph2PEt}PDI was obtained as pale yellow crystals in a 78% yield. The NMR data is in accordance with that in the literature. ^{1}H NMR (250 MHz, CD_3Cl, 296 K) δ 7.95 (d, *J* = 7.8 Hz, 2H), 7.70 – 7.60 (m, 1H), 7.51 (ddt, *J* = 7.4, 5.4, 2.6 Hz, 8H), 7.41 – 7.30 (m, 12H), 3.70 (q, *J* = 8.7 Hz, 4H), 2.65 – 2.51 (m, 4H), 2.31 (s, 6H). ^{31}P{^{1}H} NMR (101 MHz, CD_3Cl, 296 K) δ –17.15 ppm.

^{Ph2PPr}PDI (**L2**): ^{Ph2PPr}PDI was prepared according to the literature.[1] To a Schlenk flask equipped with water condenser, 2,6-diacetylpyridine (0.33 g, 2.02 mmol), 3-(diphenylphosphino)-1-propylamine (1 g, 4.11 mmol), *p*-TsOH (30 mg) and 4 Å molecular sieves were mixed in toluene (14 mL), followed by stirring for 24 h at 80 °C. After cooling down to room temperature, the yellow solution was filtered through Celite by a cannula device. Then the resulted yellow oil after removing solvent under vacuum was dissolved in diethyl ether (2 mL) and placed in a –35°C freezer. ^{Ph2PPr}PDI was obtained as pale yellow crystals in a 71% yield. The NMR data is in accordance with that in the literature. ^{1}H NMR (250 MHz, CD_3Cl, 298 K) δ 8.10 (d, *J* = 7.8 Hz, 2H), 7.81 – 7.66 (m, 1H), 7.47 (ddq, *J* = 9.0, 5.8, 3.6, 3.0 Hz, 8H), 7.41 – 7.30 (m, 12H), 3.63 (t, *J* = 6.8 Hz, 4H), 2.38 (s, 6H), 2.31 – 2.19 (m, 4H), 1.96 (p, *J* = 7.9 Hz, 4H). ^{31}P{^{1}H} NMR (101 MHz, CD_3Cl, 298 K) δ –15.18 ppm.

^{Ph2PPr}PDI(*p*)Cl (**L3**): The preparation of this ligand was similar to that of **L2** except that 2,6-diacetylpyridine was substituted by 4-chloro-2,6-diacetylpyridine which was synthesized following a reported protocol.[23] To a Schlenk flask equipped with water condenser, 4-chloro-2,6-diacetylpyridine (0.16 g, 0.81 mmol), 3-(diphenyl-phosphino)-1-propylamine (0.41 g, 1.68 mmol), *p*-TsOH (30 mg) and 4 Å molecular sieves were mixed in toluene (14 mL), followed by stirring for 24 h at 80 °C. After cooling down to room temperature, the yellow solution was filtered through Celite by a cannula device. Then the resulted yellow oil after removing solvent under vacuum was dissolved in a solvent mixture of MeOH and diethyl ether (2 mL) and placed in a –35°C freezer. ^{Ph2PPr}PDI(*p*)Cl was obtained as yellow crystals in a 48% yield. ^{1}H NMR (250 MHz, CD_2Cl_2, 304 K): δ 8.11 (s, 2H, H2), 7.53 – 7.39 (m, 8H, H12), 7.39 – 7.25 (m, 12H, H12/H13), 3.59 (t, *J* = 6.6 Hz, 4H, H7), 2.33 (t, *J* = 1.0 Hz, 6H, H5), 2.27 – 2.16 (m, 4H, H9), 1.90 (p, *J* = 8.6, 8.1 Hz, 4H, H8). ^{31}P{^{1}H} NMR (101 MHz, CD_2Cl_2, 304 K): δ –15.35 ppm.

^{Ph2PPh}PDI (**L4**): To a Schlenk flask, 2,6-diacetylpyridine (0.10 g, 0.61 mmol), 2-(Diphenylphosphino)aniline (0.34 g, 1.22 mmol) and *p*-TsOH (20 mg) were mixed in toluene (12 mL). A Dean-Stark trap was set up to separate the water from the reaction. Upon stirring under reflux for 40 h, the initial colorless solution turned to yellow. The reaction was cooled to room temperature, then the yellow solution was filtered through Celite by a cannula device. The resulted yellow viscous oil obtained after removing solvent under vacuum was dissolved in a hot MeOH/$CHCl_3$ mixture (4 mL) and slow solvent evaporation under N_2 atmosphere gave a spot of pale yellow crystals of ^{Ph2PPh}PDI. ^{1}H NMR (250 MHz, CD_2Cl_2, 301 K) δ 8.03 (d, J = 7.8 Hz, 2H), 7.76 – 7.67 (m, 1H), 7.37 (d, J = 7.7 Hz, 2H), 7.30 (dd, J = 5.1, 4.0 Hz, 20H), 7.05 (t, J = 7.5 Hz, 2H), 6.95 – 6.87 (m, 2H), 6.75 (dd, J = 7.4, 4.8 Hz, 2H), 1.98 (d, J = 0.9 Hz, 6H) ppm. ^{31}P{^{1}H} NMR (101 MHz, CD_2Cl_2, 301 K) δ –13.50 ppm.

[Ni(^{Ph2PPr}PDI)(Cl)](Cl) (**1**(Cl)): Crystalline **L1** (50 mg, 0.081 mmol) was dissolved in 2 mL hot ethanol under N_2 inert atmosphere and a 4 mL ethanol solution of $NiCl_2{\cdot}6H_2O$ (19.6 mg, 0.082 mmol) was added dropwise. The mixed solution turned to blue immediately. The reaction was allowed to stir overnight at 80 °C before being reduced under vacuum to approximately 1 mL left. Adding diethyl ether to the

concentrated solution gave a dark blue-purple precipitate. Crystals suitable for X-ray diffraction were obtained by slow diffusion of diethyl ether to a dichloromethane solution of the complex. Yield: 85%. ESI-MS: *m*/*z* = 706.2 [Ni(^{Ph2PPr}PDI)(Cl)]$^+$. Anal. Calc. for [Ni(^{Ph2PPr}PDI)(Cl)][Cl] + 2H_2O ($C_{39}H_{45}O_2Cl_2N_3NiP_2$): C, 60.10; H, 5.82; N, 5.39. Found: C, 59.95; H, 5.78; N, 5.37.

[Ni(^{Ph2PPr}PDI(*p*)Cl)(Cl)](Cl) (**2**(Cl)): An 8 mL ethanol solution of $NiCl_2 \cdot 6H_2O$ (44 mg, 0.185 mmol) was added dropwise to a 7 mL hot ethanol solution of ligand **L3** (120 mg, 0.185 mmol) under N_2. The mixed solution became dark green immediately, and darker after stirring overnight at 80 °C. The work-up was similar to that for **1**(Cl) and crystals suitable for X-ray diffraction were obtained by slow diffusion of diethyl ether to the dichloromethane/ethanol solution of the complex. Yield: 87%. ESI-MS: *m*/*z* = 742.0 [Ni(^{Ph2PPr}PDI(*p*)Cl)(Cl)]$^+$. Anal.Calc. for [Ni(^{Ph2PPr}PDI(*p*)Cl)(Cl)][Cl] + 3H_2O ($C_{39}H_{46}O_3Cl_3N_3NiP_2$): C, 56.31; H, 5.57; N, 5.05. Found: C, 54.87; H, 5.15; N, 5.01.

3.5 References

(1) Bockris, J. O. In *Environmental Chemistry*; Springer US: Boston, MA, **1977**; 549–582.

(2) Lyaskovskyy, V.; de Bruin, B. *ACS Catal.* **2012**, *2*, 270–279.

(3) Solis, B. H.; Maher, A. G.; Dogutan, D. K.; Nocera, D. G.; Hammes-Schiffer, S. *Proc. Natl. Acad. Sci. U. S. A.* **2016**, *113*, 485–492.

(4) Eisenberg, R.; Gray, H. B. *Inorg. Chem.* **2011**, *50*, 9741–9751.

(5) Ben-Daat, H.; Hall, G. B.; Groy, T. L.; Trovitch, R. J. *Eur. J. Inorg. Chem.* **2013**, *2013*, 4430–4442.

(6) Ghosh, M.; Weyhermüller, T.; Wieghardt, K. *Dalt. Trans.* **2010**, *39*, 1996–2007.

(7) Russell, S. K.; Bowman, A. C.; Lobkovsky, E.; Wieghardt, K.; Chirik, P. J. *Eur. J. Inorg. Chem.* **2012**, *2012*, 535–545.

(8) Myers, T. W.; Berben, L. A. *J. Am. Chem. Soc.* **2013**, *135*, 9988–9990.

(9) Stieber, S. C. E.; Milsmann, C.; Hoyt, J. M.; Turner, Z. R.; Finkelstein, K. D.; Wieghardt, K.; DeBeer, S.; Chirik, P. J. *Inorg. Chem.* **2012**, *51*, 3770–3785.

(10) Scott, J.; Gambarotta, S.; Korobkov, I.; Knijnenburg, Q.; Bas de Bruin, A.; Budzelaar, P. H. M. *J. Am. Chem. Soc.* **2005**, *127*, 17204–17206.

(11) Myers, T. W.; Sherbow, T. J.; Fettinger, J. C.; Berben, L. A. *Dalt. Trans.* **2016**, *45*, 5989–5998.

(12) Pal, R.; Groy, T. L.; Bowman, A. C.; Trovitch, R. J. *Inorg. Chem.* **2014**, *53*, 9357–9365.

(13) Biernesser, A. B.; Li, B.; Byers, J. A. *J. Am. Chem. Soc.* **2013**, *135*, 16553–16560.

(14) Varela-Álvarez, A.; Musaev, D. G. *Chem. Sci.* **2013**, *4*, 3758–3764.

(15) Pal, R.; Groy, T. L.; Trovitch, R. J. *Inorg. Chem.* **2015**, *54*, 7506–7515.

(16) Chen, Z.; Wang, T.; Sun, T.; Chen, Z.; Sheng, T.; Hong, Y. H.; Nan, Z. A.; Zhu, J.; Zhou, Z. Y.; Xia, H.; Sun, S. G. *Chinese J. Chem.* **2018**, *36*, 1161–1164.

(17) Reed, B. R.; Stoian, S. A.; Lord, R. L.; Groysman, S. *Chem. Commun.* **2015**, *51*, 6496–6499.

(18) Thompson, E. J.; Berben, L. A. *Angew. Chem Int. Ed.* **2015**, *54*, 11642–11646.

(19) Chen, L.; Chen, G.; Leung, C. F.; Yiu, S. M.; Ko, C. C.; Anxolabéhère-Mallart, E.; Robert, M.; Lau, T. C. *ACS Catal.* **2015**, *5*, 356–364.

(20) Mukhopadhyay, T. K.; MacLean, N. L.; Gan, L.; Ashley, D. C.; Groy, T. L.; Baik, M.-H.; Jones, A. K.; Trovitch, R. J. *Inorg. Chem.* **2015**, *54*, 4475–4482.

(21) Mukhopadhyay, T. K.; MacLean, N. L.; Flores, M.; Groy, T. L.; Trovitch, R. J. *Inorg. Chem.* **2018**, *57*, 6065–6075.

(22) Pal, R.; Laureanti, J. A.; Groy, T. L.; Jones, A. K.; Trovitch, R. J. *Chem. Commun.* **2016**, *52*, 11555–11558.

(23) Lieb, D.; Kenkell, I.; Miljković, J. L.; Moldenhauer, D.; Weber, N.; Filipović, M. R.; Gröhn, F.; Ivanović-Burmazović, I. *Inorg. Chem.* **2014**, *53*, 1009–1020.

(24) Fang, X.; Zhang, C.; Chen, J.; Zhu, H.; Yuan, Y. *RSC Adv.* **2016**, *6*, 45512–45518.

(25) Chuang, W. J.; Narwane, M.; Chen, H. Y.; Kao, C. L.; Huang, B.; Hsu, K. M.; Wang, Y. M.; Hsu, S. C. N. *Dalt. Trans.* **2018**, *47*, 13151–13157.

(26) A Verhoeven, D. G.; Negenman, H. A.; Orsino, A. F.; Lutz, M.; Moret, M. E. *Inorg. Chem.* **2018**, *57*, 10846–10856.

(27) Cooper, M. K.; Downes, J. M.; Duckworth, P. A.; Kerby, M. C.; Powell, R. J.; Soucek, M. D. *Inorg. Synth.* **1989**, *25*, 129–133.

(28) Cosquer, N.; Lefebvre, E.; Douziech, B.; Houille, S.; Michaud, F.; Gómez-García, C. J.; Conan, F. *Inorganica Chim. Acta* **2018**, *479*, 1–9.

(29) Haas, R. M.; Hern, Z.; Sproules, S.; Hess, C. R. *Inorg. Chem.* **2017**, *56*, 14738–14742.

(30) Hope, H.; Olmstead, M. M.; Power, P. P.; Viggiano, M. *Inorg. Chem.* **1984**, *23*, 326–330.

(31) de Bruin, B.; Bill, E.; Bothe, E.; Weyhermüller, T.; Wieghardt, K. *Inorg. Chem.* **2000**, *39*, 2936–2947.

(32) Santo, R.; Miyamoto, R.; Kinoshita, I.; Ichimura, A. *Redox Chemistry of Novel Copper Complexes with Carbanion and Halogen Coordination*; **2004**.

(33) Lindley, B. M.; van Alten, R. S.; Finger, M.; Schendzielorz, F.; Würtele, C.; Miller, A. J. M.; Siewert, I.; Schneider, S. *J. Am. Chem. Soc.* **2018**, *140*, 7922–7935.

(34) J. Krzystek; Ju-Hyun Park; Mark W. Meisel; Michael A. Hitchman; Horst Stratemeier; Louis-Claude Brunel; Joshua Telser. *Inorg. Chem.* **2002**, *41*, 4478–4487.

(35) Schilter, D.; Gray, D. L.; Fuller, A. L.; Rauchfuss, T. B. *Aust. J. Chem.* **2017**, *70*, 505–515.

(36) Bender, G.; Stich, T. A.; Yan, L.; Britt, R. D.; Cramer, S. P.; Ragsdale, S. W. *Biochemistry* **2010**, *49*, 7516–7523.

(37) Ali, M.; Ray, A.; Sheldrick, W. S.; Mayer-Figge, H.; Gao, S.; Sahmes, A. I. *New J. Chem.* **2004**, *28*, 412–417.

(38) Greg A. N. Felton; Richard S. Glass; Dennis L. Lichtenberger, A.; Evans, D. H. *Inorg. Chem.* **2006**, *45*, 9181–9184.

(39) Solis, B. H.; Maher, A. G.; Dogutan, D. K.; Nocera, D. G.; Hammes-Schiffer, S. *Proc. Natl. Acad. Sci. U. S. A.* **2016**, *113*, 485–492.

(40) Elgrishi, N.; McCarthy, B. D.; Rountree, E. S.; Dempsey, J. L. *ACS Catal.* **2016**, *6*, 3644–3659.

(41) Hong, D.; Tsukakoshi, Y.; Kotani, H.; Ishizuka, T.; Ohkubo, K.; Shiota, Y.; Yoshizawa, K.; Fukuzumi, S.; Kojima, T. *Inorg. Chem.* **2018**, *57*, 7180–7190.

(42) Haddad, A. Z.; Cronin, S. P.; Mashuta, M. S.; Buchanan, R. M.; Grapperhaus, C. A. *Inorg. Chem.* **2017**, *56*, 11254–11265.

(43) Haddad, A. Z.; Kumar, D.; Ouch Sampson, K.; Matzner, A. M.; Mashuta, M. S.; Grapperhaus, C. A. *J. Am. Chem. Soc.* **2015**, *137*, 9238–9241.

(44) Lee, C. H.; Dogutan, D. K.; Nocera, D. G. *J. Am. Chem. Soc.* **2011**, *133*, 8775–8777.

(45) Sondermann, C.; Ringenberg, M. R.; Wang, B.; Zhao, X.; Su, L.; Chen, S.; Tong, P.; Luo, Y.; Qu, J.; Duboc, C. *Dalt. Trans.* **2017**, *46*, 5143–5146.

(46) Zarkadoulas, A.; Field, M. J.; Papatriantafyllopoulou, C.; Fize, J.; Artero, V.; Mitsopoulou, C. A. *Inorg. Chem.* **2016**, *55*, 432–444.

(47) Dutta, A.; Lense, S.; Hou, J.; Engelhard, M. H.; Roberts, J. A. S.; Shaw, W. J. *J. Am. Chem. Soc.* **2013**, *135*, 18490–18496.

(48) Armarego, W. L. F.; Chai, C. *Purification of Laboratory Chemicals, 6th Edition*; Elsevier Science, **2009**.

(49) Gaussian 09, Revision **D.01**, Frisch, M. J.; Trucks, G. W.; Schlegel, H. B.; Scuseria, G. E.; Robb, M. A.; Cheeseman, J. R.; Scalmani, G.; Barone, V.; Mennucci, B.; Petersson, G. A.; Nakatsuji, H.; Caricato, M.; Li, X.; Hratchian, H. P.; Izmaylov, A. F.; Bloino, J.; Zheng, G.; Sonnenberg, J. L.; Hada, M.; Ehara, M.; Toyota, K.; Fukuda, R.; Hasegawa, J.; Ishida, M.; Nakajima, T.; Honda, Y.; Kitao, O.; Nakai, H.; Vreven, T.; Montgomery, J. A., Jr.; Peralta, J. E.; Ogliaro, F.; Bearpark, M.; Heyd, J. J.; Brothers, E.; Kudin, K. N.; Staroverov, V. N.; Kobayashi, R.; Normand, J.; Raghavachari, K.; Rendell, A.; Burant, J. C.; Iyengar, S. S.; Tomasi, J.; Cossi, M.; Rega, N.; Millam, J. M.; Klene, M.; Knox, J. E.; Cross, J. B.; Bakken, V.; Adamo, C.; Jaramillo, J.; Gomperts, R.; Stratmann, R. E.; Yazyev, O.; Austin, A. J.; Cammi, R.; Pomelli, C.; Ochterski, J. W.; Martin, R. L.; Morokuma, K.; Zakrzewski, V. G.; Voth, G. A.; Salvador, P.; Dannenberg, J. J.; Dapprich, S.; Daniels, A. D.; Farkas, Ö.; Foresman, J. B.; Ortiz, J. V.; Cioslowski, J.; Fox, D. J. Gaussian, Inc., Wallingford CT, **2009**.

(50) Chai, J.D.; Head-Gordon, M. *Phys. Chem. Chem. Phys.* **2008**, *10*, 6615–6620.

(51) Grimme, S.; Antony, J.; Ehrlich, S.; Krieg, H. *J. Chem. Phys.* **2010**, *132*, 154104.

(52) Hehre, W. J.; Ditchfield, R.; Pople, J. A. *J. Chem. Phys.* **1972**, *56*, 2257–2261.

(53) Hariharan, P. C.; Pople, J. A. *Theor. Chim. Acta* **1973**, *28*, 213–222.

(54) Francl, M. M.; Pietro, W. J.; Hehre, W. J.; Binkley, J. S.; Gordon, M. S.; DeFrees, D. J.; Pople, J. A. *J. Chem. Phys.* **1982**, *77*, 3654–3665.

(55) Hay, P. J.; Wadt, W. R. *J. Chem. Phys.* **1985**, *82*, 270–283.

(56) Wadt, W. R.; Hay, P. J. *J. Chem. Phys.* **1985**, *82*, 284–298.

(57) Hay, P. J.; Wadt, W. R. *J. Chem. Phys.* **1985**, *82*, 299–310.

(58) Feller, D. *J. Comput. Chem.* **1996**, *17*, 1571–1586.

(59) Schuchardt, K. L.; Didier, B. T.; Elsethagen, T.; Sun, L.; Gurumoorthi, V.; Chase, J.; Jun Li, A.; Windus, T. L. *J. Chem. Inf. Model* **2007**, *47*, 1045–1052.

(60) Marenich, A. V.; Cramer, C. J.; Truhlar, D. G. *J. Phys. Chem. B* **2009**, *113*, 6378–6396.

(61) Krause, L.; Herbst-Irmer, R.; Sheldrick, G. M.; Stalke, D. *J. Appl. Crystallogr.* **2015**, *48*, 3–10.

3.6 Supporting information

A- NMR Spectroscopy

B- Mass Spectrometry

C- Electrochemistry

D- Simulation of cyclic voltammograms

E- Electrocatalytic study

F- Spectroelectrochemistry

G- X-ray diffraction metrics

A- NMR Spectroscopy

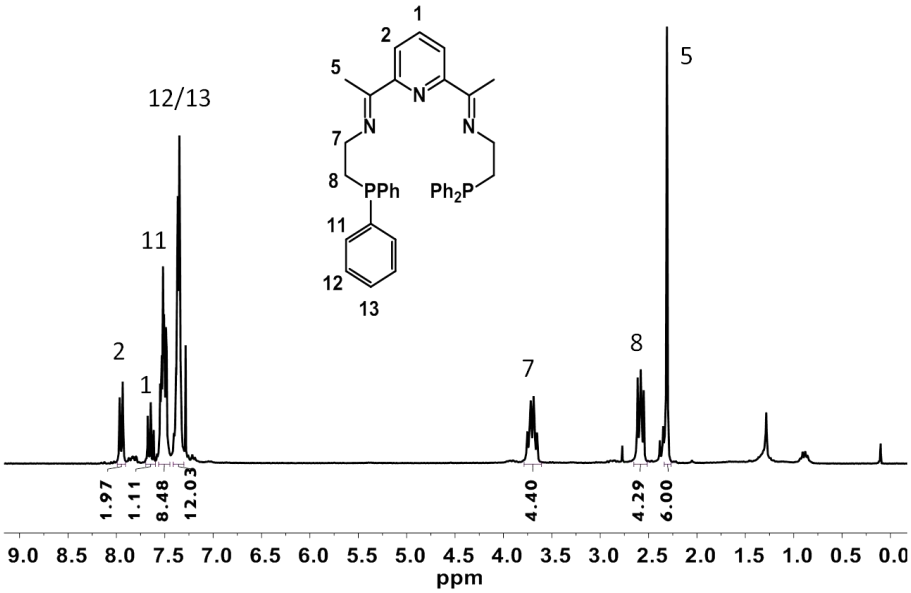

Figure S1. ^{1}H NMR spectrum of **L1** (250 MHz, CD_3Cl, 296 K).

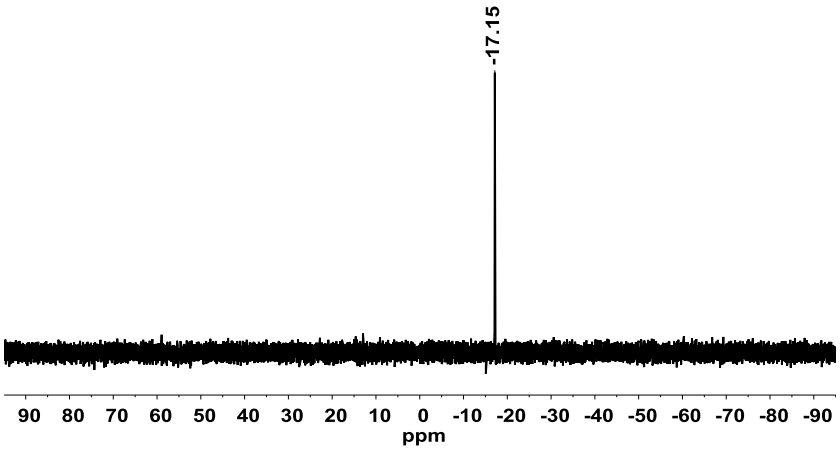

Figure S2. $^{31}P\{^{1}H\}$ NMR spectrum of **L1** (101 MHz, CD_3Cl, 296 K).

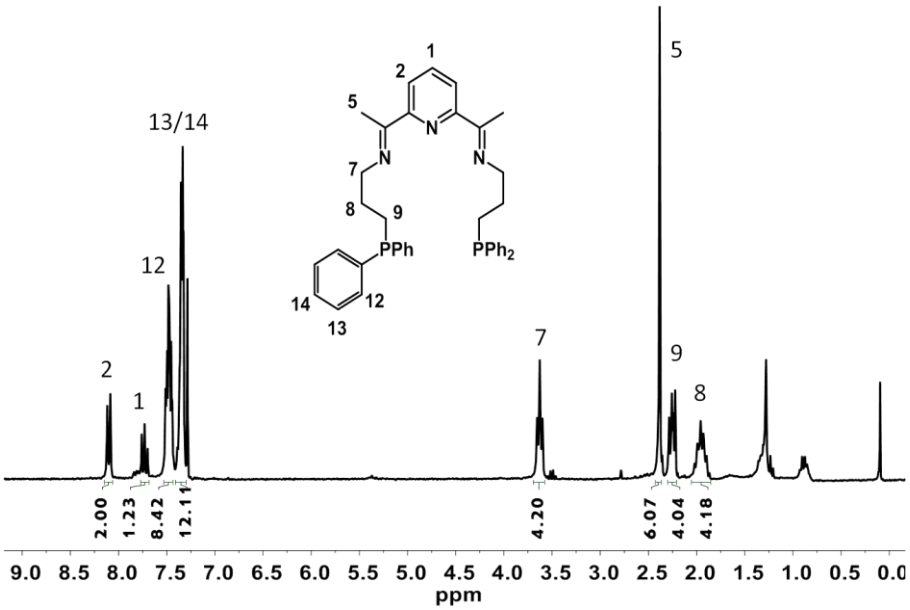

Figure S3. ^{1}H NMR spectrum of **L2** (250 MHz, CD_3Cl, 298 K).

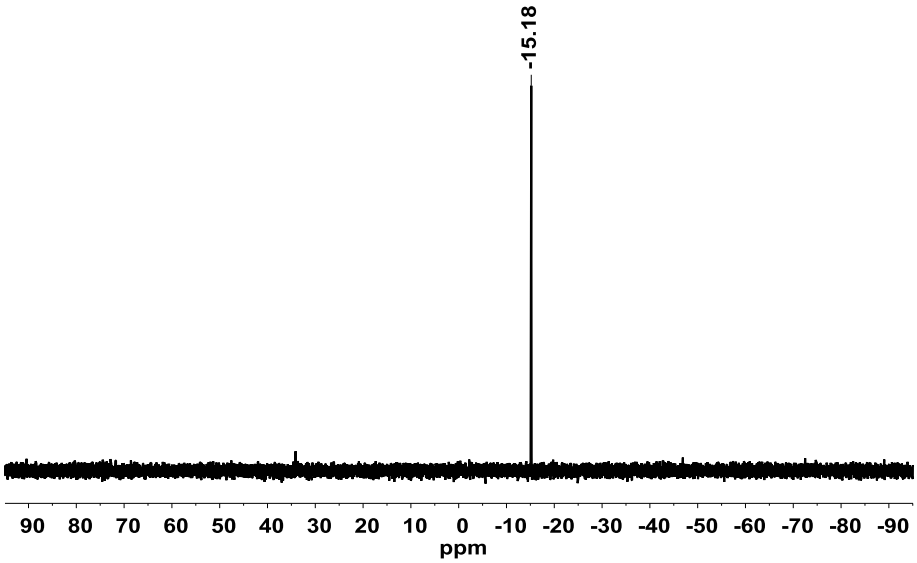

Figure S4. $^{31}P\{^{1}H\}$ NMR spectrum of **L2** (101 MHz, CD_3Cl, 298 K).

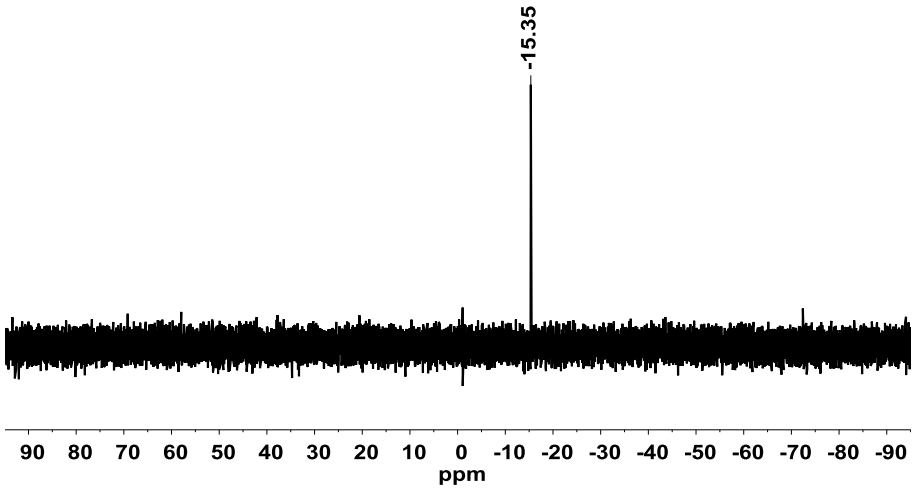

Figure S5. $^{31}P\{^{1}H\}$ NMR spectrum of **L3** (101 MHz, CD_2Cl_2, 304 K).

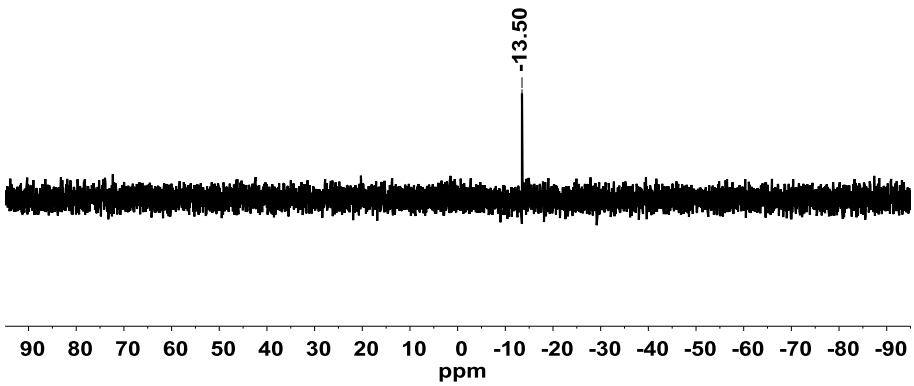

Figure S6. $^{31}P\{^{1}H\}$ NMR spectrum of **L4** (101 MHz, CD_2Cl_2, 301 K).

B- Mass Spectrometry

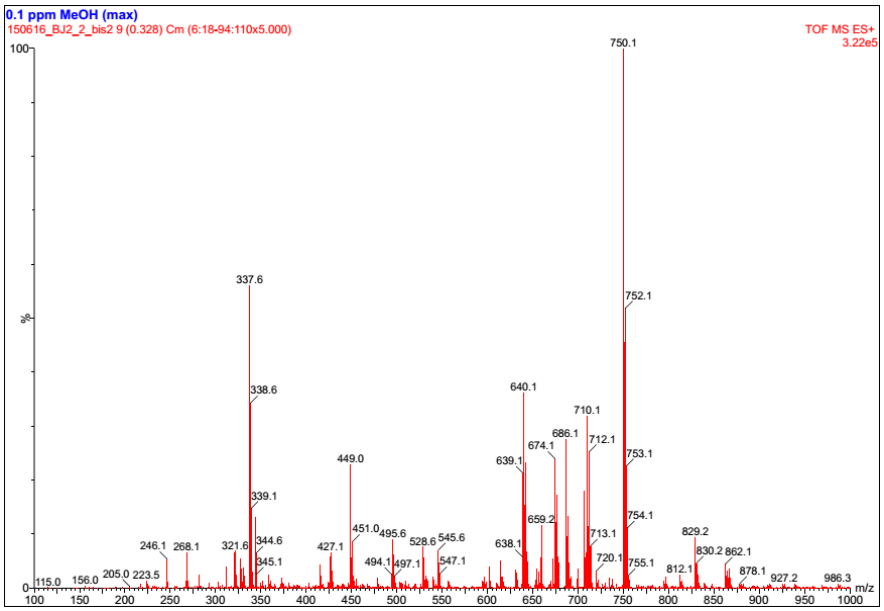

Figure S7. ESI-MS for product from reaction of **L1** and $NiCl_2 \cdot 6H_2O$.

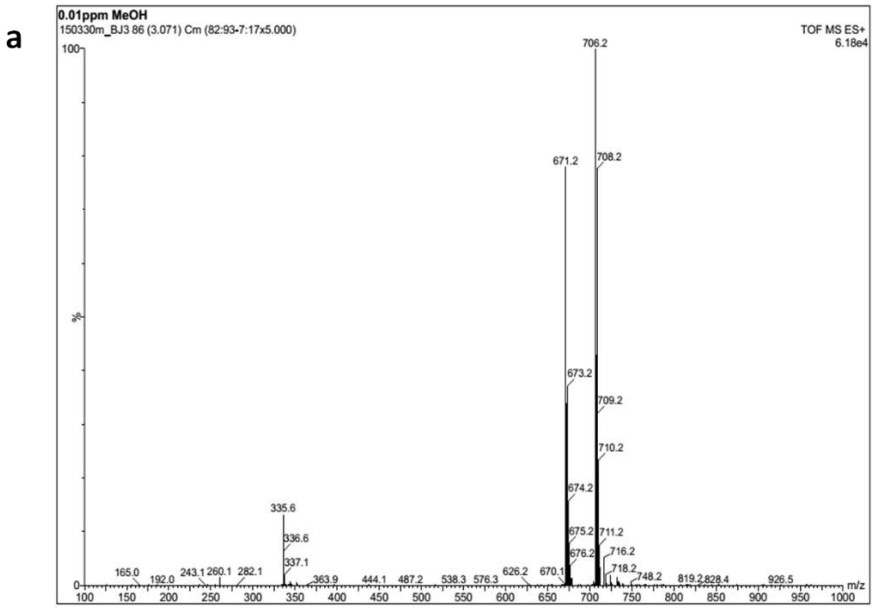

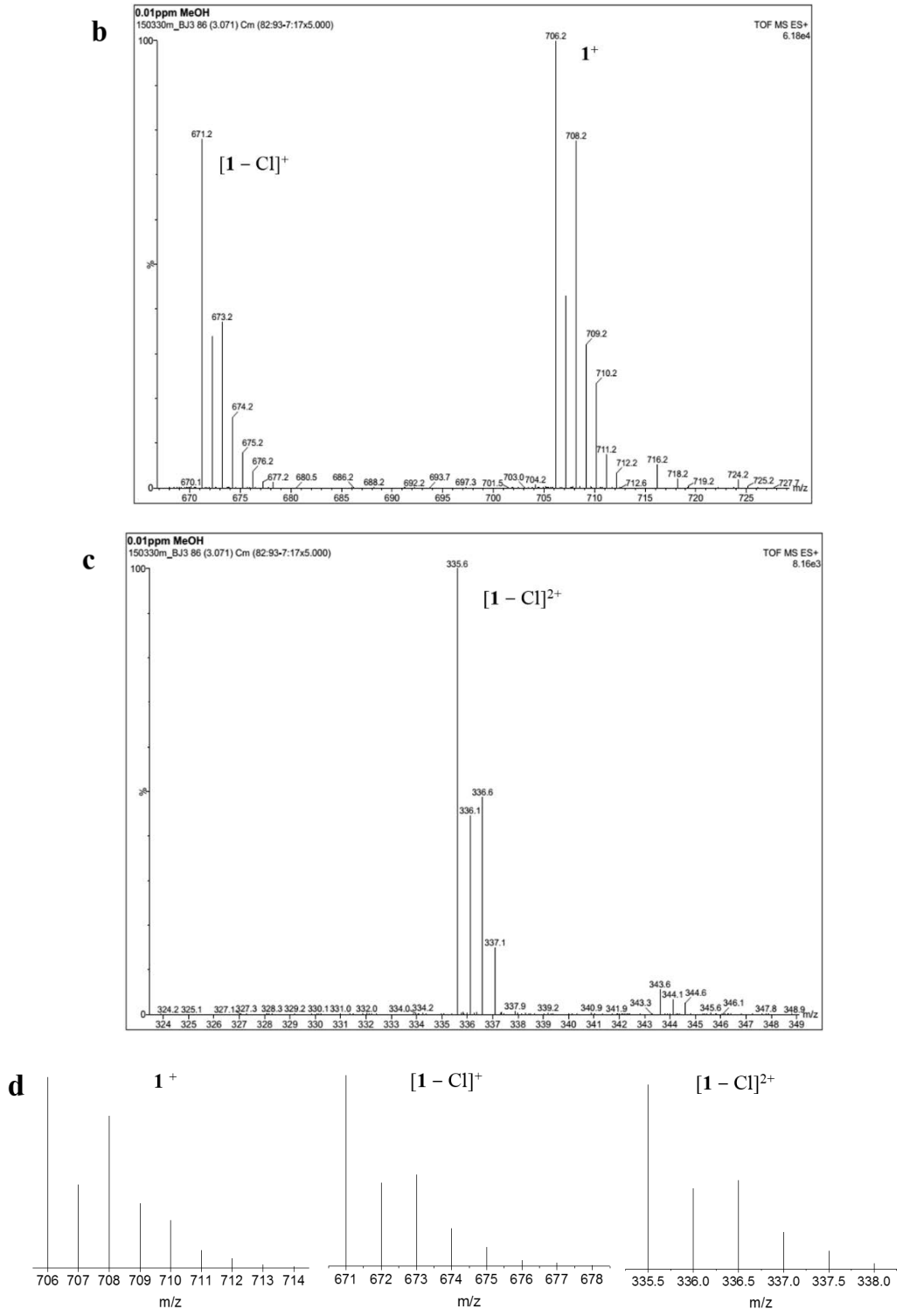

Figure S8. ESI-MS spectra for complex **1**(Cl) (a), partial zoomed view (b,c), and isotope pattern simulation of peaks *m*/*z* = 706.2 ($\mathbf{1}^{+}$); 671.2 ($[\mathbf{1} - \mathrm{Cl}]^{+}$); 335.6 ($[\mathbf{1} - \mathrm{Cl}]^{2+}$) (d).

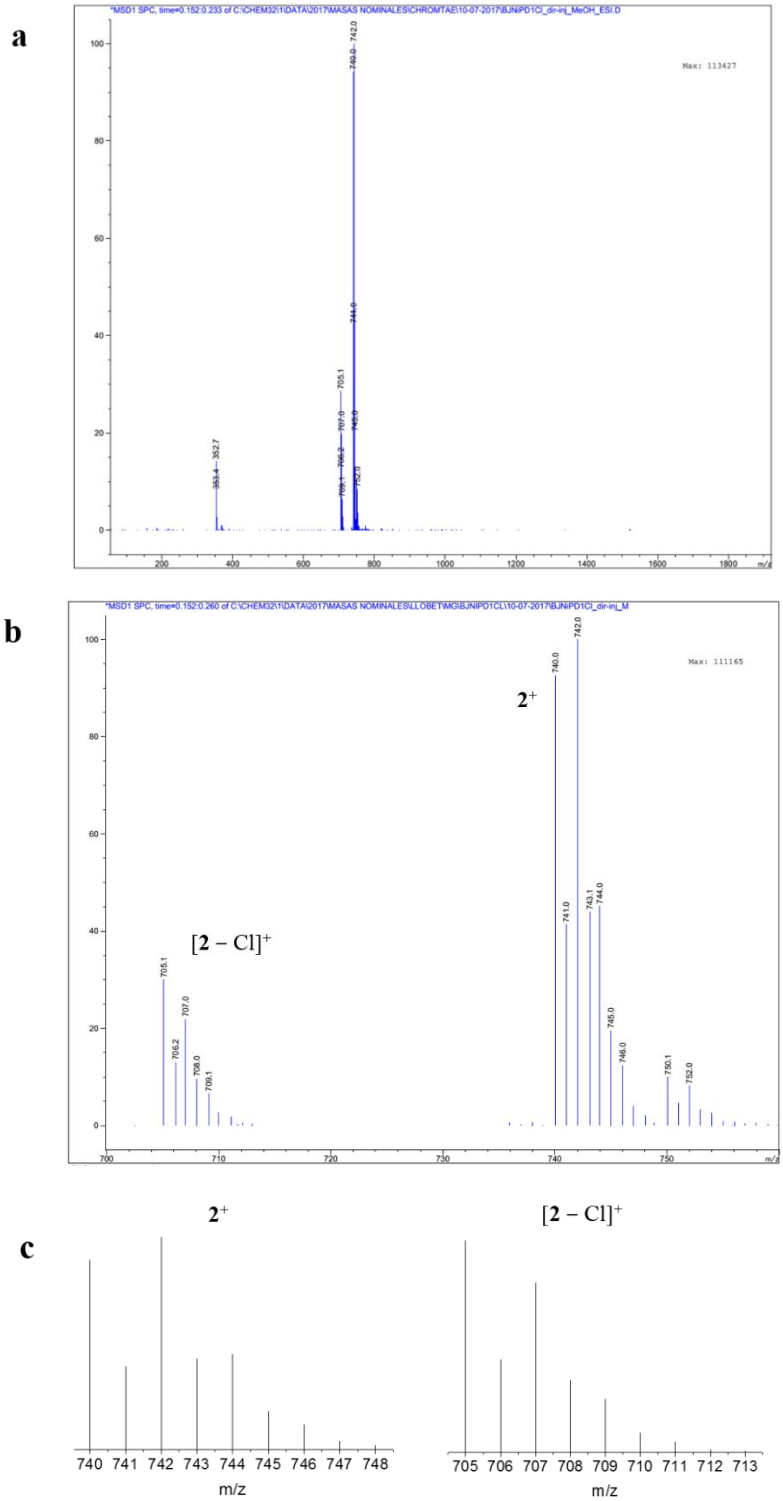

Figure S9. ESI-MS spectra for complex **2**(Cl) (a), partial zoomed view (b), and isotope pattern simulation of peaks *m*/*z* = 742.0 (**2**$^{+}$); 705.1 ([**2** – Cl]$^{+}$) (c).

C- Electrochemistry

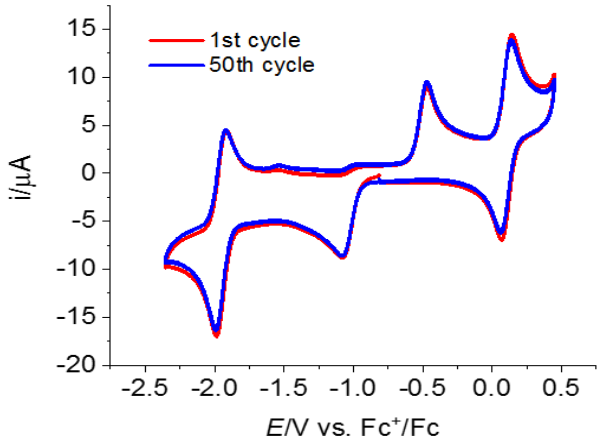

Figure S10. The first (red) and last (blue) cycles of 50 successive scanning of cyclic voltammograms for 1 mM **1**(Cl) in DMF (0.1 M nBu_4NPF_6) at 100 mV/s.

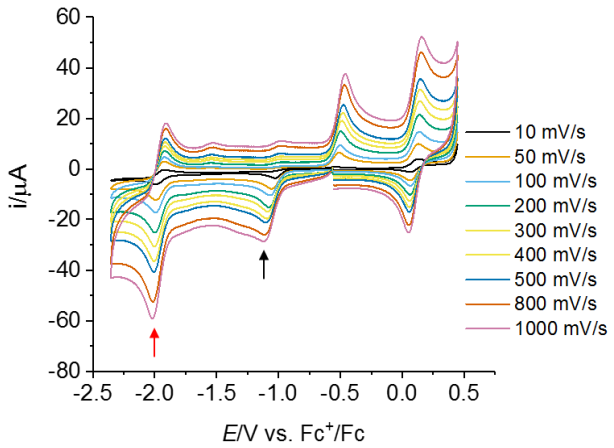

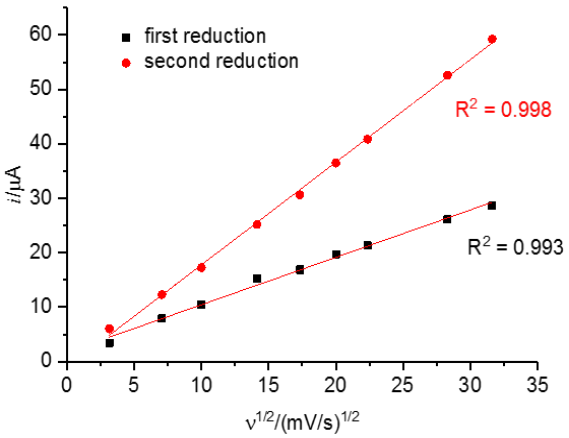

Figure S11. (top) Cyclic voltammograms of 1 mM **1**(Cl) in 0.1 M nBu_4NPF_6 DMF at various scan rates, black arrow indicates the first reduction wave, red arrow indicates the second reduction wave. (bottom) Plots of i_p (μA) vs. (Scan rate)$^{1/2}$ (mV/s) $^{1/2}$ for 1 mM **1**(Cl).

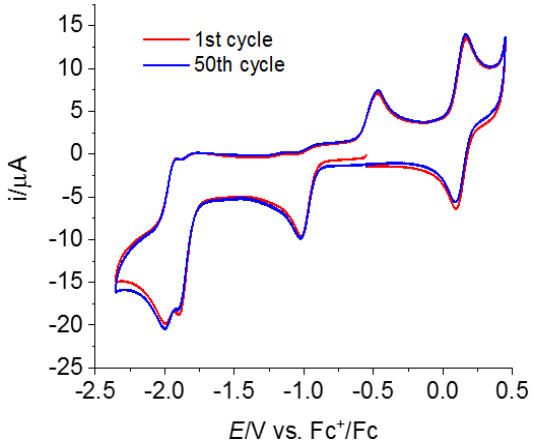

Figure S12. The first (red) and last (blue) cycles of 50 successive scanning of cyclic voltammograms for 1 mM **2**(Cl) in DMF (0.1 M nBu_4NPF_6) at 100 mV/s.

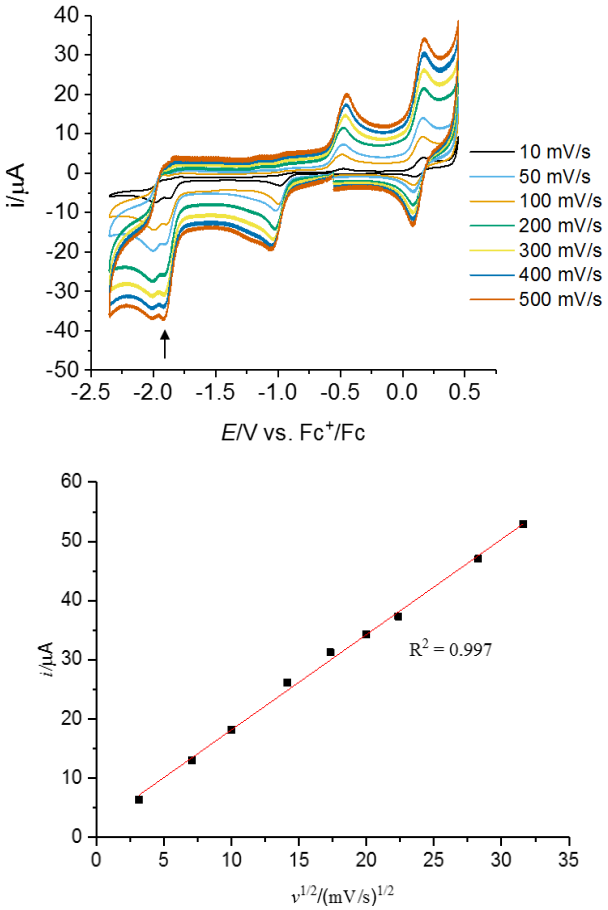

Figure S13. (top) Cyclic voltammograms of 1 mM **2**(Cl) in 0.1 M nBu_4NPF_6 DMF at various scan rates, arrow indicates the peak second reduction peak. (bottom) Peak current plots of the second reduction i_p (μA) vs. (Scan rate)$^{1/2}$ (mV/s) $^{1/2}$ for 1 mM **2**(Cl).

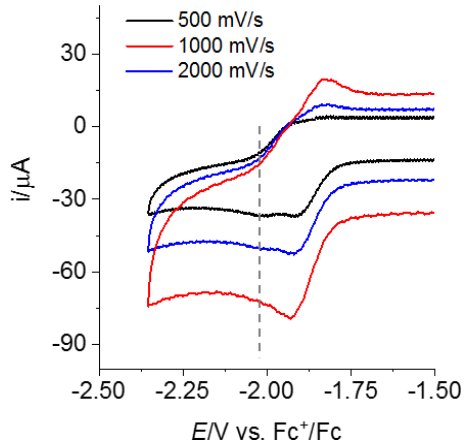

Figure S14. Cyclic voltammograms of 1 mM **2**(Cl) in 0.1 M nBu_4NPF_6 DMF at scan rate of 500 mV/s (black), 1000 mV/s (blue) and 2000 mV/s (red). Dashed line indicates the diminished reduction wave at higher scan rate.

D- Simulation of cyclic voltammograms

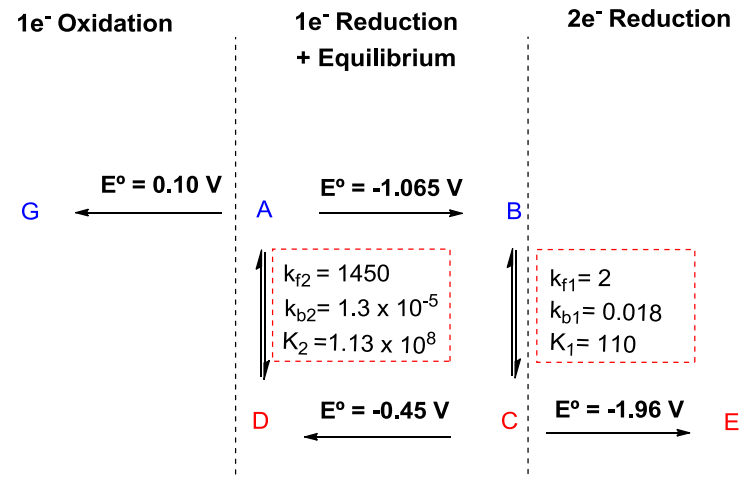

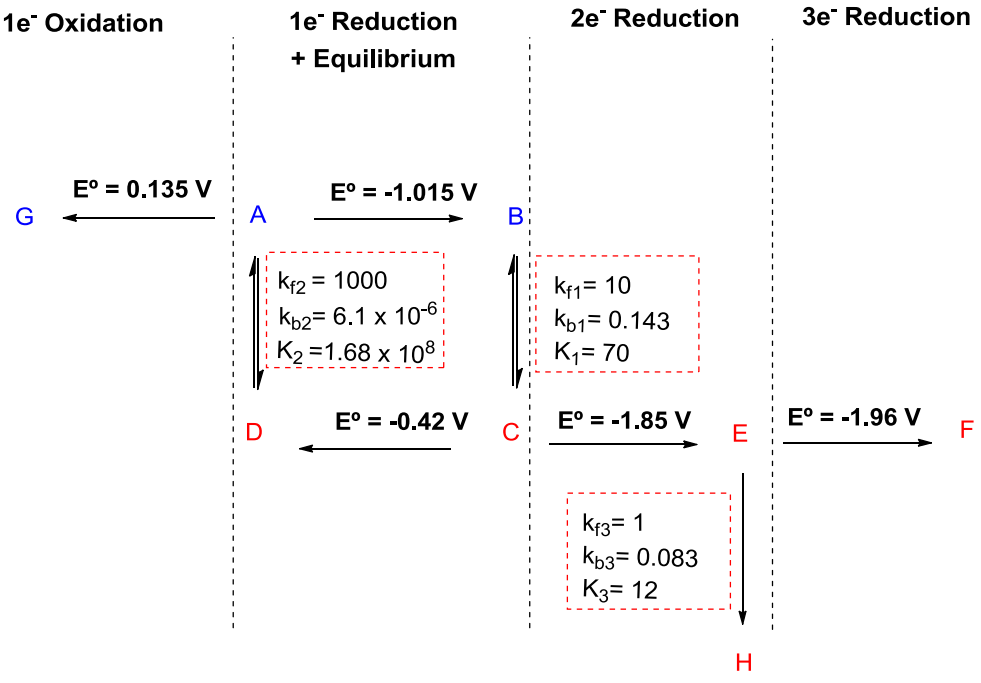

Scheme S1. Mechanisms and kinetics used for the simulation study of **1**(Cl) (up) and **2**(Cl) (bottom). A stands for the parent complex **1**(Cl) or **2**(Cl) in each case.

E- Electrocatalytic study

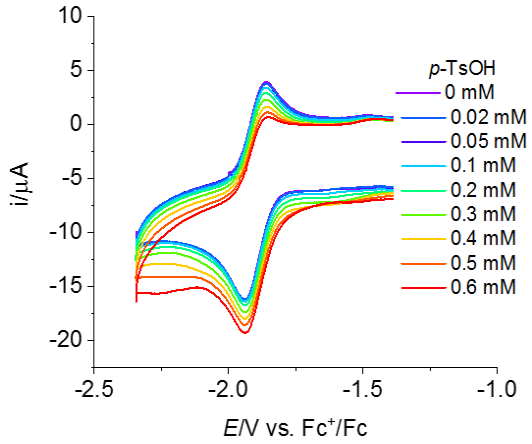

Figure S15. Cyclic voltammograms of 1 mM **1**(Cl) in 0.1 M nBu_4NPF_6 DMF in the presence of various concentrations of *p*-TsOH. Scan rate = 100 mV/s.

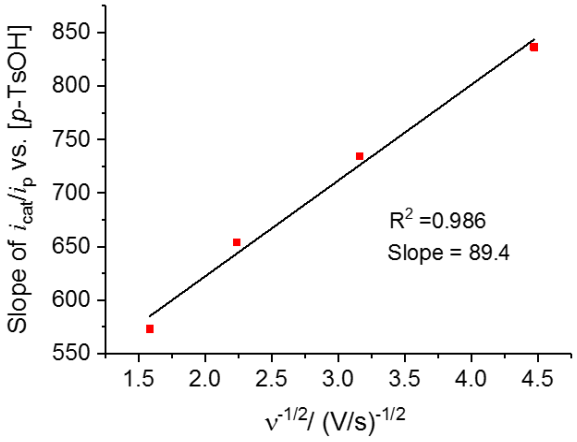

Figure S16. Double slope plot for calculation of the third order rate constant *k* of **1**(Cl). Red dots are slope values of i_{cat}/i_p versus *p*-TsOH concentration for different scan rates in Figure 3.14c; line is the linear fit of slop values versus $(1/\nu)^{1/2}$.

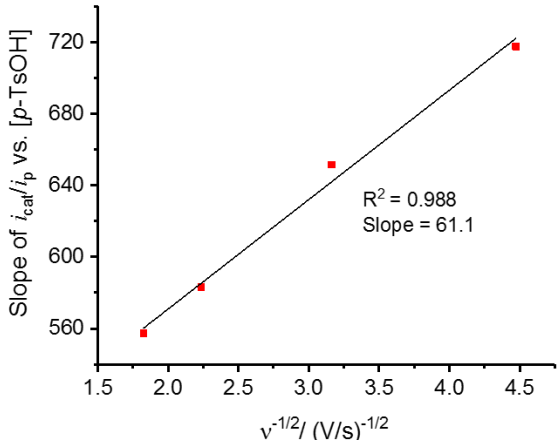

Figure S17. Double slope plot for calculation of the third order rate constant *k* of **2**(Cl). Red dots are slope values of i_{cat}/i_p versus *p*-TsOH concentration for different scan rates in Figure 3.15d; line is the linear fit of slop values versus $(1/\nu)^{1/2}$.

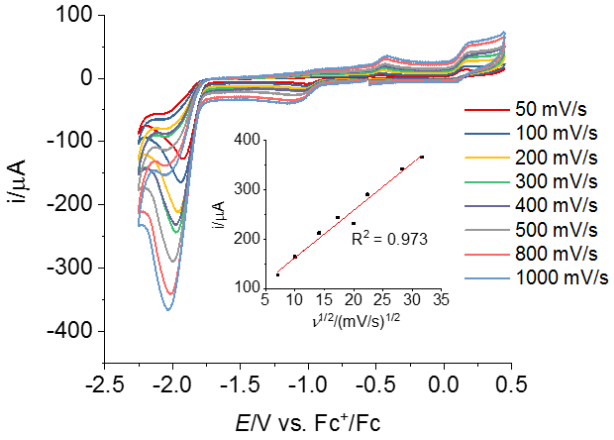

Figure S18. Cyclic voltammograms of 1 mM **2**(Cl) in DMF (0.1 M nBu_4NPF_6) in the presence of 10 mM *p*-TsOH at various scan rates. (Inset) Linear dependence of i_{cat} versus $\nu^{1/2}$.

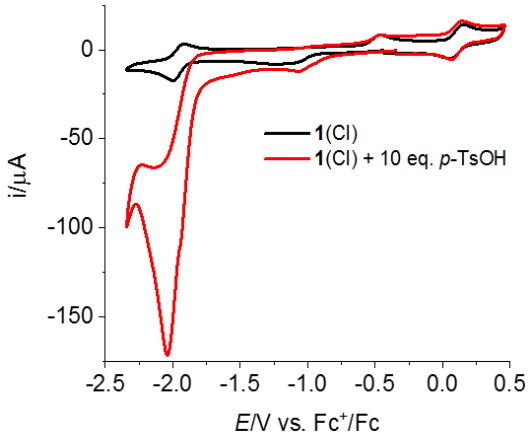

Figure S19. Cyclic voltammograms of 1 mM **1**(Cl) in H_2 purged DMF (0.1 M nBu_4NPF_6) in the absence and presence of 10 mM *p*-TsOH at a scan rate of 100 mV/s. Glassy carbon working electrode, Pt counter electrode and $Ag/AgNO_3$ reference electrode.

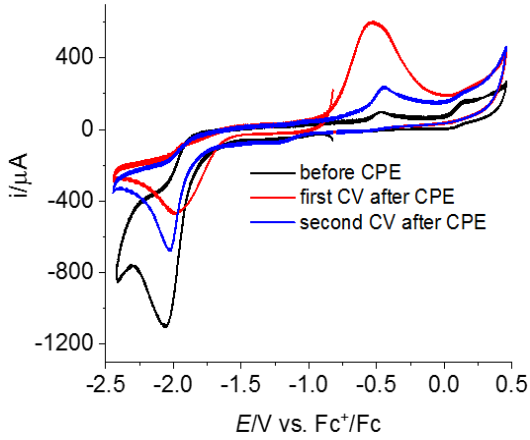

Figure S20. Cyclic voltammograms of 0.5 mM **1**(Cl) before and after 1 h bulk electrolysis in DMF (0.1 M nBu_4NPF_6) in the presence of 10 mM *p*-TsOH. Scan rate = 100 mV/s.

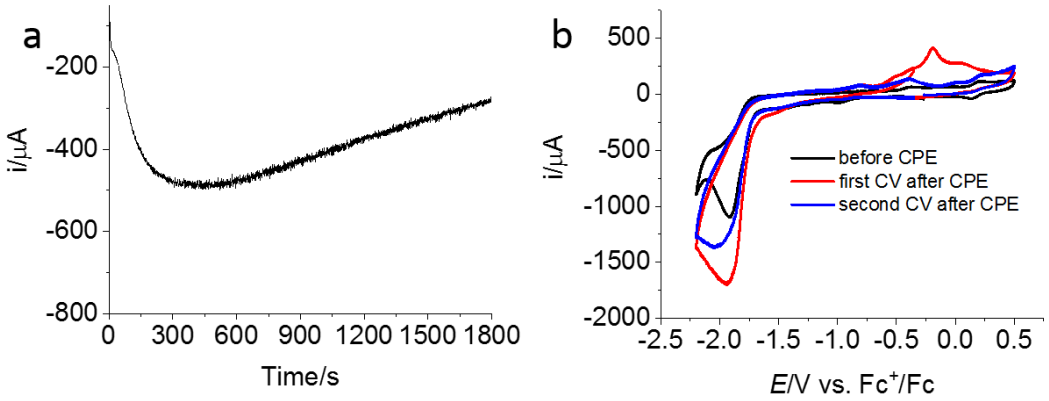

Figure S21. (a) Plot of current versus time for 30 min controlled-potential (–1.7 V) electrolysis of 0.5 mM **2**(Cl) in DMF (0.1 M nBu_4NPF_6) in the presence of 10 mM *p*-TsOH. (b) Cyclic voltammograms of 0.5 mM **2**(Cl) before and after bulk electrolysis at –1.7 V in DMF in the presence of 10 mM *p*-TsOH.

F- Spectroelectrochemistry

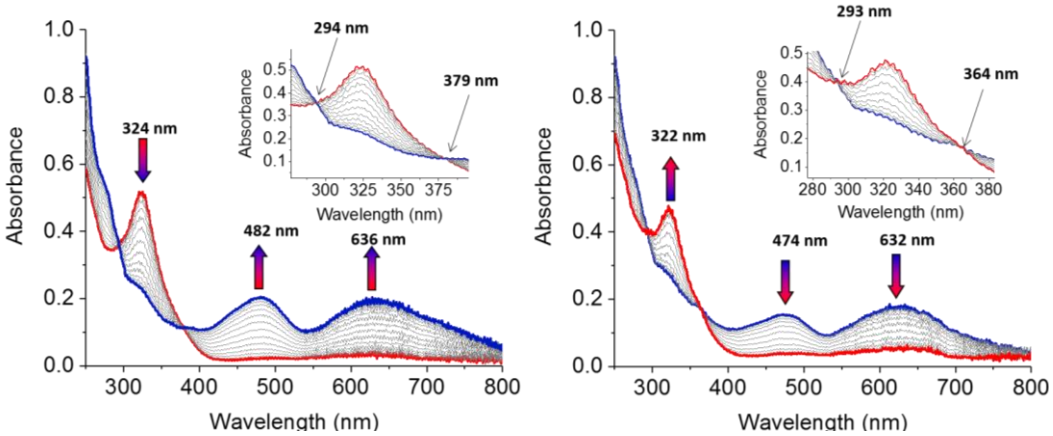

Figure S22. Spectroelectrochemical monitoring (OTTLE cell) for the one-electron reduction ($E_{pc}^{1'}$, left) and reoxidation ($E_{pa}^{1'}$, right) processes of 2 M **2**(Cl) in DMF (0.1 M nBu_4NPF_6). Arrows indicate changes in band intensity during electrolysis.

G- X-ray diffraction metrics

Table S1. Crystal data and structure refinement for **1**(Cl).

Empirical formula	$C_{39}H_{45}Cl_2N_3NiO_2P_2$
Formula weight	779.33
Temperature	100(2) K
Wavelength	0.71073 Å
Crystal system	Triclinic
Space group	P-1
Unit cell dimensions	a = 11.1091(4)Å α = 76.7810(10)°.
	b = 11.7650(4)Å β = 75.6110(10)°.
	c = 15.6663(5)Å γ = 70.8140(10)°.
Volume	1848.83(11) $Å^3$
Z	2
Density (calculated)	1.400 Mg/m^3
Absorption coefficient	0.795 mm^{-1}
F(000)	816
Crystal size	0.10 x 0.05 x 0.05 mm^3
Theta range for data collection	1.857 to 27.161°.
Index ranges	-13<=h<=13,-14<=k<=15,0<=l<=20
Reflections collected	14624
Independent reflections	14624[R(int) =?]
Completeness to theta =27.161°	92.7%
Absorption correction	Multi-scan
Max. and min. transmission	0.961 and 0.739
Refinement method	Full-matrix least-squares on F^2
Data / restraints / parameters	14624/ 163/ 527
Goodness-of-fit on F^2	1.014
Final R indices [I>2sigma(I)]	R1 = 0.0511, wR2 = 0.1163
R indices (all data)	R1 = 0.0767, wR2 = 0.1302
Largest diff. peak and hole	1.908 and -0.707 $e.Å^{-3}$

Table S2. Crystal data and structure refinement for **2**(Cl).

Empirical formula	$C_{39}H_{46}Cl_3N_3NiO_3P_2$
Formula weight	831.79
Temperature	100(2) K
Wavelength	0.71073 Å
Crystal system	Tetragonal
Space group	I4(1)/a
Unit cell dimensions	a = 14.3113(15)Å α = 90°.
	b = 14.3113(15)Å β = 90°.
	c = 37.944(5)Å γ = 90°.
Volume	7771.3(19) $Å^3$
Z	8
Density (calculated)	1.422 Mg/m^3
Absorption coefficient	0.829 mm^{-1}
F(000)	3472
Crystal size	0.20 x 0.15 x 0.02 mm^3
Theta range for data collection	1.521 to 29.655°.
Index ranges	-12<=h<=19,-18<=k<=14,-32<=l<=52
Reflections collected	21368
Independent reflections	5177[R(int) = 0.0690]
Completeness to theta =29.655°	94.3%
Absorption correction	Multi-scan
Max. and min. transmission	0.984 and 0.638
Refinement method	Full-matrix least-squares on F^2
Data / restraints / parameters	5177/ 7/ 259
Goodness-of-fit on F^2	1.031
Final R indices [I>2sigma(I)]	R1 = 0.0408, wR2 = 0.0895
R indices (all data)	R1 = 0.0718, wR2 = 0.1034
Largest diff. peak and hole	0.534 and -0.323 $e.Å^{-3}$

Chapter 4

Cobalt Molecular Catalysts Bearing Bis(imino)pyridine Diphosphine Ligands for Proton Reduction: Synthesis and Mechanistic Analysis

4.1 Introduction

Although there is no biological relevance for water splitting, cobalt is a widely used transition metal in hydrogen evolution electrocatalysis owing to its feasible electronic conversion from $3d^6$ Co^{III} or $3d^7$ Co^{II} to the lower valent $3d^8$ Co^{I} species.[1,2] The latter species is highly nucleophilic and thus readily reacts with a proton to generate Co^{III}-H species, that is frequently proposed as intermediate in the catalytic cycle.[3,4] Once the Co^{III}-H species is formed, the catalytic system can evolve through several pathways (Scheme 4.1), including the direct generation of hydrogen from Co^{III}-H or its reduced form Co^{II}-H. Generally speaking, the former mechanism arises in the presence of a strong acid, while the latter one mainly occurs in mild or weak acidic conditions. Both metal hydride intermediates can then potentially evolve hydrogen through two distinct mechanisms, i.e., homolytic or heterolytic pathways. In the homolytic mode, as the name suggests, homolysis of the Co-H bonds and reductive elimination take place between two metal–hydride complexes, thus giving half equivalent of dihydrogen per Co and one equivalent of a monoelectron-reduced Co ion. In the heterolytic mode, a metal–hydride is attacked by a proton, yielding an intermediate dihydrogen metal σ-complex, which then evolve one equivalent of dihydrogen while the Co ion maintains the original oxidation state. It is noteworthy that coexistence of homolytic and heterolytic pathways, or converting from one to the other one, can happen depending on the experimental conditions, such as the acid strength or the relative concentrations of protons and catalysts.[5]

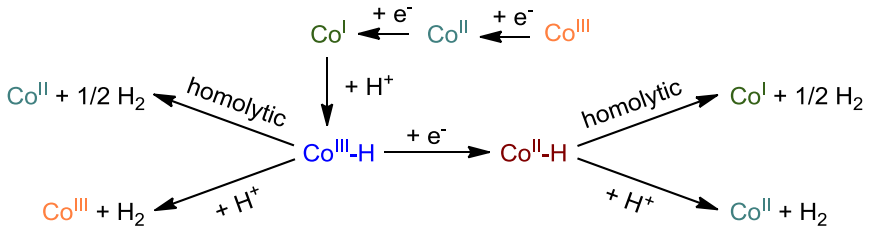

Scheme 4.1 Generalized mechanistic pathways for proton reduction catalyzed by Co complexes.

In the previous Chapter 3 two Ni-based electrocatalysts bearing the Schiff-base ligands ^{Ph2PPr}PDI (**L2**) and ^{Ph2PPr}PDI(*p*)Cl (**L3**) were reported to be capable of catalyzing the hydrogen evolution reaction in organic media. Here on, the same PDI scaffolds are coordinated to a Co center. In this Chapter we present the synthesis and thorough characterization of two new Co complexes together with a detailed mechanistic investigation (UV-vis, NMR) that shed some light to the intermediates and pathways involved when this family of complexes is used as HER electrocatalysts.

4.2 Results and discussion

4.2.1 Synthesis and Characterization

4.2.1.1 Synthesis and characterization of [Co(^{Ph2PPr}PDI)](BF$_4$) (3(BF$_4$))

The pentadentate ligand ^{Ph2PPr}PDI (**L2**) in Scheme 4.2 was employed to coordinate to a Co(II) center using Co(BF$_4$)$_2$·6H$_2$O as the metal precursor, in a THF solution at room temperature. After stirring for 1 day, the dark black-green solution was dried under vacuum. Recrystallization of the resulting powder by layering with pentane to a solution of DCM/MeOH mixture afforded black crystals of compound **3**(BF$_4$) in a relatively low yield of 26% (Scheme 4.2). The low yield is likely due to the disproportionation of the Co(II) to the Co(I) complex (**3**(BF$_4$)) and the formation of Co(III) complexes.

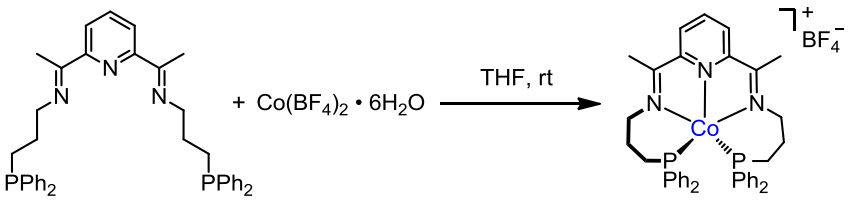

L2 **3**(BF_4)

Scheme 4.2 Synthesis of **3**(BF_4).

Compound **3**(BF_4) has been characterized by ESI mass spectrometry, single crystal X-ray diffraction, NMR and UV-vis spectroscopies as well as cyclic voltammetry. The ESI-MS spectra in Figure S18 confirmed the presence of the cation species $[Co(^{Ph2PPr}PDI)]^+$ at m/z = 672.0, and divalent cation $[Co(^{Ph2PPr}PDI)+MeOH]^{2+}$ with m/z = 352.1. The crystal structure of **3**(BF_4) (Figure 4.1) belongs to a P2(1)/n monoclinic space group. The cobalt center is five coordinated with three N atoms and two P atoms from the PDI ligand. Based on the calculated Addison parameter (obtained from the N(1)–Co(1)–N(3) and N(2)–Co(1)–P(1) angles), τ_5 = 0.613, the cobalt metal ion adopts a distorted trigonal-bipyramidal environment (τ = 0 for an ideal square pyramid and τ = 1 for a trigonal bipyramid),[6] with the pyridine nitrogen atom and two phosphorus atoms forming the equatorial plane and two imine nitrogen atoms occupying the axial positions. The relevant metrical parameters are displayed in Table 4.1. The angles of the trigonal plane, P(1)–Co(1)–P(2) = 111.27°, N(2)–Co(1)–P(2) = 123.53° and N(2)–Co(1)–P(1) = 125.19°, deviate somewhat from the ideal trigonal angle of 120°. However the sum of these angles is 360°, confirming the planarity of the trigonal plane that is composed of N(2), P(1) and P(2) atoms. The solid-state structure determined by X-ray crystallography surprisingly displays a monocationic complex with the presence of only one BF_4^- as counterion. This is in agreement with the resulting elemental analyses that confirm $[Co(^{Ph2PPr}PDI)][BF_4]$ as the molecular formula. We propose that the disproportionation of the Co(II) species, over the long reaction and crystallization time, generates Co(III) and Co(I) derivatives in solution, with the latter compound crystallized and collected.[7] Taking into account the redox non-innocent character of PDI chelates,[8] the electronic configuration of **3**$^+$ can be described as a low valent Co(I) ion stabilized by the neutral bis(imino)pyridine ligand, or can be regarded as a Co(II) ion antiferromagnetically coupled to a ligand radical anion.

Inspecting the imine C=N distances, a moderate elongation (1.3263(9) and 1.3256(9) Å compared to unreduced PDI ligands 1.28 Å) is observed in both cases.[9,10] Moreover, the C_{im}–$C_{py(o)}$, that is C(2)–C(3) and C(8)–C(7) in Figure 4.1a, bond distances (1.4449(10) and 1.4405(10) Å) are obviously contracted relative to neutral chelates (1.50 Å).[9,10] Even if these metrical parameters may imply a reduced PDI chelate as monoanion, we cannot determine this conclusion without further evidence. For instance, similar bond elongation and contraction observed in a Mn PDI complex has been attributed to Mn-to-PDI back–bonding rather than to the reduction on redox-active ligand through Density Functional Theory (DFT) calculations.[11] So $\mathbf{3}^+$ is tentatively denoted as $[Co^{I}(^{Ph2PPr}PDI)]^+$ in the present manuscript, and more insights into the electronic configuration are currently under investigation by DFT calculations.

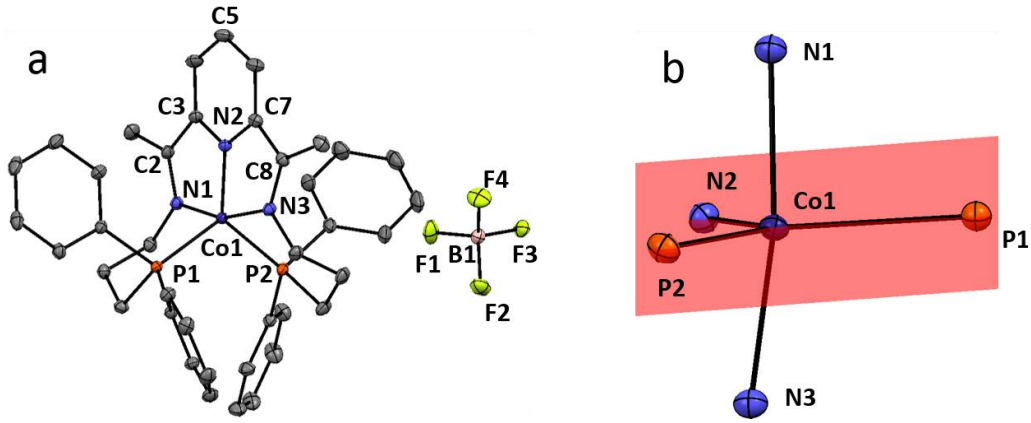

Figure 4.1 (a) ORTEP drawing of **3**(BF_4) with 50% probability thermal ellipsoids. Hydrogen atoms are omitted for clarity. (b) ORTEP representation of the first coordination sphere showing that P(1), P(2) and N(2) are located in the equatorial plane of a trigonal bipyramid.

Table 4.1 Selected bond lengths (Å) and angles (deg) determined for **3**(BF_4)

N(1)−C(2)	1.3263(9)
N(3)−C(8)	1.3256(9)
C(2)−C(3)	1.4449(10)
C(7)−C(8)	1.4405(10)
Co(1)–N(1)	1.9194(6)
Co(1)–N(2)	1.8236(6)
Co(1)–N(3)	1.9307(6)

Co(1)–P(1)	2.21258(19)
Co(1)–P(2)	2.21823(19)
P(1)–Co(1)–P(2)	111.266(7)
N(2)–Co(1)–P(2)	123.528(19)
N(2)–Co(1)–P(1)	125.185(19)
N(1)–Co(1)–N(3)	161.99(3)

Compound **3**(BF_4) is a diamagnetic low-spin Co(I) (S = 0) species, with this nature confirmed by NMR spectroscopy, and thus the complex has been fully characterized by 1D and 2D NMR spectroscopy in CD_2Cl_2. NMR analysis indicates the symmetric character of **3**(BF_4) which belongs to the C_2 point group in solution, with the rotational axis passing through C(5), the N(2) atom of the pyridine ring, and the central Co atom, thus the protons and other atoms symmetric to the C_2 axis are isochronous. As a result, only 20 ^{13}C resonances come from all 39 carbon atoms were observed in Figure S1 (^{13}C NMR spectra) and S5 (HSQC spectra), with some phenyl resonances overlapped. A singlet at 43.1 ppm, typical chemical shift range for coordinated phosphorus donor atoms,[12,13] in the $^{31}P\{^1H\}$ NMR spectrum indicated symmetric phosphine substituent coordination around the Co center (Figure S2). The ^1H NMR spectrum shows six methylene resonances, which contrasts to the three resonances (integrating four protons each) displayed by the free ligand **L2**. Upon coordination to the Co ion the methylenic protons of **L2** become diastereotopic, thus leading to differentiated ^1H NMR resonances. In addition to the propyl-bridged chelate arms, long range ^{31}P-coupling to the PDI backbone methyl (H5, t, 6 H) and *p*-pyridine (H1, tt, 1 H) resonances at 2.27 and 8.08 ppm, respectively, were also observed in Figure 4.2 (see zoom), which is a feature not detected in free ligand. **3**(BF_4) also differs from the parent free ligand **L2** in the splitting of the resonances corresponding to the phenyl substituents on the P atoms, showing six signals in the 7.55 to 6.12 ppm range instead of three due to the loss of symmetry of the phenyl moieties upon coordination.

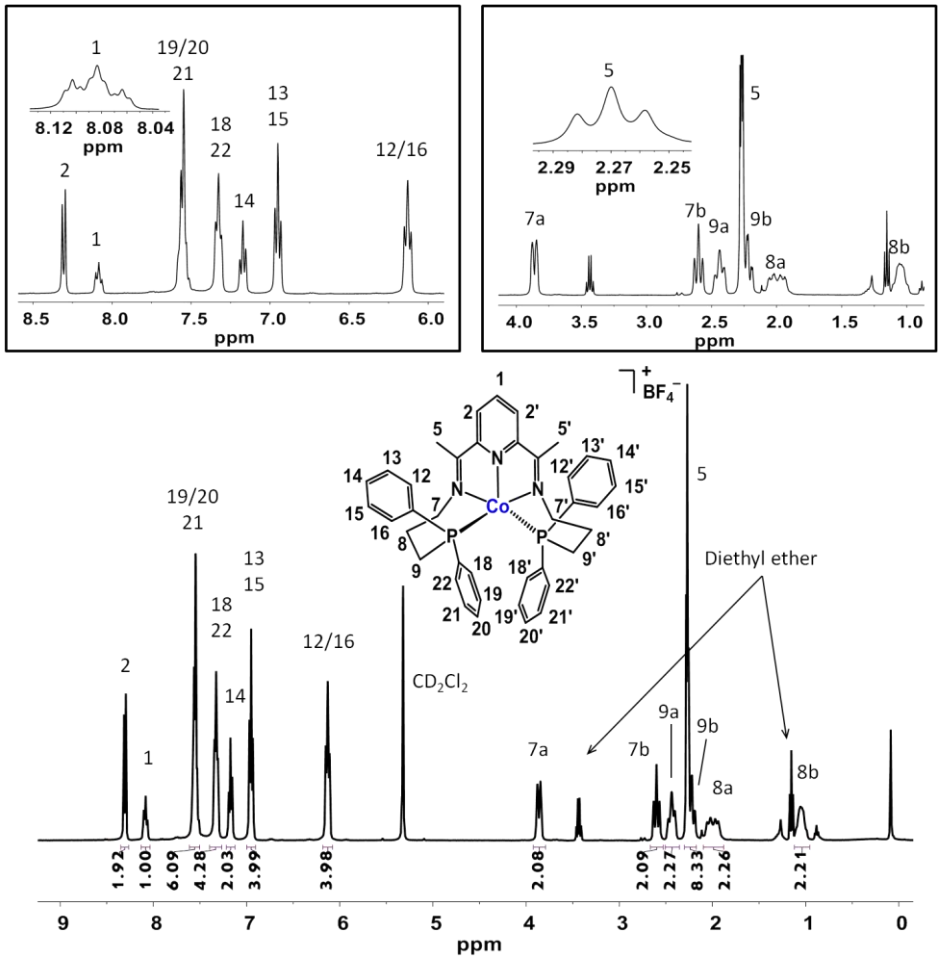

Figure 4.2 ^{1}H NMR spectrum of **3**(BF_4) (400 MHz, CD_2Cl_2, 298 K). Zooms of aromatic and aliphatic methylenic regions are shown at top left and top right, respectively.

The electronic absorption spectrum of **3**(BF_4) shown in Figure 4.3 was recorded in MeCN solution (4×10^{-5} M) at room temperature. Two intense characteristic absorption bands in the UV region at λ = 260 nm (ε = 33000 $M^{-1}cm^{-1}$) and λ = 317 nm (ε = 11000 $M^{-1}cm^{-1}$) are assigned to ligand-based $\pi\rightarrow\pi^*$ transitions. In the visible region, **3**(BF_4) displays a band of medium intensity at λ_{max} = 432 nm ($\varepsilon\sim$ 16000 $M^{-1}cm^{-1}$) which is attributed to metal to ligand charge transfer (MLCT). In addition, two broad absorption bands with relatively low intensity ($\varepsilon\sim$ 3000 $M^{-1}cm^{-1}$) are observed at 498–611 nm and 611–800 nm, more likely resulting from d–d transitions. Similar broad bands in the same spectral region have been reported for similar Co(I) compounds.[14–16]

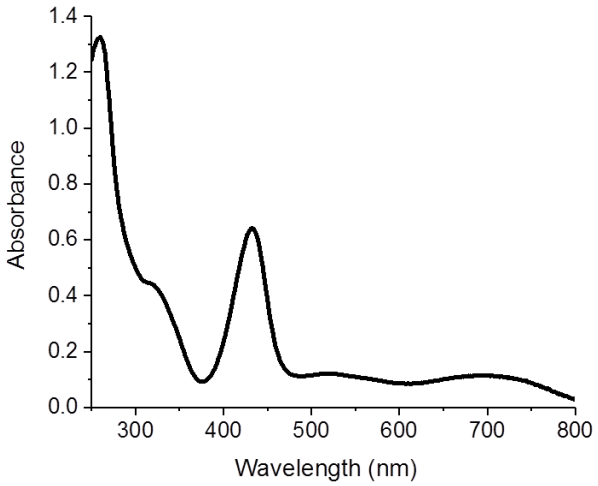

Figure 4.3 UV-vis spectrum of **3**(BF_4) in MeCN.

The redox properties of **3**(BF_4) have been studied by cyclic voltammetry (CV). As shown in Figure 4.4, in 0.1 M nBu_4NPF_6 dry DMF solution, the CV of **3**(BF_4) was found to feature two reversible waves with half-wave potentials $E_{1/2}$ = –2.02 V (ΔE_p = 79 mV) and –0.24 V (ΔE_p = 112 mV) vs. Fc^+/Fc. The less intense wave at –2.02 V observed when cathodically scanning from the open-circuit potential (OCP) is tentatively assigned to the ligand based $L^{0/-}$ couple, thus generating the (PDI^-)Co^I representation upon one-electron reduction. The more positive wave observed at –0.24 V when reversing the scan direction is attributed to the two-electron oxidation (integrates twice as compared the previous one) of **3**(BF_4) to form the corresponding Co(III) complex. The latter process was studied chemically by employing an oxidizing reagent, ferrocenium tetrafluoroborate ($FcBF_4$), causing a color change from dark green-brown to orange immediately. The reaction was monitored by UV-vis spectroscopy (Figure S20) and the final mixture was analyzed by ^{1}H NMR spectroscopy (Figure S11). With regards to UV-vis spectroscopy, a new band at 379 nm appeared while the band at 434 nm vanished upon adding aliquots of $FcBF_4$. When the chemical oxidation of **3**(BF_4) was monitored by ^{1}H NMR spectroscopy, a new diamagnetic species attributed to the generation of a Co(III) complex is observed upon addition of two equivalents of $FcBF_4$ in CD_3CN (Figure S11). This species displays significantly altered chemical shifts with regard to parent **3**(BF_4), such as the representative *m*-pyridine H2 doublet resonance at 8.37 ppm in **3**(BF_4) shifted to higher field (7.88 ppm) or the *p*-pyridine H1 triplet of triplets at 8.07 ppm moved to lower field

8.17 ppm. In addition, for this oxidized species, the resonances of phenyl protons shift to lower fields and to a narrower chemical shift range (6.76–7.79 ppm), which is consistent with the ^{1}H NMR characterization of other $Co^{III/I}$ transformations previously reported in the literature.[17]

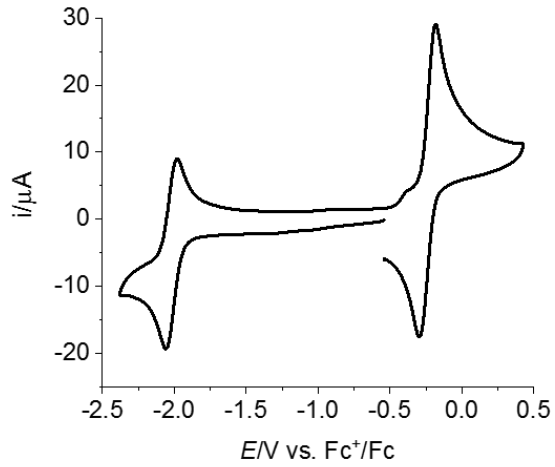

Figure 4.4 Cyclic voltammogram of 1mM **3**(BF_4) in DMF (0.1 M nBu_4NPF_6), scan rate = 100 mV/s.

4.2.1.2 Synthesis and characterization of [Co(^{Ph2PPr}PDI(*p*)Cl)](BF_4) (4(BF_4))

Complex **4**(BF_4) in Scheme 4.3 was synthesized under the same conditions used for **3**(BF_4) except that the 4-chloro-substituted bis(imino)pyridine ^{Ph2PPr}PDI(*p*)Cl (**L3**) was utilized as ligand frame. Layering pentane on a solution of **4**(BF_4) in a DCM/MeOH mixture induced the crystallization of the final product as black crystals which were suitable for single crystal X-ray diffraction analysis (Figure 4.5).

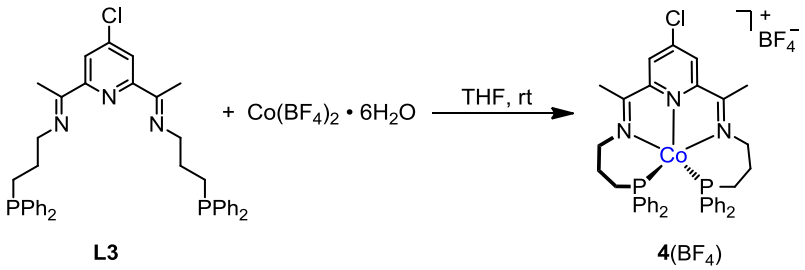

Scheme 4.3 Synthesis of **4**(BF_4).

Compound **4**(BF_4) has been characterized by ESI mass spectrometry, single crystal X-ray diffraction, NMR spectroscopy and cyclic voltammetry. ESI-MS spectra show species $[Co(^{Ph2PPr}PDI(p)Cl)]^+$ with m/z = 706.1, and simulated isotopic distributions are in agreement with the proposed molecular composition (Figure S19). Like **3**(BF_4), the pentacoordinated complex **4**(BF_4) belongs to a P2(1)/n monoclinic space group and shows the Co metal ion coordinated by the N_3P_2 core of the ^{Ph2PPr}PDI(*p*)Cl ligand. With an Addison parameter τ_5 value of 0.528, **4**(BF_4) is a distorted trigonal-bipyramidal geometry, presenting higher distortion than **3**(BF_4).

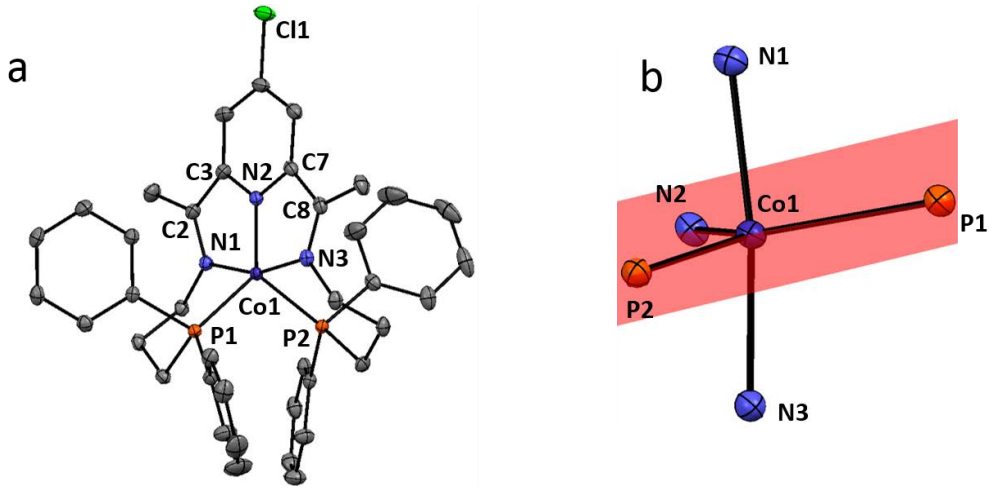

Figure 4.5 (a) ORTEP drawing of the cationic part of **4**(BF_4) with 50% probability thermal ellipsoids. Hydrogen atoms and a crystallized water molecule are omitted for clarity. (b) ORTEP representation of the first coordination sphere showing that P(1), P(2) and N(2) lie in the equatorial plane of a trigonal bipyramid.

Table 4.2 Selected bond lengths (Å) and angles (deg) determined for **4**(BF_4)

N(1)−C(2)	1.3248(16)
N(3)−C(8)	1.3226(16)
C(2)−C(3)	1.4380(19)
C(7)−C(8)	1.4385(19)
Co–N(1)	1.9226(11)
Co–N(2)	1.8185(11)
Co–N(3)	1.9281(11)
Co–P(1)	2.2263(4)

Co–P(2)	2.2170(4)
P(1)–Co–P(2)	106.438(14)
N(2)–Co–P(2)	129.59(4)
N(2)–Co–P(1)	123.95(4)
N(1)–Co–N(3)	161.25(5)

Analogously to **3**(BF_4) (see section 4.2.1.1 above) complex **4**(BF_4) is diamagnetic in nature as can be observed in its NMR spectra recorded in CD_2Cl_2. The ^1H NMR spectrum of **4**(BF_4) was consistent with the formation of a C_2-symmetric compound, showing 18 resonances assigned to the target complex (Figure 4.6). Due to the Cl-substitution at the *para* position of the PDI ligand scaffold, the two *m*-pyridine protons H2/H2' no longer show spin–spin coupling and appear as a singlet at 8.36 ppm. Ten additional resonances integrating to 20 protons in the 6.08–7.65 ppm aryl region were assigned to the bound PPh_2 moieties. 1D NOESY experiments revealing the interaction between *m*-pyridine protons (H2/H2') and four protons of *o*-phenyl (H12/H12', H16/H16') were key for the assignment of the protons in these aromatic phenyl rings bound to the P atoms (Figure 4.7). Besides, ^1H NMR revealed six chelate arm resonances, with that of H9b partially overlapping with a triplet resonance corresponding to methyl protons (H5, t, 6H) located at 2.29 ppm. The assignment of each resonance was attained by means of 2D spectra, including COSY, HSQC, and HMBC (see Figures S8–S10). Investigation of **4**(BF_4) by ^{13}C NMR (Figure S6) displayed only 20 overall carbon resonances and only three methylene resonances, confirming that the two PDI arms were symmetrically bound to cobalt. As expected, the $^{31}P\{^1H\}$ NMR spectrum of this complex features only one resonance which is located at δ = 43.1 ppm (Figure S7).

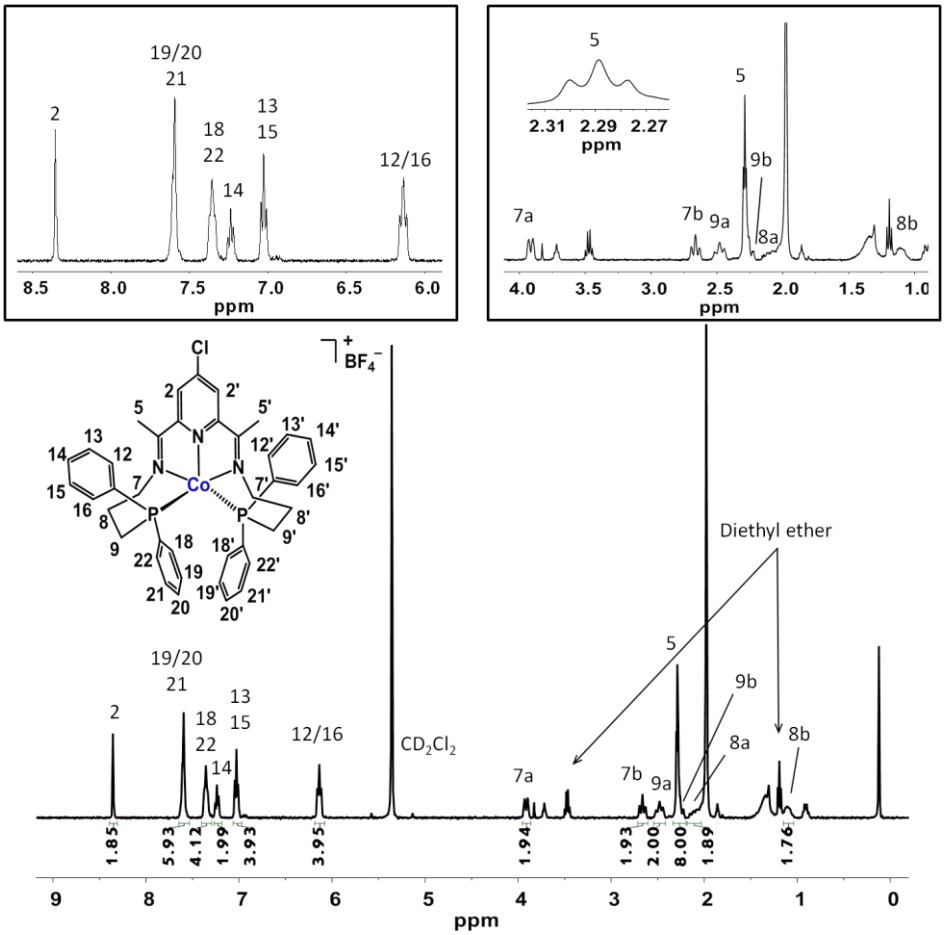

Figure 4.6 ^{1}H NMR spectra of **4**(BF_4) (400 MHz, CD_2Cl_2, 300 K). Zooms of aromatic and aliphatic methylenic regions are shown at top left and top right, respectively.

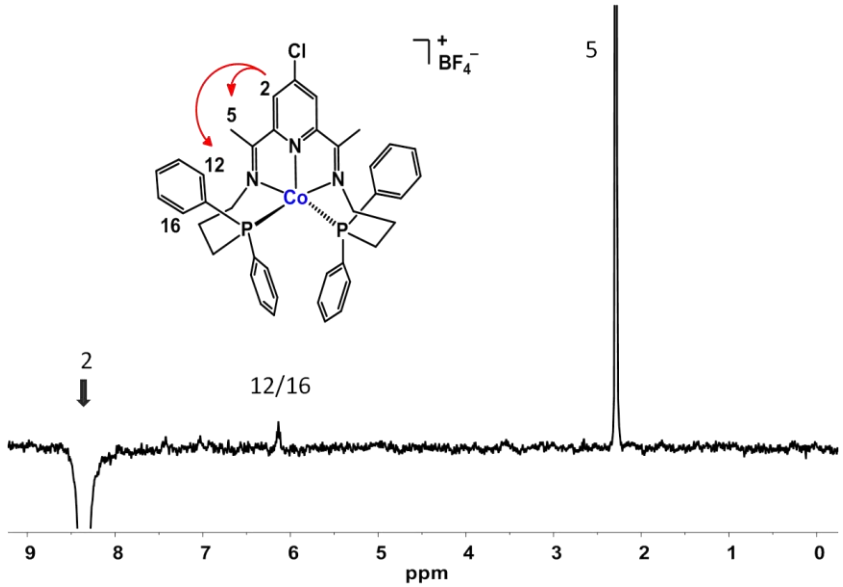

Figure 4.7 Selective 1D NOESY NMR spectra (500 MHz, CD_2Cl_2, 298 K) of **4**(BF_4) and drawing of observed interactions between H2 and H5, and H12/H16.

The redox properties of **4**(BF_4) were assessed by cyclic voltammetry in 0.1 M nBu_4NPF_6 DMF solution. As shown in Figure 4.8, a quasi-reversible transition tentatively assigned to $Co^{III/I}$ is observed at $E_{1/2} = -0.18$ V ($\Delta E_p = 0.14$ V) vs. Fc^+/Fc and a second quasi-reversible reduction is centered at $E_{1/2} = -1.87$ V ($\Delta E_p = 0.11$ V). Though these processes have not been examined by UV-vis monitoring or NMR spectroscopy like was the case for **3**(BF_4), given the measured similar structural and electrochemical data obtained, we tentatively propose analogous redox processes for this complex. Due to the addition of the electron-withdrawing Cl group at the 4-position of the pyridinic group of the ^{Ph2PPr}PDI(*p*)Cl scaffold, the two redox processes are anodically shifted (0.05 V and 0.15 V, respectively) with regards to those observed for the parent unsubstituted complex **3**(BF_4) (Figure 4.4).

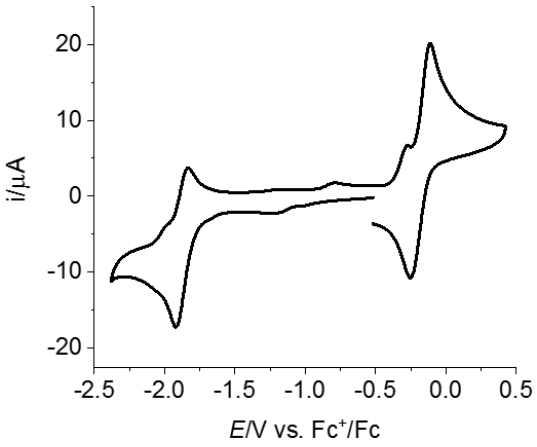

Figure 4.8 Cyclic voltammogram of **4**(BF_4) in DMF (0.1 M nBu_4NPF_6), scan rate = 100 mV/s.

4.2.2 Hydrogen evolution reaction: catalytic performance and mechanistic analysis

4.2.2.1 Reaction of 3(BF_4) with *p*-Toluenesulfonic acid (*p*-TsOH)

As shown in the cyclic voltammograms of Figure 4.9a, when *p*-TsOH (pK_a = 2.6 in DMF)[18] is added as proton source to a DMF solution of **3**(BF_4), a sharp current increase is observed with a half-wave potential of −1.91 V vs. Fc^+/Fc, which can be tentatively assigned to the electrocatalytic hydrogen evolution reaction. The observed onset potential is more positive than the assigned $L^{0/-}$ couple. Thus, a plausible scenario is the formation of the corresponding Co^{III}-H hydride species from initial Co(I) complex, which would then act as the active species in the HER. As anticipated, the addition of *p*-TsOH to a DMF solution of **4**(BF_4) also triggers the appearance of a catalytic wave whose onset potential is significantly more anodic than the quasi-reversible potential corresponding to the formation of the monoanionic species (Figure 4.9b). Furthermore, the catalytic half-wave potential at −1.81 V in case of **4**(BF_4) is 100 mV more positive than that of **3**(BF_4) due to the substitution of electron-withdrawing Cl in PDI ligand, which is in good agreement with what was found in the previous Chapter 3. Considering the similarity of **3**(BF_4) and **4**(BF_4) in structure and electrocatalytic performance as revealed by various techniques (X-ray crystallography, NMR and CV for instance), we propose an identical mechanism

for the HER reaction catalyzed by these two complexes. Therefore, the investigation for reaction pathways was conducted based on one of them, **3**(BF_4), in the following sections.

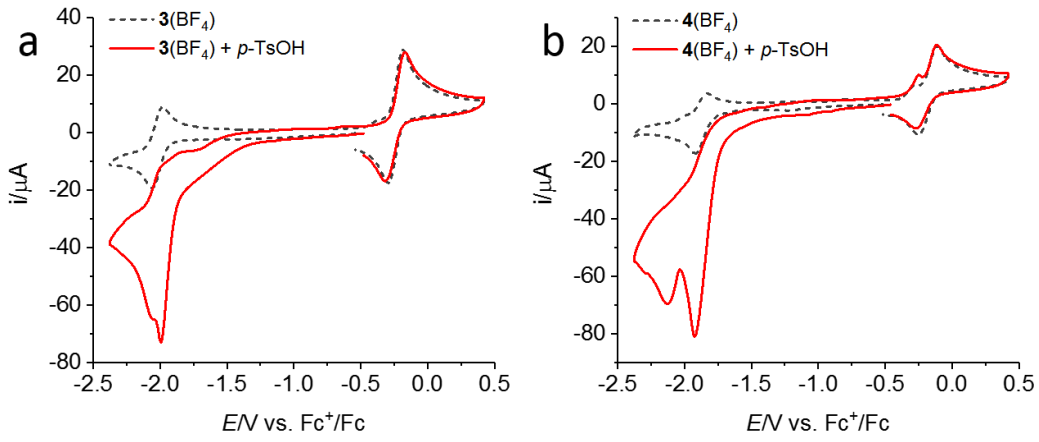

Figure 4.9 (a) Cyclic voltammograms of 1 mM **3**(BF_4) in 0.1 M nBu_4NPF_6 DMF in the absence (grey dashed line) and presence (red solid line) of 5 mM *p*-TsOH. (b) Cyclic voltammograms of 1 mM **4**(BF_4) in 0.1 M nBu_4NPF_6 DMF in the absence (grey dashed line) and presence (red solid line) of 5 mM *p*-TsOH. Scan rate = 100 mV/s.

The reaction of **3**(BF_4) with *p*-TsOH was first monitored by UV-vis in DMF under N_2 and the set of electronic spectra is shown in Figure 4.10. With the *p*-TsOH addition, the band at 424 nm and the broad bands at 482–600 nm and 600–800 nm decreased gradually while a new band at 365 nm appears. The process is slow and proceeds with isosbestic points at 345 nm and 392 nm, which indicate a clean transformation between the initial and final species (Inset of Figure 4.10). If this experiment is performed in acetonitrile, the same changes are observed (see Figure S21).

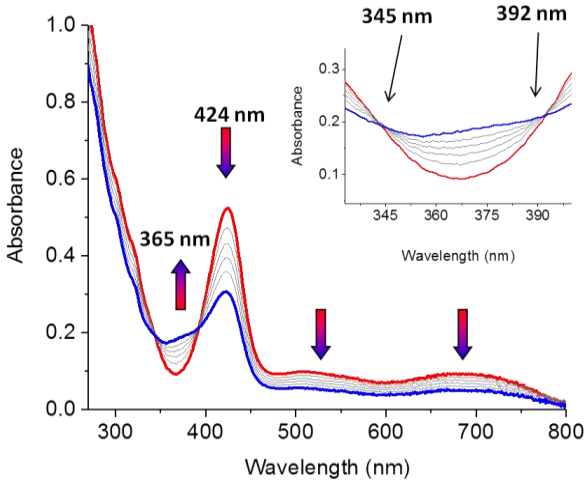

Figure 4.10 Effect of addition of 250 eq. of *p*-TsOH on the UV–visible spectrum of **3**(BF_4) in DMF under nitrogen during 130 min. Arrows indicate changes in intensity upon adding acid. Inset: zoom of the isosbestic points formed.

In addition to UV-vis, NMR experiments were performed in CD_3CN in the presence of 25 equivalents of *p*-TsOH to investigate the formation of new species. The ^1H NMR spectrum showed the gradual growing of a triplet at –9.43 ppm (with $J_{H\text{-}P}$ = 57 Hz) upon the addition of the acid, indicating that a putative Co^{III}-H (named $\mathbf{5}^{2+}$ for the cationic part) is generated in the presence of *p*-TsOH (see Figure 4.11). Consistent with the UV-vis experiments discussed above, the NMR analysis confirms the slow formation of the Co^{III}-H species $\mathbf{5}^{2+}$ in the employed conditions, with only partial conversion of the initial Co(I) complex, **3**(BF_4). Careful inspection on the aryl region of the intricate spectrum revealed eight new generated resonances (marked with asterisks in Figure 4.11), which coincides with the number of resonances of the parent complex **3**(BF_4). The $^{31}P\{^1H\}$ NMR spectrum displays two peaks at δ –45.55 and –38.87 ppm corresponding to a mixture of two cobalt complexes, that are, Co^I **3**(BF_4) and Co^{III}-H $\mathbf{5}^{2+}$ species, respectively (Figure S12). Taking all the information into account, $\mathbf{5}^{2+}$ was tentatively proposed to be structurally symmetrical with a κ^5-*N*,*N*,*N*,*P*,*P*-PDI coordination, and the unequivocal assignment will be shown in the following subsection. Keeping the mixture for several days under the employed acidic conditions resulted in an almost colorless solution, suggesting the decomposition of the complex in the acid solution over time. Recording the ^1H NMR of this colorless solution confirmed the loss of corresponding resonances to

both **3**(BF_4) and $\mathbf{5}^{2+}$ (Figure S13). The same conclusion can be reached when observing the lack of bands in the visible region of the electronic spectrum of the complex in acidic media at long reaction times (Figure S22).

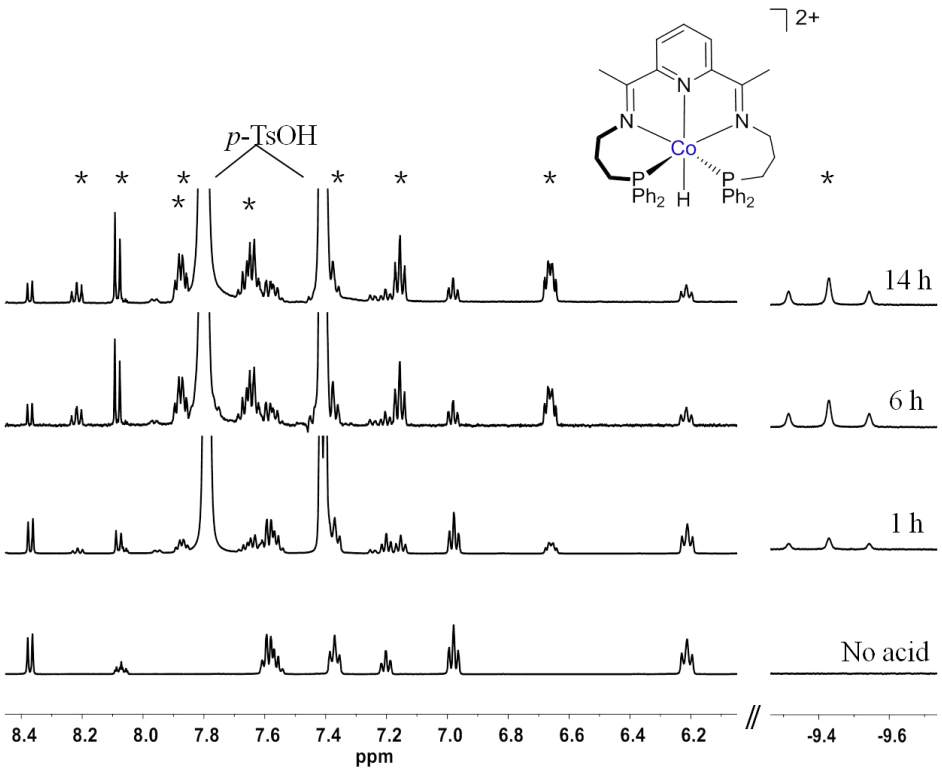

Figure 4.11 ^{1}H NMR spectra (500 MHz, CD_3CN, 300K) of **3**(BF_4) (bottom line) and *in situ* generation of the corresponding Co^{III}-H ($\mathbf{5}^{2+}$) derivative upon the addition of 25 eq. *p*-TsOH in CD_3CN, after 1 h, 6 h (middle lines) and 14 h (top line), presenting the aromatic region resonances and amplified triplet corresponding to the formed hydride at –9.43 ppm, asterisk indicates new generated signals. The drawing of the formed Co^{III}-H ($\mathbf{5}^{2+}$) species is shown above the NMR spectra.

4.2.2.2 Reaction of 3(BF_4) with trifluoromethanesulfonimide (TFSI)

The reaction of **3**(BF_4) with *p*-TsOH to give the Co^{III}-H $\mathbf{5}^{2+}$ was so slow that full conversion was not reached in a reasonable timescale and the two complexes finally decomposed under the acidic reaction conditions (see Section 4.2.2.1 above). Moreover, the decomposition process hindered the elucidation of the mechanism that leads to the catalytic evolution of molecular hydrogen in these conditions. Therefore, at this point, it

was necessary to seek for other conditions able to completely transform the Co(I) complex **3**(BF_4) to the corresponding Co^{III}-H species $\mathbf{5}^{2+}$ at a practical rate. Among the stronger acids available, trifluoromethanesulfonimide (TFSI, pK_a = –11.9 in 1,2-dichloroethane (DCE))[19] was chosen. Thus, **3**(BF_4) was dissolved in MeCN and its evolution during the addition of 10 equivalents of TFSI was monitored by UV-vis spectroscopy. The absorption monitoring showed the fading of the band at 432 nm and the two broad bands at 482–600 nm and 600–800 nm. The absorption spectrum of the final pale orange solution exhibits two transitions at 297 nm and 379 nm with ε ~ 10000 and 5000 $M^{-1}cm^{-1}$, respectively (blue line in Figure 4.12).

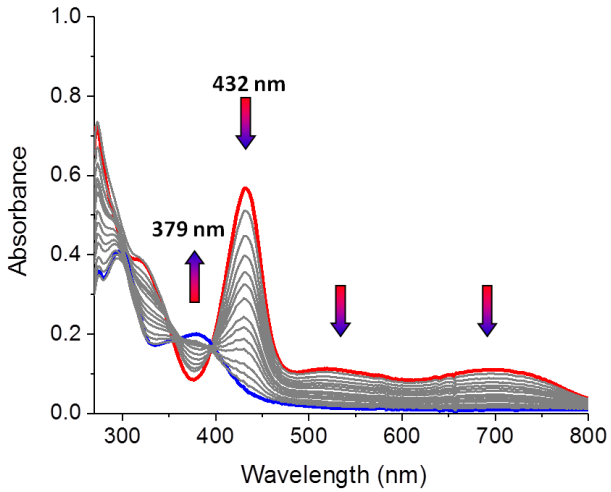

Figure 4.12 UV-vis monitoring of the addition of 10 eq. of TFSI to a MeCN solution of **3**(BF_4) (red line), forming the corresponding Co^{III}-H species $\mathbf{5}^{2+}$ (blue line).

As in the case of *p*-TsOH shown in the previous section, the addition of TFSI to **3**(BF_4) was also monitored by ^{1}H NMR. The addition of excess of acid to a CD_3CN solution of **3**(BF_4) led to an immediate color change from dark brown-green to orange, so the fast reaction rate made impossible to record the evolution of NMR over time like in Figure 4.12, due to the relatively slow nature of the technique. However, $\mathbf{5}^{2+}$ was obtained pure and the full assignment of this compound (see Figure 4.13) was achieved by the combination of 1D and 2D (COSY, HSQC, HMBC) spectra (see Figures S15–S17). $\mathbf{5}^{2+}$ displays *C*2 symmetry in solution as well, with H1, the N of the pyridine ring, the central Co ion and the generated hydride H23 situated in the axis of symmetry. A triplet at

δ −9.45 ppm ($J_{H\text{-}P}$ = 57.2 Hz) was observed in the ^{1}H NMR spectrum of the reaction mixture, supporting the formation of a Co^{III}-H species (Figure 4.13, inset). A ddt resonance and doublets integrating to 1H and 2H were located at 8.22 ppm and 8.08 ppm, corresponding to *p*-pyridine H1 and *m*-pyridine protons H2/H2', respectively. Other resonances integrating to 20H between 7.90 and 7.60 ppm were assigned to the PPh_2 moieties.

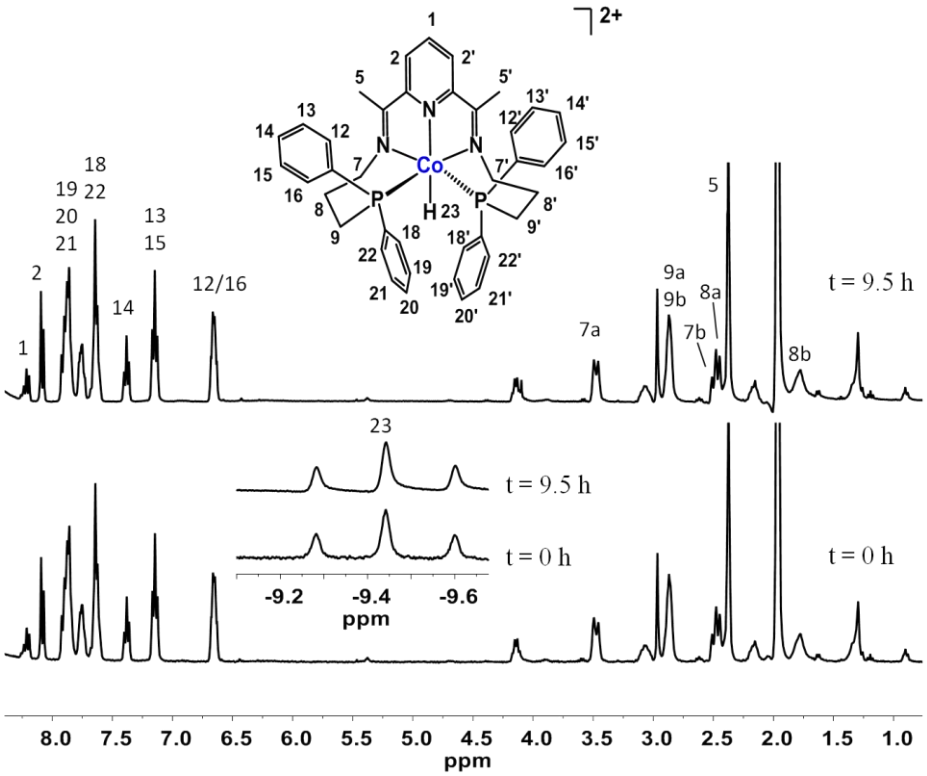

Figure 4.13 ^{1}H NMR spectra of Co^{III}-H **5**$^{2+}$ (360 MHz, CD_3CN, 296K). (Bottom) recorded immediately after excess TFSI was added to Co(I) complex **3**(BF_4), (top) recorded after 9.5 h.

Considering that M-hydride species are the gate to hydrogen evolution catalysis, the stability and reactivity under the employed acidic conditions of the newly generated Co^{III}-H species was monitored by ^{1}H NMR in order to elucidate the pathways through which this species is able to electrocatalytically evolve dihydrogen. The potential pathways through which molecular hydrogen can be generated from the Co^{III}-H derivative are indicated in Scheme 4.4. Thus, the formation of derivative species such as the Co(III)

or paramagnetic Co(II) should be considered. During a time scale of 9.5 h, the Co^{III}-H $\mathbf{5}^{2+}$ produced from the Co(I) complex $\mathbf{3}(BF_4)$ and excess TFSI did not decay to form Co(III) or Co(II) and remains stable in solution under dry and inert conditions (Figure 4.13), highlighting the high stability of this complex. This result also allows us to rule out the possible mechanistic pathways A and B in Scheme 4.4, left.

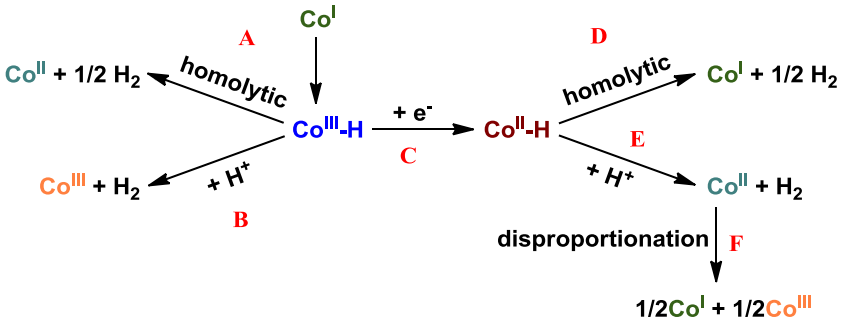

Scheme 4.4 Possible mechanistic hydrogen evolution pathways catalyzed by a Co(I) complex.

4

In order to assess paths D, E and F in Scheme 4.4, the reduction of Co^{III}-H species to yield Co^{II}-H was initially studied by adding 1 equivalent of decamethyl-cobaltocene ($CoCp^*_2$, –1.91 V vs. Fc^+/Fc in MeCN)[20] as reducing agent to a mixture of $\mathbf{3}(BF_4)$ in the presence of excess TFSI (Figure 4.14). As shown in Figure 4.14a, the addition of $CoCp^*_2$ did not make any changes neither in the hydride nor in the aryl resonances attributable to hydride species $\mathbf{5}^{2+}$. We attribute this phenomenon to the excess acid (TFSI) present in the reaction mixture, which consumes all the available $CoCp^*_2$ before reacting with the Co^{III}-H species. We proved this speculation by adding an increasing amount of solid $CoCp^*_2$ to acidic (TFSI) CD_3CN solutions in NMR tubes containing (Figure 4.14a) and not containing (Figure 4.14b) the Co^{III}-H species $\mathbf{5}^{2+}$. In both cases, gas bubbles (attributed to H_2) evolved immediately around the solid $CoCp^*_2$ with a concomitant weakening of the acid proton signal with increasing dose of $CoCp^*_2$ (Figure 4.14a, inset). In CD_3CN as solvent and in the absence of Co species a single resonance at 11.96 ppm corresponding to the acidic proton of TFSI is initially observed (Figure 4.14b). The addition of $CoCp^*_2$ provokes the displacement of this resonance to higher fields (11.91 ppm) together with a clear decrease of its integral. This peak change proved that $CoCp^*_2$ indeed react with TFSI

and that the consumption of the former in excess acid hampers the reduction of the Co^{III}-H species in the experiments described above.

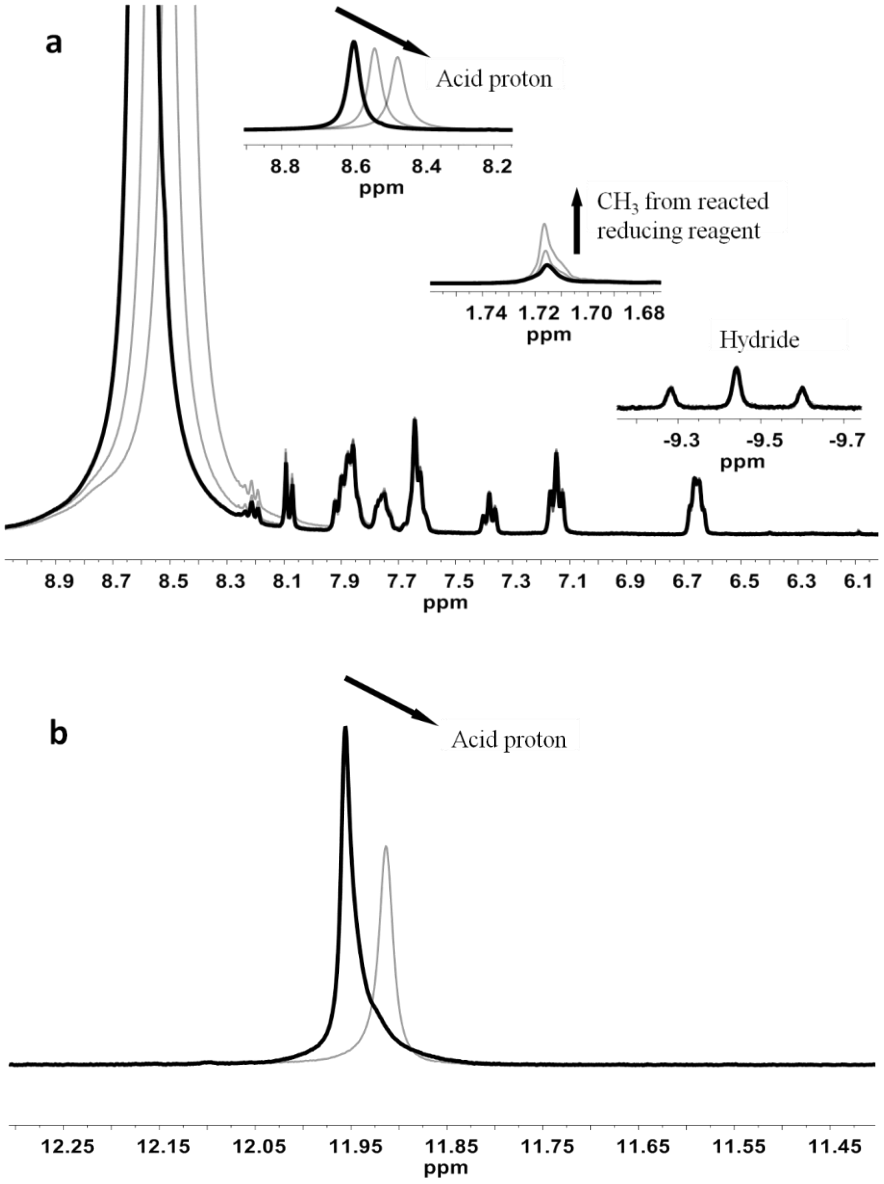

Figure 4.14 (a) Zoomed aromatic region of the ^{1}H NMR spectra (360 MHz, CD_3CN, 296K) of Co^{III}-H without $CoCp^*_2$ (black thick line) and with increasing amount of $CoCp^*_2$ (gray thin lines). Inset, ^{1}H NMR resonances of acid proton, methyl group from oxidized $CoCp^*_2$, and ydride, respectively. (b) ^{1}H NMR spectra (400 MHz, CD_3CN, 300K) of TFSI before (black thick line) and after (gray thin line) the addition of $CoCp^*_2$.

For the purpose of eliminating the side reaction of $CoCp^*_2$ with excess TFSI, a new experiment adding 1 equivalent of TFSI to a dry CD_3CN solution of the Co(I) complex **3**(BF_4) was designed. The ^1H NMR spectrum in Figure 4.15 shows the complete transformation of Co^I to Co^{III}-H after adding 1 eq. of acid. In the same line, the $^{31}P\{^1H\}$ NMR in Figure 4.16 shows how the peak at 42.4 ppm from the initial Co(I) species disappears and two new peaks appear at 35.8 and 8.2 ppm (top line). The integration of these two peaks gave a ratio number of 1 : 0.08, suggesting that the smaller peak may come from an impurity or minor isomer. The strict dryness of the used solvent is essential as traces of water lead to uncomplete Co^{III}-H formation.

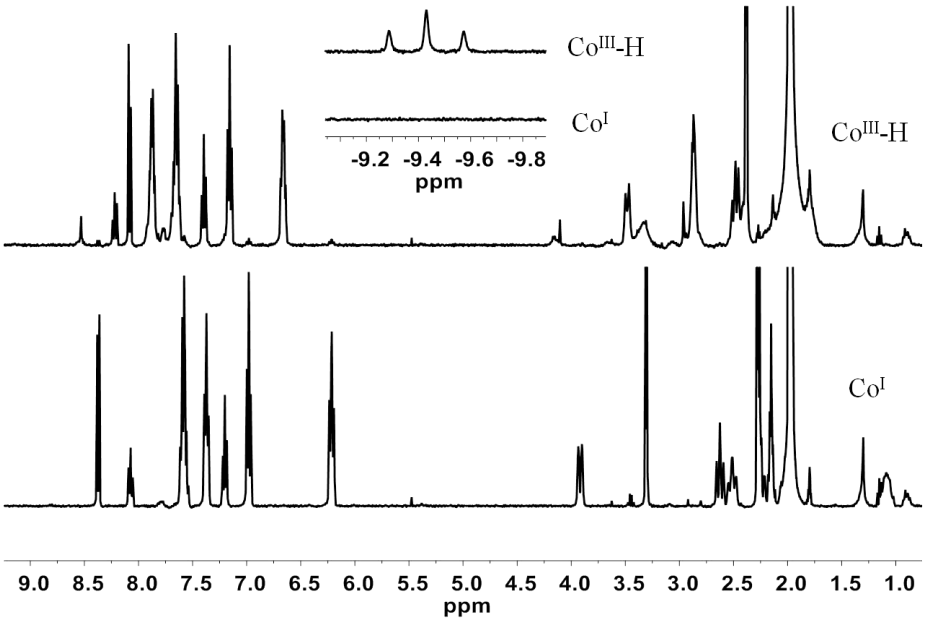

Figure 4.15 ^1H NMR spectra (400 MHz, CD_3CN, 300K) of the Co(I) complex **3**(BF_4) (bottom) and the Co^{III}-H species $\mathbf{5}^{2+}$ (top) generated after adding 1 eq. of TFSI to **3**(BF_4).

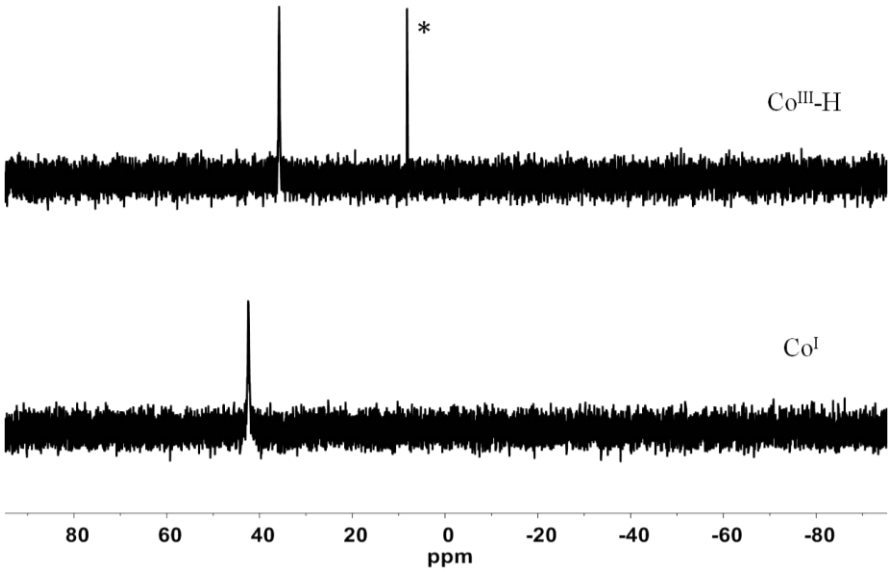

Figure 4.16 $^{31}P\{^{1}H\}$ NMR spectra (162 MHz, CD_3CN, 300K) of the Co(I) complex **3**(BF_4) (bottom) and the Co^{III}-H species (top) generated after adding 1 eq. of TFSI to **3**(BF_4), the asterisk indicates unidentified species.

Following the well stablished protocol for obtaining the desired Co^{III}-H species, 1 eq. of $CoCp^*_2$ was added to their CD_3CN solution in an NMR tube in three batches. As shown in Figure 4.17, the signals of Co^{III}-H in the ^{1}H NMR spectra gradually disappear with the addition of $CoCp^*_2$ what is concomitant with the growing of new resonances, confirming that the Co^{III}-H derivative is converted to new species after reacting with the reducing agent. A close examination and comparison of the new spectrum shows that it is exactly the same as that of the parent Co(I) complex **3**(BF_4) (Figure 4.18). The same conclusion can also be extracted from the $^{31}P\{^{1}H\}$ NMR spectrum, where the minor peak of integration at 8.2 ppm disappeared completely upon adding the first batch of 0.3 eq. of $CoCp^*_2$, and the peak at 35.8 ppm from Co^{III}-H decreases and the characteristic peak at 42.4 ppm from **3**(BF_4) raises (Figure 4.19). As displayed in Figure S17, the produced species gave the same peak at 42.4 ppm as the initial Co(I) complex, certifying the recovery of Co(I).

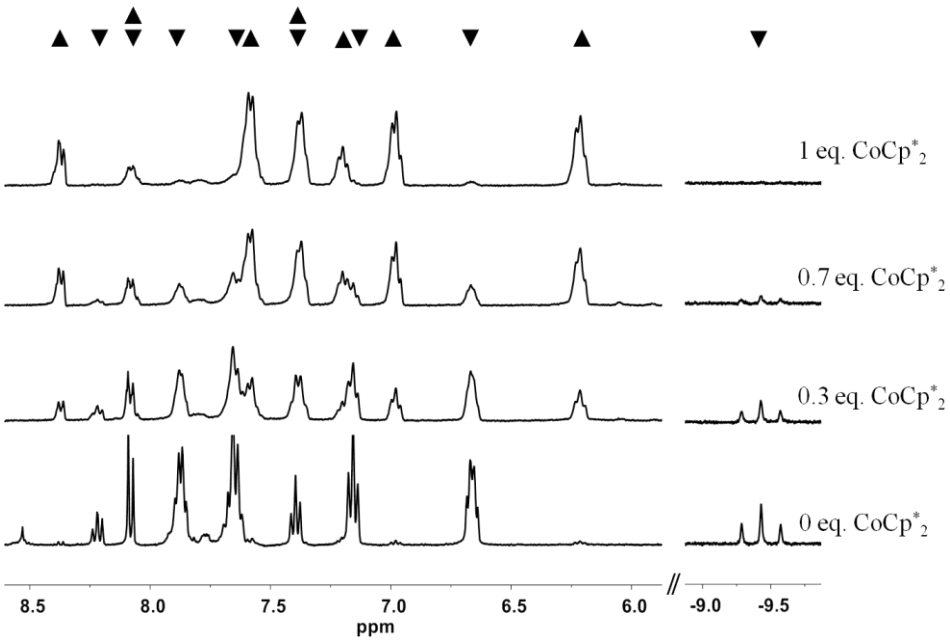

Figure 4.17 Zoomed aromatic and hydride regions of the ^{1}H NMR spectra (400 MHz, CD_3CN, 300K) of Co^{III}-H species $\mathbf{5}^{2+}$ before (bottom line) and after adding overall 0.3 eq., 0.7 eq. (two middle lines) and 1 eq. of $CoCp^{*}_2$ (topmost line). ▼ indicates peaks decreasing in intensity from Co^{III}-H, ▲ indicates growing peaks from new species.

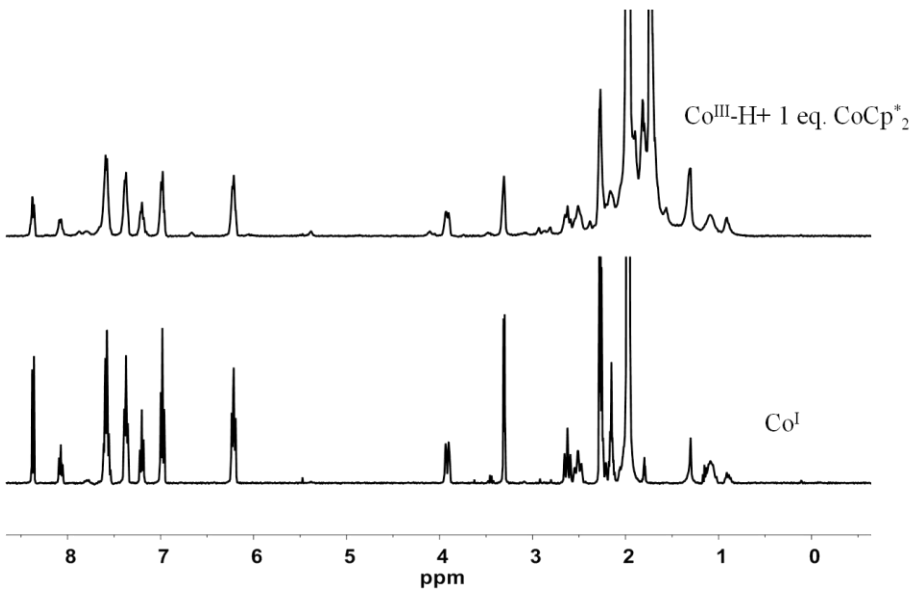

Figure 4.18 ^{1}H NMR spectra (400 MHz, CD_3CN, 300K) of the Co(I) complex **3**(BF_4) (bottom line) and the species formed by reacting the Co^{III}-H species $\mathbf{5}^{2+}$ with 1eq. of $CoCp^*_2$ (top line).

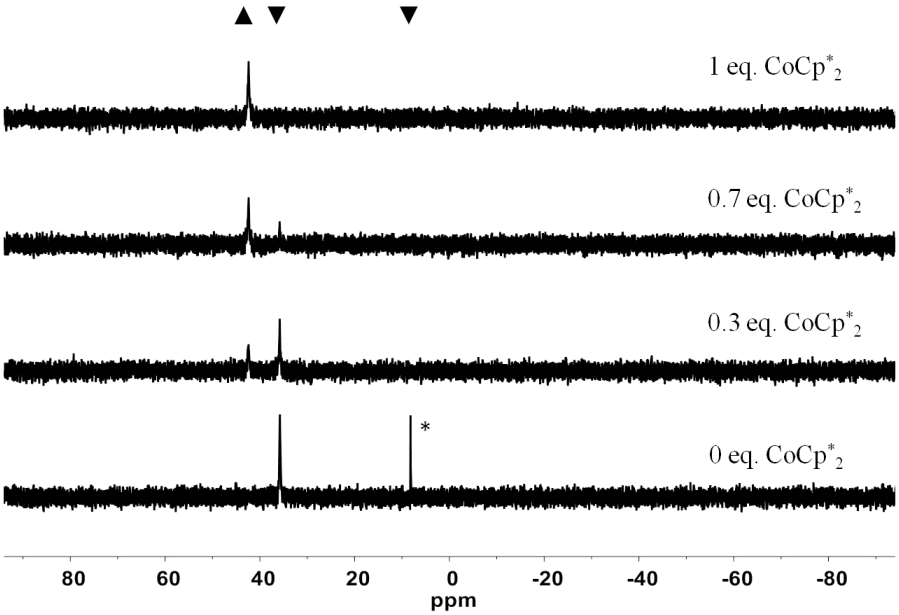

Figure 4.19 $^{31}P\{^{1}H\}$ NMR spectra (162 MHz, CD_3CN, 300 K) of Co^{III}-H species $\mathbf{5}^{2+}$ (bottom) after adding < 1eq. of $CoCp^*_2$ (two middle lines), and adding 1eq. of $CoCp^*_2$ (top). The asterisk indicates unidentified species. ▼ indicates peaks decreasing in intensity from Co^{III}-H, ▲ indicates growing peaks from new species.

In summary, the catalytic pathway towards the formation of molecular hydrogen from organic acids catalyzed by the Co(I) complex **3**(BF_4) is displayed in Scheme 4.5. It starts with the generation of the key Co^{III}-H hydride intermediate from the initial Co(I) compound. This species is very stable and needs a further $1e^-$ reduction to form the corresponding Co^{II}-H species, which is very reactive and releases H_2 through a homolytic pathway. Further experiments are necessary to experimentally detecting the evolved hydrogen gas.

Scheme 4.5 Experimentally proved mechanism for proton reduction by the Co(I) complex **3**(BF_4).

4.3 Conclusions

In this study we synthesized two new Co(I) complexes, **3**(BF_4) and **4**(BF_4) through the reaction of the pentadentate ligands ^{Ph2PPr}PDI and ^{Ph2PPr}PDI(*p*)Cl with a Co precursor, $Co(BF_4)_2{\cdot}6H_2O$, which were characterized by means of X-ray diffraction, NMR, MS, and CV. Both complexes adopt pseudo trigonal-bipyramidal geometry in the solid state as revealed by X-ray diffraction analysis, with C_2 symmetry in solution revealed by NMR analysis. Each complex exhibited two redox couples in CV that have been tentatively assigned to $Co^{III/I}$ and $\mathbf{L}^{0/-}$, according to literature data and taking into account their different integrated charge and redox potentials. The introduction of the electro-withdrawing Cl substituent in **4**(BF_4) shifts the two redox couples to more anodic potentials relative to **3**(BF_4). Both complexes were preliminarily tested by CV as electrocatalysts for the HER in DMF solution in the presence of *p*-TsOH giving catalytic waves whose onset potential are more positive than $L^{0/-}$ couple during cathodic scanning. UV-vis spectroscopy monitoring for **3**(BF_4) in the presence of *p*-TsOH shows the generation of a new species from **3**(BF_4) without need of applying a redox potential. NMR spectroscopy allowed identifying the new species as a Co^{III}-H hydride $\mathbf{5}^{2+}$, which is partially and slowly generated from **3**(BF_4) under the tested conditions. However, this reaction was considerably accelerated by utilizing the stronger acid TFSI, thus allowing complete conversion to Co^{III}-H $\mathbf{5}^{2+}$, which is a key intermediate that we use to perform hydrogen evolution mechanistic studies. Long time NMR monitoring of $\mathbf{5}^{2+}$ in the presence of excess TFSI proved the stability of this hydride species, excluding the possibility of direct hydrogen production from Co^{III}-H. Attempt to reduce $\mathbf{5}^{2+}$ by adding $CoCp^*_2$ to the acidic solution of $\mathbf{5}^{2+}$ with excess TFSI uncovered the side reaction of $CoCp^*_2$ with TFSI. Thus, adding strictly 1 eq. of TFSI was a requisite to generate $\mathbf{5}^{2+}$ in dry CD_3CN for further reduction. The addition of overall 1 eq. of $CoCp^*_2$ to $\mathbf{5}^{2+}$ for performing one-electron reduction of Co^{III}-H hydride finally yield the initial Co(I) complex **3**(BF_4), which is demonstrated by both ^{1}H NMR and ^{31}P{^{1}H} NMR. These results prove that the reduced Co^{II}-H species is able to evolve dihydrogen through a homolytic pathway.

4.4 Experimental section

Materials

$Co(BF_4)_2 \cdot 6H_2O$ and *p*-toluenesulfonic acid (*p*-TsOH) were used as received, trifluoromethanesulfonimide (TFSI) was kept and manipulated in the glove box to prevent the reaction with water traces. Organic solvents were dried following the standard procedures and distilled prior to use. The ligands **L2** and **L3** were obtained as described in Chapter 3. All synthetic reactions, NMR sample preparation and electrochemical studies were performed under an inert atmosphere inside a glovebox or by Schlenk and vacuum line techniques.

Physical measurements and instrumentation

UV-vis spectra were recorded by an Agilent/HP 8453 spectrophotometer or a Varian Cary 50 Bio UV-Visible spectrophotometer operating in a 1 cm pathlength rectangular quartz cuvette. NMR spectroscopy was carried out by a Bruker Avance DPX 360 MHz, Bruker Avance III 400 MHz or Bruker Avance 500 MHz NMR spectrometer in deuterated solvent DCM-d_2 or CD_3CN. All the measurements for the mechanistic studies were recorded by using J. Young NMR tube to avoid oxygen penetrating in. Elemental analyses were performed by a Thermo Scientific Flash 2000 CHNS Analyzer from the Servei d'Anàlisi Química of the Universitat Autònoma de Barcelona (SAQ-UAB). Electrospray ionization mass spectra (ESI/MS) were obtained on the MicroTOF mass spectrometer that was coupled with a Cryospray source (Bruker Daltonics) in Institut Català d'Investigació Química (ICIQ). All cyclic voltammetry measurements were recorded using a BioLogic SP-150 potentiostat which was connected to a glassy carbon working electrode (ca. 0.07 cm^2), a platinum mesh auxiliary electrode and an $Ag/AgNO_3$ (0.1 M in acetonitrile) reference electrode. Ferrocene was used as internal standard and all the potentials were converted to Fc^+/Fc by subtracting 0.078 V from $Ag/AgNO_3$ potential. The working electrode was polished with aqueous alumina slurry, then cleaned by sonicating for 5 min and washing with distilled water and acetone before use. DMF was used for the preparation of catalyst solution with 0.1 M nBu_4NPF_6 as supporting electrolyte.

Synthesis of complexes

[Co(^{Ph2PPr}PDI)](BF$_4$) (**3**(BF$_4$)): A 5 mL THF solution of Co(BF$_4$)$_2$·6H$_2$O (83 mg, 0.24 mmol) was slowly added to a 4 mL THF solution of **L2** (150 mg, 0.24 mmol), the initial pale yellow solution turned to brown immediately and darker in color with the addition of Co(BF$_4$)$_2$·6H$_2$O. After stirring at room temperature for 1 day, the solvent was removed, then the residue was dissolved in the minimum amount of a MeOH/DCM mixture. Layering with pentane gave the complex as black crystals suitable for single crystal XRD analysis in 26% yield. ESI/MS: *m*/*z* = 672.0 [Co(^{Ph2PPr}PDI)]$^+$. Anal.Calc. for [Co(^{Ph2PPr}PDI)](BF$_4$) + CH$_2$Cl$_2$ ($C_{40}H_{43}Cl_2BCoF_4N_3P_2$): C, 56.90; H, 5.13; N, 4.98. Found: C, 57.29, H, 5.51, N, 4.90. ^{1}H NMR (400 MHz, CD$_2$Cl$_2$, 298 K) δ 8.31 (d, 2H, *J* = 7.8 Hz, H2), 8.08 (tt, 1H, *J* = 7.9, 2.5 Hz, H1), 7.55 (h, 6H, *J* = 5.5, 4.7 Hz, H19, H20, H21), 7.40 – 7.27 (m, 4H, H18, H22), 7.17 (td, 2H, *J* = 7.6, 1.6 Hz, H14), 7.00 – 6.90 (m, 4H, H13, H15), 6.13 (dd, 4H, *J* = 9.9, 7.4 Hz, H12, H16), 3.92 – 3.79 (m, 2H, H7a), 2.60 (tt, 2H, *J* = 12.8, 2.4 Hz, H7b), 2.51 – 2.35 (m, 2H, H9a), 2.30 – 2.17 (m, 8H, H5, H9b), 2.10 – 1.88 (m, 2H, H8a), 1.12 – 0.96 (m, 2H, H8b). ^{13}C{^{1}H} NMR (126 MHz, CD$_2$Cl$_2$, 298 K) δ 158.06 (C4), 146.58 (C3), 135.91 (C17), 133.28 (C11), 132.37 (C12,C16), 131.26 (C18, C22), 130.25 (C14), 130.00 (C20), 129.35 (C19, C21), 128.39 (C13,C15), 123.73 (C1), 120.18 (C2), 53.65 (C7), 26.52 (C8), 25.47 (C9), 15.02 (C5). ^{31}P{^{1}H} NMR (162 MHz, CD$_2$Cl$_2$, 298 K): δ 43.13 ppm.

[Co(^{Ph2PPr}PDI(*p*)Cl)](BF$_4$) (**4**(BF$_4$)): A 5 mL THF solution of Co(BF$_4$)$_2$·6H$_2$O (63 mg, 0.18 mmol) was added to a 4 mL THF solution of **L3** (120 mg, 0.18 mmol), the initial pale yellow solution turned to brown immediately and darker upon addition. After stirring at room temperature for 1 day, the solvent THF was removed, then the residue was dissolved in the minimum amount of a MeOH/DCM mixture. Layering with pentane gave the complex as black crystals suitable for single crystal XRD analysis in 18% yield. ESI/MS: *m*/*z* = 706.1 [Co(^{Ph2PPr}PDI)(*p*)Cl]$^+$. ^{1}H NMR (400 MHz, CD$_2$Cl$_2$, 300 K) δ 8.36 (s, 2H, H2), 7.64 – 7.53 (m, 6H, H19, H20, H21), 7.36 (t, 4H, J = 7.0 Hz, H18, H22), 7.24 (t, 2H, J = 7.5 Hz, H14), 7.03 (t, 4H, J = 7.7 Hz, H13, H15), 6.14 (t, 4H, J = 8.7 Hz, H12, H16), 3.91 (d, 2H, J = 13.1 Hz, H7a), 2.66 (t, 2H, J = 12.6 Hz, H7b), 2.48 (t, 2H, J = 14.7 Hz, H9a), 2.32 – 2.21 (m, 8H, 6.4 Hz, H5, H9b), 2.18 – 2.03 (m, 2H, H8a), 1.16 – 1.03 (br, 2H, H8b). ^{13}C{^{1}H} NMR (126 MHz, CD$_2$Cl$_2$, 298 K) δ 157.63 (C4), 146.27 (C3), 135.35 (C17), 132.93 (C11), 132.28 (C12,C16), 131.30 (C18,C22), 130.46 (C14), 130.23

(C20), 129.46 (C19,C21), 128.55 (C13,C15), 125.79 (C1), 123.51 (C2), 54.00 (C7), 26.45 (C8), 25.22 (C9), 15.11 (C5). $^{31}P\{^{1}H\}$ NMR (162 MHz, CD_2Cl_2, 300 K): δ 43.10 ppm.

$[HCo^{III}(^{Ph2PPr}PDI)]^{2+}$ ($\mathbf{5}^{2+}$): 2 mg of **3**(BF_4) was dissolved in 0.5 mL of dry CD_3CN in J. Young valve NMR tube, followed by addition of 0.74 mg of trifluoromethanesulfonimide (1 eq.) at room temperature. The solution color turned from initial dark brown-green to orange, and the generated product from the reaction was measured directly by NMR without isolation. ^{1}H NMR (360 MHz, CD_3CN, 296K) δ 8.21 (t, 1H, *J* = 8.1 Hz, H1), 8.08 (d, 2H, *J* = 8.0 Hz, H2), 7.91 – 7.84 (m, 6H, H19, H20, H21), 7.68 – 7.60 (m, 4H, H18, H22), 7.38 (t, 2H, *J* = 7.5 Hz, H14), 7.15 (t, 4H, *J* = 7.7 Hz, H13, H15), 6.65 (q, 4H, *J* = 6.1 Hz, H12, H16), 3.48 (d, 2H, *J* = 13.0 Hz, H7a), 2.91 – 2.82 (m, 4H, H9a, H9b), 2.55 – 2.40 (m, 4H, H7b, H8a), 1.86 – 1.70 (br, 2H, H8b), –9.44 (t, 1H, *J* = 57.3 Hz, H23). $^{13}C\{^{1}H\}$ NMR (126 MHz, CD_2Cl_2, 298 K) δ 154.02 (C3), 137.07 (C1), 133.58 (C20), 131.98 (C19,C21), 131.30 (C14), 130.76 (C12,C16), 129.82 (C18,C22), 129.21 (C13,C15), 128.19 (C17), 126.94 (C2), 123.86 (C11), 52.75 (C7), 24.78 (C9), 26.46 (C8), 16.03 (C5). $^{31}P\{^{1}H\}$ NMR (162 MHz, CD_3CN, 300 K): δ 35.78 ppm.

4.5 References

(1) McCrory, C. C. L.; Szymczak, N. K.; Peters, J. C. *Electrocatalysis* **2016**, *7*, 87–96.

(2) Armstrong, J. E.; Crossland, P. M.; Frank, M. A.; Van Dongen, M. J.; McNamara, W. R. *Dalt. Trans.* **2016**, *45*, 5430–5433.

(3) Artero, V.; Chavarot-Kerlidou, M.; Fontecave, M. *Angew. Chem Int. Ed.* **2011**, *50*, 7238–7266.

(4) Gimbert-Suriñach, C.; Albero, J.; Stoll, T.; Fortage, J.; Collomb, M. N.; Deronzier, A.; Palomares, E.; Llobet, A. *J. Am. Chem. Soc.* **2014**, *136*, 7655–7661.

(5) Marinescu, S. C.; Winkler, J. R.; Gray, H. B. *Proc. Natl. Acad. Sci. U. S. A.* **2012**, *109*, 15127–15131.

(6) Addison, A. W.; Rao, T. N.; Reedijk, J.; Van Rijn, J.; Verschoor, G. C. *J. Chem. Soc., Dalt. Trans.* **1984**, *0*, 1349–1356.

(7) Jacques, P.-A.; Artero, V.; Pécaut, J.; Fontecave, M. *Proc. Natl. Acad. Sci. U. S. A.* **2009**, *106*, 20627–20632.

(8) Sherbow, T. J.; Fettinger, J. C.; Berben, L. A. *Inorg. Chem.* **2017**, *56*, 8651–8660.

(9) Myers, T. W.; Sherbow, T. J.; Fettinger, J. C.; Berben, L. A. *Dalt. Trans.* **2016**, *45*, 5989–5998.

(10) Knijnenburg, Q.; Gambarotta, S.; Budzelaar, P. H. M. *Dalt. Trans.* **2006**, *0*, 5442.

(11) Mukhopadhyay, T. K.; MacLean, N. L.; Gan, L.; Ashley, D. C.; Groy, T. L.; Baik, M.-H.; Jones, A. K.; Trovitch, R. J. *Inorg. Chem.* **2015**, *54*, 4475–4482.

(12) Ben-Daat, H.; Hall, G. B.; Groy, T. L.; Trovitch, R. J. *Eur. J. Inorg. Chem.* **2013**, *2013*, 4430–4442.

(13) Poitras, A. M.; Bezpalko, M. W.; Foxman, B. M.; Thomas, C. M. *Dalt. Trans.* **2019**, *48*, 3074–3079.

(14) Varma, S.; Castillo, C. E.; Stoll, T.; Fortage, J.; Blackman, A. G.; Molton, F.; Deronzier, A.; Collomb, M.-N. *Phys. Chem. Chem. Phys.* **2013**, *15*, 17544–17552.

(15) Hu, X.; Brunschwig, B. S.; Peters, J. C. *J. Am. Chem. Soc.* **2007**, *129*, 8988–8998.

(16) Du, P.; Schneider, J.; Luo, G.; Brennessel, W. W.; Eisenberg, R. *Inorg. Chem.* **2009**, *48*, 4952–4962.

(17) Ibrahim, A. D.; Tokmic, K.; Brennan, M. R.; Kim, D.; Matson, E. M.; Nilges, M. J.; Bertke, J. A.; Fout, A. R. *Dalt. Trans.* **2016**, *45*, 9805–9811.

(18) Greg A. N. Felton; Richard S. Glass; Dennis L. Lichtenberger, A.; Evans, D. H. *Inorg. Chem.* **2006**, *45*, 9181–9184.

(19) Lee, C. H.; Dogutan, D. K.; Nocera, D. G. *J. Am. Chem. Soc.* **2011**, *133*, 8775–8777.

(20) Connelly, N. G.; Geiger, W. E. *Chem. Rev.* **1996**, *96*, 877–910.

4.6 Supporting information

A- NMR Spectroscopy

B- Mass Spectrometry

C- UV-vis Spectroscopy

D- X-ray diffraction data

A- NMR Spectroscopy

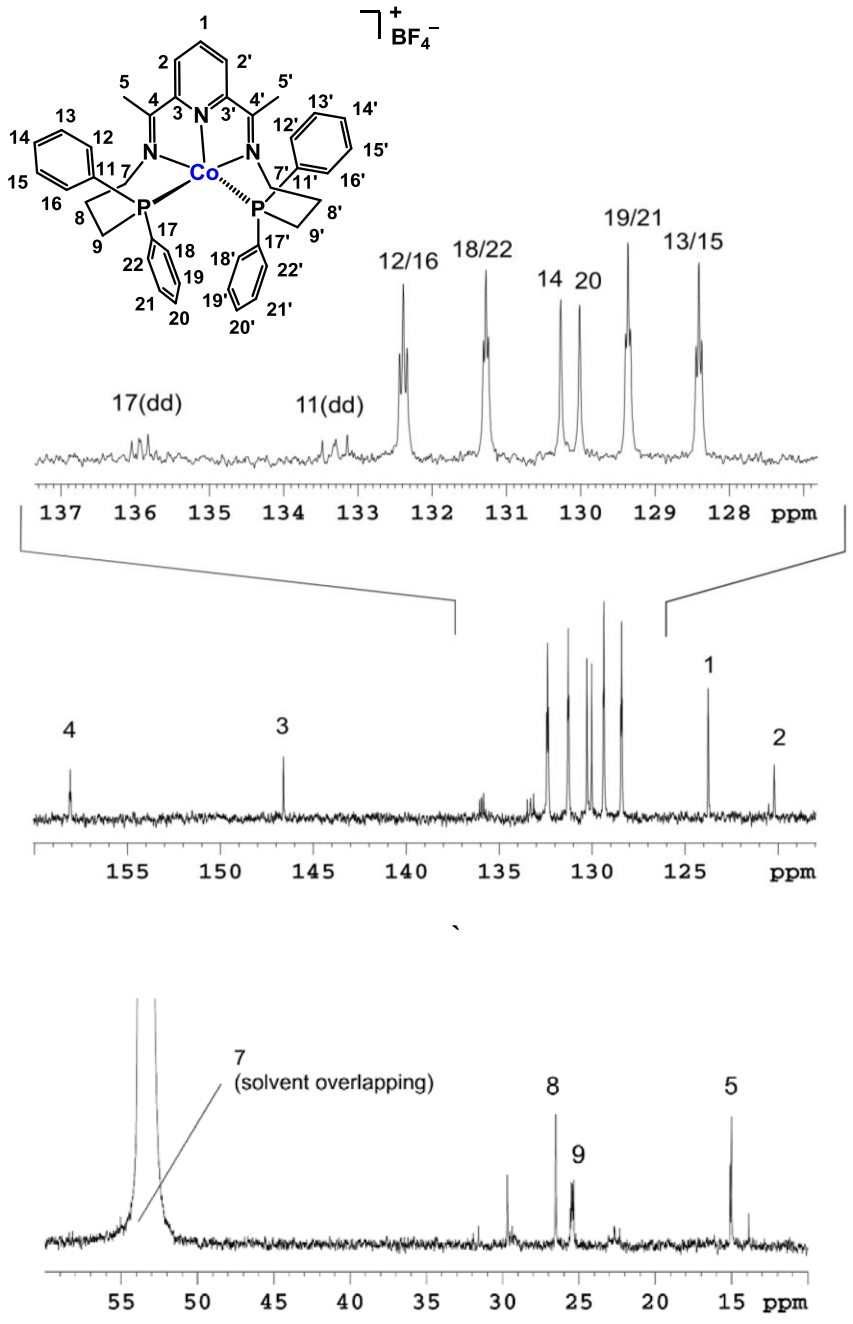

Figure S1. ^{13}C NMR spectrum of **3**(BF_4) (126 MHz, CD_2Cl_2, 298 K).

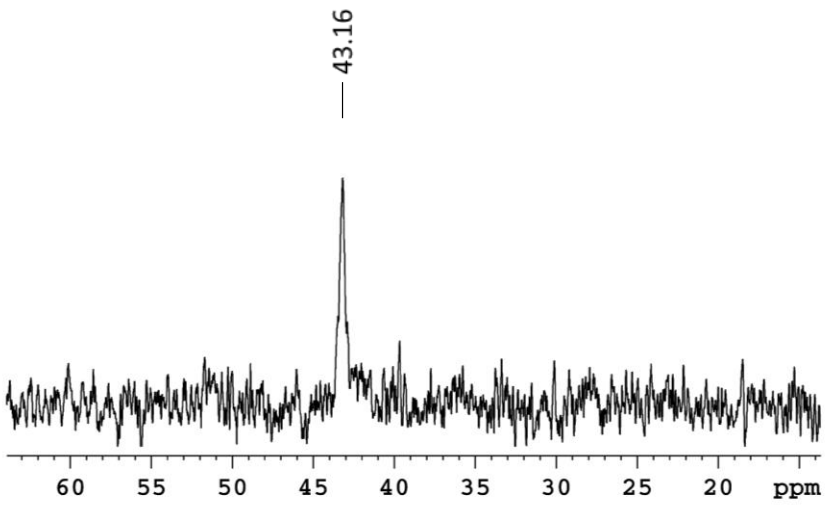

Figure S2. $^{31}P\{^{1}H\}$ NMR spectrum of **3**(BF_4) (162 MHz, CD_2Cl_2, 298 K).

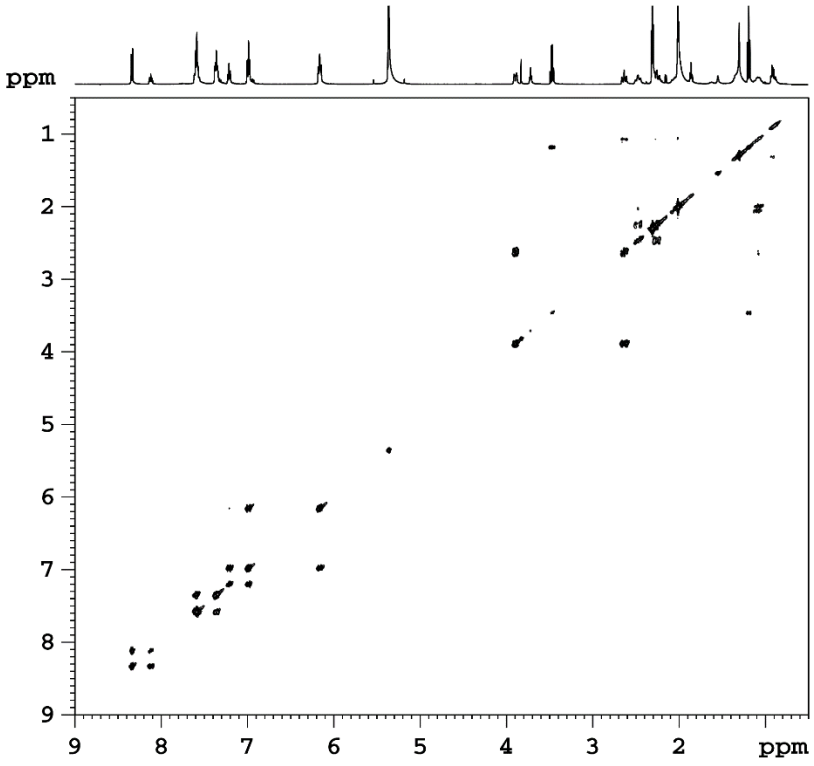

Figure S3. COSY spectra of **3**(BF_4) (500 MHz, CD_2Cl_2, 298 K).

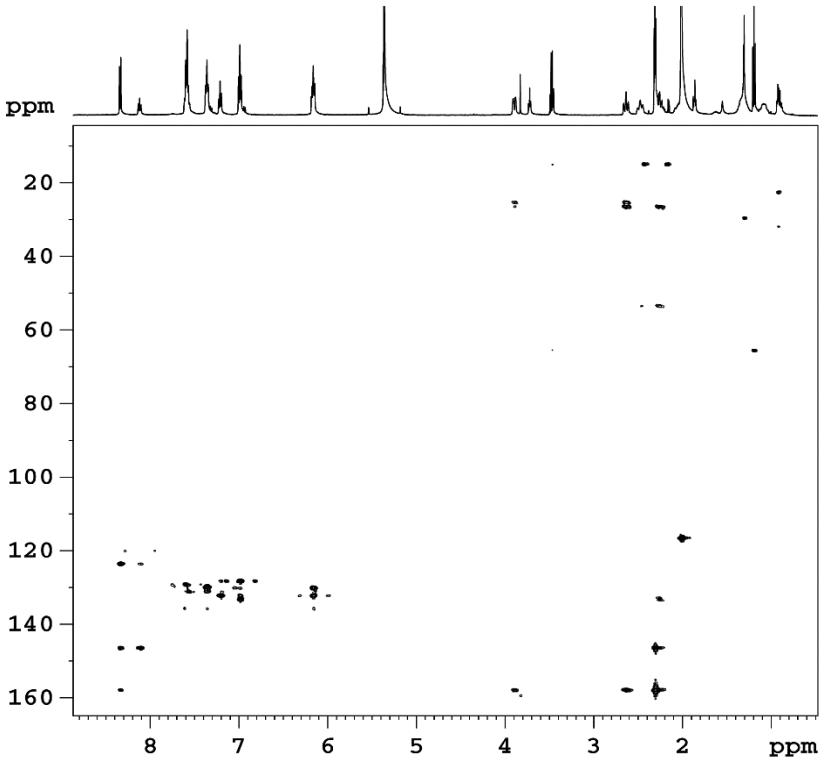

Figure S4. HMBC spectra of **3**(BF_4) (CD_2Cl_2, 298 K).

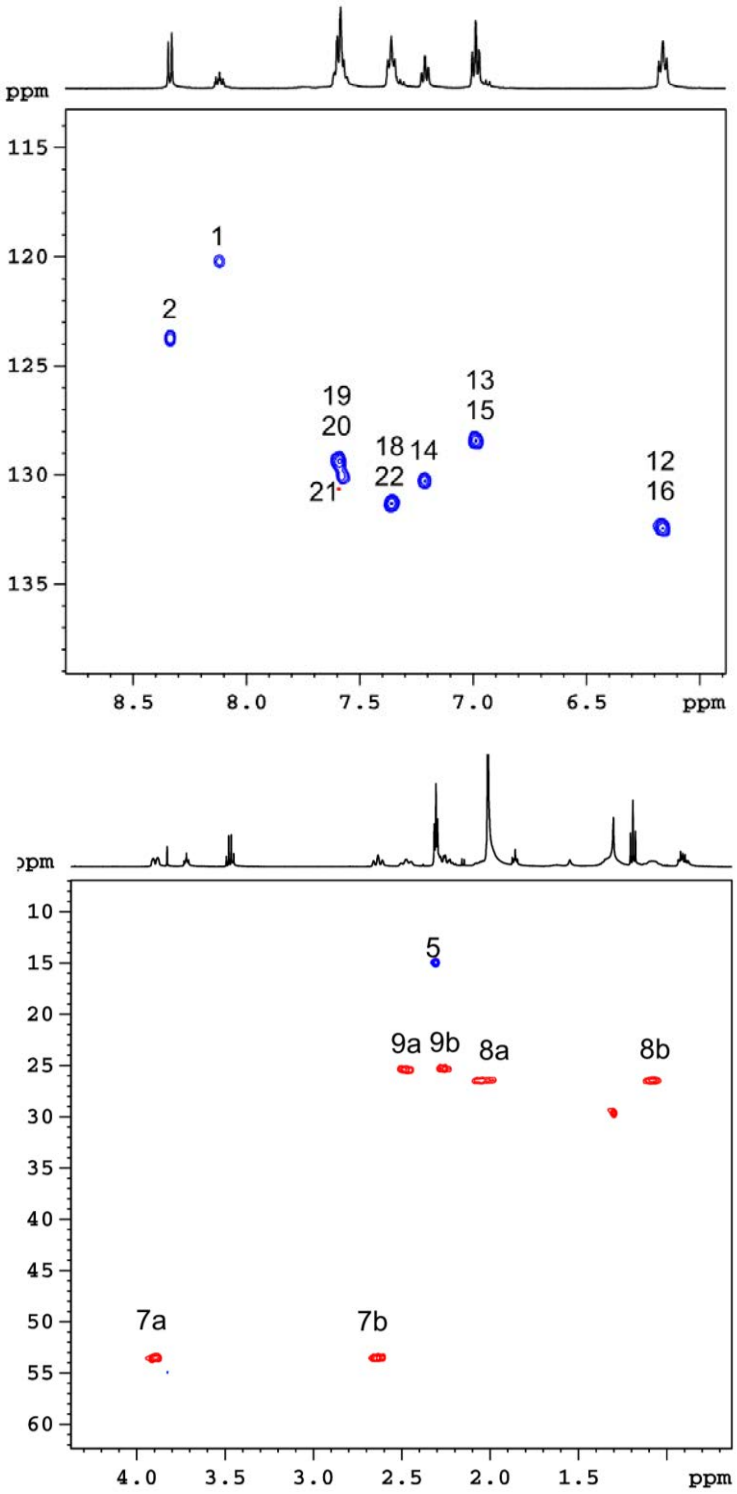

Figure S5. HSQC spectra of **3**(BF_4) (CD_2Cl_2, 298 K).

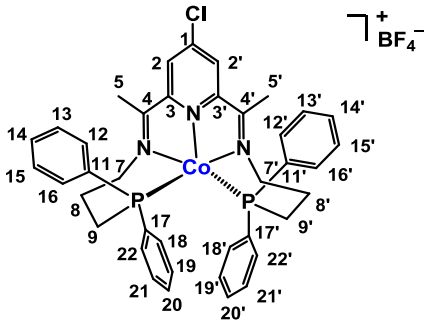
Cl
+
BF4−
Co
N
P

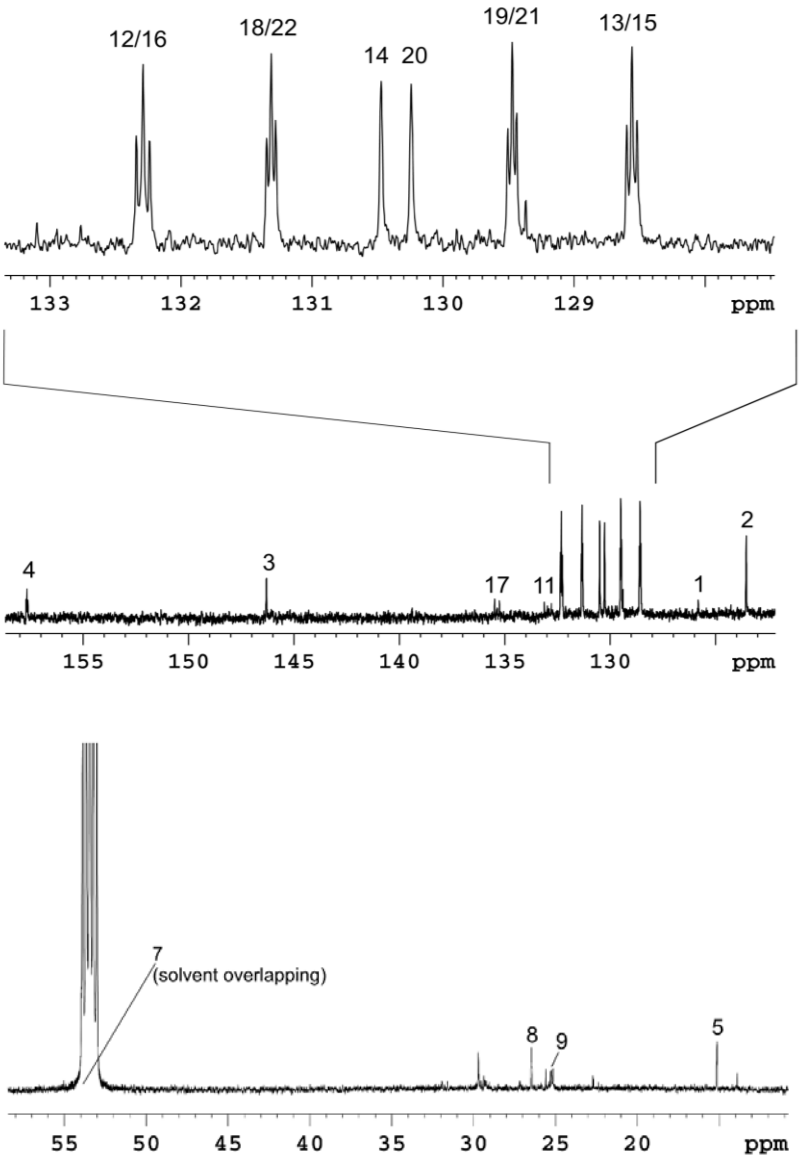
12/16
18/22
14 20
19/21
13/15
133
132
131
130
129
ppm
4
3
17
11
1
2
155
150
145
140
135
130
ppm
7
(solvent overlapping)
8
9
5
55
50
45
40
35
30
25
20
ppm

Figure S6. ^{13}C {^{1}H}NMR spectrum of **4**(BF_4) (126 MHz, CD_2Cl_2, 298 K).

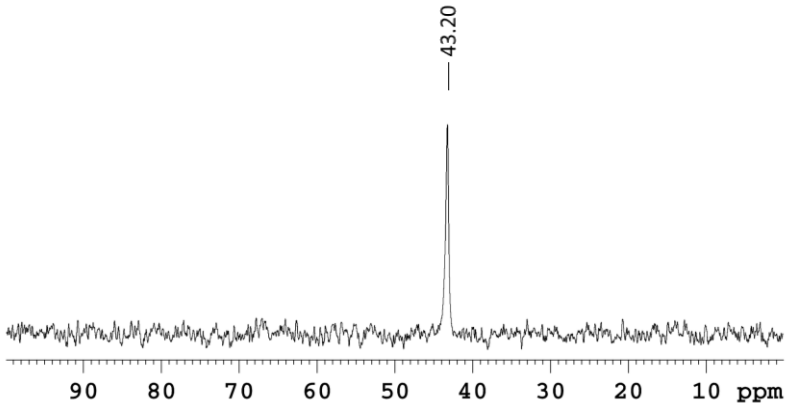

Figure S7. ^{31}P {^{1}H} NMR spectrum of **4**(BF_4) (162 MHz, CD_2Cl_2, 295 K).

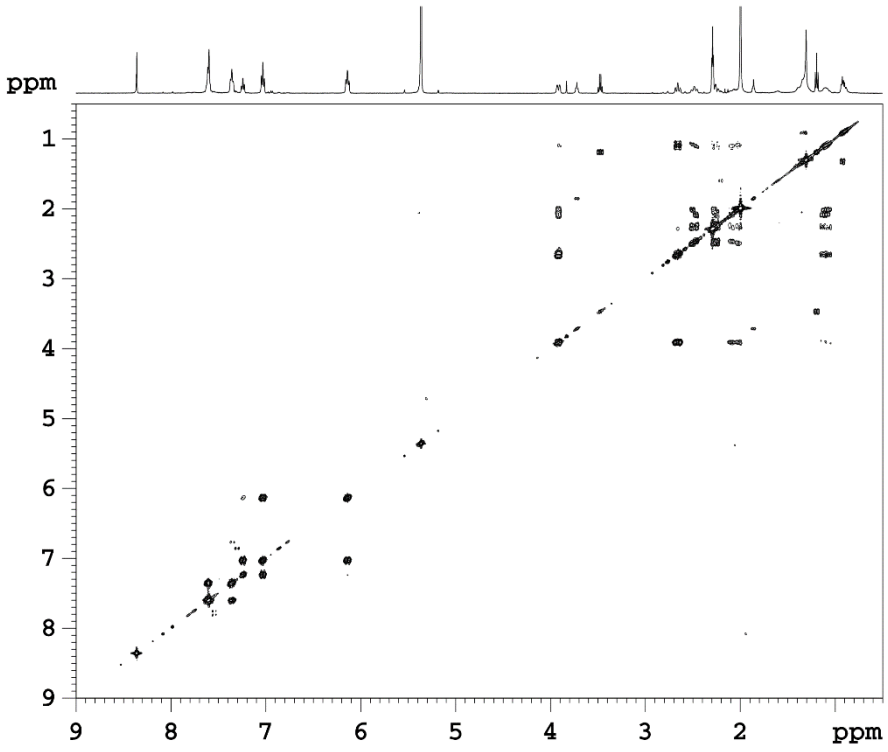

Figure S8. COSY spectra of **4**(BF_4) (500 MHz, CD_2Cl_2, 298 K).

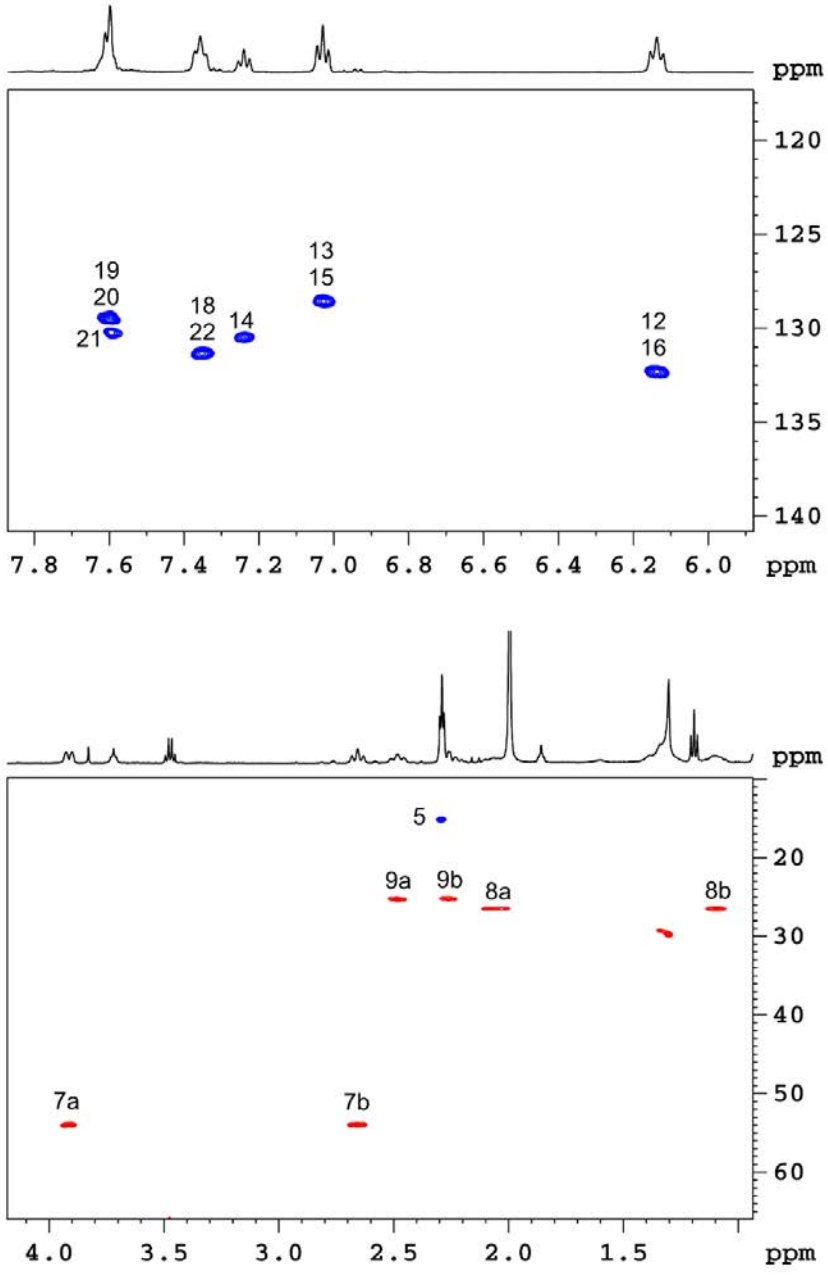

Figure S9. HSQC spectra of **3**(BF_4) (CD_2Cl_2, 298 K).

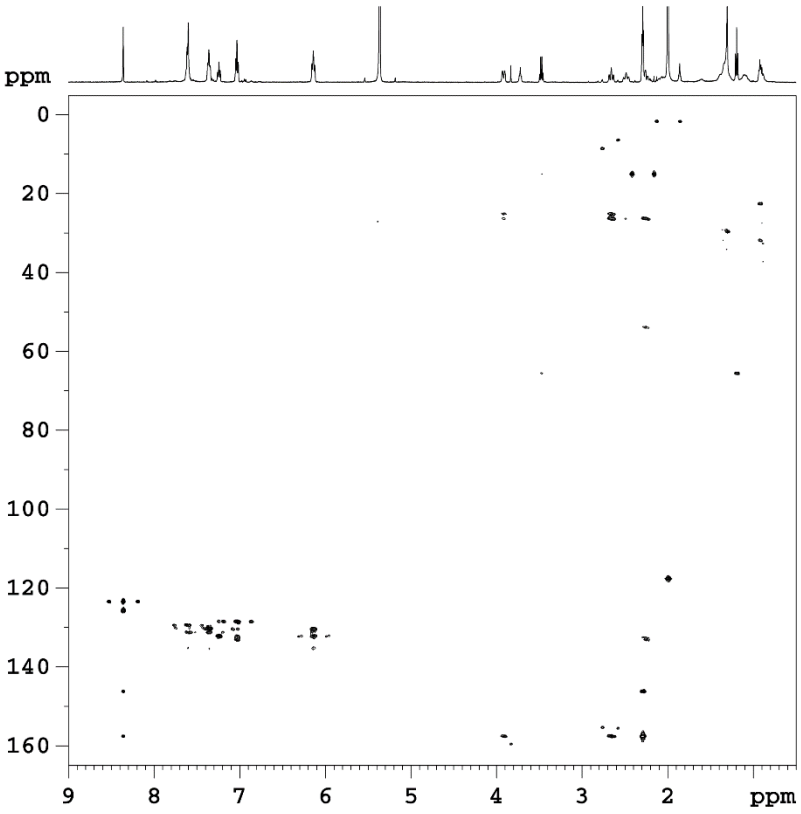

Figure S10. HMBC spectra of **4**(BF_4) (CD_2Cl_2, 298 K).

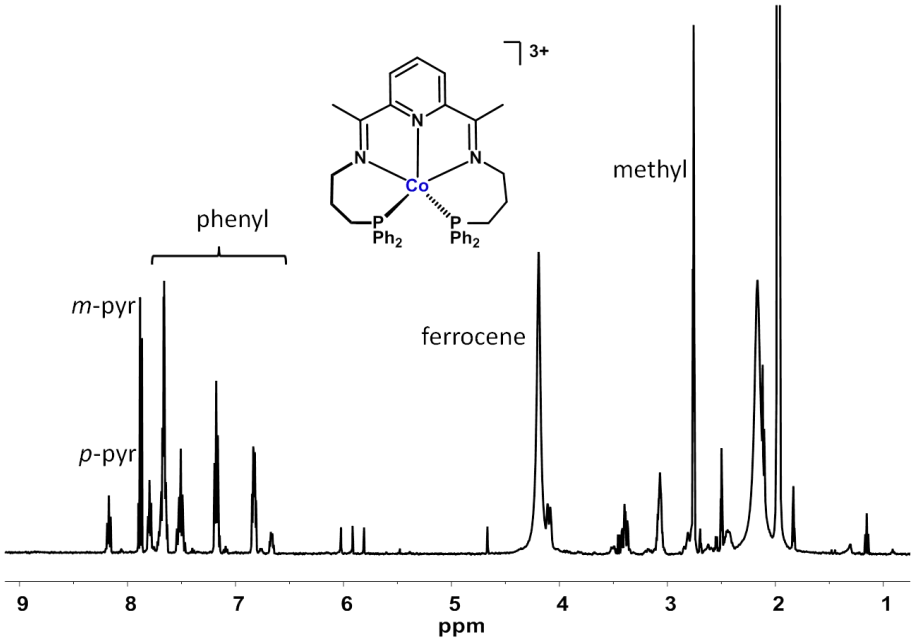

Figure S11. ^{1}H NMR spectrum (500 MHz, CD_3CN, 298 K) of Co(III) species after reaction of **3**(BF_4) with two eq. of $FcBF_4$.

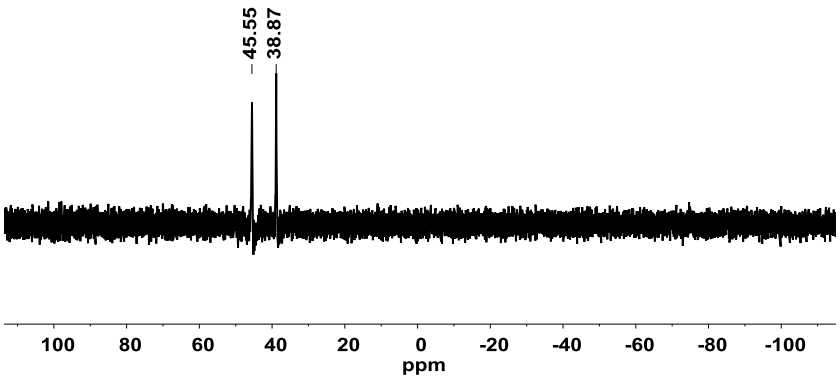

Figure S12. $^{31}P\{^{1}H\}$ NMR spectrum (162 MHz, CD_3CN, 300 K) of **3**(BF_4) in the presence of 25 eq. of *p*-TsOH, showing a mixture of Co^{I} and Co^{III}-H species.

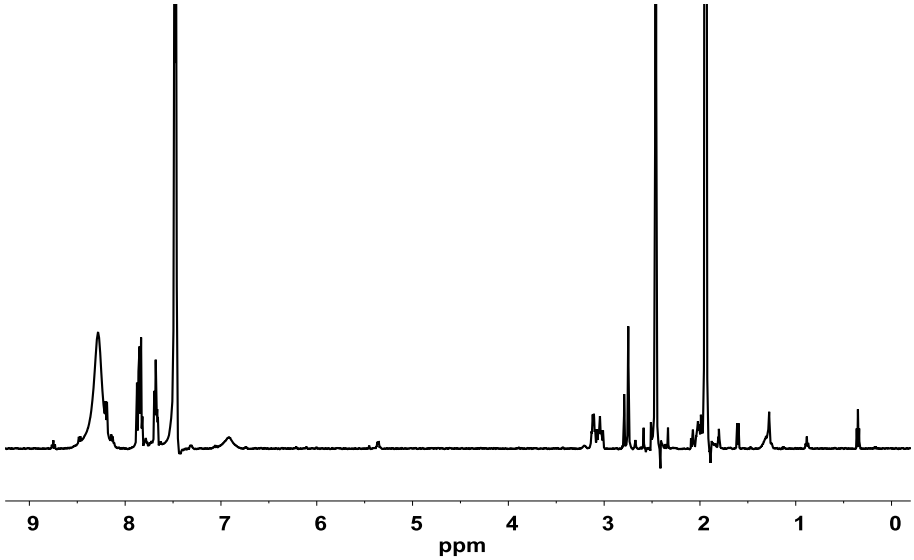

Figure S13. ^{1}H NMR spectrum (500 MHz, CD_3CN, 300 K) of resulted colorless solution of **3**(BF_4) exposured in 25 eq. of *p*-TsOH for days.

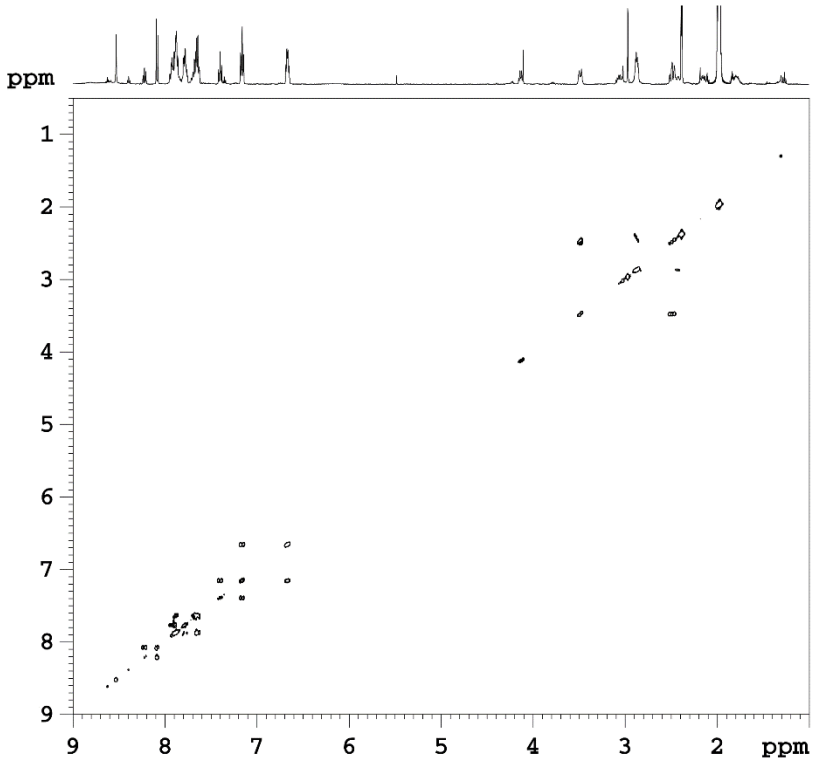

Figure S14. COSY spectra of $\mathbf{5}^{2+}$ (500 MHz, CD_3CN, 298 K).

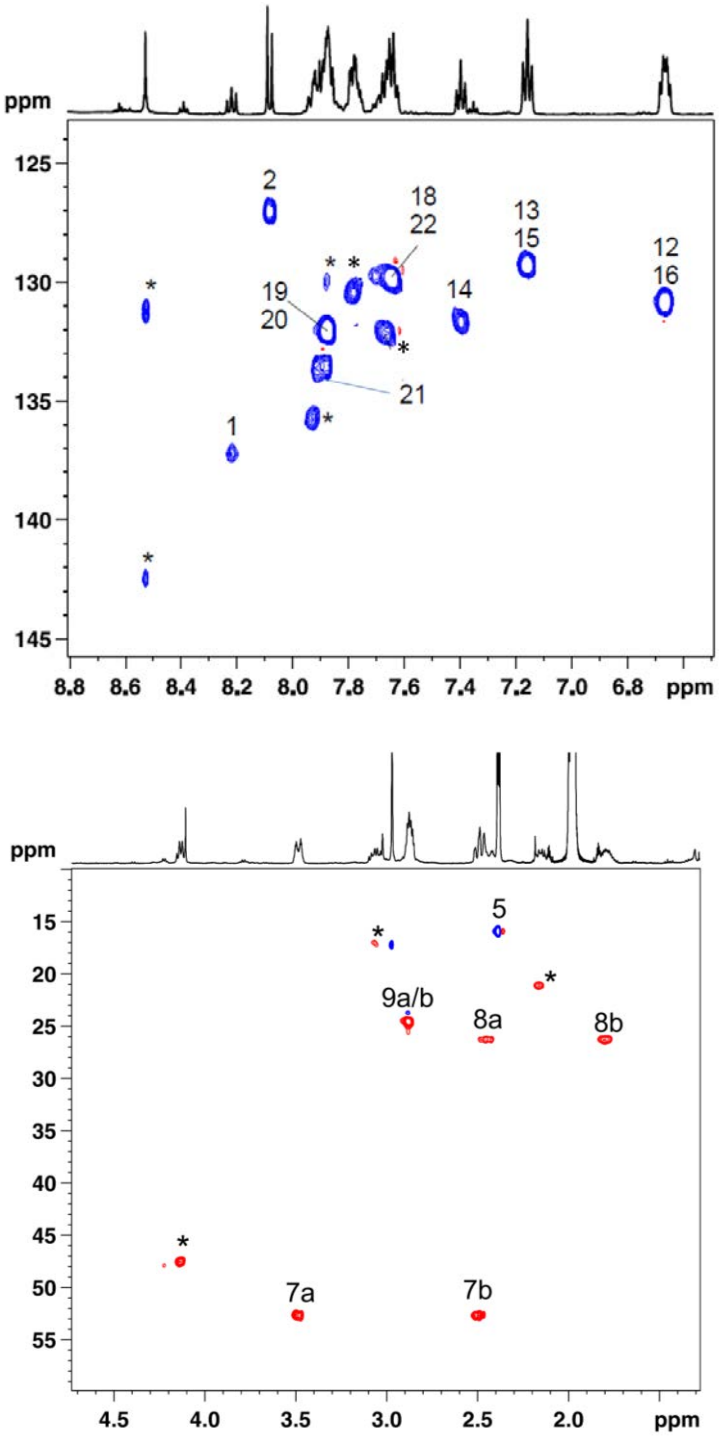

Figure S15. HSQC spectra of $\mathbf{5}^{2+}$ (CD_3CN, 298 K), asterisk indicates impurity.

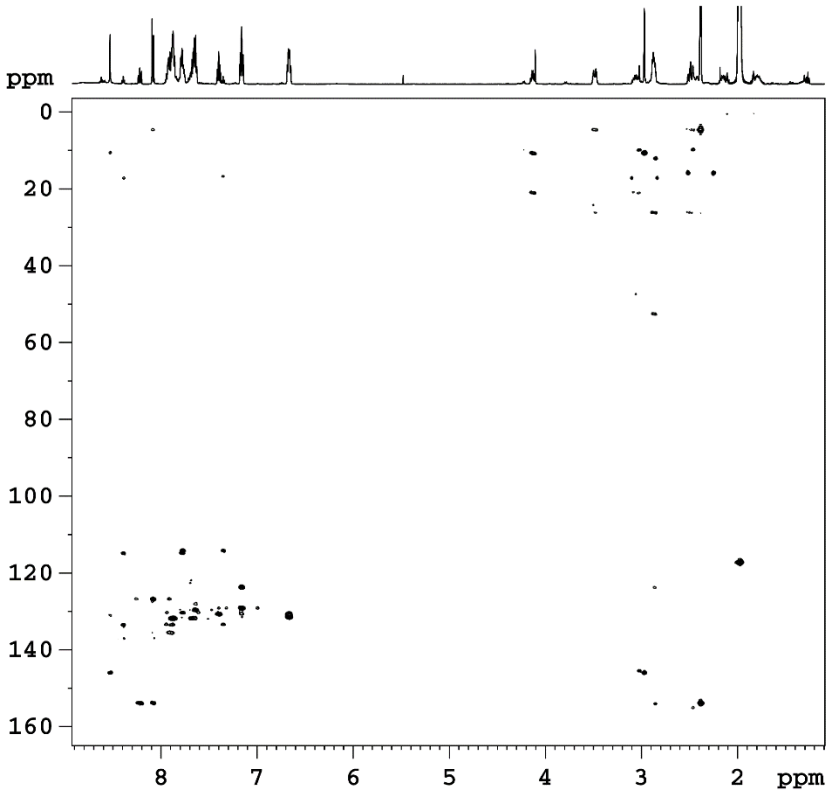

Figure S16. HMBC spectra of $\mathbf{5}^{2+}$ (CD_3CN, 298 K).

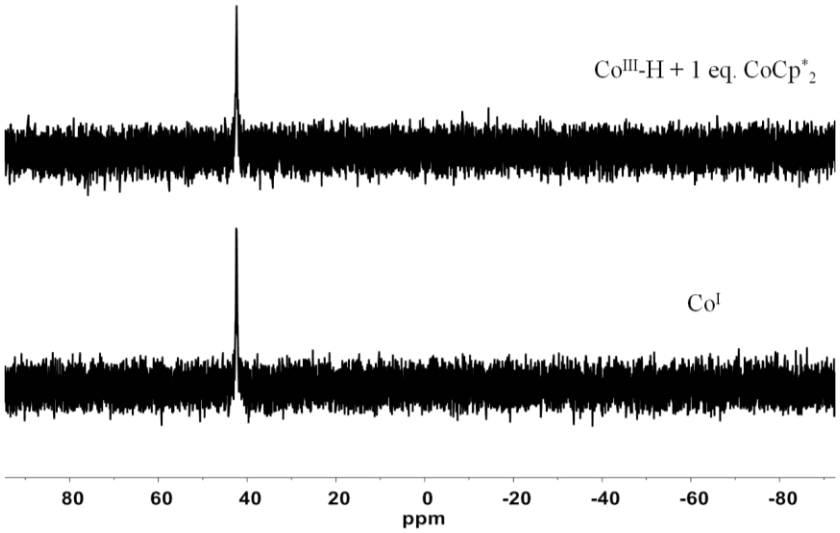

Figure S17. $^{31}P\{^1H\}$ NMR spectra (162 MHz, CD_3CN, 300 K) of Co(I) complex **3**(BF_4) (bottom) and species formed after 1 eq. $CoCp^*_2$ was added to Co^{III}-H (top).

B- Mass Spectrometry

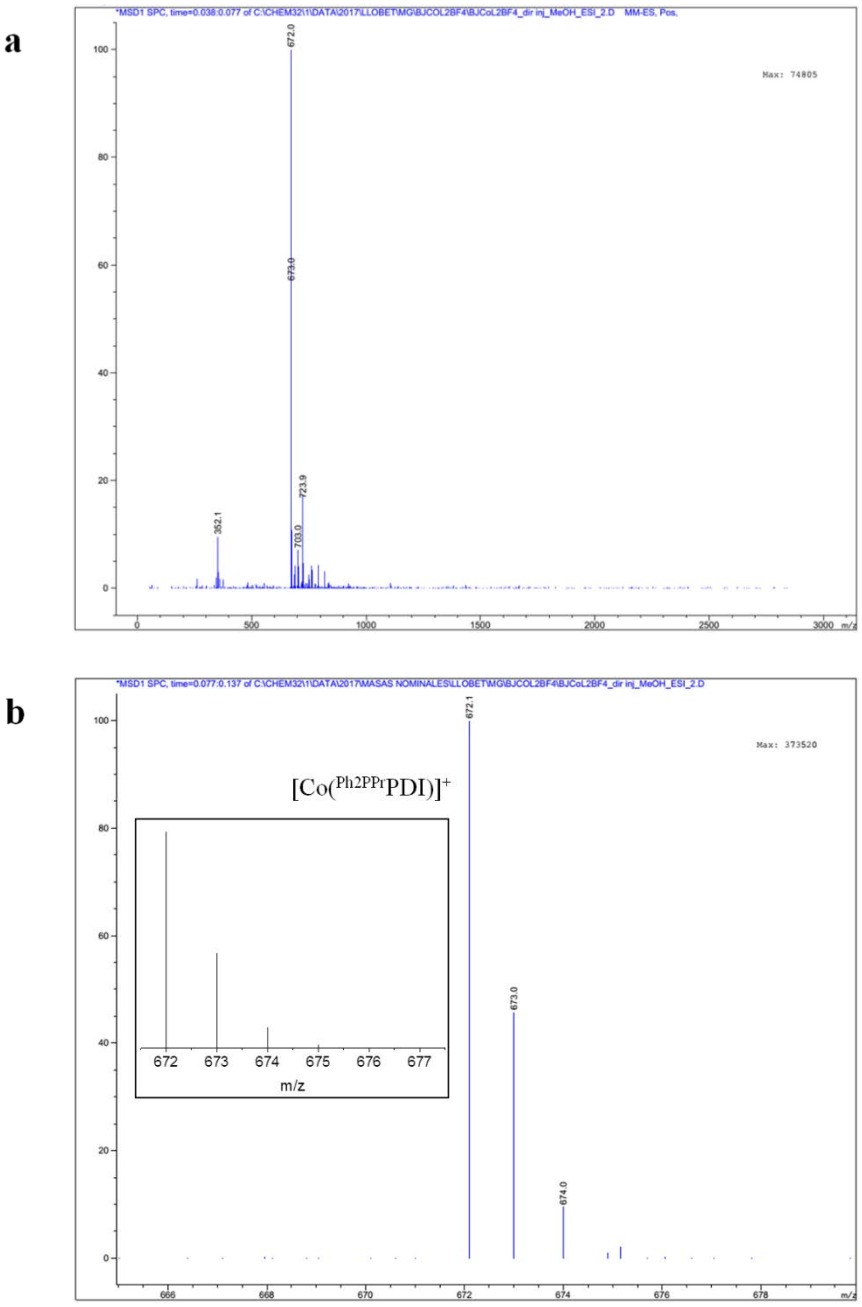

Figure S18. Experimental ESI-MS spectra for **3**(BF_4) (a) and zoom of the main peak m/z = 672.2 $[Co(^{Ph2PPr}PDI)]^+$ (b, inset is the isotope pattern simulation).

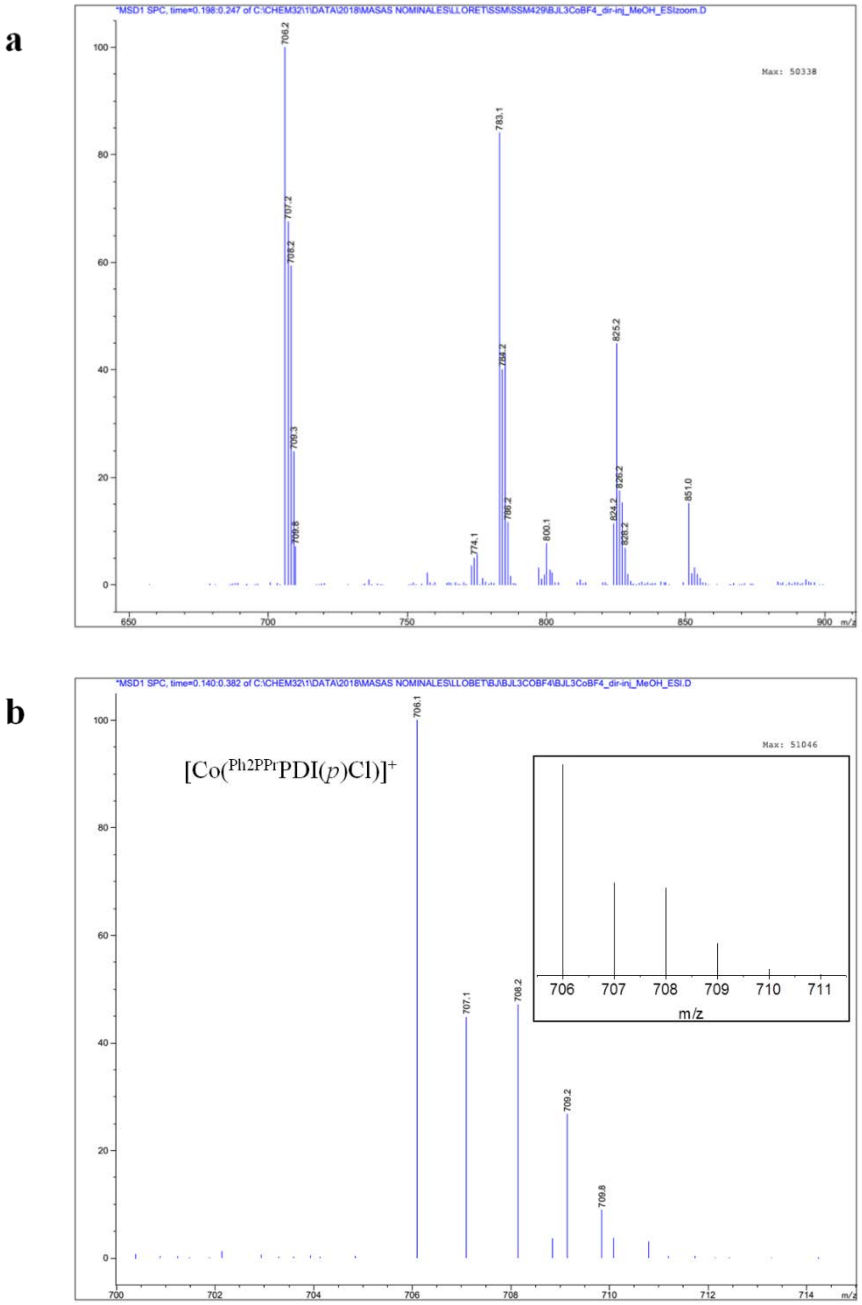

Figure S19. Experimental ESI-MS spectra for **4**(BF_4) (a) and zoom of the main peak m/z = 706.1 $[Co(^{Ph2PPr}PDI(p)Cl)]^+$ (b, inset is the isotope pattern simulation).

C- UV-vis Spectroscopy

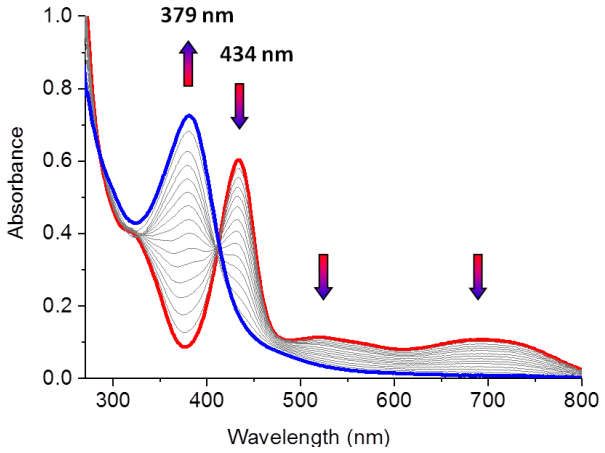

Figure S20. UV-vis monitoring of the addition of Fc^{+} to a DMF solution of **3**(BF_4) (red line) forming Co^{III} species (blue line). Arrows indicate the change of absorbance.

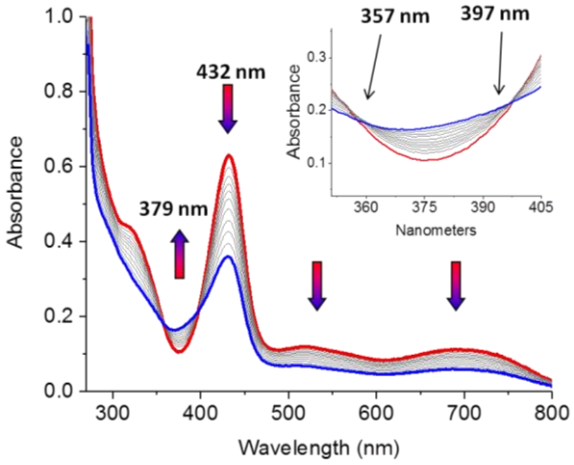

Figure S21. Effect of addition of 250 eq. of *p*-TsOH on the UV–vis spectrum of **3**(BF_4) (red line) in MeCN during 90 min. Arrows indicate the change of absorbance.

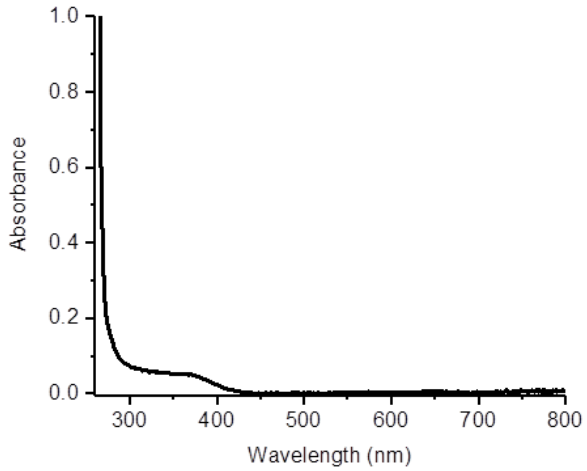

Figure S22. UV-vis spectrum of **3**(BF_4) reacting with 250 eq. of *p*-TsOH in DMF for 14 h.

D- X-ray diffraction data

Table S1. Crystal data and structure refinement for **3**(BF_4).

Identification code	**3**(BF4)
Empirical formula	$C_{39}H_{41}BCoF_4N_3P_2$
Formula weight	759.43
Temperature	100(2) K
Wavelength	0.71073 Å
Crystal system	Monoclinic
Space group	P2(1)/n
Unit cell dimensions	a = 14.0122(2)Å α = 90°.
	b = 12.86090(10)Å β = 105.3240(10)°.
	c = 20.7398(2)Å γ = 90°.
Volume	3604.63(7) $Å^3$
Z	4
Density (calculated)	1.399 Mg/m^3
Absorption coefficient	0.619 mm-1
F(000)	1576
Crystal size	0.20 x 0.15 x 0.10 mm^3
Theta range for data collection	2.237 to 40.068°.
Index ranges	-24<=h<=25,-23<=k<=22,-37<=l<=36
Reflections collected	123855
Independent reflections	22056[R(int) = 0.0441]
Completeness to theta =40.068°	98.299995%
Absorption correction	Multi-scan
Max. and min. transmission	0.941 and 0.724
Refinement method	Full-matrix least-squares on F^2
Data / restraints / parameters	22056/ 0/ 453
Goodness-of-fit on F^2	1.032
Final R indices [I>2sigma(I)]	R1 = 0.0315, wR2 = 0.0808
R indices (all data)	R1 = 0.0414, wR2 = 0.0844
Largest diff. peak and hole	0.662 and -0.602 e.$Å^{-3}$

Table S2. Crystal data and structure refinement for **4**(BF_4).

Identification code	**4**(BF4)
Empirical formula	$C_{39}H_{41}BClCoF_4N_3O_{0.50}P_2$
Formula weight	802.88
Temperature	100(2) K
Wavelength	0.71073 Å
Crystal system	Monoclinic
Space group	P2(1)/n
Unit cell dimensions	a = 14.5478(5)Å α = 90°.
	b = 13.9042(5)Å β = 98.2051(9)°
	c = 18.5768(7)Å γ = 90°.
Volume	3719.2(2) $Å^3$
Z	4
Density (calculated)	1.434 Mg/m^3
Absorption coefficient	0.674 mm-1
F(000)	1660
Crystal size	0.20 x 0.20 x 0.20 mm^3
Theta range for data collection	1.836 to 31.531°.
Index ranges	-20<=h<=17,-10<=k<=20,-27<=l<=27
Reflections collected	33567
Independent reflections	12176[R(int) = 0.0240]
Completeness to theta =31.531°	98.0%
Absorption correction	Multi-scan
Max. and min. transmission	0.877 and 0.811
Refinement method	Full-matrix least-squares on F^2
Data / restraints / parameters	12176/ 0/ 471
Goodness-of-fit on F^2	1.037
Final R indices [I>2sigma(I)]	R1 = 0.0339, wR2 = 0.0843
R indices (all data)	R1 = 0.0447, wR2 = 0.0901
Largest diff. peak and hole	0.589 and -0.619 $e.Å^{-3}$

Chapter 5
General Conclusion

Chapter 3

1. A family of pentadentate N_3P_2-PDI ligands have been synthesized, and two new Ni complexes with general formula $[Ni^{II}\mathbf{L}(Cl)](Cl)$ (**L** = ^{Ph2PPr}PDI, ^{Ph2PPr}PDI(*p*)Cl, **1**(Cl) and **2**(Cl), respectively) have been prepared by reacting **L** with the metal precursor $NiCl_2{\cdot}6H_2O$ in EtOH.

2. The Ni complexes **1**(Cl) and **2**(Cl) have been fully characterized by spectroscopic and electrochemical techniques, ESI-MS, elemental analyses, UV-vis, X-ray diffraction and CV. Though the two complexes adopt similar distorted octahedral geometries, the PDI Cl-substituted complex $[Ni^{II}(^{Ph2PPr}PDI(p)Cl)(Cl)](Cl)$ (**2**(Cl)) shows a shift in all redox potentials to a more positive region. This effect is particularly significant for the redox processes centered on the ligand (ligand-based reductions).

3. As revealed by EPR, when $[Ni^{II}(^{Ph2PPr}PDI)(Cl)](Cl)$ (**1**(Cl)) is one-electron reduced in organic solvents, a Ni(I) species is formed. As evidenced by CV analysis and supported by DFT calculations, the metal-based one-electron reduction of **1**(Cl) is followed by a coupled chemical reaction where a Cl ligand dissociates, forming the pentacoordinated $[Ni^{I}(^{Ph2PPr}PDI)]^+$ complex $[\mathbf{1} - Cl]^+$. Further one-electron reduction of this pentacoordinated species takes place in the PDI ligand scaffold (ligand-based reduction). Both DFT calculations and CV simulation support the experimental findings and the proposed mechanism.

4. Both **1**(Cl) and **2**(Cl) have been tested with regard to their ability to reduce protons to dihydrogen in organic media (DMF) and with *p*-TsOH as proton source. **2**(Cl) is superior to **1**(Cl) in terms of overpotential (c.a. 140 mV) due to the presence of the electron-withdrawing Cl substituent in the PDI ligand scaffold. However, **1**(Cl)

exhibits higher catalytic activity from the point view of TOF (54 s^{-1} vs. 16 s^{-1} for **2**(Cl)) and rate constants (1.54×10^4 $M^{-2}s^{-1}$ vs. 7.20×10^3 M^{-2} s^{-1}).

5. Kinetic studies showed that the HER is first order to the nickel complex concentration and second-order to the acid concentration, presenting an overall third-order reaction.

6. Both catalytic systems are molecular in nature according to the rinse test and the linear dependence of i_{cat} versus $v^{1/2}$.

7. During the course of controlled potential electrocatalysis for hydrogen evolution, the generation of new species capable of reducing protons at lower overpotentials and oxidize H_2 are observed electrochemically when employing both **1**(Cl) and **2**(Cl) as electrocatalysts. The short-live nature and low concentration of these new species formed under catalytic turnover prevented its further characterization through spectroscopic techniques.

Chapter 4

1. Two new Co complexes containing the PDI-based ligands ^{Ph2PPr}PDI or ^{Ph2PPr}PDI(*p*)Cl (from now on **L**) have been prepared in low yields by using $Co(BF_4)_2{\cdot}6H_2O$ as metal precursor and thoroughly characterized by multiple techniques. NMR spectroscopy, X-Ray diffraction, ESI-MS and elemental analyses have confirmed their general formula as [Co^I**L**](BF_4), with the Co^I metal ion laying in a distorted trigonal-bipyramidal environment.

2. A disproportionation reaction of Co^{II} to Co^I and Co^{III} species has been proposed to be at the origin of both, the unexpected Co^I oxidation state that present the isolated complexes and the low yield in which they have been obtained.

3. Complex [Co^I(^{Ph2PPr}PDI(*p*)Cl)](BF_4) (**4**(BF_4)), bearing the Cl-substituted PDI scaffold, exhibits more positive redox potentials in the absence of acid and lower overpotentials

under electrocatalytic acidic conditions than complex [Co^{I}(^{Ph2PPr}PDI](BF_4), **3**(BF_4), bearing the unsubstituted ligand.

4. In the presence of *p*-TsOH as proton source, the partial formation of Co^{III}-H species from the Co(I) complex **3**(BF_4) has been uncovered by UV-vis and NMR spectroscopy. The use of the stronger acid trifluoromethanesulfonimide (TFSI) allowed to complete the reaction at a practical rate and attain pure Co^{III}-H species (**5**$^{2+}$) that were fully characterized by UV-vis spectroscopy and NMR analysis.

5. The Co^{III}-H species **5**$^{2+}$ is stable in acidic solution and does not evolve H_2 spontaneously. The addition of a reducing agent, in this study $CoCp^*_2$, has been found to be necessary to reduce **5**$^{2+}$ and further evolve dihydrogen. Thus, one-electron reduction of **5**$^{2+}$ by the addition of 1 equivalent of $CoCp^*_2$ allows recovering the initial Co^{I} complex, as confirmed by both ^{1}H and ^{31}P{^{1}H} NMR. The full regeneration of the original Co^{I} species from the Co^{II}-H intermediate in acidic conditions advocate for a homolytic mechanism for HER by this system.